

**CRANFIELD UNIVERSITY**

**S HERRING**

**DESIGN & EVALUATION OF TURBINES FOR USE IN OWC POWER  
PLANTS**

**SCHOOL OF ENGINEERING**

**PhD THESIS**



**CRANFIELD UNIVERSITY**

**SCHOOL OF ENGINEERING**

**PhD THESIS**

**Academic Year 2006-2007**

**S HERRING**

**The design and evaluation of turbines for use in OWC power plants**

**Supervisor: P. Pilidis**

**February 2007**



## **Abstract**

The thesis describes the work carried in developing a process for designing an impulse turbine for use in an Oscillating Water Column power plant, and the design, commissioning, and use of a unique laboratory-based test facility for evaluating such turbines. The test facility is unique both in enabling a wide range of oscillatory flow conditions to be simulated, and in being of a sufficiently large scale to give confidence in the performance results obtained. The use of the test facility to gather performance data for a datum turbine configuration is described and results presented which show good agreement between the predicted and measured performance. In addition to this, the development of a novel turbine configuration which is expected to lead to a step-change in the performance of such devices, and a proof-of-concept turbine configuration which is to be tested in the facility are described. The work has led to a number of conclusions and recommendations for further improvements to both the turbine design and the test facility.



## **Acknowledgements**

The author would like to acknowledge the support of Peter Brotherhood Ltd. and the Department of Trade and Industry in making the work described in this thesis possible. He would also like to express his thanks to all his colleagues at Cranfield University and Peter Brotherhood Ltd., whose work has contributed to the rapid progress and success of the HydroAir project.

## List of contents

List of contents.....	
List of figures.....	
Notation.....	
Abbreviations.....	
1. Introduction.....	1
1.1 Background.....	1
1.2 Structure of thesis.....	2
1.3 Author's contribution.....	2
2. Literature Review.....	4
2.1 OWC devices.....	4
2.1.1 Objectives.....	4
2.1.2 Current Position.....	4
2.1.3 Types of OWC Installation.....	5
2.1.4 Details of current OWCs.....	8
2.1.5 Design of Current OWCs.....	9
2.1.6 Wave Energy Levels.....	10
2.1.7 Summary.....	13
2.2 OWC Turbine Review.....	14
2.2.1 Objectives.....	14
2.2.2 General Requirement.....	15
2.2.3 Overview of turbines considered for OWC power plants.....	15
2.2.4 The Denniss-Auld Turbine.....	17
2.2.5 Reaction Turbine.....	18
2.2.6 The Wells turbine.....	19
2.2.7 Impulse Turbine.....	26
2.2.8 Comparison of performances of Wells & Impulse turbines.....	39
2.2.9 HydroAir Performance Requirements.....	45
2.2.10 Conclusions.....	48
2.3 OWC Turbine Test Facilities.....	50
2.3.1 General.....	50
2.3.2 The Saga University test facility.....	50
2.3.3 The Limerick University Test facility.....	52
2.3.4 Summary.....	53
2.4 Scaling.....	53
2.4.1 Non-dimensional parameters.....	53
2.4.2 Reynolds number effects.....	55
2.4.3 Frequency effects.....	57
2.4.4 Summary.....	64
3. Test Facility Development.....	66
3.1 Operating Principle and Sizing.....	66
3.1.1 Operating Principle for facility.....	66
3.1.2 General Arrangement.....	67
3.1.3 Sizing of flow generator.....	67
3.2 Instrumentation Requirements.....	69
3.2.1 Basic requirements.....	69

3.2.2	Instrumentation Specification .....	70
3.2.3	Software .....	72
3.3	Component Definition .....	73
3.3.1	Pressure Probes/Ports .....	73
3.3.2	Ducting General Considerations .....	74
3.3.3	Inlet/Outlet .....	75
3.3.4	Duct Bullet .....	77
3.3.5	Duct Conical Diffuser/Contraction .....	78
3.3.6	Porous Calibration Plate .....	79
3.4	Description of Test Facility .....	81
3.4.1	General Overview .....	81
3.4.2	The PWG .....	82
3.4.3	Drive System.....	83
3.4.4	Test Duct.....	85
3.4.5	Turbine Test Module.....	86
3.4.6	Power Off-take System.....	87
3.4.7	Description of PWG Control System.....	88
3.4.8	Instrumentation and Data Acquisition .....	92
4.	Commissioning of Test Facility.....	99
4.1	Fundamentals .....	99
4.1.1	Dimensions of PWG and swept volume .....	99
4.1.2	Development of PWG control system .....	99
4.1.3	Specification of ‘wave’ input parameters .....	100
4.1.4	Development of initial operating envelope.....	101
4.1.5	Cycle Repeatability .....	102
4.1.6	Sealing of PWG .....	104
4.1.7	Rig Adjustments.....	104
4.2	Installation of Porous plate .....	106
4.2.1	Envelope .....	106
4.2.2	Flow quality in PWG .....	107
4.3	Determination of Mass/Volumetric flowrate .....	113
4.3.1	Uncertainties .....	113
4.3.2	Range of Calibration .....	114
4.3.3	Transducer calibrations.....	115
4.3.4	Flow Uniformity .....	115
4.3.5	Transducer drift.....	121
4.3.6	Impact of Transducer Drift .....	124
4.4	Instrumentation Plane Discharge Coefficients.....	128
4.4.1	Procedure .....	128
4.4.2	Traverse data acquired .....	128
4.4.3	Effect of flowrate on CD.....	130
4.4.4	Effect of Period on CD .....	132
4.4.5	Final values of discharge coefficient .....	134
4.4.6	Pitot probe position for measuring flowrate .....	135
4.4.7	Mass/Volumetric Flowrate calibration .....	135
5.	Design of Datum Turbine .....	136
5.1	Turbine Design Point & Sizing.....	136
5.1.1	Objectives .....	136

5.1.2	Information used .....	136
5.1.3	Turbine Design Point .....	136
5.1.4	Turbine sizing .....	137
5.2	Development of Datum Turbine design.....	141
5.2.1	CFD analyses of baseline designs.....	141
5.2.2	Choice of datum turbine type.....	142
5.2.3	Aerodynamic specification .....	142
5.2.4	Basic design of rotor and guide vane blades.....	143
5.2.5	Development of Geometry of Datum Turbine.....	147
5.2.6	Design Characteristics of HydroAir Datum Turbine .....	153
6.	Oscillating flow simulation program .....	157
6.1	Fundamental equation .....	157
6.2	Developed Program .....	157
7.	Testing of Datum Turbine.....	159
7.1	Installation of Turbine.....	159
7.1.1	State of manufactured turbine .....	159
7.1.2	Turbine inertia and break-out Torque .....	160
7.1.3	Noise Measurements .....	161
7.1.4	Test Condition Noise Measurements .....	162
7.2	Performance Data.....	164
7.2.1	Test Conditions .....	164
7.2.2	Precautions in Testing.....	164
7.2.3	Test Procedure .....	166
7.2.4	Windage and bearing losses.....	166
7.2.5	Hysterisis.....	168
7.2.6	Actual RMS Flowrates.....	169
7.2.7	Range of flow ratios obtained .....	173
7.2.8	Instrumentation related observations .....	173
7.2.9	Starting Characteristic.....	175
7.2.10	Performance Data.....	175
7.2.11	Discussion of results .....	184
8.	Development of Concept for Advanced Turbine.....	187
8.1	Evaluation of Guide Vane Blowing.....	187
8.1.1	Concept .....	187
8.1.2	Computational mesh .....	188
8.1.3	Boundary Conditions .....	189
8.1.4	Results.....	191
8.1.5	Further Analyses .....	194
8.1.6	Discussion .....	196
8.1.7	Summary .....	198
8.2	Varying Radius Duct Concept .....	200
8.2.1	Physical Basis .....	200
8.2.2	Initial test case.....	203
8.2.3	Improved duct geometry .....	205
8.2.4	Increasing Efficiency by increasing duct length & offset.....	207
8.2.5	Further varying radius duct analyses .....	211
8.2.6	Effect of twisting stator blades .....	213
8.2.7	Effect of incorporating guide vane sweep and lean .....	214

8.3	Advanced Turbine Concept .....	215
9.	Definition of HydroAir Proof-of-concept turbine.....	216
9.1	Initial Considerations .....	216
9.2	Determination of test geometry .....	217
9.3	Specification of proof-of-concept turbine.....	219
10.	Discussion .....	220
10.1	General .....	220
10.2	Performance Data.....	221
10.3	Accuracy of test data.....	221
10.4	Test Facility Performance .....	222
10.5	CFD.....	223
10.6	Additional Turbine Performance Considerations .....	223
10.7	Boundary Layer Blowing.....	223
10.8	Further Increasing Turbine Performance & Scaling up of Results.....	224
10.9	Flow Regime & Frequency Effects.....	225
10.10	Development of simulation program .....	226
10.11	Wave-to-wire model & Control .....	227
11.	Conclusions.....	229
11.1	General Conclusions .....	229
11.2	Detailed Conclusions .....	229
11.2.1	Test Facility Performance .....	229
11.2.2	CFD Analyses .....	230
11.2.3	Turbine Design.....	231
11.2.4	Datum Turbine .....	231
11.2.5	Guide Vane Blowing.....	231
11.2.6	Noise .....	232
12.	Recommendations.....	233
12.1	Further development of turbine design .....	233
12.2	CFD Validation .....	233
12.3	Test Facility and Process Improvement.....	234
12.4	Data Analysis .....	236
12.5	Testing and Development of Control Strategies .....	236
12.6	Real Life Performance Effects.....	236
12.7	Guide vane blowing .....	237
12.8	Noise .....	237
	References.....	238
	Appendix A – Wave Spectra.....	243
A.1	Spectral Parameters.....	243
A.2	Long-crested Irregular waves .....	245
	Appendix B – Calculation of Efficiency.....	248
B.1	Definitions.....	248
B.2	Determination of total-to-static efficiency.....	249
	Appendix C – Scaling Spreadsheet calculations.....	250
C.1	Scaling Spreadsheet .....	250
C.2	Variation in test facility parameters .....	251
	Appendix D – Instrumentation Response .....	253
	Appendix E – Actual Test Facility Dimensions .....	255
	Appendix F - Matlab Input Parameter Code.....	257

Appendix G – Test Rig Configurations .....	260
G.1 Empty Duct .....	260
G.2 Porous Plate .....	260
G.3 Datum Turbine Duct Configuration.....	261
Appendix H – Evaluation of discharge coefficient.....	263
Appendix I - CFD Simulations of turbines .....	264
I.1 Baseline Wells Turbine Simulation .....	264
I.1.1 Baseline Wells turbine design.....	264
I.1.2 Derived Performance Data.....	264
I.1.3 Details of CFD model .....	265
I.1.4 Results.....	265
I.2.1 Baseline Impulse turbine design .....	267
I.2.2 Details of CFD model .....	267
I.2.3 Results.....	268
I.3.1 Input power coefficient .....	268
I.3.2 Torque coefficient.....	268
Appendix J – Turbine Design Procedure .....	274
J.1 Method and definitions .....	274
J.2 Inputs.....	275
J.3 Preliminary Calculations.....	275
J.4 Nozzle Calculations .....	276
J.5 Rotor Calculations .....	277
J.6 Blade dimensions .....	278
J.7 Stage Performance Calculations .....	278
Appendix K- Development of Rotor Blade Geometry .....	280
K.1 Profile 1.....	280
K.2 Profile 2.....	280
K.3 Profile 3.....	281
Appendix L - Derivations of system simulation equations.....	282
L.1 Basic Equation .....	282
L.2 Determination of power output from turbine.....	284
L.3 Variation in Generator RPM.....	285
Appendix M – Test Conditions for Datum Turbine.....	286
Appendix N - Calculation of turbulent Stokes parameter.....	287

## List of figures

<i>Figure 1 – The LIMPET OWC (Queen's University Belfast, 2002)</i> .....	10
<i>Figure 2 - Comparison of wave powers and heights deep water and near shore</i> .....	11
<i>Figure 3 – Range of wave heights and periods in deep and shallow water</i> .....	11
<i>Figure 4 - Variation in average wave power level with water depth and location (Thorpe, 1999)</i> .....	12
<i>Figure 5 – Variation in volumetric flow rate in NIO OWC plant (Setoguchi et al 2003)</i> .....	15
<i>Figure 6 – Denniss-Auld turbine (Oxford Oceanics, 2005)</i> .....	17
<i>Figure 7 - Performance of 8 blade, 1/3 scale Denniss-Auld turbine (Oxford Oceanics, 2005)</i> .....	18
<i>Figure 8 – Typical performance curves for a Wells turbine (a) Pressure drop-flow ratio (b) efficiency-flow relationship (Raghunathan, 1995)</i> .....	20
<i>Figure 9 – Effects of hub/tip ratio and solidity on ability of monoplane Wells turbine to self start (Raghunathan, 1995)</i> .....	21
<i>Figure 10 – Definition of pitch setting angle (Setoguchi, 2003)</i> .....	22
<i>Figure 11 – Configuration of test turbine (Setoguchi et al 2003)</i> .....	23
<i>Figure 12- Efficiency of Wells turbine with fixed guide vanes - pseudo-sinusoidal flow (Setoguchi, 2003)</i> .....	23
<i>Figure 13 – Velocity triangles for bi-plane Wells turbine without guide vanes (Raghunathan,1995)</i> .....	24
<i>Figure 14 – Efficiency characteristic for contra-rotating Wells turbine (Raghunathan, 1995)</i> .....	25
<i>Figure 15 – Rotor blade profiles a) simple profile b) elliptic profile (Setoguchi et al, 2001)</i> .....	27
<i>Figure 16 – Rotor inlet and outlet vector triangles</i> .....	28
<i>Figure 17 - Velocity contours on outlet guide vane of baseline impulse turbine design, showing large separated region adjacent to the pressure face</i> .....	28
<i>Figure 18 – Geometric definition of guide vanes (Setoguchi et al, 2001)</i> .....	29
<i>Figure 19 – Turbine mean efficiency characteristics under sinusoidally oscillating flow (Maeda, 1999)</i> .....	31
<i>Figure 20 – Impulse turbine with self-pitch controlled guide vanes (Setoguchi et al, 2001)</i> .....	32
<i>Figure 21 – Turbine characteristics in steady flow simple profile rotor with mono-vane (Setoguchi, 2001)</i> .....	33
<i>Figure 22 – Comparison of pitch angles for mono-vane and splitter guide vanes in reciprocating flow (Setoguchi, 2001)</i> .....	34
<i>Figure 23 – Impulse turbine with self-pitching linked guide vane arrangement (Setoguchi, 2001)</i> .....	34
<i>Figure 24 – Comparison of mean efficiencies in sinusoidal flow</i> .....	35
<i>Figure 25 – Test Irregular wave based on ISSC spectrum (Setoguchi et al)</i> .....	36
<i>Figure 26 – Comparison of turbine mean efficiencies (Setoguchi et al)</i> .....	36
<i>Figure 27 –Starting characteristics in sinusoidal flow (a) impulse turbine with self pitching guide vane and Wells turbine (b) impulse turbine with self pitching</i>	

<i>linked guide vanes and Wells turbine (c) impulse turbine with fixed guide vane and Wells turbine (Setoguchi, 2001)</i> .....	37
Figure 28 – Comparison of turbine torque coefficients (Kim, 2001) .....	40
Figure 29 – Comparison of input power coefficients (Kim, 2001) .....	41
Figure 30 – Comparison of conversion efficiency of wave energy (Kim, 2001) .....	42
Figure 31 – Comparison of wave heights in chamber (Kim, 2001).....	42
Figure 32 – Predicted and actual efficiency for Islay Wells turbine (Raghunathan, 1995) .....	43
Figure 33- Comparison of actual and predicted efficiency for LIMPET (QUB, 2002) .....	44
Figure 34 – Predicted efficiency characteristic for uni-directional impulse turbine (PBL).....	46
Figure 35 – Variation in time on-line with minimum wave height for operation.....	47
Figure 36 – Schematic of Saga University test rig (Setoguchi et al, 2003).....	51
Figure 37 – Cross section of turbine test section in Limerick University test rig (Danasekavan & Govardskhan) .....	52
Figure 38 – Variation of loss with Reynolds number (Horlock) .....	56
Figure 39 – Hysterisis effect on axial force coefficient (Raghunathan 1995).....	59
Figure 40 – Effect of frequency on cyclic efficiency (Raghunathan, 1995).....	59
Figure 41 – Effect of frequency and Reynolds number on pressure loss (Santhakumar) .....	61
Figure 42 – General arrangement scheme for PWG (Peter Brotherhood Ltd).....	67
Figure 43 – Predicted response of transducer on total pressure probe to 5kPa step input .....	74
Figure 44 – Location of HydroAir test facility in Test House 2 and 2-3 Link.....	81
Figure 45 – Basic Structure of PWG with outlet duct removed .....	82
Figure 46 – Pressure vessel and transition section .....	83
Figure 47 – Mounting of drive motor and gearbox .....	84
Figure 48- ABB VSD for driving the ABB SDM6B3 motor .....	84
Figure 49 – Basic test duct and outlet .....	86
Figure 50 – Installation of turbine test module in test duct.....	86
Figure 51 – Convertteam MV3000 and 37kW loadbank .....	87
Figure 52 – Keypads and HMI on Convertteam MV3000 .....	88
Figure 53 – Schematic of control and communication elements .....	89
Figure 54 – PLC associated modules and linkages.....	90
Figure 55 – Schematic of instrumentation system .....	92
Figure 56– Rotadata actuator with pitot probe mounted on instrumentation ring .....	93
Figure 57 – National Instruments SCXI Chassis and modules.....	94
Figure 58 – Flap position encoder .....	94
Figure 59 – Torquemeter and frequency to voltage converter .....	95
Figure 60 –Installation of torquemeter within turbine module .....	95
Figure 61 – Honeywell 26PCBFA1D differential pressure transducers.....	96
Figure 62 – Signal conditioning units for pressure transducer signals .....	96
Figure 63 – Heads of total pressure probes for Rotadata actuators .....	97
Figure 64 – Thermocouple recording total temperature in instrumentation ring.....	98
Figure 65 – Initial duct configuration .....	99
Figure 66 – Comparison of trapezoidal profiles for accelerations of 11 and 56 .....	102
Figure 67 – PWG test envelope with datum turbine installed .....	105

Figure 68 – PWG operating envelope with porous plate .....	106
Figure 69 – Comparison of PWG pressures low flow, long period.....	107
Figure 70 – Variation in PWG max/min pressure levels with RMS flowrate, for porous plate.....	109
Figure 71 – Variation in PWG pressure amplitude with peak incompressible flow rate .....	109
Figure 72 – Relationship between volumetric flowrates calculated from flap movements and pressure difference across porous plate .....	112
Figure 73 – Differences between total and static pressures and their averages for plane 1, data point 384 .....	117
Figure 74 – Differences between total and static pressures and their averages for plane 2, data point 384 .....	118
Figure 75 - Differences between total and static pressures and their averages for plane 1, data point 386 .....	119
Figure 76 – Differences between total and static pressures and their averages for plane 2, data point 386 .....	120
Figure 77 –Changes in rig temperatures during test.....	121
Figure 78 – Changes in plane 1 pressure transducer zero readings.....	122
Figure 79 – Change in plane 2 pressure transducer readings .....	123
Figure 80 – Effect of pressure transducer temperature drift, data points 384 & 390 .....	124
Figure 81 – Corrected dynamic pressure data for data points 384 and 390 .....	126
Figure 82 – Dynamic pressure data for data points 384 and 390 corrected by final method.....	127
Figure 83 – Instrumentation section velocity profiles $Q_{rms}=2.3 \text{ m}^3/\text{s}$ .....	130
Figure 84 – Velocity profiles taken for cycles of $Q_{rms}=1.77\text{-}2.65 \text{ m}^3/\text{s}$ .....	131
Figure 85 - Variation in derived discharge coefficient for rms flowrates of $Q=1.5 - 2.65 \text{ m}^3/\text{s}$ .....	132
Figure 86 – Velocity profiles for traverses taken at cycle periods of 5, 7, and 9 seconds.....	133
Figure 87 – Variation in discharge coefficients for traverses taken at cycle periods of 5, 7, and 9 seconds .....	134
Figure 88 – Effect of adding OGV on performance of Setoguchi baseline design....	144
Figure 89 – Static pressure distribution around stage with circular arc guide vanes (Banks).....	144
Figure 90 – Geometry of ‘Hockey stick’ guide vane .....	145
Figure 91 – Predicted characteristic for turbine with ‘Hockey stick’ guide vanes...	146
Figure 92 – Static pressure distribution through stage with ‘Hockey stick’ guide vane (Banks).....	146
Figure 93 – Flow separation on Hockey stick guide vanes operating as OGVs (Banks) .....	147
Figure 94 – Separation on airfoil guide vane.....	148
Figure 95 - Geometric definition of guide vanes .....	149
Figure 96 – Progression of efficiency results for pseudo-2-D simulations .....	150
Figure 97 – Two types of pseudo-2-dimensional solution .....	151
Figure 98 – Comparison of predicted efficiency of Cranfield datum turbine with geometries of Setoguchi et al. ....	153
Figure 99 – Geometry of datum turbine (2-D view) .....	154

Figure 100 – Simulation of $Q_{rms}=2.3$ , $T=7$ profile and datum turbine at 850 rpm...	158
Figure 101 – Finish and machining steps on rotor blisk.....	159
Figure 102 – dp182 run down of rotor speed and torque from datum wave profile .	161
Figure 103 – Positions of noise measurements .....	162
Figure 104 – Test data repeatability .....	165
Figure 105 – Rotor speed decay .....	167
Figure 106 - Hysterisis evaluation data .....	168
Figure 107 - Calculated rms flowrates for nominal rms flowrate of $1.77\text{m}^3/\text{s}$ .....	169
Figure 108 – Calculated rms flowrates .....	170
Figure 109 – Scatter in calculated rms flow rate date .....	171
Figure 110 – Relationship between actual and specified rms flowrate.....	172
Figure 111 – Variation in minimum average rpm achieved with actual rms flow rate .....	173
Figure 112 – Thermocouple readings at end of testing with $Q_{rms}=2.44\text{ m}^3/\text{s}$ .....	174
Figure 113 – $1.64$ and $1.99\text{ m}^3/\text{s}$ data.....	177
Figure 114 – $2.21$ and $2.44\text{ m}^3/\text{s}$ data.....	178
Figure 115- $Q_{rms} = 1.64$ and $1.99\text{ m}^3/\text{s}$ corrected data .....	180
Figure 116 – $Q_{rms} = 2.21$ and $2.44\text{ m}^3/\text{s}$ corrected data.....	181
Figure 117 – Datum turbine performance data $Q_{rms}=1.64\text{-}1.99\text{ m}^3/\text{s}$ .....	182
Figure 118 – Datum turbine performance data $Q_{rms} = 2.21$ and $2.44\text{ m}^3/\text{s}$ .....	183
Figure 119 – Growth of turbulent boundary layer .....	185
Figure 120 –Comparison of flowratio/period characteristics of 5 & 14 second waves .....	186
Figure 121 - Geometry of impulse turbine with airfoil guide vanes (Setoguchi et al, 2001) .....	187
Figure 122 - Plot of complete domain showing connectivity (extended inlet and outlet not shown). (Banks, 2006) .....	189
Figure 123 - Comparison of experimental and predicted efficiency characteristics for baseline turbine design .....	190
Figure 124 - Location of the slot used to blow air from (Banks) .....	190
Figure 125– Sensitivity of performance improvement to injection momentum .....	192
Figure 126 - Velocity contour plots around OGV without and with jet (Banks).....	192
Figure 127 - Streamline plot around OGV trailing edge for $C_\mu = 1.026$ demonstrating attached flow (Banks) .....	193
Figure 128– Graph of massflow ratio against pressure drop reduction ratio .....	193
Figure 129 – Locations of simulated jet (Banks).....	194
Figure 130 – Sensitivity of performance to injection momentum .....	197
Figure 131 – Velocity vectors for datum turbine geometry, $\phi = 1.0$ .....	200
Figure 132 -Flow annulus geometry for offset guide vane rows .....	201
Figure 133 – Initial geometry for datum blade design with varying radius duct, $h_r =$ $3.6$ , $h_r= 4$ .....	204
Figure 134 - Variation of efficiency with guide vane radial offset for axial duct length of $4h$ .....	205
Figure 135 – Modified duct geometry .....	206
Figure 136 – Effect of modifying duct geometry for axial duct length of $4h$ .....	206
Figure 137 – Efficiency characteristics for datum configuration & configuration with varying radius ducts.....	207
Figure 138 – Variation in efficiency with guide vanes at duct length of $5h$ .....	208

<i>Figure 139 – Variation in efficiency for duct lengths <math>h_l = 5</math> and <math>6</math> .....</i>	<i>208</i>
<i>Figure 140 – Variation in efficiency with number of guide vanes, <math>h_l = 6</math>, <math>h_r=7.91</math> ...</i>	<i>209</i>
<i>Figure 141 – Variation in number of guide vanes required for duct length <math>h_l = 6</math> ...</i>	<i>210</i>
<i>Figure 142 – Peak efficiency curves for ducts of length <math>5h</math> and <math>6h</math>.....</i>	<i>210</i>
<i>Figure 143 – Range of varying radius ducts analysed .....</i>	<i>212</i>
<i>Figure 144 – Effect of incorporating spanwise twist distribution into guide vanes ..</i>	<i>214</i>
<i>Figure 145 – Predicted effect of guide vane sweep on performance.....</i>	<i>214</i>
<i>Figure 146 – Predicted effect of guide vane lean on performance.....</i>	<i>215</i>
<i>Figure 147 – Annulus geometry of varying radius duct proof-of-concept build .....</i>	<i>217</i>
<i>Figure 148 – Schematic of components within design and evaluation process .....</i>	<i>220</i>
<i>Figure 149 – Power variations in PWG, instrumentation planes, and turbine shaft</i>	<i>228</i>
<i>Figure 150 – Difference between total-to-total, and total-to-static efficiency .....</i>	<i>248</i>
<i>Figure 151 – Scaling spreadsheet for Wells turbine .....</i>	<i>250</i>
<i>Figure 152 – Schematic of line-cavity system.....</i>	<i>253</i>
<i>Figure 153 – Trapezoidal approximation to Sine wave.....</i>	<i>258</i>
<i>Figure 154 – modified trapezoidal approximation to Sine wave.....</i>	<i>259</i>
<i>Figure 155 - Comparison of CFD and experiment baseline Wells turbine design ...</i>	<i>266</i>
<i>Figure 156 - Comparison of CFD and experiment for baseline impulse turbine design</i> <i>.....</i>	<i>269</i>
<i>Figure 157 - Plot showing streamlines and total pressure contour for <math>\phi = 0.3</math> (Banks)</i> <i>.....</i>	<i>270</i>
<i>Figure 158 – Comparison of predicted and measured efficiencies with flow coefficient</i> <i>(Dhanasekaran and Govardhan) .....</i>	<i>272</i>
<i>Figure 159 - Plot showing velocity contour around outlet guide vane for <math>\phi =</math></i> <i>0.7(Banks) .....</i>	<i>273</i>
<i>Figure 160 – Guide vane velocity vectors and angles .....</i>	<i>274</i>
<i>Figure 161 – Rotor velocity vectors and angles .....</i>	<i>274</i>
<i>Figure 162 – Definition of first rotor blade profiles.....</i>	<i>280</i>
<i>Figure 163 – Definition of second rotor blade profiles .....</i>	<i>281</i>
<i>Figure 164 – Definition of third rotor profile.....</i>	<i>281</i>

## Notation

$A_c$	cross-sectional area of air chamber
$A_t$	turbine flow passage area
$AR$	aspect ratio
$C_A$	input power coefficient
$C_T$	torque coefficient
$D_{tip}$	turbine tip diameter
$E$	kinetic energy
$G$	gap between planes of turbine
$H$	wave height (difference between peaks and troughs)
$H_s$	significant wave height
$H_{1/3}$	significant wave height
$K$	non-dimensional wave period ( $mr_R/H_{1/3}$ )
$Q$	volumetric flow rate
$S_r$	rotor blade space
$T$	period
$\bar{T}$	mean period in irregular flow
$T_e$	zero-up-crossing period/energy (mean) period
$T_e$	energy (mean) period
$T_p$	spectral peak period
$T_O$	torque
$Tu$	turbulence level at inlet to turbine
$T_Z$	zero-up-crossing period
$U$	rotational velocity at mean radius
$W$	work out
$X_I$	non-dimensional moment of inertia ( $I/\pi\rho_a r_R^5$ )
$b$	blade span
$c$	blade chord
$d$	depth of water
$f$	frequency of air flow
$g$	gravity
$h$	blade height
$h$	blade hub/tip ratio
$l$	chord length
$m$	area ratio ( $A_t/A_c$ )
$m_n$	the $n^{\text{th}}$ spectral moment
$p^*$	non-dimensional pressure drop $\Delta p / (\rho \omega^2 D_t^2)$
$r_R$	mean radius
$t$	time
$t_c$	tip clearance
$v$	wave velocity
$v_a$	mean axial velocity
$z$	number of rotor blades

$\Delta p$	total to static pressure drop
$\alpha$	porosity/absolute flow angle
$\beta$	relative flow angle
$\delta$	camber angle of guide vane
$\varepsilon$	error
$\varepsilon'$	Soderbergs loss coefficient
$\varepsilon''$	Soderberg's loss coefficient corrected for aspect ratio
$\varepsilon'''$	Soderberg's loss coefficient corrected for Re
$\phi$	flow ratio
$\gamma$	blade inlet/outlet angle for impulse turbine
$\eta$	efficiency
$\eta_s$	stage efficiency
$\lambda$	wavelength/sweep angle
$\lambda_n$	nozzle loss coefficient
$\mu$	viscosity
$\rho$	density
$\nu$	wave frequency/dynamic viscosity
$\rho$	density
$\rho_a$	density of air
$\sigma$	solidity
$\omega$	angular velocity of rotor

## Abbreviations

CU	Cranfield University
DTi	Department of Trade and Industry
EMEC	European Marine Energy Centre
ETSU	Energy Technology Support Unit
IEA	International Energy Agency
IPR	Intellectual Property Rights
ISSC	International Ship Structure Congress
HMI	Human Machine Interface
LIMPET	Land Installed Marine Powered Energy Transformer
NIOT	National Institute for Ocean Technology
OWC	Oscillating Water Column
PBL	Peter Brotherhood Limited
PLC	Programmable Logic Controller
PWG	Pneumatic Wave Generator
VSD	Variable Speed Drive
WEC	Wave Energy Converter/World Energy Council

# 1. Introduction

## 1.1 Background

The work reported in this thesis was conducted as part of the HydroAir Air Turbine Development project, which was jointly financed by the Department of Trade and Industry (DTi) and Peter Brotherhood Ltd (PBL). The project was scheduled to run between June 2005 and June 2007, and was concerned with the extraction of power from waves by the use of a turbine connected to an Oscillating Water Column (OWC). Although a considerable amount of research has been conducted into the design of OWC power plants over the past 30 years or so, the overall levels of wave-to-wire efficiency need to be considerably improved in order for such plants to become economically viable, and a major hurdle in achieving this is to greatly improve the efficiency of the turbine. The objective of the HydroAir project was thus to achieve ‘a dramatic reduction in cost per kWh of OWC devices through innovative integration of power electronics, turbine design, and control algorithms’(Peter Brotherhood Ltd. and Cranfield University, 2005). To achieve this, it was envisaged that a new turbine would be developed that could extract useful energy from a much broader range of sea states, and enabled a whole system efficiency of 65% to be achieved. This was a very ambitious target given the timescale of the project and experience with OWCs to date. Nevertheless, if it could be achieved it would leave PBL well positioned to exploit the technology due to the growth in activity in renewables in general, and the limited developments in wave energy in particular.

Whilst neither PBL, or Cranfield University (CU), had been involved in working with OWC devices previously, it was believed that a synergistic combination of PBL’s knowledge and experience in power take-off, and CU’s knowledge and experience in turbomachinery would lead to a breakthrough. In particular, it was believed that the work conducted by previous researchers had concentrated more on the design of the OWC itself than the detailed design of the turbomachinery, and that by applying their detailed knowledge of turbomachinery, and the advanced design principles employed in the design of blades for gas turbines, CU could significantly enhance the turbine performance. The other fundamental difference in the philosophy of the HydroAir project from that of previous studies was in its assumption that the turbine solution should be validated in an appropriate on-shore test facility, the design of which would be driven by CU’s experience in testing turbomachinery. The other critical role to be fulfilled by CU in developing the turbine solution was to rigorously establish an independent intellectual property (IPR) trail.

The overall management of the project resided with PBL, whilst the author led the activities at CU. With regard to the development of the test facility installed at CU, responsibility for sizing and geometric definition lay with CU, whilst PBL undertook the detailed design and manufacture. All the work concerned with the definition of the turbine geometries was undertaken at CU by, or under the direction of, the author.

## **1.2 Structure of thesis**

The thesis is divided into 12 sections which enables the work carried out to be described in a logical and structured manner. However, this is artificial, as in reality the project timescales were challenging and tasks were carried out in parallel rather than sequentially. This meant, for example, that whilst detailed definition of components for the test facility was being carried out, work was also progressing on the design of the datum turbine and exploration of further concepts.

Section 2 of the thesis describes the detailed literature review conducted. This is a substantial proportion of the thesis, and no apology is made for this. As noted in section 1.1 neither PBL or CU had been involved with OWC devices previously, and as the project not only required the development of a turbine concept and design methodology, but also the design and commissioning of a unique test facility a wide ranging literature review was required. In addition, the relative immaturity of OWC turbine and power take-off technology compared to other fields of study meant that a wide range of options needed to be considered.

Sections 3 and 4 describe the development and commissioning of the test facility. This follows the sequence of events in the project, which required that the development of the test facility commenced ahead of designing the first test turbine. The sizing process employed for the datum turbine is then best understood in this context, and so the facility is described first.

Sections 5 and 7 describe the design and testing of the datum turbine in detail. They are separated by Chapter 6 which describes the oscillating flow performance model which was a critical to evaluating the test data.

Sections 8 and 9 describe the work that led to the identification of the advanced turbine concept, and definition of the proof-of-concept geometry. Following this section there is a discussion of the results of the project before presentation of the conclusions and recommendations

.

## **1.3 Author's contribution**

Through carrying out the work presented in this thesis, the author has been instrumental in:

1. The development of a novel turbine configuration whose performance can dramatically reduce the cost per kWh of power from OWCs.
2. The definition and establishment of a unique test facility for testing turbines for OWCs under representative conditions and at a suitable scale.

The first of these has led to the application for a patent (Herring, Freeman, and Banks, 2006), whilst the second has included the definition and development of a suitable instrumentation system and data analysis process.

The degree of novelty within the project, need to protect the IPR generated, combined with the timescales for its completion, have meant that there has been little opportunity for the generation of publications. However, a paper on one aspect of the work was presented at a seminar (Banks and Herring, 2007), a further paper will be presented at the ASME ITGE & Turbo-Expo 2007, in Montreal (Herring and Banks, 2007a), and an abstract has been accepted for the 7<sup>th</sup> European Wave and Tidal Energy Conference (Herring and Laird, 2007).

## **2. Literature Review**

### **2.1 OWC devices**

#### **2.1.1 Objectives**

It is obvious that any turbine in a wave energy system will have to operate over a range of conditions, and that the annual power output depends upon the wave amplitudes and frequencies experienced. Consequently any turbine and power take-off solution needs to be matched to the range of conditions likely to be encountered, and an appreciation of the range of operating conditions was considered critical to the HydroAir project. This was especially important because of the intention to validate the turbine and power take-off solution in a purpose built test facility which needed to produce an appropriate range of conditions. To achieve this meant following a rigorous scaling process to size both the facility and the turbine. This approach was perhaps in contrast to that other researchers, who had appeared to put more emphasis on modelling and evaluating the OWC characteristics using wave tanks, and less on optimising the design of the pneumatic components attached to it. The initial objective of the literature search was thus to obtain an understanding of the state-of-the-art in terms of OWC development. The objectives included: identifying the range of OWC plants under consideration in terms of location and power output, the issues associated with turbine operation, and how the range of flow conditions varied with OWC location.

#### **2.1.2 Current Position**

The current UK government position is that renewable energies must inevitably become the world's main energy sources, as fossil fuels are depleted. Furthermore, they are needed to address the increasingly important issues of security of energy supplies, climate change, and environmental pollution. The government has set a target for renewable energy to provide 10 percent of UK electricity supplies as soon as possible with a '10% by 2010' renewables target, rising to 15% by 2015 and aspires to 20% by 2020. These targets form a crucial part of its strategy for realising a target reduction in greenhouse gas emissions of 12.5% by 2008-2012 (DTi, 1999). The magnitude of these targets have to be seen against the fact that in 1992 renewables provided less than 1% of the UK primary energy supply, compared to approximately 6% across the European Community (DTi, 1994).

Whilst at present there is only one 500kW OWC power plant in the UK, wave energy is attractive because if the correct technology can be found, then it potentially offers a large source of renewable energy which the UK has ready access to. It has been estimated that allowing for technical, practical and environmental limitations, wave energy could generate up to one sixth of the UK's electricity consumption, and that by 2020 the wave energy market in the UK could be worth £0.2 billion (South West Regional Development Agency). The reason that wave energy could provide such a large proportion of our energy requirements is that gravity waves store wave energy in a very dense form. For example, a one metre width of wave frontage around South

Uist in the Outer Hebrides delivers 500 times as much energy each year as could be gathered from sunlight falling on a flat horizontal surface (Mustoe, 1984).

At the second European Wave Power Conference in 1996 OWC systems were recognised as first generation devices due to their simple principle of operation and because they were closest to commercial maturity (Lewis, Fraenkel and Elliot, 1995). Despite this Perdigao and Sarmento (Perdigao and Sarmento, 2005) observed that after more than 20 years of R&D, wave energy was not competitive with other renewable forms of producing electrical energy, and that this applied in particular to OWC plants. For them to become viable and compete with other renewable energy sources, such as wind turbines, it is necessary for there to be a dramatic change in the design, construction, and material content of the plant and to operate at a load factors of at least 30% (WaveNet, 2003).

The high capital costs of wave energy systems are driven by the need to engineer them to withstand the extremely high loadings to which they may occasionally be subjected, and because of the hostile working environment experienced by both personnel and equipment during construction. Survivability is a much larger factor in wave energy projects than other renewable energy technologies, and is decisive in determining their success. Whilst the capital costs identified above are largely outside the scope of the current project, there is still a need to consider the likely capital cost of the turbine solution, and consideration of the load factor to be achieved is critical.

### **2.1.3 Types of OWC Installation**

Four types of OWC installation can be identified (DTi, 1994):

1. Shoreline OWCs – where the device is constructed on land at the shore or in cliffs.
2. Break-water OWCs – where the OWC is built into or close to a harbour break-water.
3. Near-shore OWCs – where the device is either floating or bottom mounted in 10-25m depth of water.
4. Off-shore OWCs - Floating OWCs moored in water depths greater than 40m.

Shoreline OWCs are referred to as first generation devices, whilst floating or off-shore devices are termed second generation, and fourth generation is used when referring to devices which rely upon technology which is not yet available (Wavenet, 2003). First generation shoreline devices are the only wave energy devices to have reached the large scale prototype stage, been deployed at sea, and have achieved significant operational use.

There are different issues associated with near-shore and off-shore OWC generating plants: for off-shore devices the high cost of connection to the grid and maintenance are major issues, but the energy resource is greater, whilst for near-shore/on-shore devices the infrastructure may be less costly, location better suited to developing systems, but energies are significantly lower and may be difficult to estimate with sufficient accuracy. Common issues are the lack of planning procedures and relevant

design codes, and the need for more information on operation to promote confidence in the longevity of OWC systems: that they can survive significant storms, withstand marine fouling and corrosion.

In 1985 the ETSU view was that large scale off-shore devices were unlikely to become economic in the foreseeable future, and that efforts should be concentrated on small-scale modular shoreline devices. This was because even though the largest part of the resource was off-shore, much of the basic technology needed to be developed and proven before it could be exploited, and this was best done at small-scale shore based sites. WaveNet also found that the moderate efficiency and limited potential for large scale application of shoreline devices meant that they would only be used in the initial development of technologies for application offshore, or in breakwater devices (WaveNet, 2003). This remains the situation, as the Marine Energy Challenge instigated by the Carbon Trust (CT) and carried out by ARUP and e-on (Webb, Seaman, and Jackson, 2005), performed a comprehensive critical review of OWC technology and concluded that *near-shore* OWCs could be developed within a reasonable timescale to provide renewable power generation within the UK framework, without needing additional government support. It also concluded that these devices could provide power to isolated communities. This re-iterated the finding of the DTi 1999 review, but added that shoreline installations were preferable in terms of power output cost for developments below 2MW, however, it was also concluded that a ‘concept shift’ such as Wavegen’s roof-only LIMPET was required to reduce costs to a level which would lead to the installation of a significant number of units.

An alternative to a stand-alone OWC for commercialising the technology is to reduce the cost of the pneumatic chamber by incorporating it into a breakwater (Pontes, Candido, Henriques and Justino, 2005; Martins, Siveira Ramos, Carrilho, Justino, Gato, Trigo and Neumann, 2005; Martins et al, 2005). The construction costs are then shared between the breakwater and the wave energy device. As well as producing some hydrodynamic advantages, this approach is said to provide a realistic alternative to traditional methods of coastal protection, and facilitates access for construction, operation, and maintenance of the plant. There are currently plans for a number of OWC/breakwater combinations to be built on the Iberian Peninsula, including one close to the city of Porto in northern Portugal (Gato, Justino and Falcao, 2005). However, this route appears to provide rather limited opportunities, as one of the main barriers identified to shoreline OWCs providing a significant part of the UK national power consumption was that from the (cursory) survey conducted, only 8km of the coastline was suitable for shoreline OWCs (Thorpe, 1999). This was in comparison to 141km of frontage which was suitable for near shore OWCs, which it was estimated could potentially supply 1.8 million households (7.8 TWh/annum). However, this is still small in relation to the amount of generating capacity required if wave energy is to become a significant component of the UK power supply.

A number of research and development priorities were identified by the Marine Energy Challenge and WaveNet for delivering the improvements required to make wave energy viable. Those of particular relevance to the HydroAir project were:

1. Comprehensive benchmarking of fixed-bladed turbine, guide vane, throttle valve and control systems using CFD tools validated against large-scale prototype devices followed by investigation into variable pitch blade control.
2. Development of performance standards for defining the performance characteristics of OWC installations to allow like-for-like comparisons.
3. Investment in the use of LIMPET as a proper test-bed for OWC technology.

These recommendations indicate a general need for a more rigorous approach both to the development and testing of turbine and power take-off solutions, and evaluating them in a calibrated facility. This is in agreement with the approach adopted by HydroAir.

It can be concluded that the relative immaturity of the technology cited above, coupled with the lack of experience and risk associated with developing off-shore installations, means that the general perception is that the basic technology of OWC devices needs to be developed and proven in relatively small-scale shoreline or near-shore facilities of less than 2MW, before it can be exploited in larger, more commercially viable, off-shore facilities.

The growth in ‘wet-renewables’ research and development is now leading to projects for off-shore devices, and the setting up of the infrastructure necessary to evaluate them. This is evidenced by the setting up of the European Marine Energy Centre (EMEC) in Orkney, and allocation of some of the government £50 million Marine Renewables Deployment Fund to the Wave Hub project, which is also backed by the South West Development Agency.

Wave Hub will provide a 30MW electrical ‘socket’, located in 50m of water some 10 miles off the north coast of Cornwall. The purpose of this is to expedite the commercialisation of arrays of Wave Energy Converters (WECs), by providing a sub-sea cable and grid connection, simplifying consents, and providing operational support (Gillanders and Taylor, 2005). The system will have a capacity of 30MW, which is divided between 4 power converters to allow different companies to ‘showcase’ their products. Although the hub is yet to be completed, 3 of the slots have already been taken up by: Ocean Prospect (with Pelamis), Ocean Power Technology (with powerBuoys), and Fred Olsen. Wave Hub illustrates the high cost associated with creating a grid connection, as the original cost of £15 million has now risen to £20 million due to price increases in labour and copper (Professional Engineering, 2006). Even when the infrastructure is in place, there remains a large amount of uncertainty to be addressed with respect to the cost effective operation and maintenance of such offshore systems, and further uncertainties with respect to permitting the development of such power plants (Previsic and Sacramento, 2005). From this it may be concluded that infrastructure will shortly exist in UK waters which will enable OWC buoys to be deployed and evaluated without incurring the substantial overhead costs of having to obtain consents and provide a grid connection. Nevertheless, before this step is taken, the basic technology needs to be proven to the degree that an installation of several MW could be designed which would have low maintenance requirements.

## 2.1.4 Details of current OWCs

The first OWC system was the ‘Kaimei’ wave power generator, built in 1978 for an International Energy Agency (IEA) experiment, under the auspices of Canada, Ireland, Japan, the UK and US. Kaimei was a 80m long by 12m wide barge which was initially fitted with 3 turbine-generator units, then later re-built with 7 turbine-generator units and tested in Japan in 1979-80. The collection efficiency was reported as 4% (World Energy Council, 1994). At present there are no fully commercial OWC plants operating in the world. There are, however, a number of large scale prototype OWC plants and these are listed in Table 1. OWCs are the only significant wave energy systems to have been deployed in the UK. The first was a 75kW device, from which a 500kW Land Installed Marine Pneumatic Energy Transformer (LIMPET) was later developed. Both of these devices were situated on Islay, off the west coast of Scotland.

Location	Device	Type	Generating capacity	Completed	Collector width (m)	Comments
Islay, UK	LIMPET	On-shore	500kW	2000	21.0	Coastal OWC
Pico, The Azores	PICO	On-shore	400kW	1999	12.0	Coastal OWC
Port Kembla Australia	Port Kembla	Near-shore	300kW	2005	36.0	Uses Dennis-Auld turbine
Vizhinjam, India	Vizhinjam, OWC	Break-water	150kW	1991	10.0	Built onto breakwater
Sakata Port, Japan	Sakata	Break-water	60kW	1989	20.0	5 chamber OWC built as part of harbour wall

*Table 1 – Currently Operational OWCs*

In addition the OWCs in the Table 1, it is worth mentioning the Ocean Swell Powered Renewable Energy (OSPREY) device. This is the largest prototype constructed to date. It was a near-shore bottom standing device which was to have been towed into position and sunk 100m off the coast of Dounreay in Scotland in 1995. It was designed to have a 2MW output from a 20.0 m width collector, but unfortunately, a large wave smashed open the ballast tanks during construction, and it had to be abandoned. OSPREY differed from the OWCs in Table 1, in that it was made of steel, rather than concrete. Another project worthy of mention was the Japanese ‘Mighty Whale’ floating OWC (which had a Wells turbine) was in operation from 1998-2002, although not connected to the grid.

It is apparent from the table that the maximum output of 400-500 kW of the currently operational OWCs is very modest. The performance of these devices in terms of

efficiency is shown in Table 2 (Webb et al, 2005). Table 2 shows that overall conversion efficiencies of the 2 OWCs for which actual performance data is available is less than 10%. Reports show that the efficiency of conversion was considerably over-estimated at every stage in LIMPET, and particularly with regard to the mechanical to electrical conversion process. These outputs and efficiencies can perhaps be put in context of the requirement, by comparing them with the Connah Quay combined-cycle gas turbine power station in Wales. This achieves 53% efficiency from 4 generating units, including the 1,420MW Unit 4, whilst Unit 1 has achieved 99.6% availability over a decade of operation (Professional Engineering, 2006).

Device		Efficiency of energy conversion process			
		Wave to pneumatic	Pneumatic to mechanical	Mechanical to electrical	Overall
LIMPET	Estimated	80	60 (average)	100	48
	Actual	64	40 (average)	32	8
PICO	Estimated		~50 (average) 75 (peak)		35
Port Kembla	Estimated	67	54 (average) 80 (peak)	90	32.4
Vizhinjam	Actual	50	25	50	6.3

*Table 2 - Efficiencies of current OWCs*

All of the OWCs in Table 2 have used Wells turbines, except the Port Kembla one, which is using the variable pitch Denniss-Auld turbine. If this delivers its predicted performance, then it does not appear unreasonable that an overall efficiency of around 30% will be achieved, which would represent a significant advance in performance and cost reduction in terms of power output versus capital cost. It is also to be noted that the PICO OWC is currently commissioning a Wells turbine with variable pitch blades. From these projects it can perhaps be concluded that the consensus is that a fixed pitch Wells turbine will not deliver the conversion efficiency required, and either variable pitch, or a different type of turbine is needed. It is also worth noting that a remote noise monitoring station has been set up near the LIMPET facility, clearly demonstrating that noise is considered to be a significant issue. The anticipated noise output of the turbine should therefore be a consideration of the HydroAir project.

### **2.1.5 Design of Current OWCs**

Recognition of the site specific nature of wave climate has led to all operational OWCs (Jan 2007) being bespoke designs for particular locations (Thiruvankatasamy and Sato, ), and to the author's knowledge, no design of any significant scale has ever been tested in more than a single location.

Whilst the geometric form of the collector chamber is generally considered to depend upon the general wave climate, the greater prevalence of larger breaking or near breaking waves at the shallow Northeast Atlantic shoreline sites meant that a sloping

chamber was incorporated in LIMPET for greatest efficiency (Figure 1). The concrete OWCs constructed to date have not sought to focus the wave energy, but the Port Kembla departs from this in incorporating a parabolic reflector. Given the sensitivity of the overall efficiency of the OWC plant to capture efficiency, this appears to be a way of reducing risk through reducing reliance on local bathymetry.

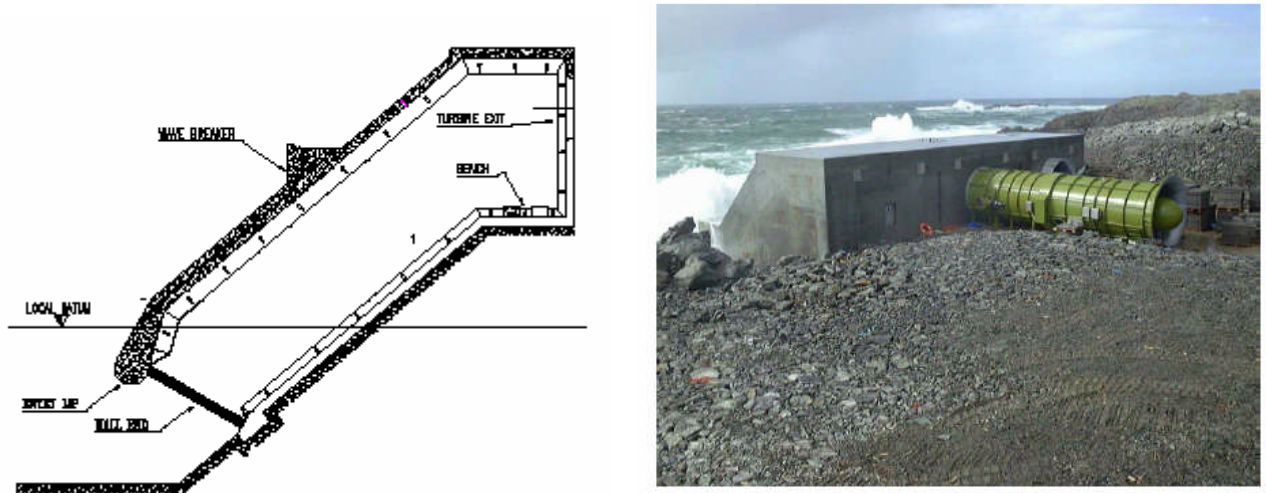


Figure 1 – The LIMPET OWC (Queen's University Belfast, 2002)

The above facts support the HydroAir philosophy that development of the turbine solution should be de-coupled from the OWC itself, and validated in an on-shore test facility which is able to provide representative test conditions which can then be correlated with the input that a particular OWC might provide.

### 2.1.6 Wave Energy Levels

In order to develop a turbine solution that operates over a sufficiently broad range of flow conditions it is necessary to understand the range of conditions that might be encountered. The range of wave energy levels that might be expected around the UK, and the difference between the energies of deep water and near-shore waves is illustrated by the data plotted in Figure 2 and Figure 3. The Figures show typical deep water data as presented by Thorpe in ETSU report ETSU-R120 (1999), and Islay near-shore data taken at the 8m contour, as presented in the Carbon Trust Marine Energy Challenge Report (Webb et al, 2005).

Figure 2 shows that the maximum power near shore (green points) is around 150 kW/m and maximum wave heights around 6m, but in deep water (blue points) the wave power may be up to 400 kW/m and wave heights up to 9m. Figure 3 shows that the wave periods tend to increase with wave height and power (note the colour scale used to indicate power level is capped at 100 kW/m), and that over the whole spectrum wave periods may vary from 6 to 18 seconds, but near shore the longest period is about 15 seconds.

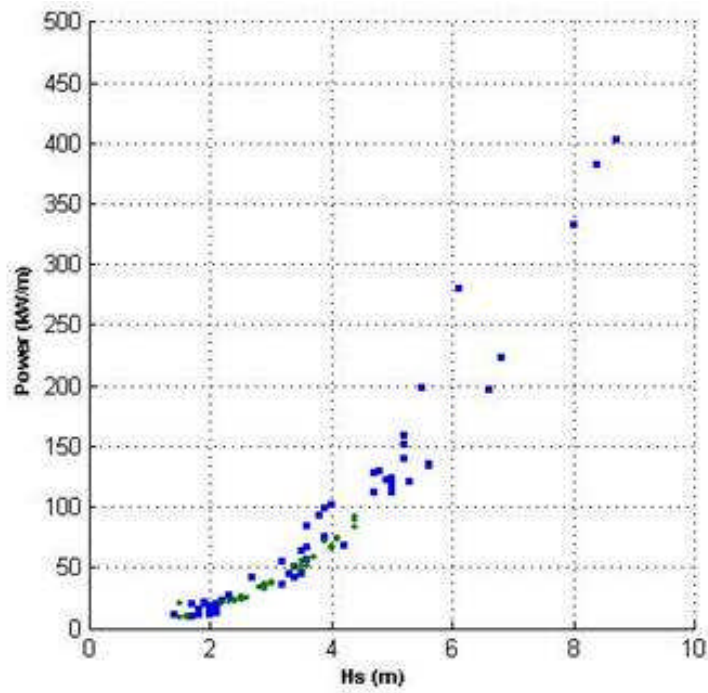


Figure 2 - Comparison of wave powers and heights deep water and near shore

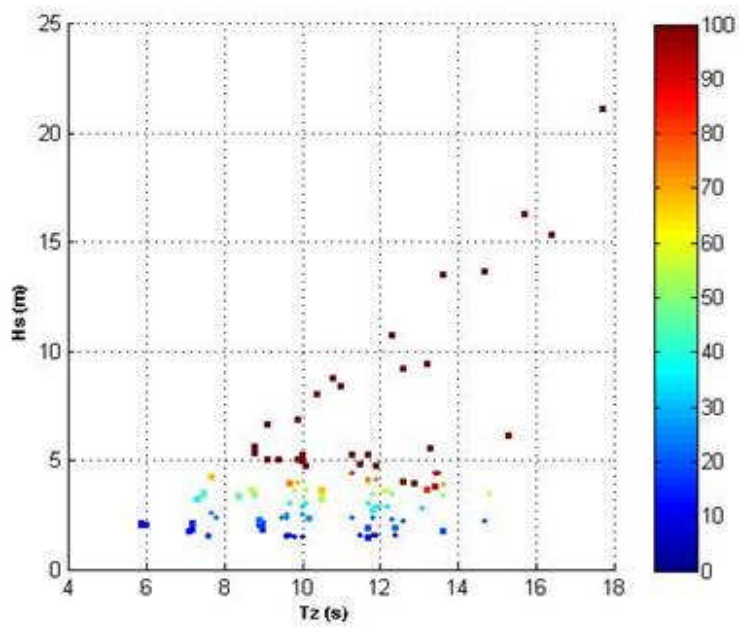
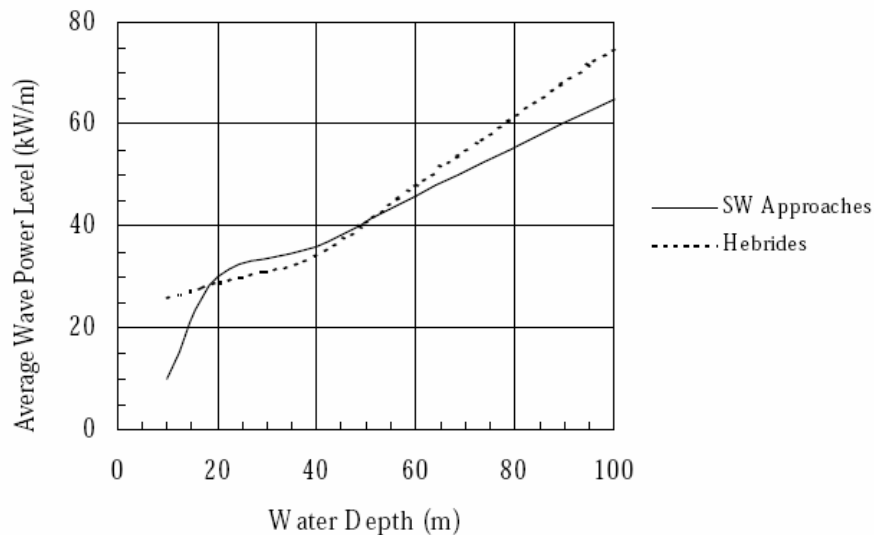


Figure 3 – Range of wave heights and periods in deep and shallow water

The figures demonstrate that OWCs designed for near shore or off-shore locations will receive quite different ranges of waves in terms of heights, periods and powers. The range of waves which will be received mean that high power conversion efficiency can only be achieved by ensuring that the OWC collector, turbine, and generator system have good efficiency over the full range of wave conditions experienced.



*Figure 4 - Variation in average wave power level with water depth and location (Thorpe, 1999)*

An average wave power energy map of the seas around the British Isles shows that the highest energy densities occur on the west coasts, due to the long fetch across the Atlantic Ocean. Energy densities are slightly higher around the Hebrides than off southwest England because the wind speeds are greater at the higher latitudes (Mustoe, 1984). The variation in average wave power level with depth and location for the south west approaches is shown in Figure 4. The Figure shows that the near shore wave resource at 20m depth is 25-35 kW/m in Cornwall, and 30-40 kW/m around the Shetland Isles, whilst the shoreline resource is very site specific (Thorpe, 1999).

Analysis of wave data has shown that there is significant randomness in the wave energy resource over short and long timescales, which presents a major problem in designing OWC power plants. The approach generally taken is to adopt the methods employed in designing off-shore structures. This is to assume that the complex random process can be represented as a stationary stochastic process described by a wave spectra (see Appendix A). This enables wave amplitude versus time functions approximating to sea states to be generated for input into system analyses. This use of mathematical wave spectra provides a foundation for developing a general design and evaluation process for OWC turbines, which is adequate for the relatively fundamental and non-site specific nature of the HydroAir project. It appears probable

though that when designing for a particular installation access to site specific data would be highly desirable.

The impact of the range of waves encountered on the system on performance is not confined to matching the turbine characteristic. A particular point made in the Marine Energy Challenge report was of the need to match the power train to the actual resource encountered, as a number of prototype OWCs have had too great an installed power compared to the actual resource encountered, i.e. the overall load coefficient has been too low.

Due to the directional effects, and attenuation of wave energy towards the coast, it is probable that in terms of demonstrating economic viability in relation to turbine performance, the near-shore situation is the most challenging. If it is possible to demonstrate that on-shore/near-shore OWC systems can be economic, then it is probable that achieving viability with off-shore ones is probably less challenging (from the turbine power off-take perspective).

Given that a test facility was to be made, a significant project concern at the outset was that the test turbine should be as large a scale as possible to minimise Reynolds number scale effects. The maximum model scale is, however, determined by the size of the full scale devices. The full scale diameters of turbines in comparison to their generator sizes are shown in Table 3.

OWC	Turbine diameter (m)	Generator Power (kW)
LIMPET	2.6	500
Pico	2.3	400
Port Klemba	1.6	200/300
Vizhinjam	-	-
Sakata	1.337	60

*Table 3 - Comparison of turbine diameters and generating capacities of OWCs*

In terms systems close to commercial viability for power generation, it is only LIMPET and Pico which are of interest. Both these devices have turbine diameters in excess of 2.0m, and it would perhaps be expected that the turbines in more powerful near and off-shore devices would be larger still. Hence, in terms of scaling the model turbine should be considered to represent a full scale device of diameter 2.5m or more.

### **2.1.7 Summary**

The above considerations suggest that for the purposes of relating work in the current project to reality, the LIMPET OWC should be used for comparison, as there is a significant amount of information available in the public domain. It also represents the state-of-the-art, in terms of closeness to commercial viability, and the turbine system

is representatively large. New turbine configurations can then be defined assuming that they are to replace that in LIMPET, and simulations and testing conducted on the basis of the information available regarding the sea state, conditions in the OWC, and output power produced.

The range of wave conditions which an OWC will be subjected to mean that high efficiency can only be achieved by ensuring that firstly that the OWC has good capture efficiency over the range of input wave conditions, and that secondly, the turbine and generator system has good efficiency over a wide operating range. There is no consensus as to the load factor which an OWC should achieve, but it appears to be at least 30%, and probably higher.

Experience with present OWC installations, and trends in turbine development suggest that a fixed geometry Wells turbine will not deliver the conversion efficiency required, and that a variable pitch solution and/or a different type of turbine should be developed.

Noise is likely to be a significant issue for large OWC installations, and the level of noise that will be produced by the HydroAir turbine needs to be a design consideration from the project outset.

It is likely that any HydroAir solution will have to be proven in a shoreline or break-water device, before it could be applied offshore.

## **2.2 OWC Turbine Review**

### **2.2.1 Objectives**

The objective of the OWC turbine review was to establish the ‘state-of-the-art’ with regard to the design and performance of turbines for OWC power plants, and from this determine the configurations and features which showed greatest promise, and the design performance targets for the HydroAir turbine.

The review first presents a brief overview of the range of turbine solutions for OWC power plants examined by other researchers, and then focuses on the 2 types that have been most researched. These are the Wells turbine and the impulse turbine. These have both been tested in a number of variants which are described, and the design rules for the most ‘optimal’ solutions are identified where possible. The relative performances of the Wells and impulse turbines are then considered.

An important part of the exercise was to identify 2 baseline turbine designs – one Wells turbine, and one impulse turbine - against which the performance of the HydroAir turbine could be benchmarked. Most importantly though, performance data was required which could be analysed in order to arrive at the target performance required by the HydroAir turbine.

## 2.2.2 General Requirement

The essential requirement for a turbine for use with an OWC is that it is able to extract energy from a bi-directional flow. There are two fundamental approaches to this problem. These are to either use a system of valves to enable a uni-directional turbine to be used, or to employ a self rectifying turbine. Whichever approach is pursued, the turbine design must be matched to the wave climate and scale of the OWC, but in addition, for maximum performance the design process must also recognise that the pressure changes in the OWC are dependent upon the turbine characteristics, and if valves are incorporated to control the flow to the turbine these further modifies the process of energy extraction (Brito-Melo, Gato, and Sarmiento, 2002).

In terms of the air flows, closer examination of the characteristics of OWCs shows that the axial airflow velocity during exhalation (i.e. peak flow from the air chamber to atmosphere) is higher than that during inhalation (i.e. from atmosphere to air chamber). The airflow rate  $Q$  measured with time in the wave energy plant of National Institute of Ocean Technology of India is shown in Figure 5. The positive sign of  $Q$  corresponds to exhalation, and it can clearly be seen that the flow rate is not symmetric with respect to direction (Setoguchi, Santhakumar, Takao, Kim and Kaneko, 2003).

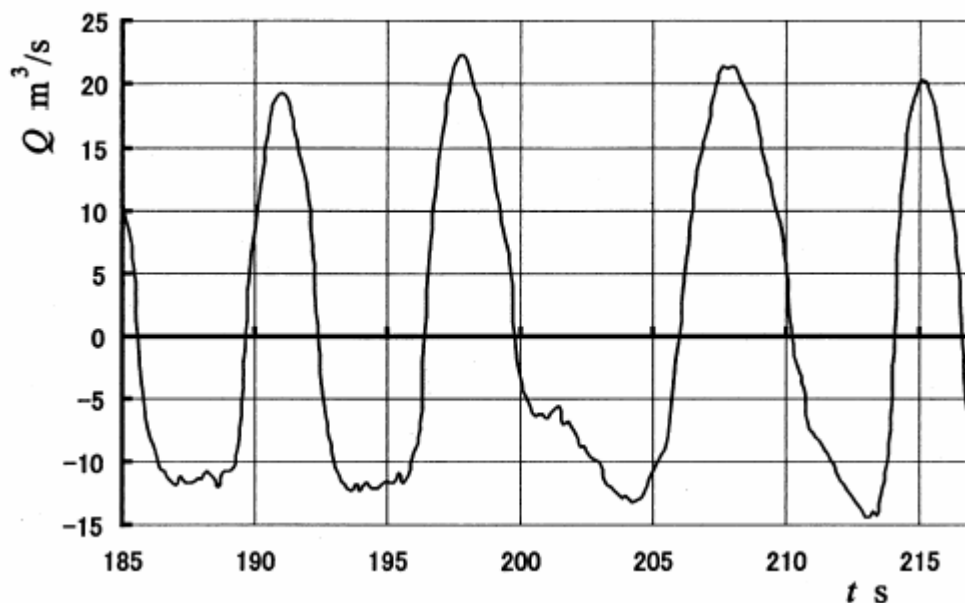


Figure 5 – Variation in volumetric flow rate in NIO OWC plant (Setoguchi et al 2003)

## 2.2.3 Overview of turbines considered for OWC power plants

In the early days of OWC development conventional turbines were used with flow rectifying valves and guide-vanes until the introduction of the Wells turbine concept by Prof. A.A. Wells in 1976 (Dhanasekaran and Govardhan, 2005). Since then the Wells turbine has been the universal choice for all OWC power plant projects which have reached the large scale prototype stage. Nevertheless, a wide range of self-rectifying turbines have been investigated, and a cursory review of these (Table 4)

was presented by Kaneko, Setoguchi, and Raghunathan (Kaneko, Setoguchi, and Raghunathan, 1991). The various turbines were evaluated on the basis of the following characteristics:

1. Their running characteristic i.e. efficiency versus flowrate.
2. Peak efficiency, and stall margin
3. The starting characteristic

Turbine type	Sub types
Wells type	Without guide vanes With guide vanes Self pitch controlled blades Leading edge slat Biplane without guide vanes Biplane with outer guide vanes Biplane with outer and inner guide vanes Biplane using cambered blades Biplane with pre-set blade incidence Triplane Double propeller
Impulse type	Babintsen Filipenco Modisette Double volute turbine Flap nose turbine Impulse turbine with self pitch controlled guide vanes McCormick counter-rotating turbine
Radial turbines	Double volute turbine Normal radial turbine
Cross flow turbine	
Savonius turbine	

*Table 4 – Self rectifying turbines for wave energy conversion*

The authors concluded that the Wells turbine with outer guide vanes was the best device. This was despite saying that in comparison the starting characteristic of the impulse turbine with self pitching guide vanes was superior; that the lower rotational speed of an impulse turbine was desirable to reduce noise and ease mechanical design; and that the impulse turbine had high efficiency over a wider flow range.

It appears that the conclusion that the Wells turbine was the best option, was based purely on the relatively low efficiency achieved by an impulse turbine with fixed guide vanes under sinusoidal flow conditions (28% as compared to around 44% for a bi-plane counter-rotating Wells turbine), and the average efficiency of around 30% achieved by a prototype model of the McCormick turbine (an impulse type turbine with 2 counter rotating rotors coupled by gears). Very little was said regarding the characteristics of the other turbine types, but the maximum efficiency values

presented for the radial and Savonius turbines were 29% and 27% respectively, which are too low to indicate any great promise.

#### 2.2.4 The Denniss-Auld Turbine

The Denniss-Auld turbine

Figure 6 is essentially a Wells turbine with actively controlled, variable pitch, blades. However, it uses non-standard aerofoils, and its benefits are said to be that it operates at slower speeds with greater air flows, so giving greater torque. The concept appears to have been developed from work on Wells turbines with self-pitch-controlled blades, which have demonstrated the highest efficiencies achieved by Wells turbines (see 3.5).

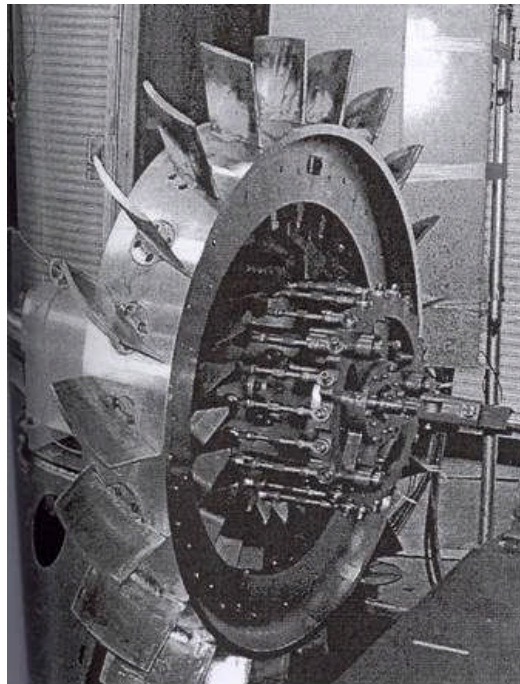


*Figure 6 – Denniss-Auld turbine (Oxford Oceanics, 2005)*

The Denniss-Auld turbine is to be used in the 300kW Port Kembla OWC. Figure 7 shows that the turbine achieves its highest efficiency of 65% at relatively low flow ratio of  $\sim 0.5$ , but the characteristic is considerably broader than that of a Wells turbine (see section 3). It is assumed that data presented is for steady flows, but it is not clear whether the efficiency is a total-to-total or total-to-static calculation. It is evident from Figure 6 that the number of moving components is relatively large, and the arrangement quite complicated, which raises questions with regard to maintenance and reliability.

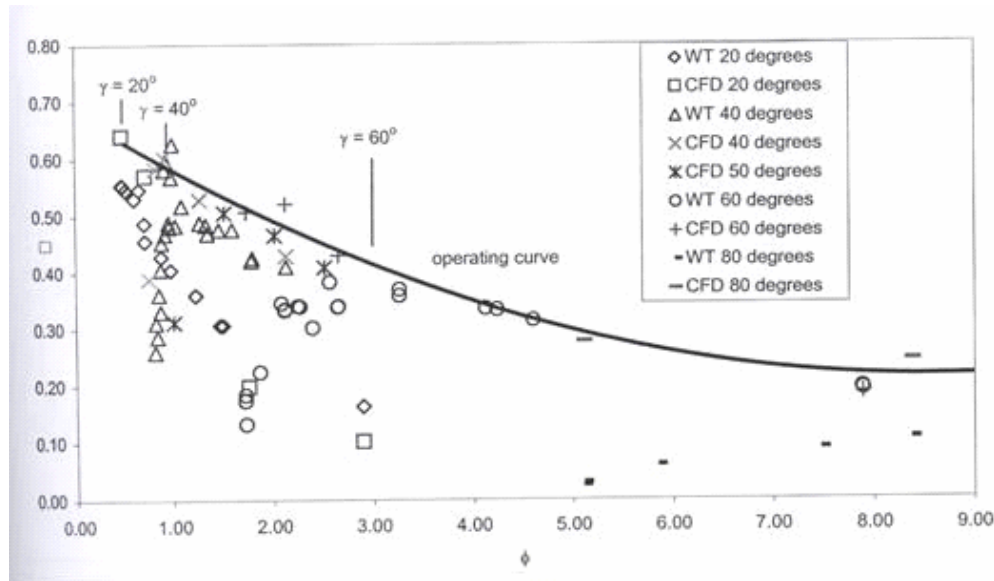


Figure 7 - Performance of 8 blade, 1/3 scale Denniss-Auld turbine (Oxford Oceanics, 2005)

### 2.2.5 Reaction Turbine

The attraction of using a reaction turbine is that this would be expected to give the highest levels of efficiency, and the design point could be fixed by referring to the well known Smith chart. However, in order to use a reaction turbine the oscillating air flow has to be rectified to provide a uni-directional airflow. A number of valve arrangements have been researched, and a valve arrangement was used in an OWC powered navigation buoy in the 1960's. The difficulties with this approach are that for high levels of efficiency to be achieved the valves must have close to no leakage, and the system needs to have a high level of reliability over a large number of cycles: if it is assumed that the average wave period is 10 seconds, say, then the valves would have to operate 3.15 million cycles per year, or around 80 million cycles over a 25 year life.

From the point of view of the HydroAir project, the valve and reaction turbine approach was considered to be more a question of how to engineer the necessary level of valve sealing effectiveness and reliability, rather than how to achieve a high level of turbine performance once the flow was rectified. Given the potential benefits, a search was made for a valve type which would satisfy the requirements of high sealing effectiveness, combined with low losses, and high reliability. No valve type could be found that appeared to satisfy these requirements, and so this approach was dropped in favour of concentrating on self rectifying turbines. Some further description of the valve types investigated is given in (Herring and Banks, 2007b).

## 2.2.6 The Wells turbine

### General

Kaneko, Setoguchi, and Raghunathan described the Wells turbine as the simplest and most economical self rectifying turbine for wave energy conversion (Kaneko et al, 1991), and it has been the first choice turbine for all OWC based wave energy plants built in Norway, Japan, UK, India, and China (Setoguchi, Santhakumar, Maeda, Takao and Kaneko, 2001). The details of the turbine designs have varied, but they have generally been fairly similar, as shown in Table 5 .

	No. of blades	Solidity	Hub/tip ratio	RPM	Re	Section	Comments
Koola	4	0.6	0.6			NACA0021	Constant & variable chord
Brito-Melo Sarmiento	8	0.64	0.68	1500	$3.9 \times 10^5$	NACA0015	Constant chord
Gato et al 1993	6		0.68			NACA0015	Constant chord
LIMPET	7	0.33	0.62	1050	$2.5 \times 10^6$	NACA0015	Biplane turbine 2.6 m diameter swept profile blades, constant chord

*Table 5 – Turbines used in prototype OWCs*

A Wells turbine consists of a number of untwisted rotor blades with symmetrical aerofoil sections set radially at 90 degrees stagger. It is generally recognised to have only moderate peak efficiency in comparison to other turbine types, but has the advantage that unlike most turbines it is intrinsically bi-directional (or self-rectifying). At small flow rates the drag component of a Wells turbine is greater than its lift, and so the power output is low, or even negative, whilst at large flow rates the blades stall and the efficiency drops sharply above a critical point. This means that there is only a narrow band of flow coefficient within which the Wells turbine operates at high levels of efficiency. This means that if the turbine is of fixed geometry then it is essential that the running speed is varied to avoid excessive periods of rotor stall (Queen's University Belfast, 2002). This has been borne out with experience with Limpet which showed the need to change the mean turbine speed with available input power to minimise parasitic losses, maximise efficiency, and limit stall at times of high wave activity (Wavegen, 2002).

Raghunathan has studied the characteristics of the Wells for many years and has presented extensive design guidance based on his work (Raghunathan, 1995). Typical performance curves for Wells turbines presented by Raghunathan are shown in Figure 8. It should be noted that Raghunathan evaluates efficiency on the basis of total-to-total pressure drop across the turbine which gives efficiencies several percent higher than using total-to-static pressure drop.

The curves in Figure 8 show a reasonable peak efficiency of 65%, and that at low flow rates (i.e. low blade incidences) the drag component is greater than the lift, and so the efficiency is negative. Raghunathan said that if the variation in input flow

velocities was sinusoidal then the power lost at small flow rates was only a small part of the time averaged output, amounting to 5-10% of the energy. However, he went on to say that in random airflows small incidences (and hence negative efficiency) could be experienced for significant periods of time, and so the averaged efficiency could dip further. It is also the case that non-axisymmetric flow can have a substantial effect on the efficiency of a Wells turbine, such that it is more beneficial to reduce the flow asymmetry than improve the turbine (White, 1995).

From a mechanical engineering perspective, the oscillating lift of a Wells turbine produces an oscillating axial thrust which must be reacted by suitable bearings. The variation in torque produced by sinusoidal or random flows can be smoothed by incorporating a high inertia flywheel/rotor, as was done in LIMPET.

Figure 8a shows that at a given rotational speed there is an approximately linear relationship between non-dimensional turbine pressure drop and flow rate up to the stall point.

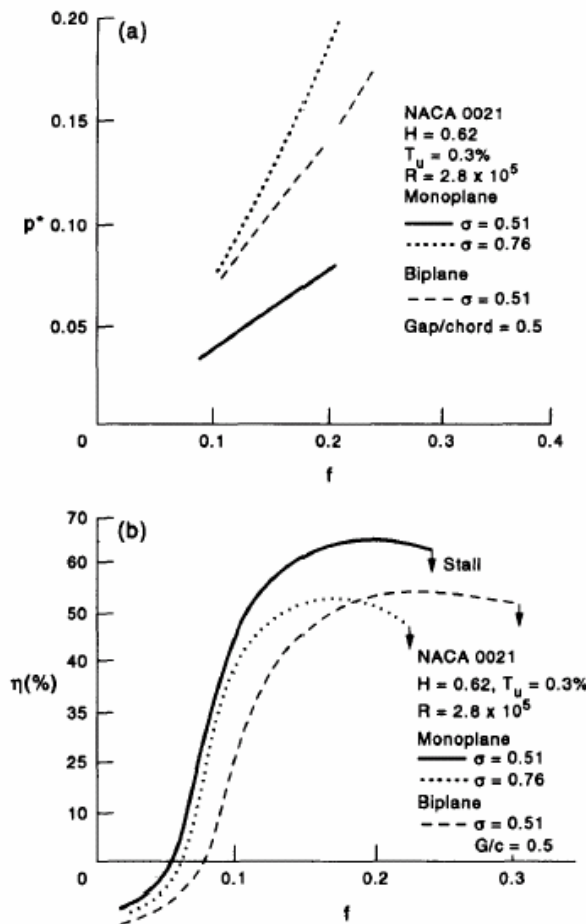


Figure 8 – Typical performance curves for a Wells turbine (a) Pressure drop-flow ratio (b) efficiency-flow relationship (Raghunathan, 1995)

Raghunathan stated that the linear relationship was essential for matching the turbine to the OWC, which had a similar characteristic. The pressure drop across a single plane Wells turbine is proportional to the square of the rotor tip Mach number, and the pressure drop is increased by increasing the turbine solidity.

### Design of mono-plane Wells turbines

From the information given by Raghunathan (Raghunathan, 1995) it would appear that the optimum mono-plane Wells turbine configuration would be as defined in Table 6. The analysis which leads to this is presented in (Herring and Banks, 2007b).

Parameter	Value
Hub/tip ratio	0.6
Solidity	0.5
Aerofoil section thickness/chord	0.2
Blade aspect ratio	0.5
Blade off-set	0.15
Tip clearance	<0.02

Table 6 – Optimum parameter values for Wells turbine

It should be noted that as Raghunathan himself said, some caution should be exercised in using his results as they were primarily based on *small scale model tests*. For example, he notes that some rather low efficiency values were obtained because of the small model blade chords.

A significant consideration in the OWC application is that not all monoplane Wells turbines are self-starting. The extensive tests carried out by Raghunathan et al have shown that low values of hub/tip ratio ( $h$ ) and high values of solidity ( $\sigma$ ) are required for self-starting as shown in Figure 9.

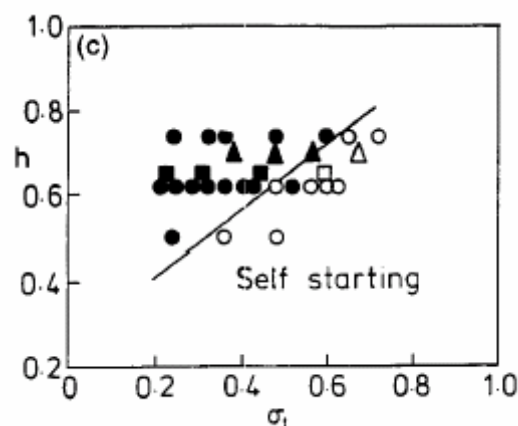


Figure 9 – Effects of hub/tip ratio and solidity on ability of monoplane Wells turbine to self start (Raghunathan, 1995)

Consideration of the velocity triangles of a Wells turbine shows that a fundamental characteristic of these devices is that the exit flow includes an added swirl component, so the absolute velocity is increased. This exit swirl represents a loss of kinetic energy, and so one of the first modifications to the basic Wells turbine was to add guide vanes in an effort to remove the exit swirl, and so increase efficiency. Raghunathan found that adding guide vanes increased efficiency by 3-5% (as did Setoguchi et al (see 3.3.1 and Figure 8), but he also found that the turbine stalled at a lower flow rate. However, the addition of guide vanes also improved the starting characteristics.

### Variations on the basic Wells turbine

As the airflow velocities in the exhalation direction are greater than in the inhalation direction, Setoguchi et al (Setoguchi et al, 2003) investigated whether setting the blades to a pitch angle  $\gamma$  resulted in higher mean efficiency.

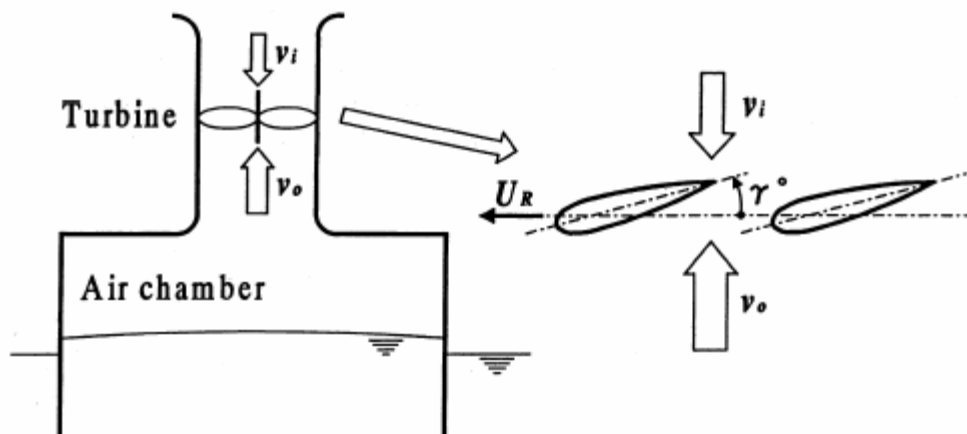


Figure 10 – Definition of pitch setting angle (Setoguchi, 2003)

The rotor blade setting angle  $\gamma$  was defined as shown in Figure 10, so that a positive setting decreased the effective incidence in the exhalation phase. The basic turbine design used for this test was similar to that used in the ‘Mighty Whale’<sup>1</sup>, and was fitted with guide vanes as shown in Figure 11. Data was obtained at steady flow conditions with the blades pitched to angles of -4, -2, 0, 2, and 4 degrees in the Saga University test rig, with and without guide vanes. It should be noted that the efficiency values derived by Setoguchi et al appear to be significantly below those of Raghunathan because the efficiency calculation is based on the total-to-static pressure drop, rather than total-to-total pressure drop. The difference between these 2 measures is described in Appendix B.

<sup>1</sup> The Mighty Whale was rated at 110kW, and tests commenced in Gokasho Bay Japan in 1998, where  $H_s=1\text{m}$ ,  $T_e=5\text{-}8\text{s}$ , mean power density 4kW/m. The mean power output was 6-7kW in energy periods of 6-7s, which gave an overall efficiency of 15%.

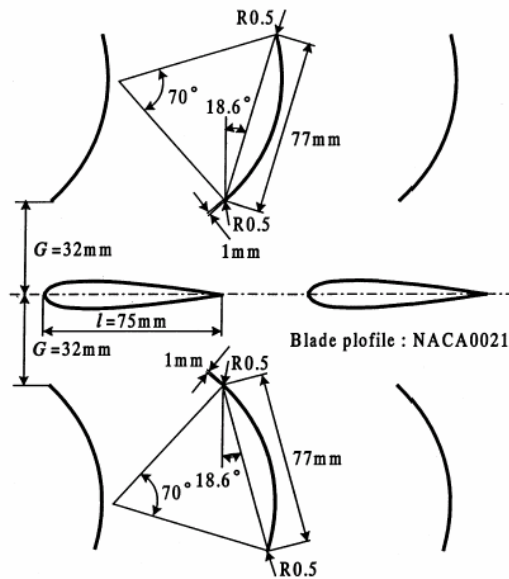


Figure 11 – Configuration of test turbine (Setoguchi et al 2003)

The steady state characteristic data obtained (Figure 12) was used to calculate a quasi-steady simulation to predict the mean efficiency with a time varying airflow. Pseudo-sinusoidal inputs were assumed in this process, in which the positive part of the pressure cycle had a greater amplitude than the negative, as this was representative of reality. Inhalation/exhalation amplitude ratios ( $V_i/V_o$ ) of 1.0, 0.8, and 0.6 were used. The results showed that the benefit was limited to about a 1% increase in efficiency for a blade setting angle of +2 degrees for  $V_i/V_o = 0.6$  case.

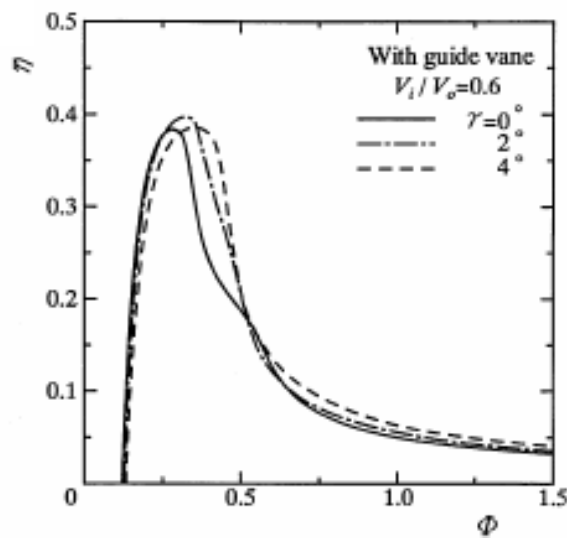


Figure 12- Efficiency of Wells turbine with fixed guide vanes - pseudo-sinusoidal flow (Setoguchi, 2003)

Koola et al found that their variable chord Wells turbine had greater operating range than a constant chord turbine, but that it was not self-starting.

### Multi-row arrangements

From monoplane arrangements Wells turbines have been developed into multi-row configurations, which have also been described by Raghunathan (Raghunathan, 1995). The pressure drop across a Wells turbine is proportional to the square of tip speed, and so the maximum pressure drop is practically limited by the onset of tip compressibility effects. If the required pressure drop – or power to be absorbed – is too great for a single turbine – i.e. the Mach number becomes too high, then one option is to move to use a bi-plane arrangement. The negative effect of adding blade rows is that the kinetic energy losses are increased, due to the increased exit swirl. The effect is shown by the velocity triangles in Figure 13. It also means that for a given flow rate, multi row arrangements must operate at lower rotational speeds than single plane ones as the rotational speed of multi-row arrangements is determined by the onset of transonic flow on the final blade row.

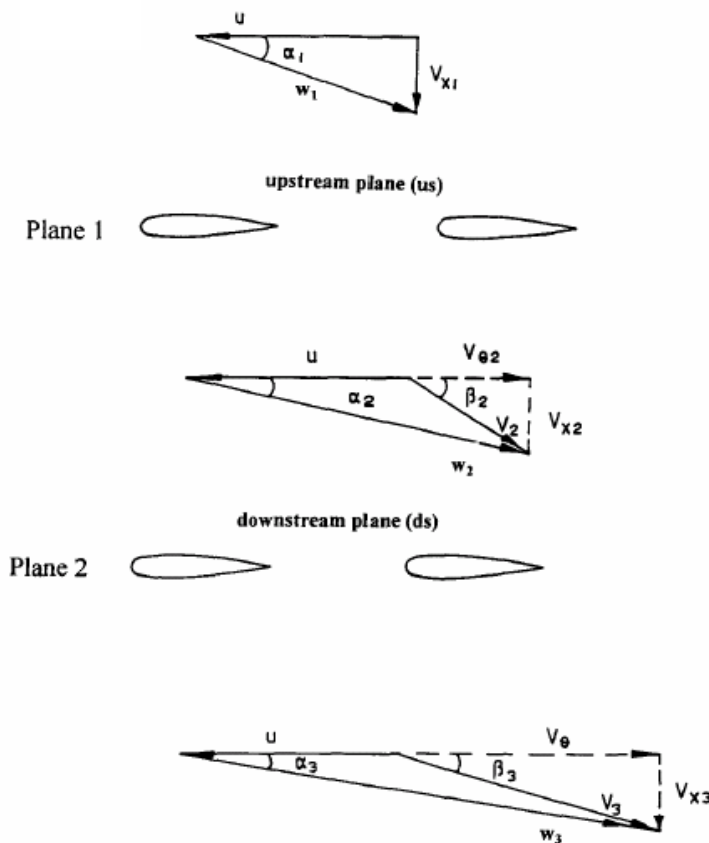


Figure 13 – Velocity triangles for bi-plane Wells turbine without guide vanes (Raghunathan, 1995)

If inlet and outlet guide vanes are added to a multi-row Wells turbine running at its design speed then a mis-match between the blade rows is produced. However, if the

running speed is increased then the same operating point can be attained as for a turbine without guide vanes, but with a reduced exit swirl and hence reduced kinetic energy loss.

A multi-blade row configuration of particular interest has been the contra-rotating Wells turbine which offers the possibility of virtually eliminating exit swirl, and significantly reducing losses. Raghunathan predicted very high efficiency values for this configuration as shown in Figure 14, and this was the configuration installed in LIMPET. However, the predicted performance has not been realised in practice. This was presumably due to poor matching between the turbine, power take-off arrangement, and the actual oscillating flows, which meant that the turbine was rarely operating in its design flow range.

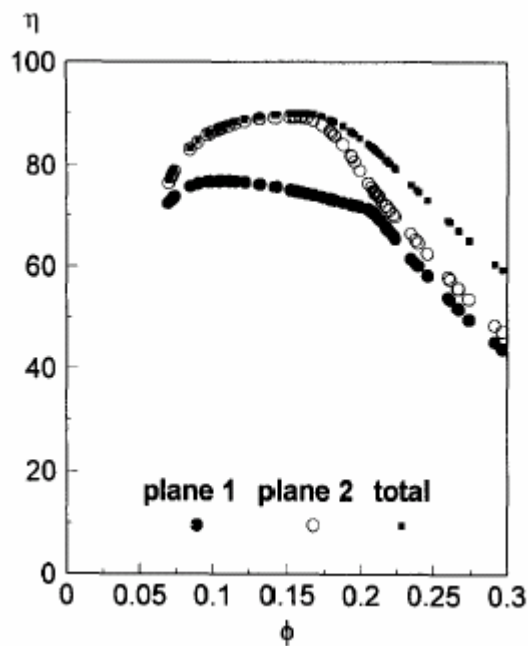


Figure 14 – Efficiency characteristic for contra-rotating Wells turbine (Raghunathan, 1995)

### Performance of Wells turbines

A large number of tests have been carried out on a wide range of Wells turbine arrangements, which have been summarised by Kaneko, Setoguchi, and Raghunathan (Kaneko et al, 1991). The motivation behind the research appears to have been to find a configuration which had both high peak efficiency, and large flow range i.e. where the peak efficiency occurred at a high flow ratio. The results were presented as non-dimensionalised with respect to a reference monoplane turbine without guide vanes. Fortunately, results in the table appear to include the monoplane turbine with guide vanes used by Kim et al in their performance comparison (see section 2.2.8), and based on this the peak efficiency and flow ratio of the reference turbine can be found to be 37%, and  $\phi = 0.32$ . Examination of the data in the table then shows that highest efficiency attained was 59%, by a monoplane turbine with self-pitch-controlled blades, whilst the highest flow ratio at which peak efficiency occurred was  $\phi = 0.62$ ,

for a bi-plane turbine with outlet guide vanes. The table did not include results for a contra rotating turbine, but it is evident that Raghunathan's predicted performance of 90% was substantially higher than the results presented.

It is to be expected that without the use of a sophisticated control system that actively controls the turbine rotational speed, the narrow flow range of a Wells turbine would mean that given the wide range of wave powers, and the fact that small waves are very frequent whilst large ones are infrequent, that a Wells turbine in an OWC would be expected to either spend much of its time operating at low flow ratios and low efficiency, or that it would end up operating in the deep stall range. In the latter case not only would the turbine have low efficiency but it would also experience large unsteady forces which could limit blade life and be noisy.

Overall it can be concluded that a large amount of research has been conducted into the development of Wells turbine configurations, and a good deal of design information is available. The highest peak efficiency achieved appears to be Raghunathan's 90% (total-to-total) contra-rotating arrangement, which was installed in LIMPET. The next best has been ~60% (total-to-static) for a monoplane device with self-pitch-controlled blades. The highest flow ratio achieved at the peak efficiency point has been  $\phi = 0.62$ .

## 2.2.7 Impulse Turbine

### General

Whereas the Wells turbine was developed specifically for extracting power from the oscillating air flow in OWCs, impulse turbines are more usually to be found extracting power from uni-directional high pressure steam flows. Impulse turbines are similar to Wells turbines in that the rotor is symmetric about its mid-plane perpendicular to the axial flow through it, but there are many more aerofoils, and the principle of operation is quite different.

Impulse turbines have been investigated as a means of overcoming the deficiencies of Wells turbines, typically described as:

1. Low off-design efficiency
2. Poor starting characteristics
3. Narrow operating band (at unstalled flow conditions)
4. High rotational speed leading to high noise and high axial thrusts

In addition, it is also likely that the rotational speed of an impulse turbine will be closer to the preferred rotational speed of the generator.

The output provided by an impulse turbine in an OWC depends firstly upon having an efficient rotor design that is well-matched to the flow provided by the inlet guide vanes/nozzle blade row. In their review of impulse turbines Setoguchi et al (Setoguchi et al, 2001) described two rotor blade geometries which they described as the 'simple profile' and the 'elliptic profile', which are shown in Figure 15. The

simple profile was constructed by using two circular arcs and then projecting straight lines to form the leading and trailing edges to form a constant width passage between neighbouring blades. The elliptic profile, on the other hand was formed by a circular arc on the pressure side, and a segment of an ellipse on the suction side, such that the passage was slightly wider at the mid-chord point to restrict the flow velocities there.

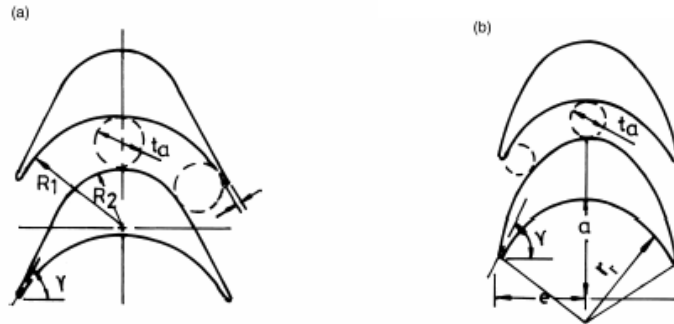


Figure 15 – Rotor blade profiles a) simple profile b) elliptic profile (Setoguchi et al, 2001)

Setoguchi et al conducted a number of tests (Setoguchi et al, 2001) to establish whether the simple or elliptic profile rotor geometry was best, and the effect on performance of guide vane setting angle, space-chord ratio, flow path width/rotor blade space, and sweep. In addition, the effect of tip clearance on performance was investigated in a CFD study carried out by Thakkar et al (Thakkar, Hourigan, Dhanasekaran, Henry, Usmani, and Ryan, 2005), who concluded that the tip clearance should be 1% or less. The results of these studies can be combined to define the optimum elliptical profile rotor configuration defined in Table 7.

Parameter	Value
Profile	elliptic
Inlet angle ( $\gamma$ )	60°
Space/chord ratio ( $S_r/l_r$ )	0.5
Flow path width/rotor blade space ( $t_a/S_r$ )	0.4
Rotor blade sweep ( $\lambda$ )	-7.5°
Ratio of ellipse Semi major/semi minor axis of ellipse ( $a/e$ )	3
Tip clearance	<1%

Table 7 – Optimum parametric values for rotor with elliptical profile blades

The problem with using an impulse turbine is that there is a fundamental requirement for a nozzle or guide vane row to accelerate the flow into the rotor at a desired angle, and an oscillating flow requires that there are nozzle/guide vane rows on both sides of the rotor, which lead to large losses across the mis-matched downstream nozzle/guide vane row. Figure 16 shows how for an impulse turbine close to its optimum operating point, the inlet guide vanes turn the flow to produce the absolute rotor inlet velocity  $C_2$ , and how the flow leaves the rotor almost axially with the absolute velocity  $C_3$ , as

the magnitudes of the rotor relative velocities  $V_2$  and  $V_3$  are the same. This leads to the outlet guide vane having a very high incidence to  $C_3$ , and so a large region of separated flow develops, as illustrated by the CFD solution velocity contour plot shown in Figure 17, calculated for the geometry of Setoguchi et al.

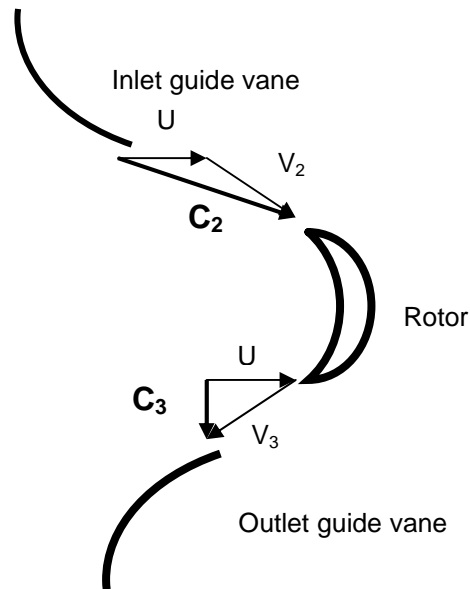


Figure 16 – Rotor inlet and outlet vector triangles

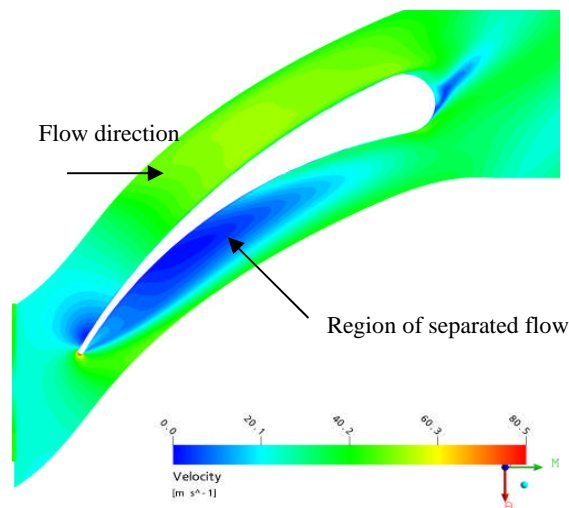


Figure 17 - Velocity contours on outlet guide vane of baseline impulse turbine design, showing large separated region adjacent to the pressure face

### Impulse Turbines with fixed guide vanes

To address the operational problems found with self-pitching guide vane impulse turbines, Setoguchi and Maeda et al (Maeda, Santhakumar, Setoguchi, and Takao, 1999) (Setoguchi et al, 2001) made a number of studies using the Saga University test rig which investigated the level of performance which could be attained under both steady state and oscillating flow conditions with fixed pitch plate guide vanes. The scope of the studies covered:

1. Testing with rotors with inlet flow angles of 50 and 60 degrees.
2. Use of plate guide vanes with setting angles  $\theta = 15, 22.5, 30, 37.5,$  and 45 degrees.
3. Evaluation of the effect of the gap between the guide vanes and rotor.
4. The effect of hub/tip ratio.
5. The use of an aerofoil guide vane design.

The geometry of the plate guide vanes consisted of a straight section and a circular arc, whilst the plate itself was 0.5mm thick. The geometry of the plate guide vanes is shown in Figure 18.

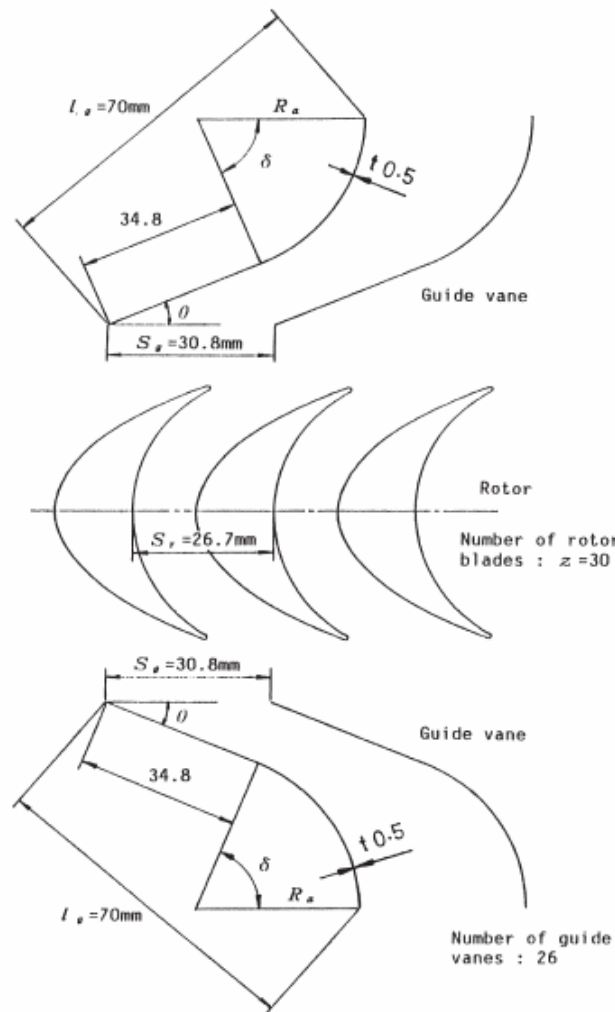


Figure 18 – Geometric definition of guide vanes (Setoguchi et al, 2001)

The results of tests carried out by Maeda and Setoguchi et al showed that:

1. Significantly higher efficiencies resulted from using the rotor with an inlet angle  $\gamma = 60^\circ$ , than the rotor with  $\gamma = 50^\circ$
2. The 'optimum' guide vane setting was 30 degrees, which gave a peak efficiency of 39% in steady flow conditions.
3. The hub/tip ratio had a large impact on steady flow performance.
4. The optimum guide vane/rotor spacing was  $G/l_r = 0.37$ , which gave the highest value of mean efficiency, as well as low sensitivity to guide vane setting angle.

Of the parameters varied hub/tip ratio had the greatest effect. When the hub/tip ratio was increased from 0.7 to 0.85 peak steady flow efficiency was reduced by 13%, from 44% to 31%. The fact that the input coefficients were very similar suggests that the loss in performance was due to increasing end-wall effects and losses. Further numerical and experimental work by Thakker (Thakker et al, 2005) on Setoguchi et al's published optimum design turbine, at Limerick University predicted that the turbine efficiency could be raised by 7%, by reducing the hub/tip ratio from 0.7 to 0.6. The immediate conclusion is that hub/tip ratio has a large effect on performance, and that a hub/tip ratio of  $h = 0.6$  gives best performance.

The optimum gap/chord ratio found was within the range of 0.2-0.5 usually employed in gas turbine designs. In these a low value of 0.25 might be chosen only to reduce length and weight and a value closer to 0.5 is often used (Saravanamuttoo, Rogers, and Cohen, 2001). In fact, depending upon the magnitude of the errors, the data presented could indicate an optimum value of  $G/l_r$  closer to 0.5.

In addition to the parametric variations discussed above Setoguchi et al (Setoguchi et al, 2001) investigated the effect of vane profile by testing an aerofoil type guide vane design (Figure 17), with a turning angle of  $60^\circ$  ( $\theta = 30^\circ$ ) and compared the results with those for a plate guide vane (the number of guide vanes was the same in both cases). The test results showed that the effect of using the aerofoil guide vanes rather than plate guide vanes in oscillating flow conditions was negligible at flow rates below the peak efficiency point, and at higher flow rates the performance was actually marginally reduced. No explanation was given for this.

The results obtained by Maeda for oscillating flow conditions were compared with those of a 6 bladed Wells turbine design with guide vanes, which had been the most promising design found in a previous study. Both turbines had the same hub/tip ratio of 0.7, full details of the Wells turbine design are given in Table 8.

Blade	Parameter	Value
Rotor	Profile	NACA0020
	Chord length $l_r$	90mm
	Solidity at mean radius	0.67
	Aspect ratio	0.5
	Tip diameter	298mm
	Tip clearance	1mm
	Hub/tip ratio	0.7
Guide vane	Profile	Circular arc
	Thickness ratio	0.011
	Solidity at mean radius	1.25
	Camber angle	60°
	Aspect ratio	0.5
	Gap-to-chord ratio	0.43
	Stagger angle	16.3°
	Leading trailing edges	Semi-circular r=0.5mm
Rotor guide vane gap	39mm	

Table 8 – Specification of Wells turbine with guide vanes

The comparison (Figure 19) showed that the Wells turbine had a peak mean efficiency about 8% higher than that of the impulse turbine with guide vanes at  $\theta = 30^\circ$ , i.e. 47% rather than 39%. A significant point to be considered in comparing the data, however, is that the Re of the impulse turbine was only  $0.4 \times 10^5$ , as compared to a value of  $2 \times 10^5$  for the Wells turbine. This is significant as it is generally accepted that blade Re values of at least  $2 \times 10^5$  are required in order to provide confidence in data with regard to Re effects.

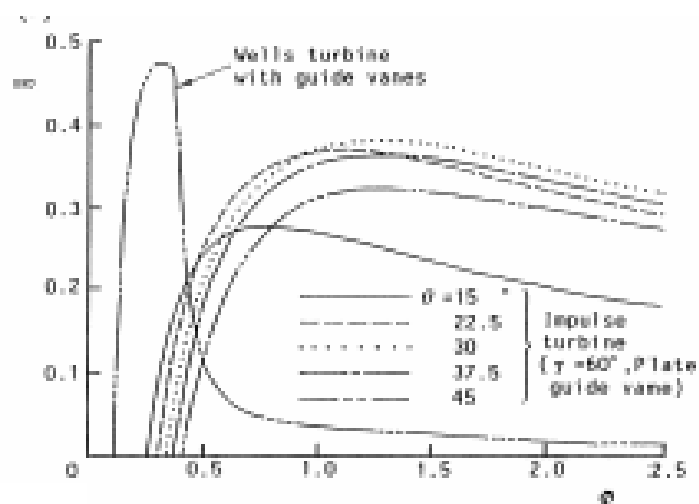


Figure 19 – Turbine mean efficiency characteristics under sinusoidally oscillating flow (Maeda, 1999)

### Impulse turbines with movable guide vanes

To overcome the deficiencies of the Wells turbine Setoguchi et al evaluated the performance of impulse turbines with self-pitching guide vanes, and then linked guide vanes which pitched at the wave input frequency, These demonstrated superior performance to the Wells in the laboratory, and when a 1.0 m diameter device was installed in the Indian NIOT Vizhinjan OWC facility performance improvements were still initially realised. However, maintenance and operating life problems were revealed. It was seen that the need for the guide vanes to pitch at the wave frequency required ‘robust’ mechanical design to withstand the large number of oscillations per day, and that the number of moving parts led to costly maintenance and operating life problems.

The self-pitch-controlled impulse turbine designed by Setoguchi et al is shown in Figure 20. The guide vanes were pivoted and were free to rotate under the influence of the aerodynamic moments acting on them between two preset angles determined by mechanical stops. The figure shows how the guide vanes were set on a spherical hub to maintain the hub clearance at a constant 0.5mm as the vanes rotated, however, the tip clearance at the outer casing varied from 0.5 – 3.0 mm as the vanes pitched from 50 to 15 degrees.

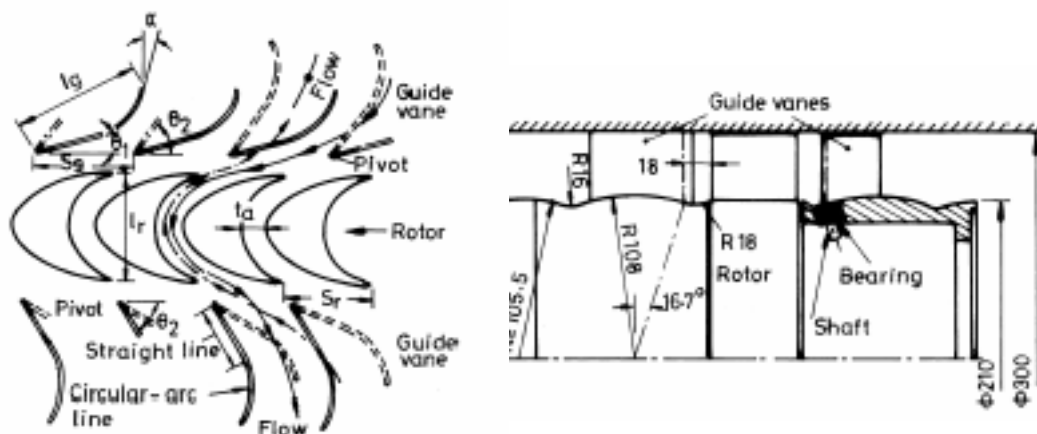


Figure 20 – Impulse turbine with self-pitch controlled guide vanes (Setoguchi et al, 2001)

Two different types of vane were tested: mono vane type and the splitter vane type. The former is shown in Figure 20. In the first instance the steady flow efficiency characteristic with a ‘simple profile’ rotor was measured. The data showed how the better diffuser geometry of the self-pitching mono-vanes led to an increase in peak efficiency from the low 40’s achieved by the fixed guide vane geometries to a steady flow peak efficiency of 60% (Figure 21). It should be noted that the inlet flow angle to the rotor is also  $\gamma = 70^\circ$ , and higher performance would be expected with the elliptic profile rotor design (see Table 4, 4.2.2) with  $\gamma = 60^\circ$ .

Comparative tests carried out in steady flow conditions with the mono-vane and an optimal splitter type guide vane arrangement showed that the mono-vane guide vane arrangement gave higher values of maximum efficiency for all outlet setting angles ( $\theta_2$ ) and guide vane space chord ratios ( $S_g/l_g$ ) tested. The mono-vane guide vanes had better performance at a given diffuser angle because the diffuser angle which the splitter type vanes could achieve was limited. Further tests to investigate the effect of guide vane space-chord ratio ( $S_g/l_g$ ) on performance showed that the optimum value of  $S_g/l_g$  for the mono vanes was  $<0.65$ . When the mono vane arrangement was tested with the optimum elliptic profile rotor it was found that the optimum nozzle angle for the mono-vane arrangement was  $\theta_1 = 15^\circ$ , and this arrangement gave a peak efficiency of 61%.

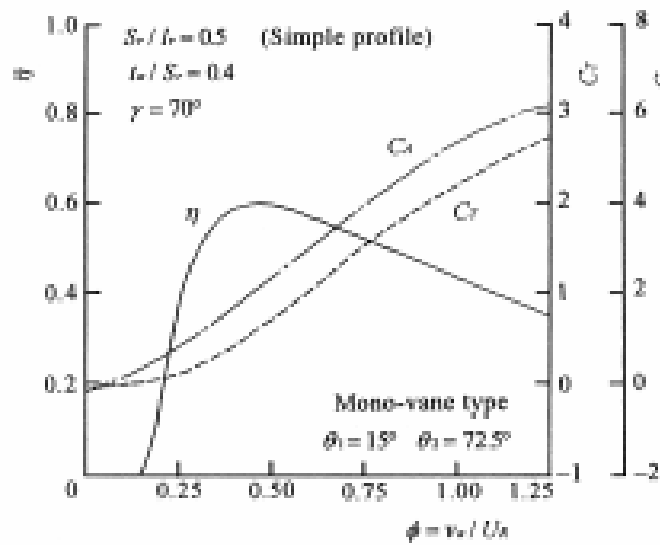


Figure 21 – Turbine characteristics in steady flow simple profile rotor with mono-vane (Setoguchi, 2001)

Whilst all the above steady flow results indicated the favourability of the mono-vane arrangement, when the arrangement was tested in a sinusoidal flow it was found that the guide vanes on the downstream side of the turbine did not rotate and maintain the desired diffuser angle. The angular position of both mono and splitter guide vanes were recorded by a potentiometer, and their behaviour was plotted (Figure 22). The desired behaviour was demonstrated by the splitter type vanes (shown by the solid lines), whilst the behaviour of the mono-vanes followed the dotted lines. It can be seen that when the flow velocity had its maximum negative value, the angle of the mono-vane was actually close to the angle  $\theta_1$ , rather than being  $\theta_2$ . This would obviously reduce efficiency significantly, but Setoguchi et al did not present any data showing how large the impact was. However, in Setoguchi's paper referring to the linked guide vanes, he presented a plot which suggested that the performance was  $<30\%$ , as shown in Figure 24. It is clear, though, that the performance in sinusoidal flows must have been close to a that of a turbine with fixed guide vanes, as they immediately moved on to linking the guide vane rows together.

Setoguchi et al did not present any data showing the performance of the splitter-type arrangement in sinusoidal flow conditions. From the data presented it appeared that the maximum efficiency of the splitter vane configuration with the same rotor and nozzle setting would be 51%, as compared to 61% for the mono-vane arrangement under steady flow conditions. This was a significant improvement over the performance achieved with fixed guide vanes. It could be that the splitter vanes were not pursued because the benefit may have been eroded under sinusoidal flow conditions, or that the complexity was considered too great for the benefit obtained in relation to pursuing the linked guide vane approach.

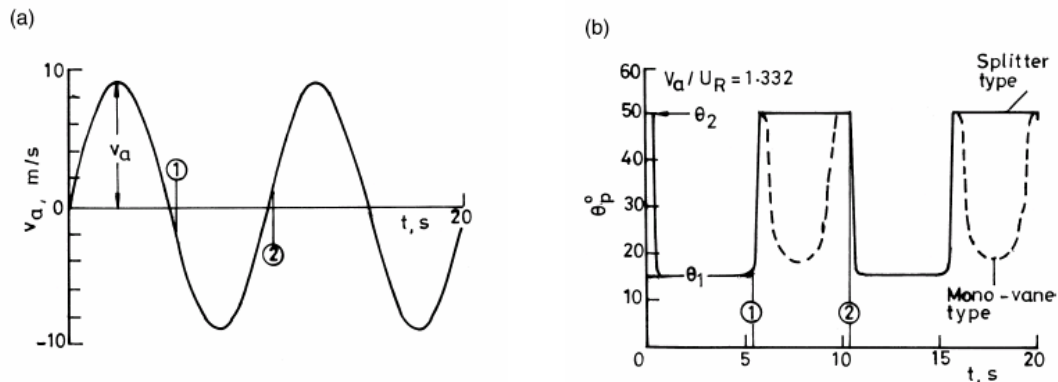


Figure 22 – Comparison of pitch angles for mono-vane and splitter guide vanes in reciprocating flow (Setoguchi, 2001)

To overcome the problem of the mono-vane guide vanes not maintaining the desired diffuser angle in sinusoidal flows, Setoguchi et al designed the self-pitching linked guide vane arrangement shown in Figure 23. This used the same rotor and guide vane designs as the self-pitching tests. Tests then proved that the links caused the mono-vane guide vanes to operate in the desired fashion.

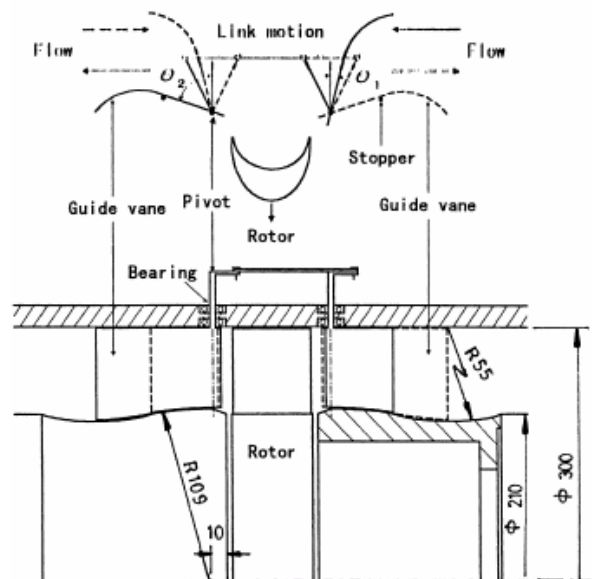


Figure 23 – Impulse turbine with self-pitching linked guide vane arrangement (Setoguchi, 2001)

Figure 24 shows the mean efficiency characteristics, under sinusoidal flow conditions, of a Wells turbine, an impulse turbine without linked guide vanes, and an impulse turbine with moving linked guide vanes, plotted against the flow ratio based on mean axial velocity. This plot shows that the impulse turbine with links had a peak efficiency of about 52%, which was significantly better than the other two configurations. However, comparison with the data in Figure 19 shows that Wells turbine and impulse turbine with fixed guide vane configurations are available that have peak efficiencies of 48% and 39% respectively. It is also to be noted that the moment of inertia of the rotor ( $X_I$ ) has an influence on the behaviour under sinusoidal flow conditions, and whilst a value is given for the Wells turbine in Figure 24, no information was given for the impulse turbines, and there is no discussion of such factors. It was suggested, however, that the efficiency of the linked turbine could be further improved by making the casing spherical to maintain a constant tip clearance, but this could only be expected to have a marginal effect.

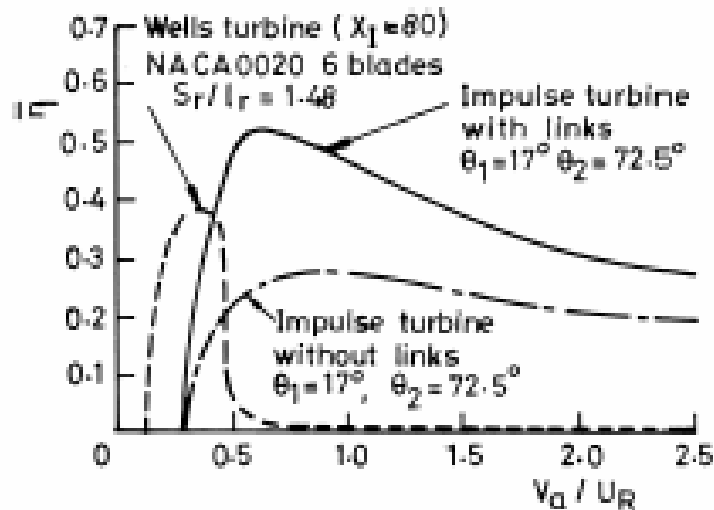


Figure 24 – Comparison of mean efficiencies in sinusoidal flow

In the final part of the review Setoguchi et al presented a plot of the mean efficiencies of Wells and impulse turbines with guide vanes derived from a simulation of operation under irregular flow conditions. The test wave was generated using the International Ship Structure Congress (ISSC) spectrum and is shown in Figure 25. The values of significant wave height ( $H_{1/3}$ ), mean frequency  $\bar{f}$  and area ratio  $m$  (area of turbine/chamber cross-section) were: 1.0 m, 0.167 Hz (i.e. 6 second period), and 0.0234 respectively.

The simulation assumed that the flow was incompressible, and quasi-steady, so the steady state flow characteristics could be used, and that the running speed was kept constant. The simulation was then run for a wide range of rotational speeds, to produce solutions at a corresponding range of  $1/k\omega^*$ . The results in Figure 26 show a reduction of ~5% in the peak efficiency of the impulse turbine with self pitching guide vanes to 48%, but rather surprisingly, a peak efficiency of ~38% for the impulse

turbine with fixed guide vanes, suggesting it is rather insensitive to the flow conditions. It is not apparent why the effect on the fixed guide vane configuration is so much less, and no explanation was provided.

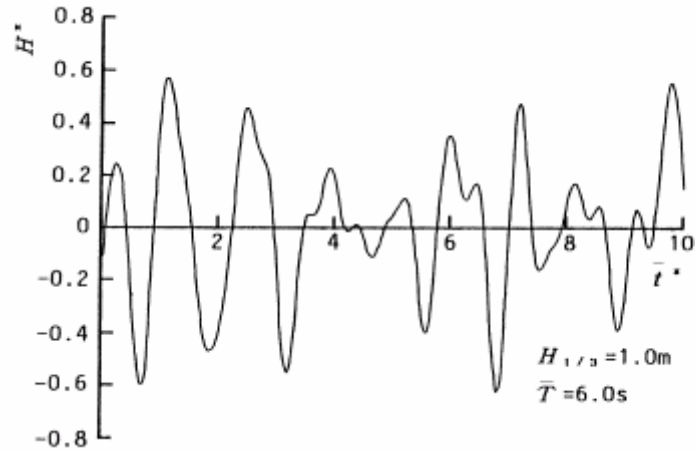


Figure 25 – Test Irregular wave based on ISSC spectrum (Setoguchi et al)

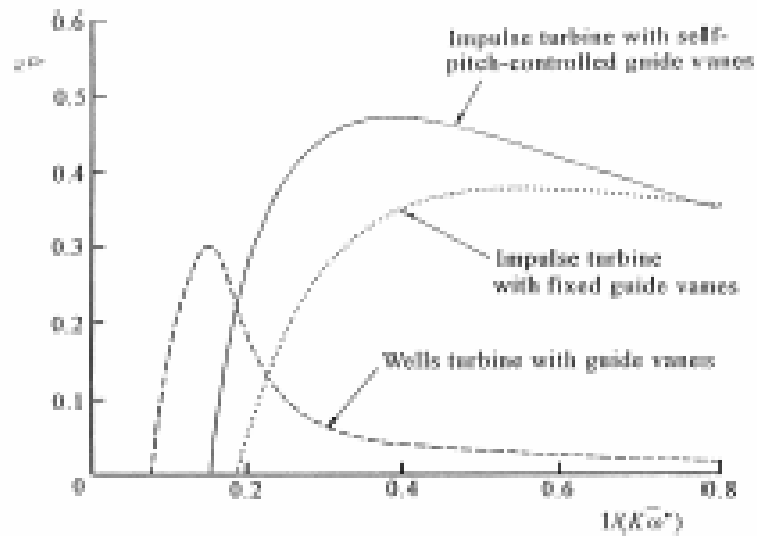


Figure 26 – Comparison of turbine mean efficiencies (Setoguchi et al)

### Starting Characteristics

Setoguchi et al presented the starting characteristics of Wells and impulse turbines with and without guide vanes as shown in Figure 27. A comparison of the plots in the figure showed the following:

1. All the impulse turbine configurations accelerated up to running speed much more rapidly than the Wells turbines.
2. All the impulse turbine configurations accelerated in a similar way, reaching their running speeds in about 3 cycles, although reducing the guide vane angle (and so increasing its turning) did marginally increase the acceleration as would be expected, and is consistent with the steady flow torque characteristic.
3. The use of aerofoil rather than plate guide vanes made no difference to the starting characteristics
4. The running speeds of the impulse turbines were a third to a half of that of the Wells turbine.

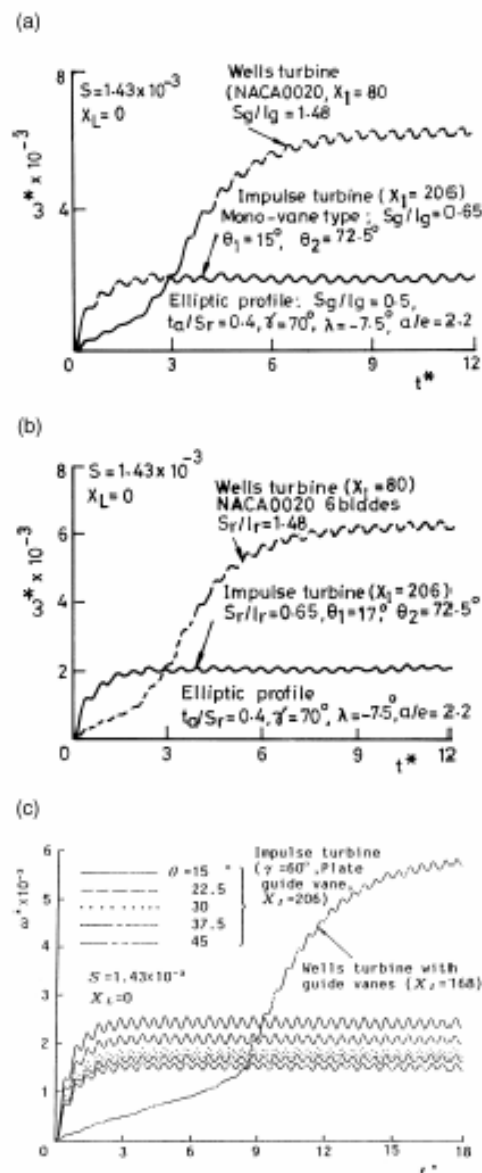


Figure 27 –Starting characteristics in sinusoidal flow (a) impulse turbine with self pitching guide vane and Wells turbine (b) impulse turbine with self pitching linked guide vanes and Wells turbine (c) impulse turbine with fixed guide vane and Wells turbine (Setoguchi, 2001)

## Discussion/Summary

Setoguchi et al concluded from their work that the impulse turbine either with self-pitch-controlled linked guide vanes or even with fixed guide vanes was superior in performance to the Wells turbine in irregular flow conditions. Added to this, the impulse turbines started in a much shorter time than the Wells, and ran at a much lower speeds, which would lead to lower noise and ease mechanical design.

If the results for the fixed and linked guide vanes are put together then the peak efficiencies of the designs under the various flow conditions are shown in Table 9. Whilst there is significant deterioration in the performance of the self-pitching-linked guide vane arrangement, it is surprising that there is so little difference in the performance of the fixed guide vane arrangement, but this was not discussed by Setoguchi et al.

Guide vane arrangement	Steady flow (Experiment)	Peak efficiency (%)	
		Sinusoidal flow (Experiment)	Irregular flow (Simulation)
Fixed	39	38 (Figure 19)	38 (Figure 26)
Self-pitching-linked	61 (Figure 21)	52 (Figure 24)	48 (Figure 26)

*Table 9 – Comparison of peak efficiencies at different flow conditions*

In terms of blade design, Setoguchi et al determined (within the scope of their study), that the optimum impulse turbine rotor for use with either linked or fixed guide vanes, was defined by the parameter values in Table 10. Added to this is the finding by Thakker et al that the tip clearance should be no more than 1%, and that the hub/tip ratio should be 0.6.

Parameter	Value
Profile	elliptic
Inlet angle ( $\gamma$ )	60°
Space/chord ratio ( $S_r/l_r$ )	0.5
Flow path width/rotor blade space ( $t_a/S_r$ )	0.4
Rotor blade sweep ( $\lambda$ )	-7.5°
Ratio of ellipse Semi major/semi minor axis of ellipse ( $a/e$ )	3
Hub/tip ratio ( $v$ )	0.6
Tip clearance	<1%

*Table 10 – Optimum parametric values for rotor*

They also defined optimum design values for the guide vanes as shown in Table 11.

Parameter	Linked guide vanes	Fixed guide vanes
Space/chord ( $S_g/l_g$ )	<0.65	-
Inlet angle ( $\theta_1$ )	15 – 17.5°	30
Outlet angle ( $\theta_2$ )	55 -72.5°	30

*Table 11 – Optimum values for guide vanes*

The effect of guide vane space/chord ratio ( $S_g/l_g$ ) was not investigated in the fixed guide vane studies, but that used was 0.44 (Maeda), which corresponded to 26 vanes. Examination of the geometry suggests that application of the Zweifel number would suggest that fewer guide vanes could be used. It was also concluded that for fixed guide vane arrangements the performance was unaffected by the use of plate or aerofoil guide vanes.

One of the most significant things revealed in the work conducted by Setoguchi et al and Thakker et al is the large effect of hub/tip ratio on performance. The results showed that the difference in peak efficiency at steady flow conditions, between hub/tip ratios of 0.85 and 0.6 could be 20%. However, some caution should be exercised in accepting this, as indeed all the results because the Saga University rig was rather small scale (0.3m diameter) and the Reynolds numbers achieved were low at  $0.4 \times 10^5$ , and although the Limerick University rig was larger scale (0.6m diameter), the Reynolds numbers were still low at  $0.7 \times 10^5$ .

## **2.2.8 Comparison of performances of Wells & Impulse turbines**

### **Study by Kim et al**

A useful experimental and theoretical comparison of the performance of the most promising Wells and Impulse turbine arrangements investigated by previous researchers was carried out in 2001 by Kim et al (Kim, Takao, Setoguchi, Kaneko and Masahiro, 2001). The scope of the comparison made was of self starting designs which were already, or were to be, incorporated in ‘full scale’ OWC facilities. The stated objective was to compare the turbine performances under irregular wave conditions. The 5 turbines examined are detailed in Table 12.

Examination of the characteristics of the Wells turbines showed that they were close to the optimum values recommended by Raghunathan (section 2.2.6, Table 6), whilst the two impulse turbine designs reflected the optimal configurations identified in the work of Maeda, and Setoguchi et al in section 2.2.7.

Turbine	ID	Facility	Characteristics
Wells with guide vanes	WTGV	Mighty Whale	NACA0020, AR=0.5, $l_r=90$ , $\sigma_{rR}=0.67$ , $\sigma_{gR}=1.25$
Wells with self-pitch controlled blades	TSCB	Pico	NACA0020, AR=0.5, $l_r=90$ , $\sigma_{rR}=0.67$ , preset angle=6°
Bi-plane Wells with guide vanes	BWGV	LIMPET	NACA0020, AR=0.5, $l_r=90$ , $\sigma_{rR}=0.45$ , $\sigma_{gR}=1.25$
Impulse with self pitch controlled guide vanes	ISGV	NIOT (India)	$t_a/S_r=0.4$ , $l_r=54$ , $\gamma=60^\circ$ , $\sigma_{rR}=2.02$ , $\sigma_{gR}=2.27$ , $\theta_1=17^\circ$ , $\theta_2=72.5^\circ$ , $\lambda=-7.5^\circ$
Impulse with fixed guide vanes	IFGV	(India, China, Ireland)	$t_a/S_r=0.4$ , $l_r=54$ , $\gamma=60^\circ$ , $\sigma_{rR}=2.02$ , $\sigma_{gR}=2.27$ , $\theta=30^\circ$ , $\lambda=-7.5^\circ$

Table 12 – Turbines reviewed by Kim et al, 2001

Plots (Figure 28 and Figure 29) were presented of the torque and input coefficients of all the turbines in the flow range  $\phi = 0-1.0$ . Figure 28 shows how the torque coefficient of the Wells turbines climbed rapidly at first, but suddenly dropped when the stall condition was reached, whereas that of the impulse turbines was lower at low flow ratios, but then climbed steadily.

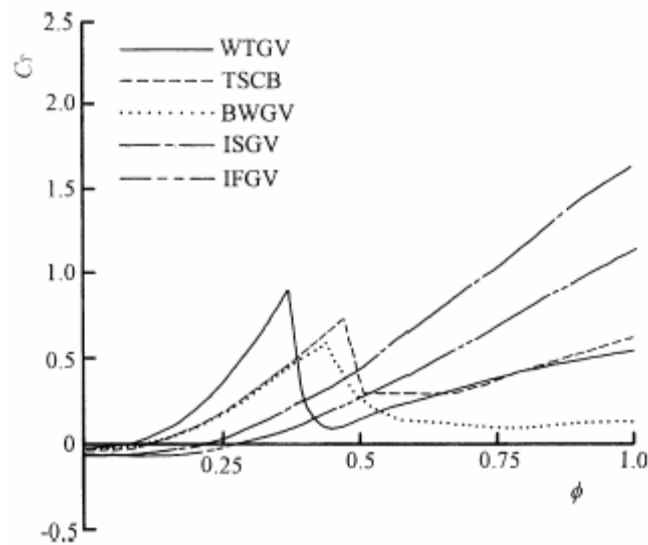


Figure 28 – Comparison of turbine torque coefficients (Kim, 2001)

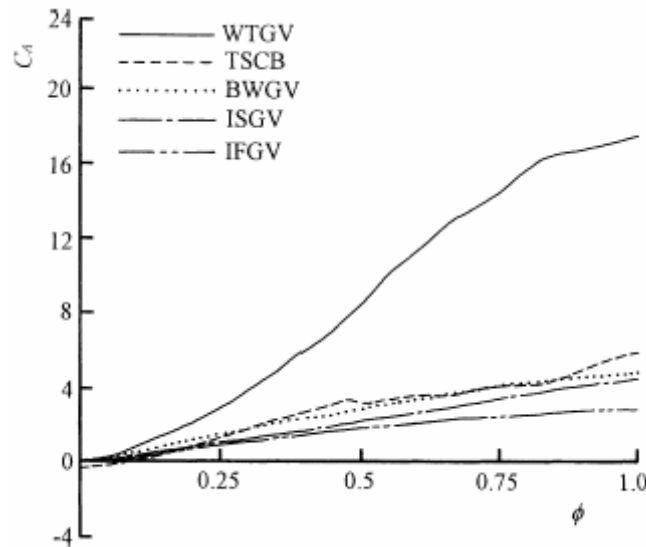


Figure 29 – Comparison of input power coefficients (Kim, 2001)

Figure 29 showed that the Wells turbine with guide vanes had a significantly higher input coefficient than all the other designs, but also how the lowest input coefficients were for the impulse turbines. What this means is that using the Wells turbine with guide vanes led to the highest pressures in the OWC chamber, whereas the pressure rise required was lowest for the impulse turbines.

The data in Figure 29 and Figure 30 may be used to estimate the peak efficiencies of the Wells turbines from:

$$\eta = \frac{C_T}{\phi C_A}$$

Substitution of the appropriate values gives the peak efficiencies shown in Table 13, and from section 4, the peak efficiencies of the ISGV and IFGV configurations would be expected to be ~61% and ~39% respectively.

Turbine	Peak efficiency (%)
WTGV	44
TSCB	46
BWGV	53

Table 13 – Steady flow peak efficiencies of Wells turbines

The performance comparison was carried out using the same mathematical model, and exactly the same irregular input wave and OWC assumptions as used by Setoguchi et al (section 4.4.4 and Figure 25). The relative efficiencies of the turbines were then compared by plotting the average cyclic efficiency against  $1/K\bar{\omega}^*$ . This revealed that the conversion efficiency of impulse turbines was significantly better than Wells turbines at higher values of  $1/K\bar{\omega}^*$ , with the ISGV having a peak efficiency of 48% - some 15% higher than the WTGV, and the IFGV having a peak

some 6% higher at 38%. Both impulse devices exhibited a broader operating range than the Wells turbines, and the results were said to be similar for any  $H_{1/3}$ .

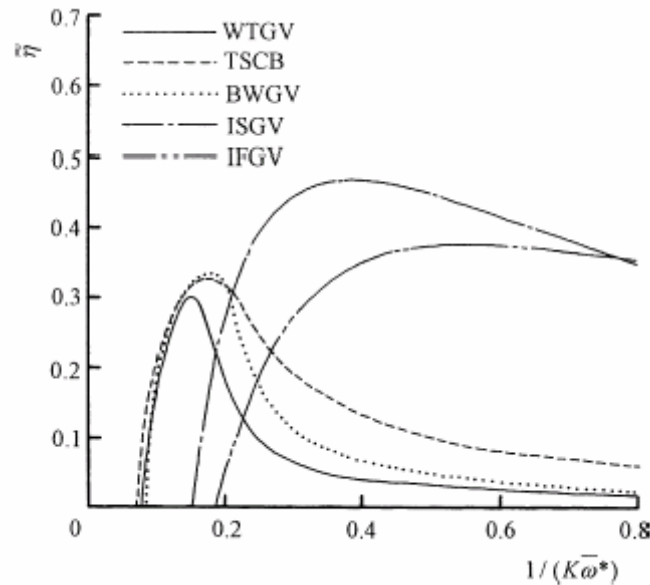


Figure 30 – Comparison of conversion efficiency of wave energy (Kim, 2001)

A comparison of wave height in the chamber at the maximum efficiency conditions for the WTGV and IFGV turbines showed that the levels of  $h^*$  were higher for the impulse device than the Wells device. This difference was attributed to the higher chamber pressures required by the WTGV which suppressed motion in the OWC, i.e. the damping effect of the impulse turbine was less than that of the Wells turbine.

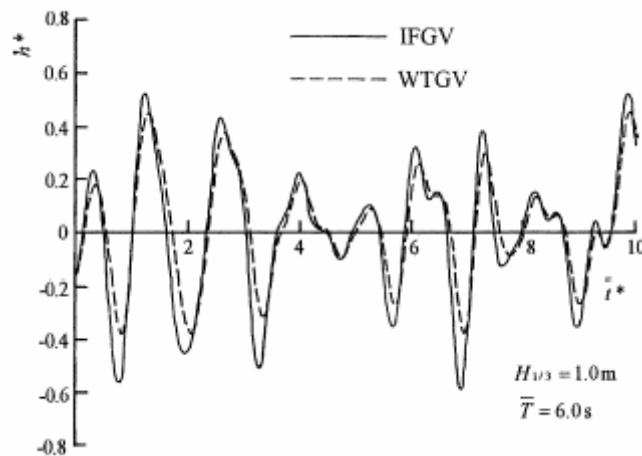


Figure 31 – Comparison of wave heights in chamber (Kim, 2001)

Overall, it was concluded that the higher peak efficiencies achieved by the impulse turbines shown in Figure 30 demonstrated that they could achieve better performance

than Wells turbines under irregular flow conditions, because they had no rotor stall. Furthermore, there were additional benefits in their having much lower speeds and axial forces, which would reduce noise and ease mechanical design. However, this comparison ignored both the contra-rotating, and the self-pitch-controlled Wells turbines, for which higher steady flow efficiencies have been predicted.

### Comparison of actual and predicted BWGV performance

One of the turbines examined by Kim et al in 5.1 was the bi-plane Wells turbine design with guide vanes, which they said had been selected for LIMPET. This appears to actually refer to the 75kW installation which preceded LIMPET, as the turbine fitted in LIMPET was a 2.3 m diameter contra-rotating Wells turbine. The characteristics of all 3 turbines are given for comparison in Table 14, and it can be seen that the BWGV is broadly similar to the QUB 75kW bi-plane design, except that the QUB 75kW design had a significantly thinner blade section.

Parameter	BWGV	QUB 75kW (bi-plane)	LIMPET (contra rotating)
Profile	NACA0020	NACA0012	NACA0012
No. of blades (z)	4	4	7
Hub/tip ratio	0.7	0.62	0.62
AR	0.5	0.57	1.37
$r_R$	0.1275	0.486	0.9315
Solidity at $r_R$ ( $\sigma_R$ )	0.45	0.524	0.383

Table 14 – Comparison of Wells turbine design parameters

A comparison of predicted and actual efficiency based on real irregular flow input data recorded at the 75kW installation on Islay was given by Raghunathan (Raghunathan, 1995) which is reproduced in Figure 32.

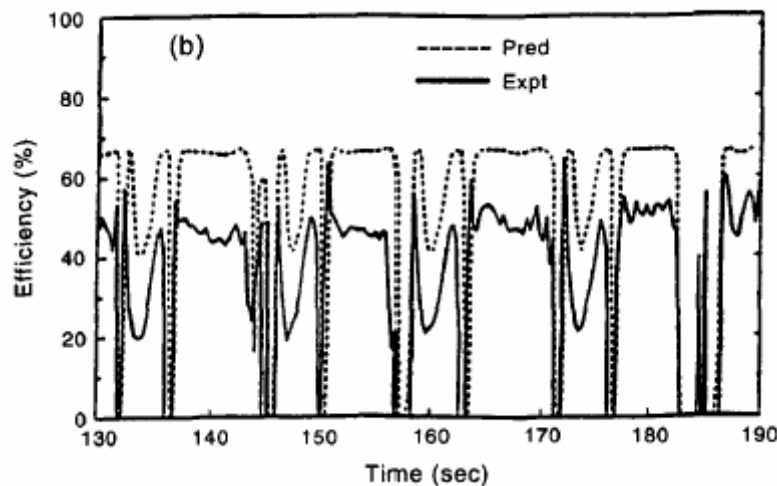


Figure 32 – Predicted and actual efficiency for Islay Wells turbine (Raghunathan, 1995)

The data was taken at the turbine design speed of 1500rpm, and so is assumed to reflect peak performance. A visual assessment of the actual efficiency shown in Figure 32 suggests that the average efficiency is around 35-40%. However, Raghunathan also appears to evaluate efficiency from the total-to-total pressure drop, rather than the total-to-static pressure drop. This means that to compare this data with the results of Kim's analysis we would expect to reduce the average efficiency by ~5%, this would suggest that the average peak efficiency in irregular flow was 30-35% - which agrees with Kim's analysis. This result provides compelling evidence for the credibility of the analysis carried out by Kim et al and their conclusions<sup>2</sup>.

Further support for the validity of the above results is provided by a comparison of predicted and actual efficiency values for LIMPET shown in Figure 33 (Queen's University Belfast, 2002). Although no real detail of the conditions and calculations are given, it can be seen that the peak predicted steady flow efficiency is 75%, which is assumed to be based upon total-to-total pressure drop (although this is significantly below the 90% determined by Raghunathan), and it was stated that the actual average turbine efficiency was around 35%.

It is evident in both Figure 32 and Figure 33 that the efficiencies in the 2 flow directions were markedly different. It has been suggested that the efficiency on the inflow part of the cycle in LIMPET could be improved by putting guide vanes in the acoustic chamber, perhaps indicating that some of the loss in efficiency is due to poor flow quality. It is also pertinent to note that one of the conclusions was that the contra-rotating Wells turbine did not appear to offer a sufficient improvement in either peak performance or bandwidth to justify the additional cost of duplication of mechanical and electrical components.

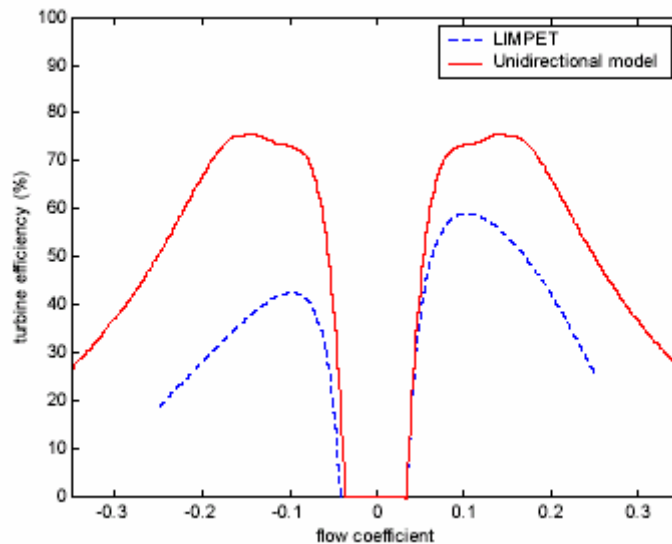


Figure 33- Comparison of actual and predicted efficiency for LIMPET (QUB, 2002)

<sup>2</sup> The Islay LIMPET wave power plant report produced by QUB says that in its final configuration the 75kW bi-plane turbine achieved was 50% efficiency, although no additional data was provided to support this.

## 2.2.9 HydroAir Performance Requirements

### Current Turbine Efficiencies

From the analysis of the literature reported in the foregoing sections, the state-of-the-art in OWC turbine performance would appear to be as summarised in Table 15. The value for the Denniss-Auld turbine is bracketed because it is not known whether this is a total-to-total, or total-to-static value. Whilst the steady flow performance of the Denniss-Auld turbine is in the range expected with variable geometry, it is not clear what its irregular flow performance would be, particularly in comparison to the impulse with self-pitching linked guide vanes which can be supposed to have advantages in terms of starting characteristic and lower rotational speed.

Turbine	Peak Efficiency (%)	
	Steady flow	Irregular flow
Wells with guide vanes	44	30
Bi-plane Wells with guide vanes	53	35
Denniss-Auld turbine	(65)	-
Impulse with fixed guide vanes	39	38
Impulse with self-pitching linked guide vanes	61	48

*Table 15 – Comparison of peak efficiencies achieved by turbine types*

It is interesting to note that only the impulse turbine with self-pitching linked guide vanes achieved a peak efficiency greater than the 45% power take-off efficiency under irregular flow conditions assumed in the 2002 DTi evaluation of floating OWCs – which was based upon a fixed pitch Wells turbine. This suggests that such assessments have made wildly optimistic assumptions regarding turbine efficiencies under real conditions.

The amount of research work which has been conducted into OWC turbines and values of peak efficiency in Table 15 suggest that a project target peak efficiency of 90% is not very realistic, and that to achieve a whole system efficiency of 65% in irregular flow would probably require a turbine peak efficiency around 75-80% - based on total-to-static efficiency, which would imply a peak total-to-total efficiency in steady flow conditions of over 90%, which is the sort of level of performance attained only by the best axial flow turbines.

Based on the evidence collected, and calculations made, it appears that a turbine design that could be made to operate reliably with a peak efficiency in irregular flows of 50% would be a major advance. Moreover, a turbine which attained a peak efficiency of 60% in irregular flows – i.e. a 50% improvement in performance - would be a dramatic advance.

From the differences shown in Table 15 a peak efficiency of 60% in irregular flows would probably require a peak steady flow total-to-static efficiency of 70-80%. Such a level of performance represents a ‘step-change’ and requires the development of a turbine concept which is radically different from all those to date. The magnitude of

the challenge is illustrated by the predicted efficiency characteristic produced by PBL for a uni-directional impulse turbine stage design shown in Figure 34, which has a peak efficiency of 70% (total-to-static). This was only a first pass design, but the simulation was made with zero tip clearance.

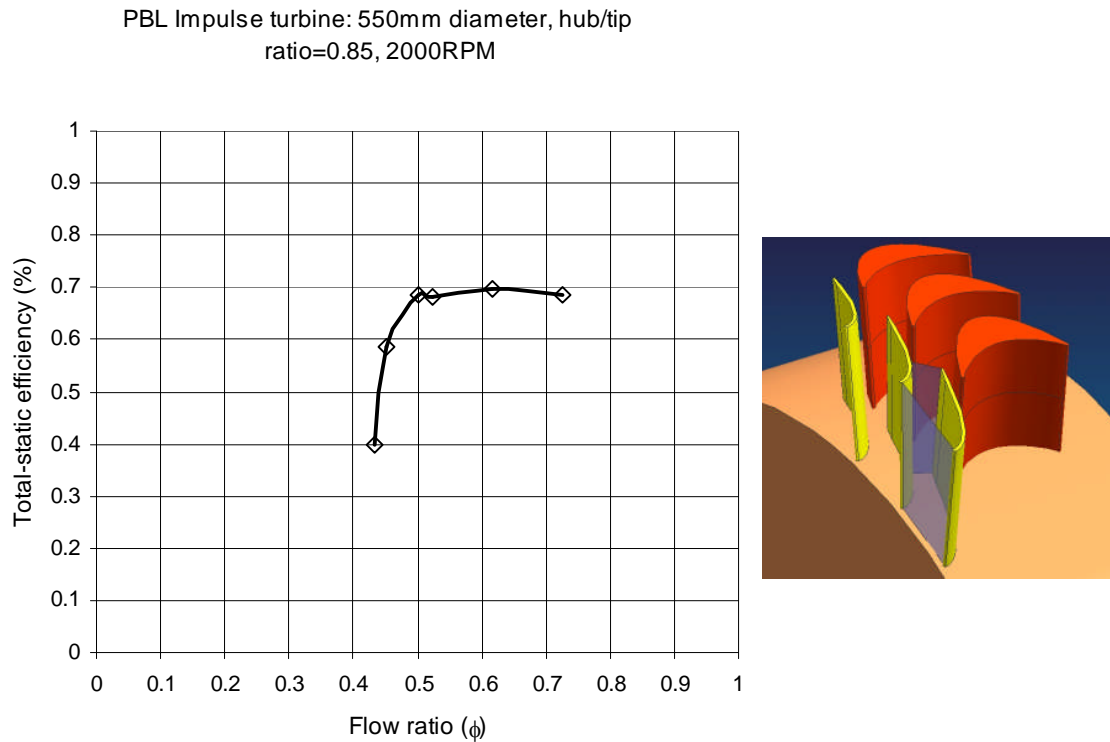


*Figure 34 – Predicted efficiency characteristic for uni-directional impulse turbine (PBL)*

It is therefore proposed that, given the ambitious project objectives, the turbine efficiency performance targets are: for a peak efficiency in steady flow conditions of at least 70%, and a peak efficiency under irregular flow conditions of at least 55%, (based on total-to-static pressure).

### Range of Operation

From the information in the LIMPET reports it was evident that the turbine losses under the irregular flow conditions were much greater than expected. It was said that using steady flow data to predict the cyclic performance of single and bi-plane turbines had previously proved satisfactory, and further work was required to understand why the inaccuracies were so much greater for a contra rotating device. In addition to the poor turbine performance there was a high power overhead in the electrical and mechanical components, such that an average minimum of 100kW of pneumatic power was required before power was supplied to the grid. This meant that the plant was only on-line for 50% of the year, and the clear inference of this was that this was too low. Examination of wave frequency data from Islay shows that even

ignoring losses then for the power plant to be on-line for more than 50% of the time, then the smallest wave from which the turbine must be able to extract useful power is  $H_S = 1.0\text{m}$  (Figure 35), where the wave energy is  $<10\text{kW/m}$ . Conversely, if the turbine only extracts useful power when  $H_S = 3\text{m}$  or more it would only be on line 10% of the time.

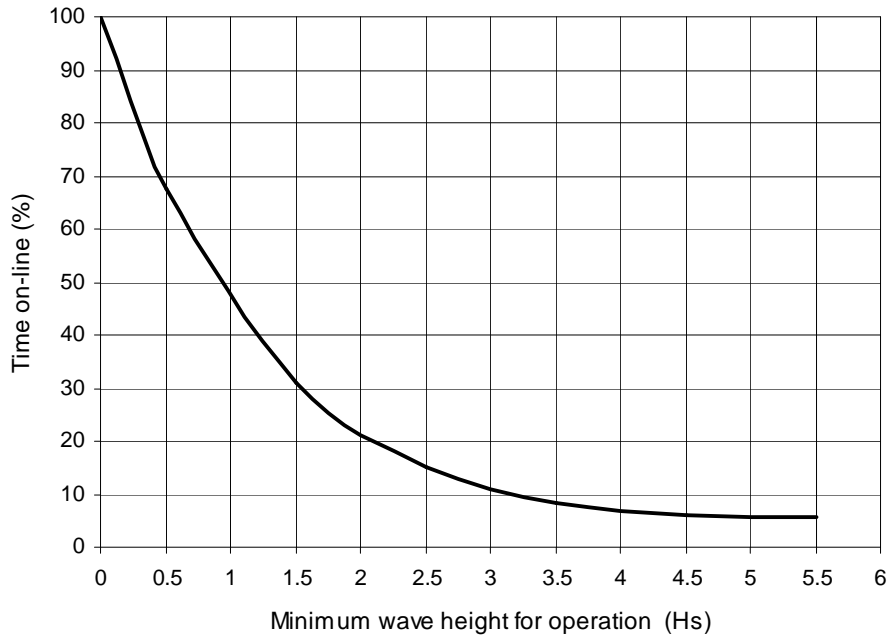


Figure 35 – Variation in time on-line with minimum wave height for operation

The other factor to be considered along with what proportion of the time the plant is on-line is what its load factor is, i.e. what its average power output is relative to its installed capacity. The report on the LIMPET power plant (Queen's University Belfast, 2002) concluded that experience had shown that the notional load factor of 30% often quoted for wave energy plants (e.g. the 2002 DTi evaluation of floating OWCs assumed the rated power of the installations was  $3\times$  annual average) was too low, in that fixed equipment losses became a disproportionately high proportion of generated power (although it was suggested that the mechanical and electrical configuration was less than optimum for LIMPET). It concluded that the ideal load factor had yet to be established, but that operational experience indicated that it was likely to be close to 50%. Given the need to extract useful energy from the relatively frequent but low energy waves of levels of tens of kW/m, there is a fundamental incompatibility between doing this and achieving a 50% load factor if it is also required to absorb the maximum wave energies of over 200kW/m. The solutions to this are either to restrict the power going through the turbine, or incorporate a level of adaptability in the generating system. This is not a turbine design issue, and it is therefore ignored at this point.

The turbine design requirement is to be able to extract useful energy from significant wave heights of less than 1.0m. It also required to have good efficiency over as large a

range of flow conditions as possible. This requirement in the proposal suggests that it cannot be assumed that the power electronics and control algorithms will be able to control the RPM of the turbine to give the optimum value of flow ratio i.e.  $V_A/U$ .

### **Starting characteristics**

If the turbine is to extract useful energy at very low wave energy conditions, then it must have good starting characteristics, and must certainly be self-starting.

### **Reliability**

Ocean energy projects are capital intensive and in order to be economic they must operate reliably with little maintenance and cost for long periods of time (Wavenet). This forms the over-riding consideration that must be applied to the development of any new turbine/power-take-off solution. This means that any practical turbine solution should not incorporate any features likely to lead to reliability problems.

## **2.2.10 Conclusions**

There are a number of conclusions which may be drawn from the work presented in the literature and these are presented below.

### **Required characteristics**

The turbine solution should have the following characteristics:

- It must be self-starting.
- It should be able to extract useful energy from significant wave heights of less than 1.0m.
- It is required to have good efficiency over as large a range of flow conditions as possible.
- It should not incorporate any features likely to lead to reliability problems.
- Operate at speed compatible with generator
- Target peak efficiency (based on total-to-static pressure) in steady flow conditions of at least 70%.
- Target peak efficiency (based on total-to-static pressure) under irregular flow conditions of at least 50%.

### **Turbine types**

**Axial flow turbine** - No valve solution could be identified that appeared to combine the characteristics of low loss, high sealing effectiveness and reliability required to make a valved axial flow turbine arrangement attractive.

**Denniss-Auld Turbine** - The Denniss-Auld turbine appears to offer improved levels of efficiency, and a rather greater operating range than a conventional Wells turbine. Insufficient information was available to determine whether its irregular flow performance was better than an impulse turbine with self-pitching linked guide vanes.

**Wells turbine** - The narrow band of flow coefficient within which the Wells turbine operates at high levels of efficiency, means that it is essential that the running speed of a fixed geometry Wells turbine is varied to avoid excessive periods of rotor stall

**Impulse turbine** - The hub/tip ratio has a large effect on the performance of impulse turbines, and a hub/tip ratio of  $h = 0.6$  gives best performance

The test results showed that the aerofoil guide vane design used by Setoguchi et al did not reduce the extent of the separation effects on the downstream guide vanes, and actually increased them slightly at flow ratios beyond the peak efficiency point

### **Most promising existing turbine type**

An evaluation of the turbine design requirements and the information on the performance and operating characteristics of existing turbines in the literature unequivocally shows the impulse turbine to be the most promising turbine for use in OWCs. The relevant factors can be summarised as follows:

- Impulse turbines are self starting and run up to their operating speeds within a very few cycles
- Impulse turbines achieve higher efficiencies than Wells turbines under irregular flow conditions due to their lack of stalling.
- A variable geometry impulse turbine has demonstrated efficiencies close to the target values identified

## 2.3 OWC Turbine Test Facilities

### 2.3.1 General

The majority of the experimental investigations of turbines for use in OWCs reported in the open literature have employed steady-flow tests, such as those carried out by Wavegen (Tease, ) and at IST in Lisbon (Raghunathan, 1995). When steady-flow experiments are carried out, the turbine is usually connected to a load system, often comprising a driven disk coupled to a mechanical brake. The turbine experiment consists then of a series of runs at distinct steady flow speeds, and for each of these different turbine rotational speeds are set by varying the load. The performance is then evaluated by measuring the turbine rpm, its output torque, the mass flow rate through it, and the pressure drop across it.

The most notable exception to the general steady-state testing approach has been the work of a combined Japanese and Indian team carried out at the Saga University in Japan, and usually reported by Setoguchi, where a rig capable of producing an oscillating flow was used. However, despite having a turbine test rig which could apparently produce an oscillating flow, the researchers have generally derived their turbine characteristics for pseudo-sinusoidal flows by measuring the steady flow turbine performance, and then making an assumption of quasi-steady flow, used a simulation program to obtain the oscillating flow performance (Setoguchi et al, 2003).

### 2.3.2 The Saga University test facility

#### General

A schematic of the Saga University turbine test facility this has been used to evaluate a large number of OWC turbine designs is shown in Figure 36. The basic operating principle of the rig is the use of a piston to provide the air flow through the turbine. The piston runs on 3 ball screws which are synchronised by a chain and sprocket drive. The chain is driven by a computer controlled DC motor. When the rig is in operation the air passes from the piston into a settling chamber, before going into the 300 mm diameter turbine test section, which has a bellmouth fitted at each end. It is said that the drive system enables a wide range of time varying flow rates to be produced, or steady flows for short periods. The turbine is connected to a servomotor/generator so that power can be taken off, or the turbine can be run up to a pre-determined test speed.

The information presented in the literature obtained is incomplete, and does not enable a detailed understanding of the rig to be formed. From the information that is presented, it appears that the operating parameters and instrumentation are as described below.

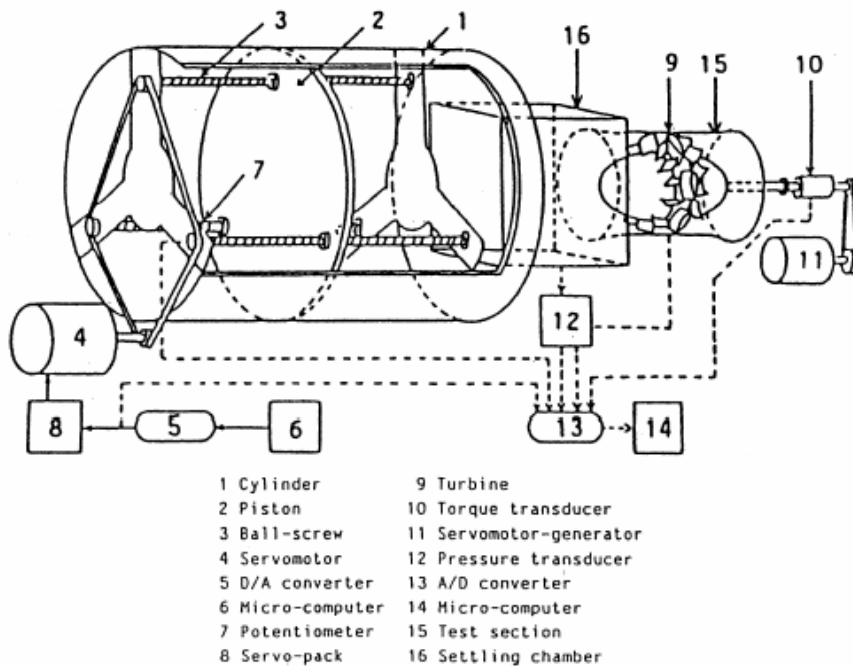


Figure 36 – Schematic of Saga University test rig (Setoguchi et al, 2003)

### Dimensions and capability

The literature stated that the maximum flow rate attained in tests was  $0.63 \text{ m}^3/\text{s}$ . If the diagram of the rig (Figure 36) is to scale, it suggests that the piston has a radius of  $0.4\text{m}$ , and length of  $1.0\text{m}$ , giving an overall volume of  $0.5\text{m}^3$ , which would mean that the ball screws are driven at up to  $1.26 \text{ m/s}$ , and that the maximum steady flow rates are only attained for a fraction of a second. The turbine pressure drops recorded have been in the range  $200\text{-}800 \text{ Pa}$ , whilst the range of rotational speeds used was up to  $370 \text{ rads/s}$  ( $3500 \text{ rpm}$ ) for impulse turbines, and up to  $471 \text{ rads/s}$  ( $4500 \text{ rpm}$ ) for Wells turbines. The accuracy quoted for the efficiency measurements was  $\pm 2\%$ .

A limitation of the rig is that (based on the calculated dimensions) whereas the  $Re$  based upon blade chord was  $2 \times 10^5$  for a Wells turbine, it was only  $0.4 \times 10^5$  for the impulse turbines tested (based on rotor chord length,  $l_r = 54\text{mm}$ ).

The rig enables the starting characteristics of the test turbine to be measured simply by recording the turbine rotational speed.

### Instrumentation

The performance of the turbine at any instant is determined by measurements of turbine rotational speed, shaft torque, and the average flowrate, and pressure drop, where the flow rate is measured using a pitot tube survey, and the total pressure drop across the turbine is measured as the difference between the pressure recorded by a

transducer in the settling chamber and atmospheric pressure. This means that all losses are attributed to the turbine.

### 2.3.3 The Limerick University Test facility

#### General

A conventional steady flow test facility with higher flowrate, but smaller test section diameter, exists at Limerick University. This is of interest because the groups at Saga and Limerick Universities are linked through the Wave Energy Research Team (WERT), and tests of similar designs have taken place in the Saga and Limerick facilities.

#### Dimensions and capability

The Limerick University test facility is driven by a 4kW blower which provides an optimum static pressure rise of 2000 Pa and a flow of  $1.1\text{m}^3/\text{s}$  to the turbine test section via a 250 mm diameter pipe. A diagram of the turbine test section is shown in Figure 37.

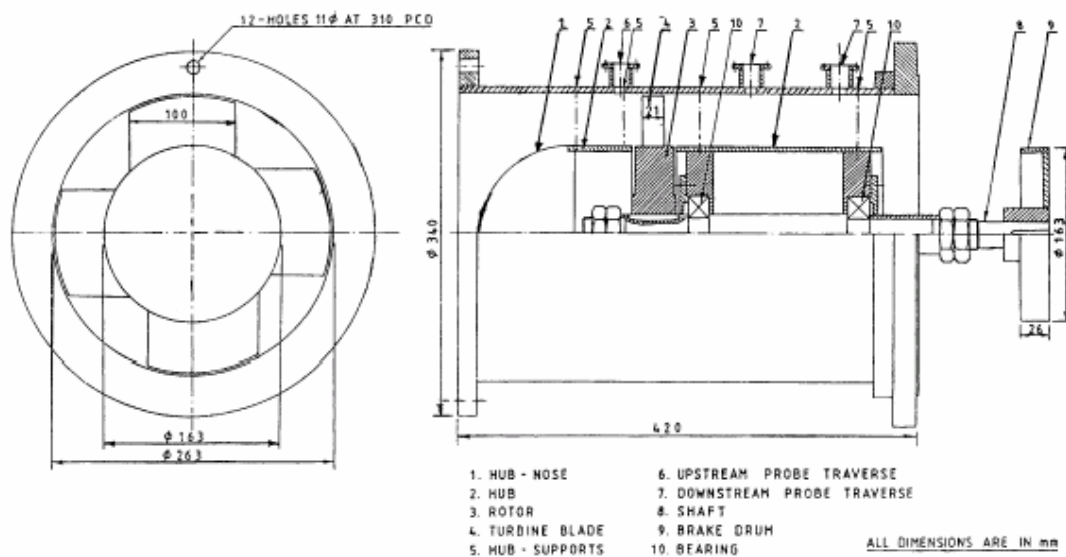


Figure 37 – Cross section of turbine test section in Limerick University test rig (Danasekavan & Govardskhan)

The diameter of the turbine test section is 265 mm, and has typically been configured to have a hub diameter of 163 mm, giving a hub/tip ratio of 0.619 and annular area of  $0.0343\text{m}^2$ . Given a volumetric flowrate of  $1.1\text{m}^3/\text{s}$ , the axial velocity through the test section would be 32 m/s. This arrangement gave a Reynolds number of  $4 \times 10^5$  for a 4 blade Wells turbine with 100mm blade chord turning at 4500 rpm. However, the Reynolds numbers achieved for an impulse type turbines would be considerably lower, as in the Saga University facility.

## Instrumentation

The turbine torque and speed are measured by a dynamometer and a non-contact tachometer. A 3 hole pitot probe was mounted 33mm ahead of the turbine to measure the 2-dimensional inflow conditions, whilst a 5 hole probe was mounted 80 mm downstream of the turbine to measure the velocity profile of exit flow. The flowrate was evaluated by taking data at 13 radial positions.

### 2.3.4 Summary

From the survey of test facilities used to evaluate the performance of turbines for application in OWCs that has been carried out, it can be concluded that they have generally been designed for uni-directional testing, and it appears that the one facility which appears capable of producing sinusoidal and irregular flow conditions is not typically used in his way. All of the facilities have been designed for turbines of 0.3m diameter or less. This diameter has given Reynolds numbers of more than  $2 \times 10^5$  for Wells turbines, but somewhat less than this for impulse turbines – suggesting that the facilities were designed to test Wells turbines. This means that to ensure that appropriate levels of Reynolds numbers can be achieved for different turbine types the test facility should be designed for testing impulse turbines.

## 2.4 Scaling

### 2.4.1 Non-dimensional parameters

The survey of previous research into the design of turbines for use in OWCs has shown that their performance has typically been evaluated under steady flow conditions, despite the fact that the turbine operates with an oscillating flow in an OWC. Given the poor correlation between prediction and reality achieved, it was considered important to recognise the frequency effect within the HydroAir project, or at least only remove it if overwhelming evidence was found that it could be neglected. Consideration of the variables associated with the operation of a turbine whose output is varying with time, leads to the idea that the power output (P) depends on the following variables (assuming that compressibility - i.e. Mach number - effects can be ignored):

$$P = f(D, N, \rho, \mu, H, f)$$

where the variables and their dimensions are defined in Table 16.

Parameter	Symbol	Units	Dimensions
Power	P	W	$ML^2/T^2$
Characteristic dimension	D	m	L
Speed of rotation	N	rad/s	L/T
Fluid density	$\rho$	$kg/m^3$	$M/L^3$
Fluid viscosity	$\mu$	$Ns/m^2$	$ML/T$
Frequency	f	Hz	1/T

Table 16 – Parameters describing turbine performance

A dimensional analysis then leads to the identification of 5 non-dimensional groups:

$$\text{Flow coefficient: } \phi = \frac{Q}{ND^3}$$

$$\text{Head coefficient: } \psi = \frac{gH}{N^2 D^2}$$

$$\text{Power coefficient: } \varepsilon = \frac{P}{\rho N^3 D^5}$$

$$\text{Reynolds number: } \text{Re} = \frac{\rho ND^2}{\mu}$$

$$\text{Strouhal number: } \text{St} = \frac{f D}{v_a}$$

The first 3 groups enable the turbine performance to be expressed in non-dimensional form, and further manipulation and substitution leads to the more commonly used groupings:

$$\phi = \frac{v_a}{U_{Mid}} \quad , \quad \psi = \frac{\Delta P}{\rho U^2} \quad , \quad \varepsilon = \frac{P}{\rho U^3 A}$$

and the efficiency is given by:  $\eta = \frac{\varepsilon}{\phi \psi}$

If geometric similarity is taken as a given, then the Reynolds and Strouhal numbers characterise the state of the fluid flow and matching them would give kinematic similarity. If a model turbine is then considered with characteristic dimension  $d$ , then the performance of the model will be related to the prototype of characteristic dimension  $D$  by the following relations:

$$\varepsilon = f_1\left(\phi, \text{Re}, \text{St}, \frac{d}{D}\right)$$

$$\psi = f_2\left(\phi, \text{Re}, \text{St}, \frac{d}{D}\right)$$

$$\phi = f_3\left(\phi, \text{Re}, \text{St}, \frac{d}{D}\right)$$

These relations show that if Reynolds and Strouhal number effects are small, then power and head coefficients, and efficiency are only dependent upon the flow ratio.

## 2.4.2 Reynolds number effects

Although dimensional analysis shows a need to match Reynolds number to achieve similarity of flow at model scale, it is immediately evident that if it is expected to conduct tests with sub-scale models that this is very difficult to do. If Reynolds number is defined in terms of characteristic dimension  $l$ , then:

$$\text{Re} = \frac{\rho v l}{\mu}$$

If  $l$  is reduced, then  $\rho$  or  $v$  have to be increased, or  $\mu$  decreased, to give the same value of Re. Of these increasing  $v$  is the most readily achievable, as altering the other parameters involves pressurised or very cold testing, or a change of fluid. Neither of the latter options were realistic within the budget of the HydroAir project. The limits within which  $v$  may be varied are determined by the capability of the test facility and the onset of compressibility effects. Although the test facility was to be designed to provide the maximum capability possible, it was evident that the maximum flow velocities that can be achieved were not likely to be greater than 50m/s, which would not be high enough to make similarity in Re achievable.

The cost and difficulty of manipulating the fluid density and viscosity mean that – as is the usual case in aerodynamic testing - scale-effects will be introduced. This means that consideration needs to be given to what Reynolds numbers can be reasonably achieved, and how data taken at low Reynolds numbers may be extrapolated to full scale Reynolds number conditions.

The Air Movement and Control Association (AMCA) and the American Society of Heating, refrigeration, and Air Conditioning Engineers (ASHRAE) joint testing standard (ANSI/AMCA/ASHRAE) Standard 210-85 (AMCA,1985) “Laboratory Methods of Testing Fans for Rating”, state that the influence of Reynolds number may be neglected if (Wright, 1999):

1. The Reynolds number of the model ( $\text{Re}_D = \frac{\rho N D^2}{\mu}$ ) is greater than  $3 \times 10^6$
2. The diameter of the model is at least 0.9m, or the model is 1/5<sup>th</sup> scale – whichever is the larger.

Unfortunately, it is unlikely that the test facility will be large enough to attain either of these criteria. More usefully, ASME Power Test Code PTC-10 (ASME, 1965) says that the efficiency of axial flow compressors can be scaled with Reynolds number according to:

$$\frac{(1 - \eta_p)}{(1 - \eta_m)} = \left( \frac{\text{Re}_m}{\text{Re}_p} \right)^{0.2} \quad \text{for } \text{Re}_D \geq 10^5$$

However, various different values have been proposed for the value of the exponent, which lead to a wide range of predicted improvements in efficiency at full scale, and there is no generally accepted formulation.

Horlock (Horlock, 1966) collected data from a number of sources relating to the effect of Re on losses, which is shown in Figure 38. It is to be noted that Re here is based upon throat hydraulic mean diameter, which is:

$$D_h = \frac{4A_t}{S_t}$$

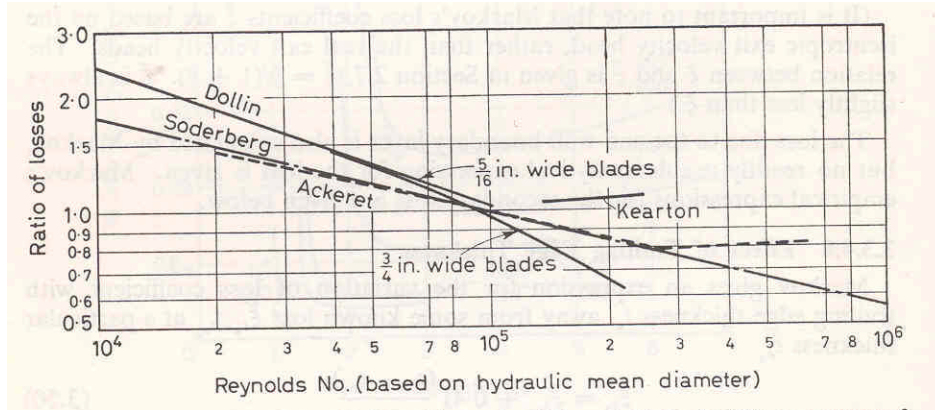


Figure 38 – Variation of loss with Reynolds number (Horlock)

Horlock said that it was clear that Soderberg's relationship provided a good approximation the effect of Re on losses i.e that the loss coefficient at Reynolds number other than  $10^5$  ( $\epsilon'''$ ) is given by:

$$\epsilon''' = \epsilon'' \left( \frac{10^5}{R_h} \right)^{\frac{1}{4}}$$

where,  $\epsilon''$  is Soderberg's loss coefficient ( $\epsilon'$ ) corrected for difference in aspect ratio from 3:1. Horlock also said that Ainley had suggested that efficiency varied with Reynolds number down to  $Re = 5 \times 10^4$  according to:

$$(1 - \eta_{TT}) \propto Re^{\frac{1}{5}}$$

but Kearton's data suggested a critical Reynolds number of around  $10^5$ .

Horlock concluded that it was important to realise that Reynolds number effects depended upon blade shape, as this affected boundary layer growth and losses, and implied that the existence of a critical Reynolds number could be influenced by the roughness of the blades. However, he suggested that Soderberg's relationship, derived from the variation in skin friction on flat plates with Reynolds number, would be adequate for most turbines. Horlock's information agreed with the ASME PTC-10 code in suggesting that there is a critical value of Re at around  $Re=10^5$ - although this is obviously dependent upon the characteristic dimension chosen. The view traditionally held at Cranfield has been that to obtain credible data turbomachinery

should be tested at Reynolds numbers of at least  $2 \times 10^5$ . This criterion is probably derived from the results of Rhoden and Lieblein, which have been presented by Cumpsty (Cumpsty, 1989). This data covered tests at a range of Reynolds numbers and incidences which showed that the loss coefficient for a C4 cascade reached an asymptotic value at  $Re = 1.8 \times 10^5$ , where the Reynolds number is calculated from the inlet relative velocity, the blade chord, and the kinematic viscosity at the static conditions for the entry flow. Use of this criterion would also suggest that application of Soderberg's loss ratio relationship should provide a realistic estimate of the performance of the full scale device.

It is thus concluded that the test turbine should be designed to have a design Reynolds number of at least  $Re = 2 \times 10^5$  based upon inlet relative velocity, blade chord, and entry static conditions, and the measured performance should be extrapolated to full scale using Soderberg's loss ratio relationship.

### 2.4.3 Frequency effects

#### General

The dimensional analysis showed that if the frequency at which the flow is oscillating through the turbine in an OWC is thought to have a significant impact upon its performance, then matching of the Strouhal number should be matched in any model testing to have similarity of flow conditions. As it is clearly simpler - and less costly - to construct a uni-directional flow test facility than an oscillatory flow one, there is a need to have evidence to support the choice of the more challenging task.

Brito-Melo et al (Brito-Melo et al, 2002) found that the greatest challenge to designers of wave energy systems was the intrinsically oscillating nature and random distribution of the wave energy resource. This meant that the air turbine in an OWC converter was subject to a randomly reciprocating flow, and was required to extract energy from air whose flow rate varied from zero to a maximum in 2 directions, and had large variations from wave to wave and with sea conditions. The negative impact of these effects has been demonstrated by the performance measurements shown in Figure 33 for the counter-rotating Wells turbine installed in LIMPET. In this case the predicted performance was derived from testing a 0.6m diameter model in the uni-directional steady flow test facility at IST in Lisbon. The large reduction in performance of the counter rotating turbine was said to be due to the random oscillatory nature of the flow through the turbine when driven by waves, which led to an earlier onset of stall in the turbine than when the flow was steady and unidirectional. In addition the stall led to more noise, which required a silencer to be fitted, which then introduced flow mal-distribution, and further degraded performance. The greater adverse effect of irregular flows than sinusoidal flows on performance was noted by Raghunathan in 1995.

It was concluded that such a dramatic difference between the unidirectional and oscillating flow performances of Wells turbines had not previously been observed due to a lack of oscillating flow facilities for testing turbines, which meant that the

performance loss in oscillating flow conditions could not have been predicted (Queen's University Belfast, 2002). It was concluded that:

*“Turbine characteristics derived from steady state unidirectional flow tests are inaccurate due to the inherent unsteadiness of the flow though the turbine of an OWC. Inaccuracies appear particularly significant for contra-rotating turbines.”*

This is significant, as Raghunathan who studied Wells turbines extensively, worked at QUB and stated that as the airflow frequency in a wave energy device was less than 1 Hz, it could be assumed that dynamic effects were negligible, and performance predictions could be made based upon quasi-steady assumptions and experiments on uni-directional airflow test rigs (Raghunathan, 1995). This provides a compelling case for testing of turbines for OWCs in a test facility that can produce representative irregular oscillating flow conditions, as part of the risk reduction process, and to establish the magnitudes of the effects of steady oscillating flows and irregular oscillating flows on turbine performance. It is apparent though, that to have a facility that could produce truly irregular flows would require it be able to produce oscillatory flows over a very high bandwidth, whereas the range of frequencies and amplitudes of air displacements which it is practicable to engineer into a test facility at reasonable cost is likely to be quite limited.

### **Effect of oscillating flows on performance**

In his comprehensive survey of Wells turbines, Raghunathan presented data showing the hysteresis effects on Wells turbines due to oscillating flows (Raghunathan, 1995). The data shows a lag in the change of lift on the turbine, in relation to the change of flowrate through it. The data was presented in terms of non-dimensional frequency, i.e.

$$f^* = \frac{f}{\bar{f}}$$

where  $f$  is the actual frequency of the motion, and  $\bar{f}$  is the mean frequency of the motion, or spectral peak frequency. Given this definition it is not clear what the value of  $f^* = 0.4 \times 10^{-4}$  associated with Figure 39 indicates, other than a very large difference in frequencies. Raghunathan attributed the hysteresis to asymmetry in the blade boundary layer development on the blades, and oscillating motion of the wake. He suggested that the effects could be smaller on large-scale turbines where the boundary layer on the blades would essentially be turbulent and relatively thinner, and that the effects were also more significant at low Reynolds numbers. Raghunathan also presented a plot of the effect of non-dimensional frequency  $f^*$  on the cyclic efficiency of a small scale Wells turbine. This showed that the normalised cyclic efficiency decreased as  $f^*$  increased as shown in Figure 40. It is again the case that without knowing what the average frequency was it would seem that the test data was gathered at very low frequencies.

It is evident from the figures that the hysteresis effect increased with solidity for Wells turbines, and that the occurrence of such effects should be considered, as Figure 40 indicates quite large reductions in efficiency as non-dimensional frequency increases.

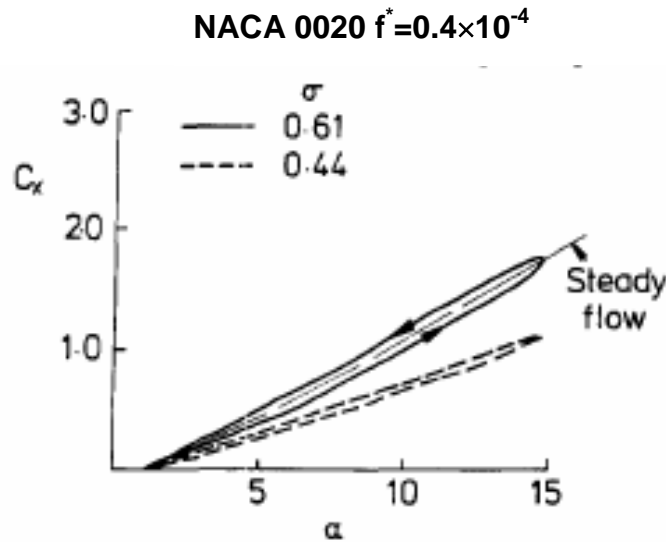


Figure 39 – Hysteresis effect on axial force coefficient (Raghunathan 1995)

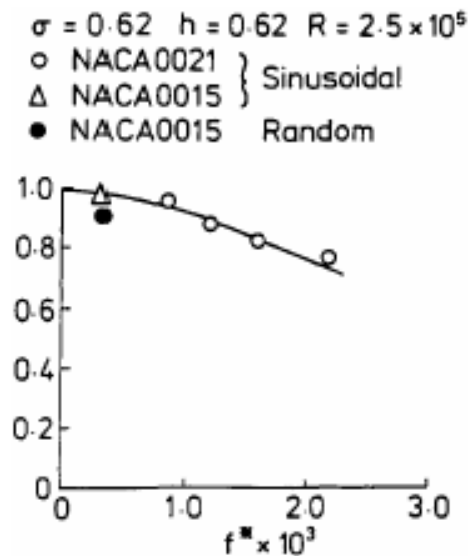


Figure 40 – Effect of frequency on cyclic efficiency (Raghunathan, 1995)

In addition to the above considerations, Dhanasekaran and Govardhan (Dhanasekaran and Govardhan, 2005) say that Raghunathan and Ombaka studied the efficiency of Wells turbines under sinusoidal oscillating flow conditions and found the efficiency decreased by 3-5%, which is not insignificant. When the likely level of uncertainty in testing is also considered – particularly in going from steady state to oscillating flow testing, and the expectation that irregular flows lead to larger differences still – the

conduct of tests with oscillating flow conditions as a part of the development/risk reduction process begins to appear very desirable.

### **Effect of oscillating flow on duct pressure losses**

Within an OWC system the potential impact of oscillating flows on performance is not confined to the turbine blade rows. The oscillating flow conditions can also lead to complex duct flows which arise from:

1. The interaction between the flow in different duct components.
2. The presence of laminar, transitional, and turbulent flows due to the oscillatory nature and high Reynolds numbers of the flow.
3. The random nature of the wave motion, resulting in a wide spectrum of flow frequencies.
4. Flow asymmetry with respect to direction of the flow, i.e. the inhaling flow is different from the exhaling.
5. It is possible that some of the exhaled air is sucked back into the system carrying with it the vorticity acquired earlier which then affects the flow.

However, the velocities and period of oscillation are typically such that compressibility effects can be neglected.

Santhakumar found that there was insufficient information available to determine the performance of interacting duct components in oscillatory flows, and that the need to simulate laminar, transitional and turbulent flows made the uncertainties in CFD too great. He therefore developed an experimental test rig to estimate the pressure loss that occurred in the ducting that carried the oscillatory airflow in an Indian NIOT wave energy plant. In this facility the wave action was simulated by a crank driven piston. The rig was a 1/5<sup>th</sup> scale, half model, which was capable of producing near full scale Re values and dimensionless frequencies  $(\bar{\omega}_{pk} = \omega D / (\bar{v}_{axial})_{peak})$  by increasing the velocity of the flow by a factor of 5 and the frequency of flow oscillation by a factor of 25. Even so, the test conditions produced were limited to those achieved using 4 different piston amplitudes and 7 different rpms, and the wave surface in the caisson was represented as a plane surface.

Santhakumar's work showed an increasingly large dimensionless peak pressure loss as dimensionless frequency and Reynolds number were increased, as shown in Figure 41. At  $Re = 1 \times 10^6$  the dimensionless peak pressure loss was 20% greater at the highest than at the lowest dimensionless frequency. This indicated that if the test Strouhal number was too low then the duct pressure losses would be underestimated, and that the magnitude of the underestimation increased with full scale Reynolds number.

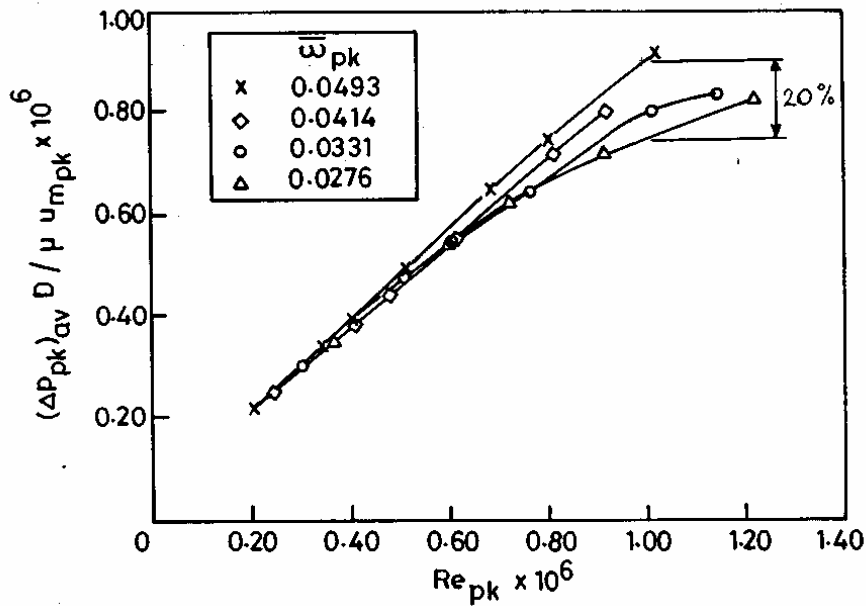


Figure 41 – Effect of frequency and Reynolds number on pressure loss (Santhakumar)

### Sinusoidal pipe flows

With reference to pressure measurement Arts et al (Arts, Boerrigter, Carbonaro, Charbonnier, Degrez, Olivari, Riethmuller, and Van den Braembussche, 1994) say that it is well known that unsteady pipe flows, whether laminar or turbulent, are characterised by time-varying velocity profiles which are different to those observed in steady flows. The presence of different velocity profiles means that the slopes at the walls and hence the coefficients of friction at the wall are different. It also means that in a pipe the velocity profile is Reynolds number dependent. This means that the time-mean velocity profile of a quasi-steady flow will be different from that in steady flow at the mean Reynolds number. The time mean flow in a pipe is affected by imposed oscillations when the oscillation frequency approaches the characteristic frequency of turbulence. Furthermore, neither the time-mean, or ensemble averaged velocity follows the universal log law at the frequencies studied (0.5-3.6 Hz, and oscillation amplitudes of 64 and 15% respectively around the mean). At both frequencies the velocity profiles were distorted, and the ensemble-averaged turbulence intensity and Reynolds shear stress were also affected by unsteadiness. Turbulent shear flows respond very differently to laminar shear flows to imposed unsteadiness.

In 1983 Tu and Ramaprian (Ramaprian and Tu, 1983) noted that there was very little information available on the structure of turbulence in unsteady or periodic turbulent shear flows, and that consequently there was a need for fundamental studies of these. They studied fully developed pipe flows in which the flow rate was forced to vary sinusoidally with time around a mean value. This built upon work conducted by Mizushima, Maruyama and Shoizaki (1973) and Mizushima, Maruyama and Hirasawa

(1975), who had found that imposed periodicity played a significant role if the oscillation frequency was higher than a critical frequency. Ramaprian and Tu observed that the time mean velocity profile was distorted at higher frequencies, and had a point of inflection, and concluded that the use of parameters such as Strouhal and Stokes number borrowed from classical laminar unsteady flow theory to characterise unsteady turbulent flows were inadequate (Ramaprian and Tu, 1980). They also concluded that time-dependent calculations were being made using steady flow turbulence models without a careful study of the implications of the different flow regimes.

Ramaprian and Tu carried out a study over flow regimes of practical interest at  $Re = 5 \times 10^4$ . They measured instantaneous velocities and wall shear stresses at oscillation frequencies of 0.5 and 3.6 Hz (Tu and Ramaprian, 1983). They found that the higher frequency was sufficient to interact with a significant part of the turbulent energy spectrum. From this work they concluded (Part 2) that the effect of the unsteadiness in periodic turbulent flow spread over a distance which could be several orders of magnitude greater than the conventional Stokes layer  $(2\nu/\omega)^{1/2}$ , at the same frequency, and that the analogous parameter characterising the unsteady turbulent flow was  $\omega D/U_*$ , which they termed the 'turbulent Stokes number'. From analysis of their own data, and that of Mizushima et al, they proposed that it was possible to classify the unsteady flow into 5 regimes based upon the value of  $\omega D/\bar{U}_*$  and  $Re$ , where it was assumed that the Stokes parameter  $\langle U_* \rangle$  could be approximated by its average value  $\bar{U}_*$ . When  $\omega D/\bar{U}_* \sim 1$  the imposed unsteadiness begins to influence the turbulent structure, and this effect begins to spread across the entire flow. From their own data and that of other researchers Ramaprian and Tu defined the pipe flow regimes shown in Table 17.

This work is of interest to the current project as there are effectively pipe flows between the OWC and the turbine, and the turbine and atmosphere, and the question is which of the regimes identified by Ramaprian and Tu are they likely to fall? This can be established by calculating the turbulent Stokes parameter, a method for determining which was presented by Ramaprian and Tu.

If it is assumed that the ducting in the rig might have a maximum diameter of 0.8m, and maximum flowrate of 5 m<sup>3</sup>/s, this would give an rms velocity of 7 m<sup>3</sup>/s, and  $Re = 4 \times 10^5$ , which is at the extreme end of the data presented by Ramaprian and Tu. If it is further assumed that the period of the oscillation is 10 seconds, then  $\omega=0.63$ , then only  $\bar{U}_*$  (the time mean friction velocity) is required to determine the turbulent Stokes number,  $\omega D/\bar{U}_*$ . Where  $\bar{U}_*$  is given by:

$$\bar{U}_* = \left( \frac{\bar{\tau}_w}{\rho} \right)^{0.5}$$

In a quasi-steady flow Tu and Ramaprian (Tu and Ramaprian, 1983) showed that the Blasius friction formula  $\lambda = 0.4265 Re^{-0.25}$  was valid in the range  $Re=20000-80000$ ,

and that consequently the wall shear stress at time-mean average velocity  $\bar{U}_m$  was given by:

$$\left| \frac{\tau_w}{\rho} \right| = \frac{1}{8} \lambda \bar{U}_m^2$$

The time-mean wall shear stress  $\bar{\tau}_w$  is then found from:

$$\frac{\bar{\tau}_w}{\tau_w | \text{Re}} = \frac{1}{2\pi T} \int_0^T (1 + \gamma_{Um} \text{Cos}(\omega t))^{\frac{7}{4}} dt$$

where  $\tau_w | \text{Re}$  represents the wall shear stress at time-mean Re. Based on the assumed values, and that the relative amplitude of oscillation  $\gamma_{Um} = 1$ , then integration of the above function, and substitution of the appropriate values leads to  $\omega D / \bar{U}_* = 3.4$ .

Regime	Description
Quasi-steady	$\omega D / \bar{U}_* \leq (\omega D / \bar{U}_*)_{quasi-steady}$ Flow behaves like steady flow. $\omega D / \bar{U}_* \leq 10^{-1}$
Low-frequency	$10^{-1} < \omega D / \bar{U}_* \leq 1$ satisfied at higher Re Departure from quasi-steady behaviour increases with $\omega D / \bar{U}_*$ , but turbulent structure is not affected. Time dependent calculation necessary to predict flow, but time-mean flow not significantly different from quasi-steady.
Intermediate-frequency	$\omega_{bL} D / \bar{U}_* < \omega D / \bar{U}_* < \bar{\omega}_b D / \bar{U}_*$ , $1 \leq \omega D / \bar{U}_* < 10$ Some interaction between turbulence structure and imposed unsteadiness. Effect increases with $\omega D / \bar{U}_*$ and spreads across substantial part of shear layer. Both the periodic and turbulent structure across a substantial part of the flow will deviate from quasi-steady flow. Deviation increases with frequency, quasi-steady turbulence models begin to fail. Time mean flow still nearly the same as quasi-steady flow.
High-frequency regime	$\omega D / \bar{U}_*$ is of order 10 The imposed oscillation interacts strongly with the turbulent bursting process at the wall, and the effect on the turbulent structure is strong. The time-mean velocity is affected and exhibits an inflective profile near the wall. The periodic flow is also affected over ~10% of the diameter, beyond which it oscillates like a solid mass. The turbulent structure exhibits total departure from equilibrium, quasi-steady turbulence modelling breaks down completely within the shear layer
Rapid-oscillation regime	$\omega D / \bar{U}_* > \omega_{bU} D / \bar{U}_*$ , $\bar{\omega}_b D / \bar{U}_*$ is of order 100 The interaction between the imposed oscillations and the turbulence structure is very strong. However, the effect on the periodic flow is confined to a very thin layer (of order 0.01D near the wall).

Table 17 – Classification of unsteady flow regimes

As this is only a preliminary calculation the sensitivity is important, but application of various different assumptions leads to values in the range 1-10, which suggests that the flows could be obtained in the test rig ducts in the 'intermediate range'. This would mean that the flow oscillations would interact with the turbulent structure of the shear layers, and that inaccuracies may develop in CFD simulations as the actual boundary layer profiles could begin to differ significantly from those of a steady flow prediction. It should be noted that Ramaprian and Tu stated that relation of their data to other boundary layer data should be done with caution, as the data obtained from pipe flow experiments was at some variance with boundary-layer data. They emphasised, however, that characterising turbulent pipe flows by the Strouhal number was not very useful in general, as the behaviour of the flow changed with  $Re$ .

#### **2.4.4 Summary**

Experience has shown that there is a significant risk in relying on steady state performance data, taken at relatively low Reynolds numbers, to predict the performance of turbines in OWC facilities under real oscillating flow conditions. Experience has also shown that performance losses are significantly greater under irregular flow conditions than under sinusoidal oscillating flow conditions. Despite advocating the quasi-steady flow assumption, Raghunathan has presented data (from relatively small scale tests) that show hysteresis effects, and a significant impact of operating frequency on efficiency.

The effects of oscillating flow on the performance of an OWC facility are not confined to the turbine itself. The flow in the ducts is likely to be complex and involve laminar, transitional and turbulent boundary layers and effects due to the flow oscillation. The experiments undertaken by Santhakumar in which full scale values of  $Re$  and  $St$  were achieved showed that pressure loss increased both with frequency and Reynolds number. Furthermore, the work on oscillatory pipe flows carried out by Ramaprian and Tu showed that use of the Strouhal number alone was not useful for characterising turbulent pipe flows as the flow behaviour changed with Reynolds number. The implication of this is that in order to have confidence in test data for oscillatory flows, the Strouhal number needs to be matched and the tests conducted at sensibly large Reynolds numbers, and any oscillatory flow test facility should be designed on this basis.

Whilst the development of a turbine solution can be de-coupled from the performance of the ducts to which it is linked, an understanding of the duct flows is highly desirable. This is because the flow entry conditions to the turbine are determined by what goes on in the ducts, and the accuracy of CFD predictions could be significantly compromised by poor assumptions regarding the inlet flow conditions and nature of the boundary layers, velocity profile across the duct, and turbulence level of the flow.

An assessment of the findings in the literature presented above leads to the following conclusions:

- A comparison with pipe flow data based on the likely size and operating frequency of the rig, suggests that the boundary layer profiles developed in the

turbine inlet and outlet ducts will deviate from those predicted by steady flow assumptions. This could lead to increased errors in CFD predictions. It is recommended that when the test facility is operational boundary layer measurements are taken which will enable the true nature of the boundary layer to be determined, and that further work is undertaken to determine how this will relate to a full scale facility.

- Given that the objective of HydroAir is to develop a turbine design that can be taken forward to full scale development, then to reduce development risk the HydroAir test facility should be capable of at least producing an oscillating flow, and should desirably have the capability to produce representative irregular flow conditions.
- The effect of flow oscillation on the flow development in the ducts is expected to be Reynolds number dependent, and so the true oscillatory flow effects will only be captured by ensuring that sufficiently high values of Reynolds number are achieved as well as matching Strouhal number.

### 3. Test Facility Development

#### 3.1 Operating Principle and Sizing

##### 3.1.1 Operating Principle for facility

There was a consensus within the project team that for the test facility to achieve its purpose in reducing risk ahead of developing the HydroAir turbine for use in a real OWC facility, it was necessary that it enabled the turbine to be tested in oscillatory flow conditions. Once this decision had been made, the problem was to identify a basic concept and operating principle for the facility which would enable it to be engineered within the budgetary and timescale constraints of the project. A number of methods of producing an oscillating air flow were considered, which are summarised in Table 18.

Method	Concerns
Bellows	Overall length Method of actuation
Reciprocating flap	Overcoming paddle inertia Controlling stroke
Piston & crank	Physical size Complexity
Hydraulically actuated piston	Physical size Cost and complexity of hydraulics

*Table 18 – Possible operating principles for test facility*

Due to the re-shaping of the project late in the day, after the withdrawal of Wavegen, the funding available for the development of the test facility was not that great: the project was not to develop a test facility, it was to develop a turbine solution. This meant that cost considerations were very much to the fore. The various options were considered on the basis of their potential to deliver a range of oscillating air flow conditions, the likely overall size, complexity, the scale of design and construction task likely to be involved, risk and cost. The most obvious approach was to construct a piston based facility as had been done at Saga University. A number of problems become evident in this approach though as soon as it is determined that a variable stroke length and variable stroke period are required. The obvious way to drive a piston facility is via a crank arm from a rotating drive. The variable period is achieved by running the drive at different speeds, but the variable stroke requires a variable length crank arm. At small scales this might be quite achievable, but engineering and operating a large scale variable crank facility could rapidly become difficult and expensive. Alternative methods of actuation such as hydraulic rams or linear drives were considered too costly. It was also the case that if the swept volume was several cubic metres, then a large space would be required for the piston itself and the movement of the crank arm. With such considerations as these in mind, the reciprocating flap was selected as this offered the potential to achieve a wide range of flows from a relatively compact facility which would be straightforward to engineer at modest cost.

### 3.1.2 General Arrangement

Once the operating principle to produce the oscillating air flow had been determined work began on establishing the general arrangement and sizing of the 'Pneumatic Wave Generator' (PWG). The general arrangement of the concept is shown in Figure 42.

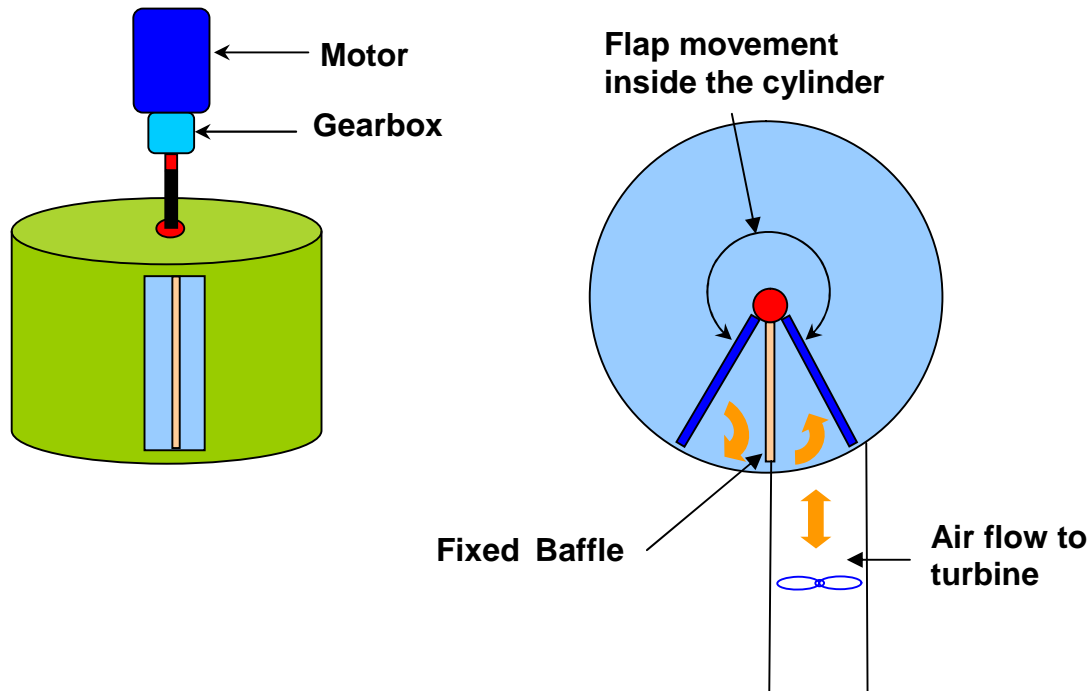


Figure 42 – General arrangement scheme for PWG (Peter Brotherhood Ltd)

A task undertaken by PBL, which progressed in parallel to the sizing and geometric definition of the PWG, was the specification of the electrical system package. At this point in the project ABB were engaged as the industrial partner for the electrical system, and it was determined that the 3-phase electrical motor that powered the flap in the PWG would be supplied and controlled by an ABB regenerative drive. In addition, rather than having a brake or dynamometer, power would be taken off the test turbine by a 3-phase generator, the power from which would be fed back into the mains via an ABB variable frequency inverter with sine filter. At this point it was undecided whether the generator would be a permanent magnet or induction machine.

### 3.1.3 Sizing of flow generator

The OWC Performance matrix and design review (Herring, 2005) had determined that the LIMPET OWC should be taken as a reference facility against which to evaluate the benefits of the HydroAir turbine solution, and that a basic Wells turbine configuration should be identified as a baseline against which the HydroAir solution could be judged. To achieve this meant that it should be possible to relate the dimensions and conditions in the test facility to appropriately scaled dimensions and conditions in LIMPET.

The desired starting point for determining the dimensions of the PWG was to consider the operating pressures and flowrates and cycle periods associated with the Wells turbine in LIMPET, and to determine what swept volume needed to be provided to simulate these when the turbine was scaled down by different factors. The next consideration was that it was required to simulate a range of flow conditions from relatively small to rather large 'waves', which would firstly require a variation in swept volume, and lead to a range of flow velocities through the rig. However, as identified in Section 4, to be used as a generic test facility the rig actually needed to be scaled to enable sensibly high Reynolds numbers to be achieved on impulse turbine configurations. This also meant that the rather different pressure drop/flow ratio characteristics of the 2 turbine types had to be kept in mind.

The basic objectives for sizing the test facility were that it enabled turbines to be tested at Reynolds numbers of at least  $2 \times 10^5$ , and with similarity in Strouhal number, and that minimum axial flow velocity through the turbine at its design point should be 25 m/s. The last objective was based on previous experience with pressure measurements on the Low Speed Research Compressor, which had shown that it is very difficult to accurately measure the dynamic pressures associated with flow velocities below 25 m/s at *steady flow* conditions. It was also desirable that the blade sizes were compatible with the installation of static tapplings, and acquisition of detailed radial traverse pressure probe data if these were considered to be desirable. The final consideration was the range of output powers might be developed by the test turbines, as these would define the size of the generator that would need to be connected to the test turbine, and the speed at which the test turbine would run would influence the choice of generator in terms of the number of poles the machine would have.

The most difficult part of the process was in determining the range of flowrate pressure drop conditions and most importantly a design point that could be associated with the full scale Wells turbine installation in LIMPET. Once this had been done it was a relatively straightforward process to construct a spreadsheet which calculated all the relevant parameter values associated with scaling down the full size device based on various assumptions. The details of the calculations and example spreadsheets are shown in Appendix C.

Insertion of appropriate values into the spreadsheet showed that whilst it was practical to achieve Reynolds numbers of  $2 \times 10^5$  for Wells and impulse turbines within the range of reasonable swept volumes and power input requirements, it was not practical to achieve similarity in terms of Strouhal number across a range of inputs, although it could perhaps be achieved at a limited number of conditions. Consideration of the possible turbine dimensions and pressure drops of interest, and uncertainties with what regard to what it might be desirable to test in the longer term, suggested that it was desirable for the PWG to have a volume of  $25\text{m}^3$ . However, manufacturing and drive motor cost considerations led to the volume being nominally fixed at  $16.5\text{m}^3$ , and the drive motor being fixed at 75kW. In terms of scale, the chosen dimensions were compatible with testing a turbine suitable for LIMPET at approximately quarter scale, whilst in comparison to the volume of the LIMPET OWC the volume of the PWG was at 1:6.25.

Once the basic size and power of the PWG had been decided, it was possible to begin the detailed design and to estimate the range of conditions that it was expected to be able to produce, this being necessary in order to decide the design point specification for the datum turbine. The calculations for the estimated capability of the test rig are summarised in Table 19.

Parameter	Value
Total swept volume	16.43 m <sup>3</sup>
Maximum flowrate	5.88 m <sup>3</sup> /s
Maximum RMS flowrate	4.15 m <sup>3</sup> /s
Maximum frequency	0.14 Hz
Minimum period for full volume oscillation	7 s
Max frequency for small oscillations	1 Hz

*Table 19 – Predicted capabilities of test rig*

## 3.2 Instrumentation Requirements

### 3.2.1 Basic requirements

The early work in the project identified the need for the test facility to be able to produce oscillating flow conditions through the turbine. The implication of this was that the instrumentation system had to be designed to record time-varying (rather than steady-state data) under oscillating, or even irregular flow conditions. The primary objective of the instrumentation was to enable the total-to-static efficiency of the test turbine to be determined from the formula (see Appendix B):

$$\text{Efficiency} \quad \eta = \frac{\omega \cdot T}{Q \cdot \Delta P}$$

where:

$\omega$  = rotational speed

$T$  = torque

$Q$  = volumetric flow rate

$\Delta P$  = the total to static pressure drop across the turbine

The need to have an instrumentation system capable of acquiring time varying, rather than steady-state data had the following impacts on the system requirements:

1. There needed to be adequate disk space for the large data files (1-2Mb, rather than 1-2kB) that would be acquired at each data point.
2. A separate pressure transducer was required for each pressure port, whereas a single transducer and scani-valve arrangement could be used to acquire steady state pressures.

3. The impact of the length and diameter of the tubing used to connect the pressure port to the transducer on the transducer response needed to be considered in order to safeguard the fidelity of the measurements.
4. A sufficient number of analogue-to-digital conversion channels needed to be provided in the data acquisition system.

The instrumentation required to measure the speed and torque was unaffected by whether steady-state or time varying data was taken. However, the requirement to have a separate pressure transducer for each pressure channel to acquire time-varying data, had serious implications with regard to the number of channels that could be used, the budgetary constraints limiting these to about 20. This meant that it was not possible to simultaneously record the pressure variations across each of the blade rows. Whilst static pressure tappings could be provided to take blade row pressure measurements for the purpose of gaining some insight into the loss distribution through the turbine, only the global efficiency measurement would be taken as a matter of course.

In addition to the larger number of pressure transducers required the task of assembling the pressure instrumentation system was made much larger due to the need to make the electrical connections to all the transducers, and the need for each transducer to have its own reference pressure. Furthermore, when the rig was operational there was an increased overhead in ensuring that all the transducers were properly calibrated.

The principal environmental concern directly within the scope of the project was noise. Before any turbine and power take-off system could be further developed some form of noise assessment would be required. It was therefore anticipated that instrumentation was required to enable measurements to be taken that would enable the level of noise associated with a full-scale device to be inferred, to establish the magnitude of the problem - if any.

The instrumentation specification was developed by constructing a schematic of the instrumentation system required.

### 3.2.2 Instrumentation Specification

The instrumentation requirements were evaluated from consideration of the efficiency calculation to be made. A classical approach to the expected error leads to the following equation where the uncertainties for each parameter are in percent:

$$\varepsilon_{rms} = \sqrt{\partial\omega^2 + \partial\tau^2 + \partial Q^2 + \partial\Delta P^2}$$

The uncertainties of the torque and speed measurements are straightforward, as these are taken from a calibrated torquemeter with speed output with the instrument uncertainty. Consideration of the possible range of torque and speed outputs led to the

selection of the IML RTA 500 strain gauge torquemeter. The other measurements are derived from pressure transducer measurements, and evaluation of their contribution to the overall uncertainty is less straightforward.

Consideration of the turbine characteristics indicated that the range of pressures to be measured in the test facility was likely to be  $\pm 10\text{kPa}$ , indicating a requirement for  $\pm 5$  psi transducers. It was initially hoped that it would be possible to make use of pressure transducers already available at Cranfield. In particular it was hoped that it would be possible to use the  $\pm 6895\text{ Pa}$  ( $\pm 1$  psi) Pressure Systems Inc. 9010 differential pressure scanning modules by over-ranging them, as these would have enabled 32 measurements to be acquired simultaneously, at the rate of 20 measurements per channel per second (assuming that the tube lengths could have been kept short enough to maintain good response). Unfortunately, however, the output communications were only configured for their use as steady-state instruments, in addition, there were only a very small number of various other unsteady pressure transducers available – the typical range of transducers used at Cranfield generally being rather higher than required for the HydroAir test facility. The instrumentation budget was insufficient to enable even a minimum number Kulite transducers to be acquired, therefore the decision was made to acquire the very much cheaper Honeywell devices, although there was no previous experience of using these. The risk was mitigated by first acquiring two which were bench tested to ensure that they were fundamentally linear in behaviour: which proved to be the case.

In order to determine the mass flow rate the density of the air needs to be known, for which the static temperature of the air is required. Fast-response ‘K’ type thermocouples mounted in recesses in the duct wall were selected for this. Although these only have an accuracy of  $\pm 1\text{ }^\circ\text{C}$ , this is quite sufficient in comparison to the impact of uncertainties in pressure measurements.

Consideration of the number of pressure transducers that could be afforded, together with the thermocouple channels, torque and speed measurements, led to the conclusion that a 32 channel A-to-D card was required.

The quoted uncertainties for the instrumentation identified for use on the test rig are shown in Table 20, and it can be seen that the expected random errors in the speed and torque measurements are small fractions of a percent.

Parameter	Accuracy	Comments
Rotational speed	$\pm 1$ rev	Probably better than this, = 0.13% at 750 RPM
Torque	$\pm 0.05\%$ FS	$\pm 0.25\text{Nm}$ for RTA 500, error @ 20 Nm = $\pm 1.25\%$
Pressure	$\pm 0.05\%$ FSO	error with 5PSI Honeywell transducers = $\pm 17.25\text{ Pa}$
Temperature	$\pm 1\text{ }^\circ\text{C}$	Standard K type thermocouple

*Table 20 – Quoted instrumentation uncertainties*

The significance of the error in pressure increases as the pressure drop diminishes. It is thus hard to ascribe a meaningful error to the pressure measurement. If it is assumed that the devices are linear, and are calibrated at the start of testing, then the error should be small even at very low pressures – as long as the transducers are not

affected by noise. The pressure drop in the efficiency calculation is evaluated from the difference between the averages of total and static pressures across the turbine. If as a worst case it is assumed that these are single measurements, then the random error will be:

$$\varepsilon = \sqrt{0.05^2 + 0.05^2} = 0.07\%$$

On the full scale range this equates to an error of 24.3 Pa.

Of the parameters in the efficiency equation, the most difficult one to determine accurately is the volumetric flow rate,  $Q$ , this is made even more difficult when the flow is not steady. The method initially proposed to ensure that the mass flow rate through the rig could be accurately calculated was to incorporate a venturi meter into the rig, which could be used to calibrate 2 instrumentation rings where total and static pressure measurements were made; the venturi meter then being replaced later by the turbine test section. However, as the design of the rig evolved it became evident that this was impractical, and it was determined that the flow through the instrumentation rings would have to be calibrated by conducting radial traverses to enable discharge coefficients to be evaluated. The accuracy of the mass flow rate calculation thus depends upon the uncertainty of the discharge coefficients (which become a bias error), as well as the accuracy of the total and static pressure measurements subsequently made. The random uncertainty should be reduced by using a number of total and static pressure measurements at all stages.

From the above it can be seen that the *random* errors in both  $Q$  and  $\Delta P$  are both associated with errors between pressures derived by averaging a number of values. If the random error in these pressure differences is assumed to be 2% - which could well be pessimistic, then the overall random error in the efficiency calculation would be:

$$\varepsilon = \sqrt{0.13^2 + 1.25^2 + 2^2 + 2^2} = 3\%$$

What has to be considered in addition to this is that firstly bias errors could be present, but (assuming they are constant) these can be neglected in build-to-build comparisons, and secondly the pressure measurements in particular may be affected by temperature drift which introduces a potentially significant source of additional error. Thus using the approach adopted the anticipated uncertainty in the evaluation of efficiency is  $\pm 2-3\%$ . To achieve better than this requires an alternative approach which enables the mass/volumetric flowrate to be determined more accurately.

### 3.2.3 Software

It was decided that the HydroAir data acquisition system would be developed in Visual Basic. This was desirable because:

1. There was significant experience at Cranfield in using Visual Basic.
2. It would save a significant amount of time and reduce risk in code development as a significant amount of previously developed instrumentation

and data acquisition code could be re-used. This included code previously developed to drive the Rotadata actuators in particular.

3. It was desirable to be able to control both the instrumentation and the PWG from a single interface, and so have the PWG ‘wave’ parameters available for writing to the data files.
4. Information could be extracted from the ABB drive activating the PWG and written to the data files.

It can be seen that there were a number of significant advantages from having such an integrated system. Once the data had been acquired it was envisaged that the data files created would be post-processed by a Matlab code. This code would be developed from scratch, as the nature of the data from the HydroAir test facility would be quite different from that from other facilities, although it would be possible to utilise a number of general plotting routines.

### **3.3 Component Definition**

#### **3.3.1 Pressure Probes/Ports**

Ideally, when time-varying pressure measurements are made the pressure transducer is mounted such that its entry port is at the measurement point. Unfortunately, the size of the transducer often means that this isn’t possible, and nor is it generally convenient for gaining access to the transducers. Section 3.2.1 identified that the length and diameter of the tube which links a pressure transducer with its port impacts the response of the transducer, and that this has to be considered when time-varying pressure measurements are being made.

The major concern with regard to the HydroAir rig was that the instrumentation plane total pressure was to be measured by using a traversable pitot probe. It was intended that the transducer would be mounted immediately on the external end of the probe, but it would be 0.7m from the tube entry. This meant that it had to be ensured that the bore of the probe was sufficiently large to give an adequate response in relation to the pressure changes which were taking place in the flow.

The solution taken to the problem was to develop a Matlab code which simulated the response of a simple combined line-cavity system to a step input using the model described by Arts et al (Arts et al, 1994), and detailed in Appendix D. The response of the system with various tube diameters to various step inputs was evaluated, and it was seen that if a 2.3 diameter tube was used the response of the system was good even to a step input of 5kPa, as shown in Figure 43. It can be seen that the response is around 0.1 s. This was judged to be more than adequate, given that the cycle periods that would be used in the facility were unlikely to be less than 5 seconds.

It was recognised that accuracy of the model used might be compromised by the relatively small volume of the cavity in relation to the line length, but there was

insufficient time to investigate this in detail, and the results from the model demonstrated a response so far in excess of that required to track the anticipated pressure changes that it was considered to be sufficient. Nevertheless, it is recommended that a more sophisticated line-cavity model based on frequency response approach of Bergh and Tijdeman and described by Arts et al (1994) is developed to enable the response characteristics of the total pressure probes to be analysed in greater detail.

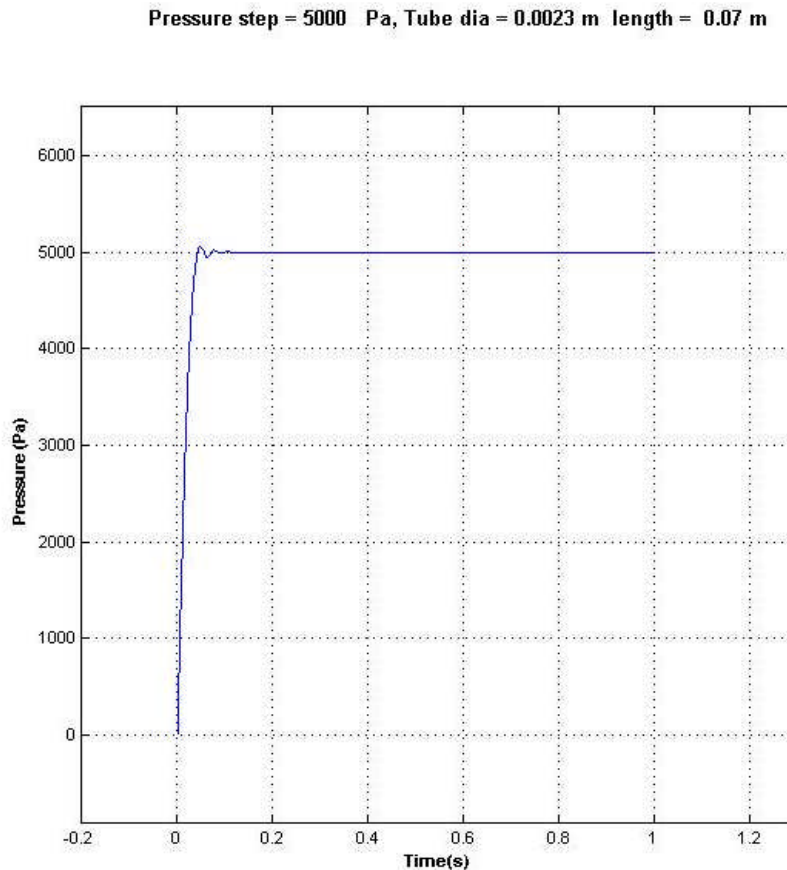


*Figure 43 – Predicted response of transducer on total pressure probe to 5kPa step input*

### 3.3.2 Ducting General Considerations

The importance of the design of the ducting and the inlet/outlet in OWCs has been revealed by practical experience with the LIMPET OWC. Curran et al (Curran, Raghunathan and Whittaker, ) identified that the aerodynamic design of the entry section of the LIMPET OWC was poor, which augmented detrimental dynamic effects, to produce boundary layer separation. This resulted in a pressure loss which meant that the turbine performance appeared greater during outflow due to the lower

amount of pneumatic energy lost. They also believed that support struts were producing some adverse effects. They concluded that:

1. Inefficient ducting could cause considerable pressure loss
2. Poor turbine inlet conditions could cause irregular flow profile and reduce turbine performance

The flow distortion induced by the separations was relieved by extending the ducting and modifying the turbine bullet design from a rather blunt design to a parabolic profile, which increased both efficiency and flow range.

Whilst the duct geometries used in the test rig would probably differ from those used in a full scale configuration, it was still desirable to try to ensure that these induced minimal losses. This was firstly to reduce the rig power requirements and increase operating range, and secondly to obtain as high a quality of flow as possible. Once the general configuration of the rig had been determined, and the diameter of the basic ducting decided upon, it was necessary to define the geometry of the transition section into the PWG, the bullets that would terminate the ends of the turbine hub, and the inlet/outlet of the rig. In addition to these, a further diffuser/contraction section had to be defined to change the outer diameter of the duct, when the decision was made later to reduce the diameter of the turbine test section. The designs of these items are described in the following sections.

### 3.3.3 Inlet/Outlet

In a conventional unidirectional turbine test facility there is a need to have an inlet and an outlet, provided by a bellmouth and diffuser for example. For the HydroAir facility though, the outlet from the turbine also has to function as an inlet. However, a geometry that provides a good inlet does not necessarily provide a good outlet. In order to maximize performance and minimise the power requirements of the rig an inlet/outlet design is required that ideally provides a uniform inflow to the turbine with low loss when operating as an intake, and good diffusion characteristics when operating as an outlet. It is impractical to diffuse the flow smoothly to ambient conditions, and so the latter requirement means expanding the flow to a sufficiently large area ratio prior to exit that the final expansion losses incurred when the flow leaves the duct are relatively small. In order to determine the optimum design there is a need to appreciate the relative magnitudes of the inlet and outlet losses associated with an inlet/outlet geometry.

If the loss in total pressure in an inlet duct is assumed to essentially be caused by friction on the walls of the duct, then the losses can be estimated using Seddon's approximate theory of friction loss (Seddon and Goldsmith, 1985). The duct loss between stations 1 and 2 is then given by:

$$\frac{\Delta P}{q_1} = \int_1^2 \left( \frac{A_1}{A} \right)^2 C_f \frac{s}{A} dl$$

where the flow enters the duct at position 1,  $A$  is the area at position  $l$ ,  $s$  is the duct perimeter length of element  $dl$ , and  $C_f$  is the coefficient of friction. If it is assumed that the inlet has a parabolic profile and has radius  $R_1$  at the inlet and  $R_2$  at the end of the length considered, and that following Seddon's procedure  $C_f$  can be replaced by  $C_F$  the effective overall friction coefficient then the equation can be re-written as:

$$K_d = \frac{\Delta P}{q_1} = C_F 2 R_1^4 \int_1^2 \left( R_1 - l^2 \frac{(R_2 - R_1)}{L} \right)^{-5} dl$$

If  $R_1 = 0.49$  and  $L = 0.6$ , and the area ratio of the duct is assumed to be 1.5, then the effective cone angle is 8.5 degrees. Assuming standard atmospheric conditions, and an inlet velocity of  $V_1 = 5$  m/s, the effective Reynolds number is:

$$R_{eff} = \frac{4A_1}{s_1} \cdot \frac{V_1}{\nu} = 3.4 \times 10^5$$

This would correspond to a laminar boundary layer on a flat plate, assuming a sine profile (Houghton and Carruthers, 1982),

$$C_F = \frac{1.312}{Re^{0.5}} = 0.00225$$

From Squire's work, for a cone of half angle 8.5 degrees  $C_{Fd} = 3C_f = 0.007$   
Evaluation of the integral then leads to a duct loss coefficient of  $K_d = 0.03$ .

The optimum rate of diffusion for a diffuser with free discharge and developed inlet flow depends upon the non-dimensional length and expansion ratio (Miller, 1990). A standard diffuser has a straight profile, however, if there is distortion in the inlet profile – as may occur downstream of the test turbine - then a trumpet shaped one may perform better, and this form is also closer to that of an inlet. Miller noted that the performance of a diffuser with an outlet pipe was less sensitive to inlet flow conditions than one with free discharge. Examination of Miller's data showed that the loss coefficient of the inlet/outlet operating as a diffuser was an order of magnitude greater than the value derived for an inlet above due to the final sudden expansion loss. Hence, the design problem was reduced to defining a suitable diffuser, which could be modified to improve its inlet performance by the addition of a flare/bellmouth.

The effect length and area on diffuser loss coefficients for standard diffusers with free discharge have been presented by Miller (Miller, 1990) fig 11.3 for developed inlet flows of  $Re = 10^6$  based on duct diameter ( $D$ ). The rms  $Re$  of the flows in the rig are likely to be of the order of  $Re = 0.5 \times 10^6$  though. Miller said the effects of  $Re$  on diffuser loss coefficients were complex, being a function of diffuser geometry and conditions upstream of the diffuser. However, loss coefficients generally increased as  $Re$  decreased below  $10^6$ , and showed greatest variation for optimum diffuser geometries. Miller provides a correction for optimum diffuser geometries:

$$K_d = K_d^* + \left( K_d^* - \frac{1}{AR^2} \right) \cdot C_{Re}$$

Where  $K_d^*$  is the loss coefficient of the optimum diffuser geometry, AR is the area ratio, and  $C_{Re}$  is the Reynolds number correction for Re based upon the hydraulic diameter. Application of Miller's correction to a range of optimum duct geometries for the anticipated rig Reynolds numbers led to the duct loss coefficients shown in Table 21.

Length (L/R <sub>1</sub> )	Optimum AR	Re=10 <sup>6</sup> K <sub>d</sub>	Corrected K <sub>d</sub>
1	1.4	0.67	-
1.5	1.5	0.6	0.69
2.5	1.6	0.51	0.58
4.7	2.0	0.4	0.49

Table 21 – Corrected loss coefficients for optimum diffuser geometries

Miller stated that when inlet flows were highly distorted it was better to have a short spacer (0.5-2.0 D) followed by an optimum angle diffuser, rather than a long diffuser with a small divergence. This was because the distorted flow decayed rapidly to produce conditions conducive to good diffuser performance. Fortunately, this was compatible with the space constraints, and the fact that poor outlet flows could result from stalled flow in the turbine.

The design objective for the inlet/outlet was to achieve the maximum possible expansion within the practical limits of overall rig length and inlet/outlet diameter. Based upon the chosen duct diameter of 0.8m it was determined that the inlet/outlet diffuser should have an overall length of 2.0m, non-dimensional length of 5, and area ratio of 1.9635, and cone half angle of 4.57 deg. The desired scheme was for the inlet/outlet diffuser to have a parabolic profile as this would assist its operation as an inlet. However, this was dropped in favour of a straightforward conical design, due to manufacturing cost considerations. The chosen dimensions should yield a close to optimal design for the inlet/outlet when operating as a diffuser with free discharge with a loss coefficient of  $K_d = 0.39$ . To improve the inlet performance a Flakt Woods flare was added which had inner and outer diameters of 1.121m, and 1.3382 m respectively.

### 3.3.4 Duct Bullet

It is evident that the turbine hub must be terminated by a bullet of form, and that there will be a region of separated flow associated with the tip of whichever bullet is downstream of the turbine where the flow is diffusing. It is also evident that the losses generated by a rather blunt bullet, which may have a fairly extensive region of separated flow, may be considerable – as found in the original LIMPET configuration.

In order to minimise the region of separated flow and avoid discontinuities in curvature where the bullet mates with the main hub, it was decided to use a tangent ogive shape defined by (ESDU, 1977):

$$\frac{r}{R} = \left\{ F^2 + (2F + 1) \left[ 1 - \left[ 1 - \frac{x}{l} \right]^2 \right] \right\}^{\frac{1}{2}} - F$$

where  $F = \frac{1}{2} \left[ 4 \left( \frac{l}{D} \right)^2 - 1 \right]$ ,  $l$ =length of body component,  $r$  = local radius,

$R$ =maximum radius,  $D$ = maximum diameter

The design requirement was for the fineness ratio of the bullet to be sufficient for it to form an efficient diffuser within the duct. The dimensions selected were again based on the data presented by Miller, but in this case for diffuser with outlet pipe.

The bullet was initially defined to expand the flow from an annulus with radii of 0.4m and 0.21 m, to give an expansion ratio of 1.38. However, the decision was then made to reduce the turbine diameter and increase the hub/tip ratio to 0.82. As the manufacture of the tooling for the bullets was already underway when this decision was made, the most cost-effective way to accommodate the design modification was to introduce a minor modification to the bullet design keeping its overall length the same, and to introduce diffuser/contraction sections into the duct casing (section 3.3.5). The resulting bullets had a base radius of 0.246m, a length of 1.0712m, giving an expansion ratio of 1.6083, and a resulting non-dimensional diffuser length of 6.9. From fig 11.6 of (Miller, 1990) this should result in a loss coefficient below 0.06 when the duct is operating as a diffuser. The final dimensions of the bullet are shown in Table 22.

Item	Value
Profile	tangent ogive
Length	1.0712 m
Max radius	0.246 m
Volume	0.1089 m <sup>3</sup>

*Table 22 – Bullet dimensions*

### 3.3.5 Duct Conical Diffuser/Contraction

When the decision was taken to reduce the diameter of the turbine, it became necessary to have sections to reduce the duct diameter from 0.8 to 0.6m. The required area ratio between the 2 annuli was 3.37. This difference meant that a very low loss diffuser section would be prohibitively long. The approach taken therefore was to utilise the maximum diffuser angle commensurate with preventing separation, which

is 15 degrees (Miller, 1990). This suggested that the non-dimensional length should be at least 6.85. The length of the conical diffuser was thus defined as 0.4m, which gave a non-dimensional length of 7.4, and a diffuser angle of 14 degrees. This would be expected to have a loss coefficient  $K_d = 0.2$ . The specification of the diffuser/contraction sections is given in Table 23.

Item	Value
Angle	14 degrees
Length	0.4 m
Max casing radius	0.4 m
Min casing radius	0.3 m
Hub radius	0.246 m
Area ratio	3.37
Volume of annulus	0.0789 m <sup>3</sup>

*Table 23 – Definition of conical diffuser*

### 3.3.6 Porous Calibration Plate

In order to establish the basic characteristics of the test facility: whether the maximum flow condition could be achieved, and to assist in developing the instrumentation system; it was decided that it would be convenient to initially install a porous plate to create the pressure drop rather than an actual turbine.

The maximum achievable flowrate from the PWG was expected to be 5.9 m<sup>3</sup>/s. At this level of flow rate the pressure drop associated with an impulse turbine as determined from the scaling spreadsheet, based on a full scale volumetric flowrate of 92 m<sup>3</sup>/s would be expected to be around 6750 Pa at model scale. However, if it was assumed that the maximum power in the fluid flow was likely to be 30kW, then the maximum expected pressure drop at model scale was expected to be ~5000 Pa, and the corresponding RMS pressure drop 3535 Pa. This suggested that a reasonable design RMS pressure drop for the porous plate would be 3000 Pa.

Given that the diameter of the duct was 0.8m, then assuming incompressible flow the axial flow velocity and loss coefficient of the porous plate required to give the required pressure drop were:

$$V_a = \frac{5.9}{\pi \times 0.4^2} = 11.7 \text{ m/s}$$

$$K_0 = \frac{3000}{0.5 \times 1.23 \times 11.7^2} = 35$$

The porosity ( $\alpha$ ) required in a sharp edged ( $t < 0.1d$ ), thin porous plate to provide this loss coefficient is 0.23 (Miller, 1990).

The diameter of the holes required in the porous plate was determined by the requirement for the flow to expand to fill the duct and static pressure recovery to be complete when it reaches the measuring section. The recovery distance given by:

$$\text{Recovery distance} = \frac{6D}{\sqrt{\alpha}}$$

where D is the diameter of the holes. Hence, for the flow to achieve recovery within 1.0 m the maximum diameter of the holes should be 6.9 cm. In order to ensure recovery and developed flow to be established by the measuring sections it was decided to use holes of 10mm diameter, and to have 50mm wide straps across the plate to ensure sufficient rigidity in use.

The above loss coefficient applied for Reynolds numbers  $>10^3$  (based on hole diameter). The mean orifice velocity at the design flow would be 50m/s, and the Re of the flow based on using 1mm plate, with 10mm diameter holes would be:

$$\text{Re} = \frac{1.2256 \times 50.0 \times 0.01}{1.714 \times 10^{-5}} = 3.6 \times 10^4$$

The characteristics of the porous calibration plate are summarised in

Parameter	Value
Porosity ( $\alpha$ )	23%
Hole diameters	10mm
Loss coefficient	35
Total open area	0.116m <sup>2</sup>
Design pressure drop	5kPa for axial flow of 15.3m <sup>3</sup> /s

*Table 24 – Design Specification for porous plate*

### 3.4 Description of Test Facility

#### 3.4.1 General Overview

This section of the thesis presents an overview of the HydroAir test facility at the time of writing. The facility was designed to provide an oscillating air flow source for volumetric flowrates of up to  $5.9 \text{ m}^3/\text{s}$ , within the limitations of maximum instantaneous work on the air remaining within 35kW, and gauge pressure within the PWG remaining with  $\pm 15\text{kPa}$ .

The HydroAir test facility can be divided into 2 parts. Firstly the pressure vessel containing the rotating flap and the transition section which is attached to its outlet, and secondly the variable ductwork containing the turbine test section, and diffuser arrangement which is attached to the transition section outlet. For the purposes of clarity within the thesis the term Pneumatic Wave Generator (PWG) will be taken to refer to the pressure vessel and transition section element together, as these are invariant for all testing. The various assemblies of ducting etc then attached to the PWG outlet will be referred to as the test duct.

The HydroAir test facility was installed in Test House 2 and the 2-3 Link in the Cranfield University turbomachinery test area. The PWG was located in test house 2, whilst the horizontal test duct extended from the PWG vessel through the wall and into the 2-3 link. This layout is shown in Figure 44.

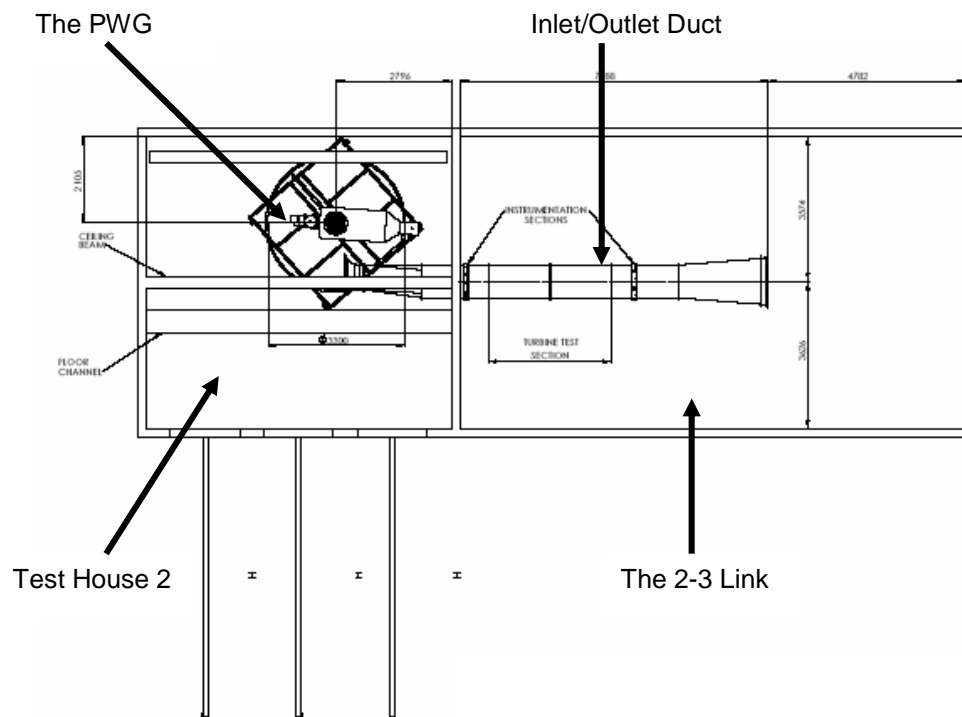


Figure 44 – Location of HydroAir test facility in Test House 2 and 2-3 Link

### 3.4.2 The PWG

The basic structure of the PWG consists of a 2.4m tall fibreglass cylinder with a segment removed, which is capped at top and bottom by 1 inch thick plywood. The fibreglass cylinder is formed by 7 identical wall sections which are bolted and sealed together to enclose 292 degrees of the perimeter of a 3.3m diameter circle, as shown in Figure 45.



*Figure 45 – Basic Structure of PWG with outlet duct removed*

The principle behind the PWG is that a paddle attached to a central shaft within the fibreglass rotates back and forth between a start position and an outlet (whose area is rather smaller than the area of the flap) to create an oscillating flow in the test duct. The flap in the PWG thus effectively operates as a piston with a rotational rather than longitudinal action. This arrangement is realised in the PWG by having a 168.3 mm diameter central shaft which holds the paddle which has a breadth of 1.566 m and height of 2.4 m, giving a flap area of 3.7578 m<sup>2</sup>.

The exit flow from the PWG is transferred into the inlet/outlet transition duct through a rectangular outlet which incorporates a 0.45m long McKenzie flare. The outlet was placed at the periphery of the cylinder, as there would be little air flow close to the central shaft. In addition, the outlet was made tall rather than wide to reduce the velocity gradient across the outflow. A 2.0m long transition section (Figure 46) is attached to the McKenzie flare which contracts the flow area by a factor of 1.6, and transforms the rectangular section into a circular one. The transition section is offset towards the periphery of the cylinder relative to the rectangular outlet (which makes it asymmetric), in order to remove some of the effect of the velocity gradient at the inlet.

At the open – or ‘Home’ - end of the paddle’s travel the PWG is left open (except for a safety grill) to allow the free movement of air in and out of the vessel behind the flap, and so reduce the power requirements.

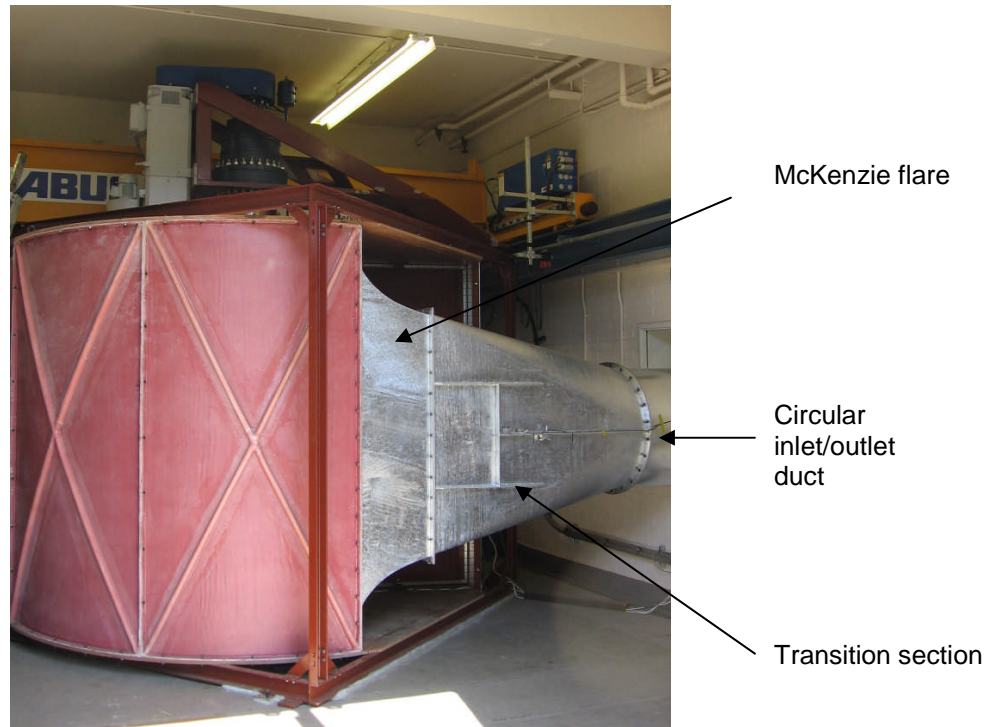


*Figure 46 – Pressure vessel and transition section*

### **3.4.3 Drive System**

The paddle is driven by a 75kW ABB SDM6B3 16.4 75kW AC motor with air inlet. The output from the motor is transferred by 2:1 belt drive reduction to a 36:1 Brevini SL6002FS/44.16/S65CR1 gearbox, to give an overall 72:1 reduction ratio between revolutions of the motor and those of the flap. The motor and gearbox are mounted on a torque arm on top of the PWG as shown in Figure 47.

The operation of the motor is controlled by an ABB ACS800-11 (ACS800-0100-3+E200+K454+L502+L503) regenerative, wall mounted, Variable Speed Drive (VSD), which includes an EMC/RFI filter and Fieldbus communication module (Figure 48). An RTAC -01 Pulse Encoder Interface module was also fitted for digital signal control, but this is redundant in the PWG as Fieldbus communication is used by the Programmable Logic Controller (PLC) which controls operation of the VSD to make the flap oscillate and produce ‘waves’. The drive can also be setup and controlled via an optical fibre communication input and the ABB DriveWindow software. The VSD is wall mounted in Test House 2 adjacent to the PWG.

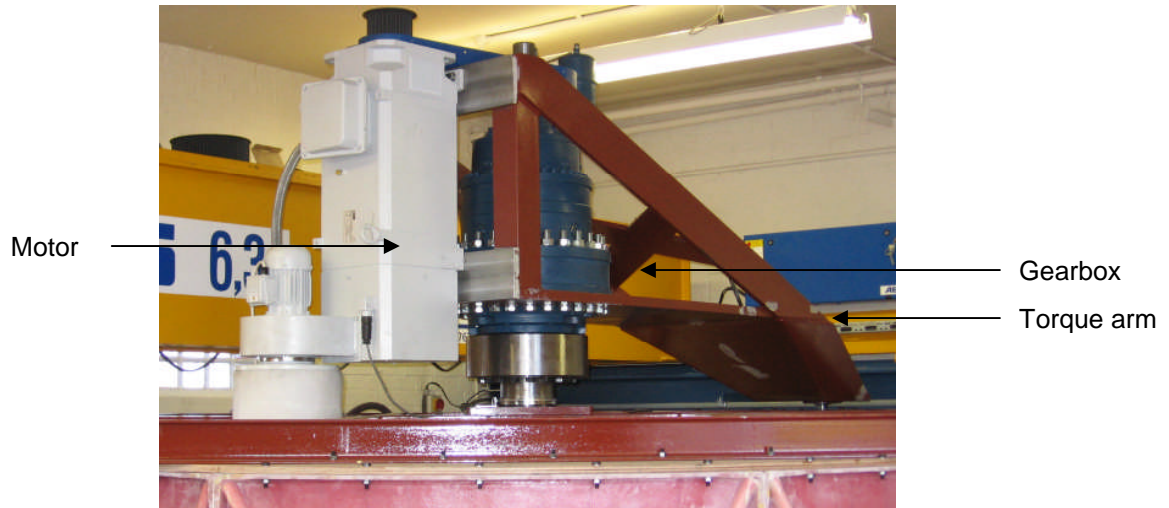


*Figure 47 – Mounting of drive motor and gearbox*



*Figure 48- ABB VSD for driving the ABB SDM6B3 motor*

The ACS800-11 is a 4-quadrant drive for AC motors. It contains a line-side converter, 2 IGBT converters, and a motor-side converter. The line-side converter is connected to the supply network, and either transfers energy from the network to the DC link, or from the DC link to the network.

The IGBT supply module rectifies the input 230V 3-phase AC current to DC, for the intermediate DC link of the drive, which then supplies the motor-side converter and runs the motor. The line filter suppresses the AC voltage and current harmonics. The module is a 4 quadrant, switch mode converter. This means that the power that flows through the converter is reversible. Control of the IGBT power semi-conductors is based on the Direct Torque Control (DTC) method, which is also used in the motor control part of the drive. The IGBT supply unit is said not to generate characteristic current or voltage overtones like traditional 6 or 12 pulse bridges.

The motor-side converter is connected to, and controls the motor/generator. The 4 quadrant operation of the ACS800 means that the connected machine can be operated either as a motor (in quadrants 1 and 3), or a generator/re-generative braking (in quadrants 2 and 4). In practice this means that power is taken from the mains to accelerate the flap, but then put back when re-generative braking is used to decelerate the flap.

It should be noted that the phases of the supply to the drive motor and the encoder in the ACS800 are reversed relative to normal conventions. This was done so that the motor would drive the flap ‘forward’ towards the transition section from the ‘Home’ position.

The motor used to drive the PWG is an ABB SDM 6B3 asynchronous squirrel cage motor designed specifically for operation with a frequency converter. The motor has a rated power of 75 kW, rated torque of 477 Nm, and base speed of 1500 RPM. The motor is cooled by a fixed speed fan which is attached to the non-drive end.

#### **3.4.4 Test Duct**

The basic test duct was formed by bolting together sections of standard 0.8m diameter Lindab ducting. At the PWG end the duct is connected to the transition section, whilst at the outlet end it is connected to a 2 part diffuser as shown in Figure 49. The first part is formed by a 2.0m long 4.57 degree half angle diffuser, which is then connected to a galvanised Flakt Woods bellmouth (Drawing D257837) which takes the diameter from 1.121 to 1.338 m.

The sectional nature of the inlet/outlet duct means that the duct can easily be reconfigured to install the turbine test module, or to insert porous or blanking plates when undertaking calibration work.



*Figure 49 – Basic test duct and outlet*

### 3.4.5 Turbine Test Module

The installation of the turbine test module in the inlet outlet duct is illustrated in Figure 50. This shows how the module is designed so that the outlet and one part of the turbine module are mounted on a trolley so that after removing a ring of bolts the turbine may be separated for immediate access to the blade rows.

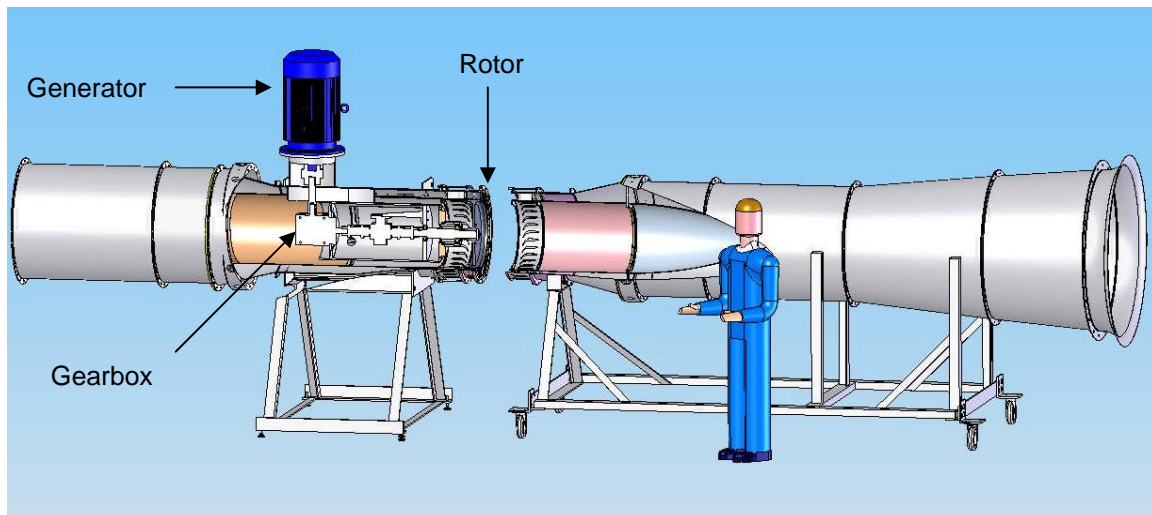


*Figure 50 – Installation of turbine test module in test duct*

The shaft power output from the turbine is transferred to the generator via a torquemeter, and right-angle gearbox as shown in Figure 50. The mounting of the

generator outside the duct, rather than within the hub, was done to remove cooling problems, enables it to be accessed easily, and to permit a wider range of hub/tip diameter turbines to be accommodated within the rig.

### 3.4.6 Power Off-take System

The output from the test turbine is fed into an ABB M3AA 225 SMA-4 marine induction motor/generator. This is a 4-pole machine with extruded aluminium alloy stator. At 1500 rpm it has an output of 37kW and operates at 93.5% efficiency with a power factor of 0.84. It is not self excited, and the magnetisation current is provided by the MV3000.

The output from the generator is fed to a Converteam HydroAir MV3000 MicroCubicle (PMVJ3071-3001, Serial no. 2392699) whose output is connected to a Metal Deploy Resistor CD03 5519, 37kW load bank. These units are shown in Figure 51.



*Figure 51 – Converteam MV3000 and 37kW loadbank*

The MV3000 cubicle contained two ALSPA MV3000e units: a ‘Mains Bridge’ and a ‘Machine Bridge’ which were connected by a DC link to produce a Sinusoidal Front End (SFE) arrangement. In general the Mains Bridge is intended for grid connection, but in the test facility was connected to the 35kW loadbank. The Mains Bridge enables the current flow to the load bank to be varied to maintain a constant DC link voltage, which permits 4-quadrant operation of the machine bridge. Whilst the

MV3000e units can be used in a number of modes of operation, only the ‘Direct On’ mode was used in the testing described in this thesis (see section 7).

The operation of the MV3000 is controlled via two Drive Data Manager keypads and a touch-screen Human Machine Interface (HMI) on the front of the cubicle, as shown in Figure 52.

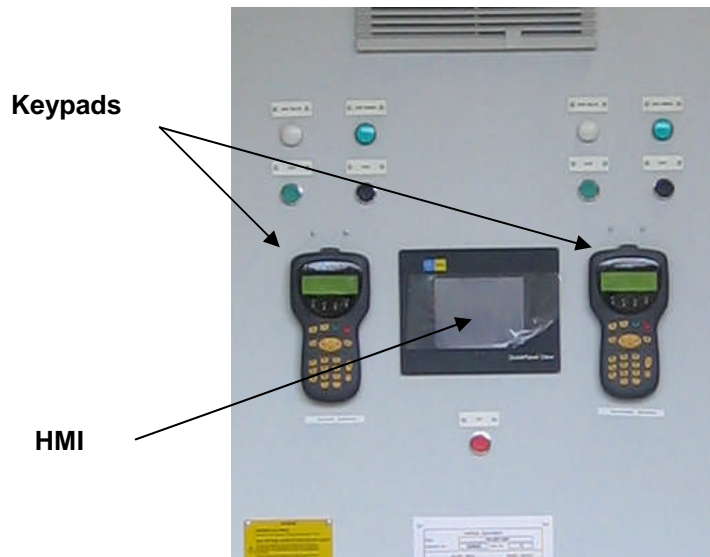


*Figure 52 – Keypads and HMI on Convertteam MV3000*

### **3.4.7 Description of PWG Control System**

#### **Overview**

There are 2 software applications provided by ABB which are associated with the control of the PWG, these are DriveWindow and CoDeSys. The flap in the PWG can be moved either using the ABB DriveWindow software which communicates with the ACS800 via a fibre optic link, or by using the ABB CoDeSys program to upload parameter information to the Programmable Logic Controller (PLC) which then communicates with the ACS800 via Profibus. This is illustrated in Figure 53. The essential differences between the 2 software packages are described below.

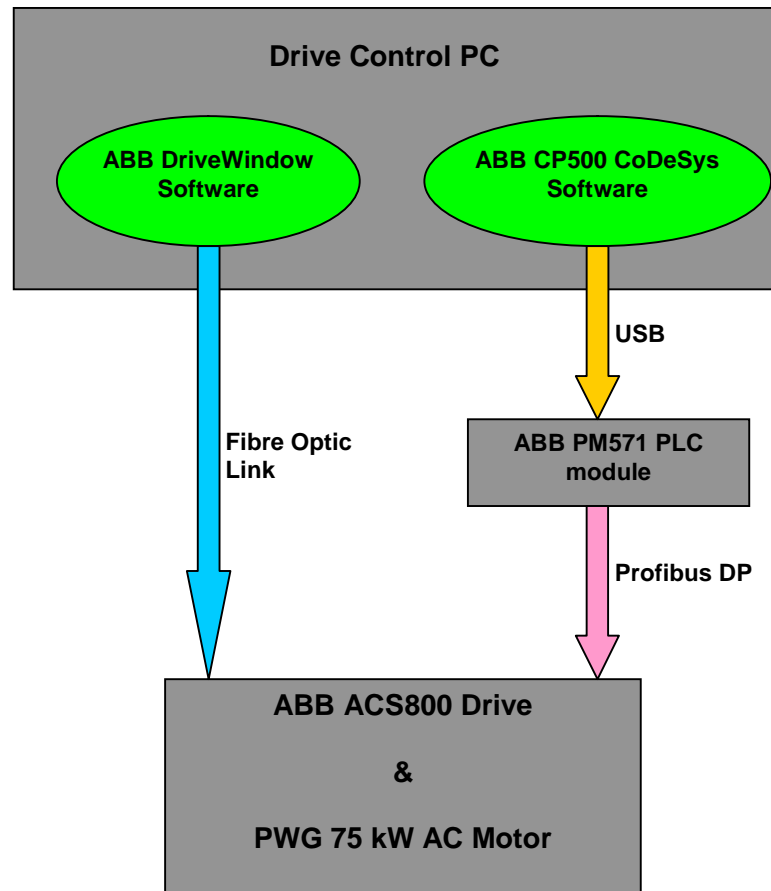


*Figure 53 – Schematic of control and communication elements*

### **Basic Control**

DriveWindow is the fundamental software tool that is used for setting the configuration of the ACS800 VSD. The parameter settings that are set within DriveWindow are uploaded to the firmware within the ACS800, and so are retained even after DriveWindow has been shut down. DriveWindow also enables the motor accelerations and speeds to be set so that the flap may be manually driven to a desired position, and enables drive parameters to be monitored, and faults investigated. What the operator cannot do though is set positions for movement and make the flap move in a repeating ‘wave’ cycle.

### **PLC Control**

The movement of the flap through repeating wave cycles in the PWG is made possible by an ABB AC500 Programmable Logic Control (PLC) system. The PLC system is designed for standard IEC 61131-3 programming, and movement of the flap in the PWG is governed by the PLC sending digital inputs to the ACS800 VSD via a

Fieldbus system. In this case the open high speed Fieldbus used is the Process Fieldbus Decentralised Periphery (DP) protocol, known as Profibus.

The PLC system consists of an ABB PM571 PLC module, coupled with a CM 572-DP Profibus DP communication module, TA 524 terminal base unit and CP-24/2.0 adj. This forms the communications system master, and communicates with the RPBA-01 Profibus DPO adapter module in the ACS800 VSD, which is then a slave, via a twisted pair cable. This is shown in Figure 54.

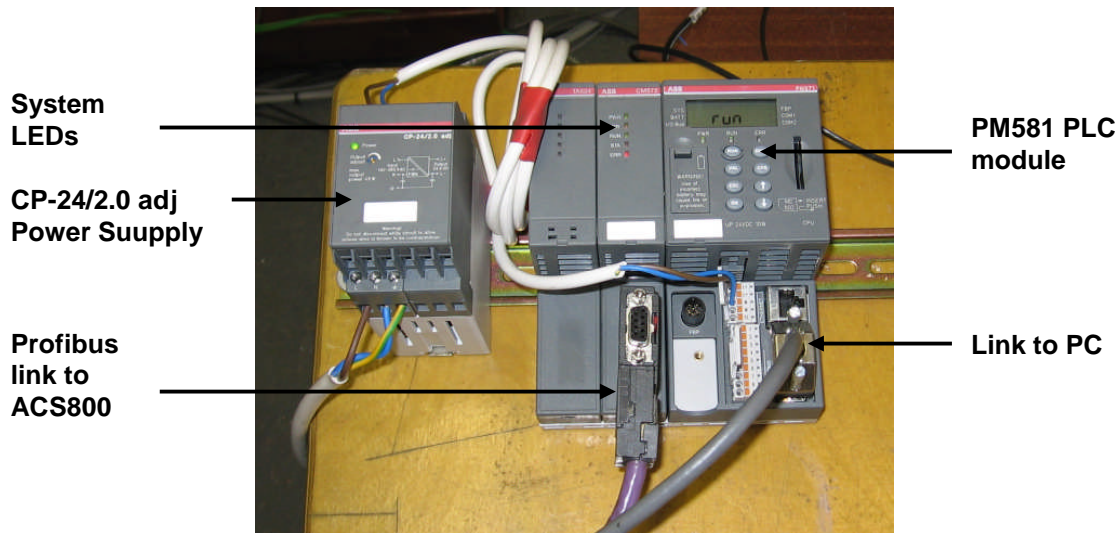


Figure 54 – PLC associated modules and linkages

The operation of the PLC is controlled by the CoDeSys software package into which is loaded the code 'PBL\_wave\_simulator\_8off2.pro'. This contains 2 ladder logic diagrams, which determine the commands sent to the VSD by the PLC. One ladder logic diagram determines the sequence of actions associated with Homing the flap, whilst the other defines the actions associated with creating a 'wave'. When the CoDeSys software is running, the user can select an existing wave from the test window, or can define a new trapezoidal profile 'wave' cycle by setting parameters in a USER data block. The CoDeSys software then uploads these to the PLC, and commands the PLC to run. The parameters input to create a trapezoidal wave are:

- a1 - the forward acceleration (motor rev/s<sup>2</sup>)
- a2 - the backward acceleration (motor rev/s<sup>2</sup>)
- sp1 - the forward maximum speed (motor rev/s)
- sp2 - the backward maximum speed (motor rev/s)
- p1 - the forward movement (motor degrees movement)
- p2 - the Home position (motor degrees movement)

The 'PBL\_wave\_simulator\_8off2.pro' allows either a single repeating wave, or a repeating sequence of up to 8 different waves to be produced.

A non-representative feature of the profiles created is that the wave ladder program has a lag defined in it which is apparent as a time delay before the flap begins to accelerate, and after it decelerates to rest. The lag was found to be necessary to ensure that the wave command sequence executed correctly, and is 100ms.

### **Home and Limit stops**

The PWG is fitted with 3 Omron safety limit switches. Two of these are used to cut the power supply to the rig in the event that the flap should be going to exceed its limits of permitted travel, whilst the third is used to set the Home position of the flap.

### 3.4.8 Instrumentation and Data Acquisition

#### General

A schematic of the instrumentation system is shown in Figure 55.

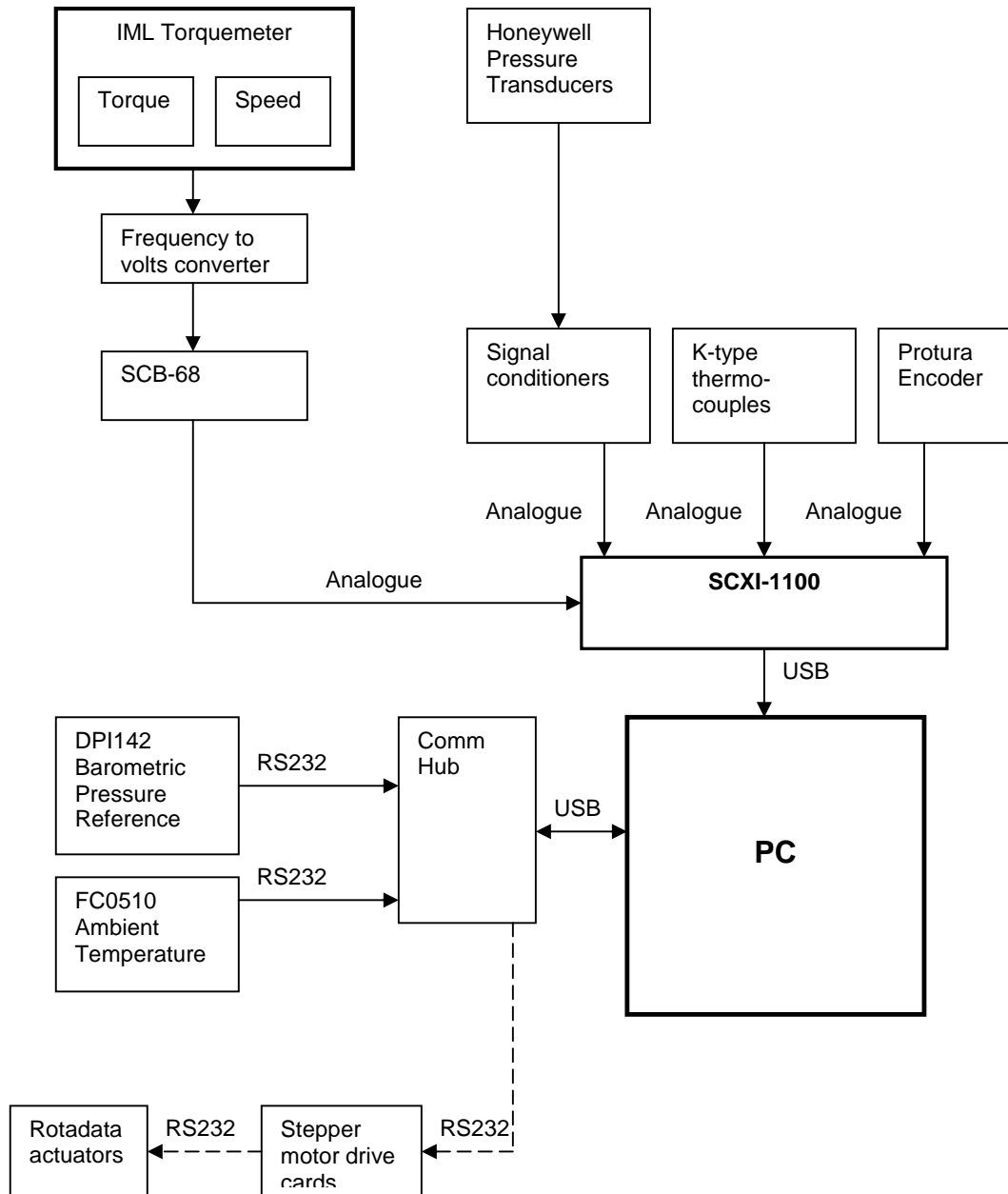


Figure 55 – Schematic of instrumentation system

The instrumentation system consisted of:

1. Pressure transducers and thermocouples in the PWG, at planes upstream and downstream of the turbine, and pressures between the blade rows of the turbine.
2. A torquemeter attached to the turbine.
3. Flap position from an encoder on the central column.
4. Barometric pressure and ambient temperature.

In addition, the pitot probes were mounted in Rotadata actuators as shown in Figure 56, so that they could be traversed across the instrumentation planes.



*Figure 56– Rotadata actuator with pitot probe mounted on instrumentation ring*

### **Data Acquisition**

The fundamental oscillatory nature of the flow in the facility meant that data had to be acquired from the instruments over specified periods of time. This was achieved by using a bespoke LabView data acquisition code which called a virtual instrument task which was set up on the National Instruments SCXI unit, and communicated with instruments to get the barometric pressure and ambient temperature.

The heart of the data acquisition system was a National Instruments SCXI-1000 4 slot chassis (Figure 57). This contained a SCXI-1100 32-channel  $\pm 10\text{V}$  analogue input module multiplexer, amplifier and signal conditioning module and a SCXI-1600 USB data acquisition and control module for 16 bit digitisation of the analogue inputs and export through a USB 2.0 output. These modules were configured, and the Virtual instrument task set up, using the associated NI-DAQmx Measurement Services software.



*Figure 57 – National Instruments SCXI Chassis and modules*

### **Flap Position**

Accurate knowledge of the position of the flap during a ‘wave’ cycle was fundamental to understanding what was going on in the test facility, and essential for processing the data acquired. The flap position was determined using a Renishaw RESC RGH40 angle encoder system, which was mounted on the flap driveshaft output side of the PWG gearbox on the (Figure 58). The encoder has 40,000 lines/360 degrees (resolution = 0.009 degrees). The output from this is fed into a Protura P202 encoder interface module which produces an analogue output of 0-10V for 0-360 degrees of movement, which is fed to the SCXI chassis.

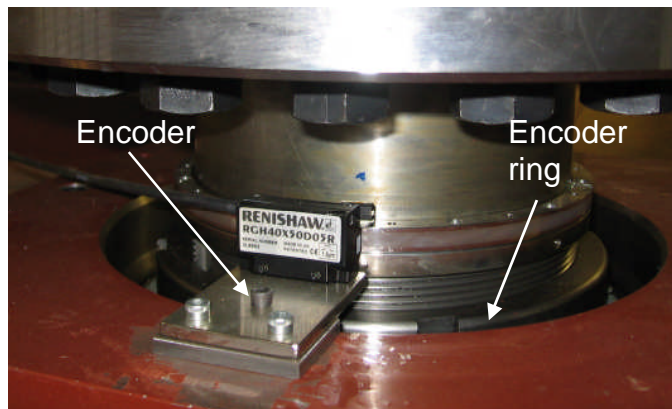


*Figure 58 – Flap position encoder*

### Turbine torque and speed

The torque and rotational speed were measured by an IML RTA500 strain gauge torquemeter with speed signal (Figure 59). The 500 Nm torquemeter produced a 0 to  $\pm 5V$  dc output directly proportional to torque. The speed signal allowed for speeds of up to 5000 rpm to be measured. In order to measure the speed an IML SY020F-V frequency to voltage converter was required, which provided an output of 2 mV/RPM, and was connected between the torquemeter and PCI A to D card (Figure 59). The installation of the torquemeter in the turbine module is shown in Figure 60.

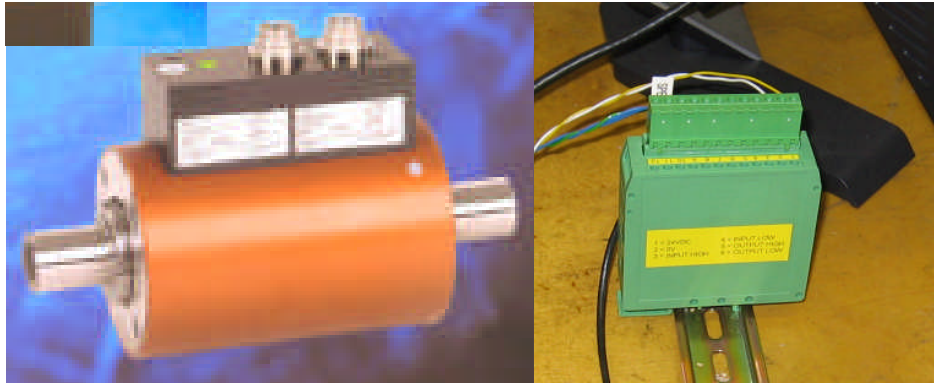


Figure 59 – Torquemeter and frequency to voltage converter

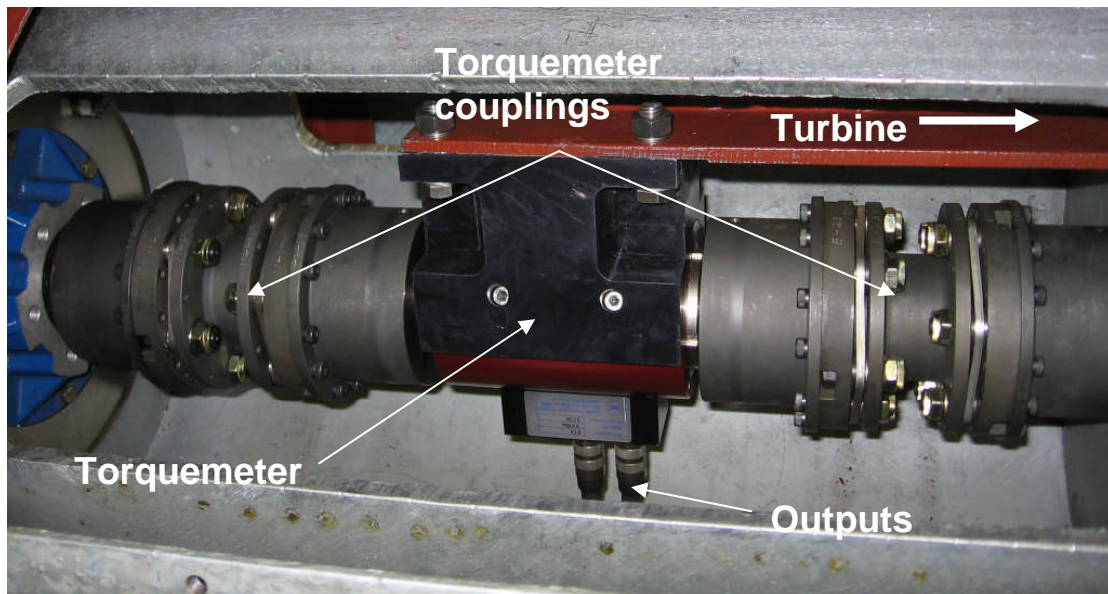


Figure 60 – Installation of torquemeter within turbine module

## Pressure Data

The pressures were measured using 0-5 psi Honeywell 26PCBFA1D, temperature compensated differential pressure transducers (Figure 61).



*Figure 61 – Honeywell 26PCBFA1D differential pressure transducers*

The outputs from the 5psi range Honeywell pressure transducers were passed to custom built signal conditioning units (Figure 62), which amplified the 0-50 mV output signals to 0-2 V, and passed them through an 800Hz low pass filter.

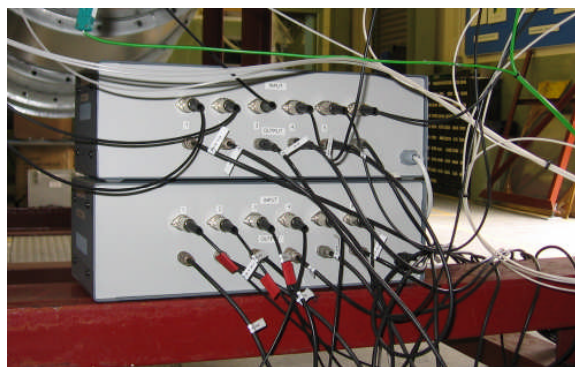


*Figure 62 – Signal conditioning units for pressure transducer signals*

The static pressure ports on the rig were 2.2mm diameter, and were connected to the pressure transducers by 2mm internal diameter plastic tubing.

## Pressure in PWG

The pressure within the PWG was measured by a static pressure port at mid-height, positioned close to the central column where it was expected that there would be little movement of the air, and so the tapping would effectively record the total pressure in the PWG.

In addition to the static tapping 2 NPL pitot probes were positioned in a plane 1023 mm from the PWG outlet plane, with the one recording the total pressure of air going into the PWG 30mm above the centreline, and the other recording the total pressure of air going out of the PWG 30 mm below. Both heads were positioned centrally in the duct in plan view.

### **Instrumentation Plane Total Pressure probes**

Six total pressure probes were mounted in Rotadata actuators, in order to obtain measurements of the total pressure in the instrumentation rings. The latter probes had a simple swan neck. The hypodermic tubing forming the probe head had an internal diameter of 2.3mm, and external diameter of 3.2mm. The overall length of the probes was 0.7m, in order to allow the probe to be positioned on the duct centreline if necessary. These probes are illustrated in Figure 63.



*Figure 63 – Heads of total pressure probes for Rotadata actuators*

The probes were not calibrated as was expected that the flow would essentially be axial through the measuring sections, the support influence would be negligible, and based on the dimensions of the probe, the ‘Barker effect’ based on  $Re < 100$  ( $Re = Ud/v$ ) (Arts et al, 1994) would only be expected to start occurring at velocities below 0.6 m/s.

### **Temperature Data**

The air total temperatures within the PWG and test duct were measured using type K thermocouples, which were connected directly to the SCXI 1100 module (Figure 64).

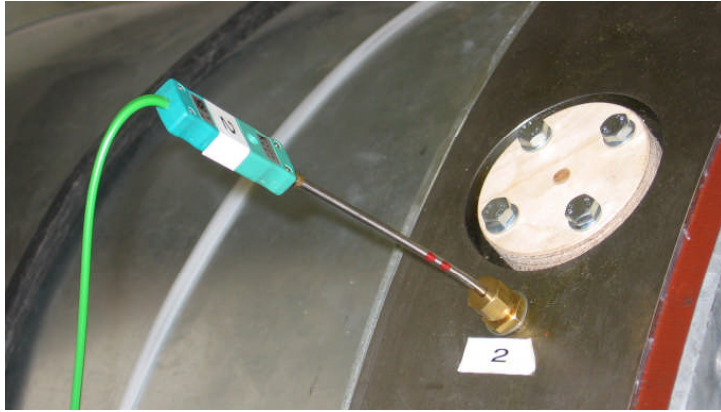


*Figure 64 – Thermocouple recording total temperature in instrumentation ring*

## 4. Commissioning of Test Facility

### 4.1 Fundamentals

#### 4.1.1 Dimensions of PWG and swept volume

The first exercise in evaluating the PWG was to establish if the actual dimensions and movement corresponded to the design specification. The measurements taken and calculations made are presented in Appendix E. It was concluded from comparison of the actual dimensions of the PWG and the range of flap movement achieved that although the specified volume was achieved, the maximum volume that could be swept by the flap was  $15.1\text{m}^3$ , which was 8% less than that specified.

#### 4.1.2 Development of PWG control system

Before a turbine could be tested, it was necessary to establish a control system for producing the desired flap movements in the PWG. It was also the case that assembly of the PWG and basic duct definition took place ahead of the design and manufacture of the turbine. This meant that when the control system was put in place a basic only an empty duct was attached to the PWG around which the instrumentation and data acquisition systems could also start to be installed, as illustrated in Figure 65.



*Figure 65 – Initial duct configuration*

The development of the control system was protracted task due to a number of unforeseen limitations and difficulties. As stated in section 3.2.4. The original intention was to have a single VisualBasic code on a PC which would send the commands to the VSD on the PWG to produce the desired flap movements, acquire the data from the instrumentation and save it to specified files. Following advice from ABB it was intended to effect control of the PWG via digital i/o signals which would be generated within the VisualBasic code. To this end a series of relays for producing the digital i/o signals were connected to the control PC.

The first problem to arise was in getting Visual Basic to interface with the National Instruments software which ran the measurements task, and no real support could be obtained from National Instruments in achieving this. Due to the need to make progress the decision was made to use LabView to develop a code to control the flap, and this was duly done with some assistance from ABB as to the sequence and format of the digital i/o commands that needed to be sent. This code was developed to the point where the flap could be made to carry out a cycle. Further difficulties with developing the LabView code, led to the decision to utilise the Profibus communication link to the VSD, rather than the hard wired digital i/o, and drive this with Visual Basic. Unfortunately, more difficulties were encountered in getting this system to function, which again could not be resolved with the support available from ABB and the Profibus supplier Softing. At this point migration of all software to Delphi was considered, but then ABB offered a PLC solution. At this point it was decided that it would be best to have one PC dedicated to control of the PWG, and a second PC dedicated to the instrumentations and data acquisition.

Once the decision had been made to separate the control of the PWG from the instrumentation system it was believed that development of the instrumentation system would be straightforward. This was not the case though, as fundamental difficulties were again uncovered in linking Visual Basic to the National Instruments virtual instrument task, and the support required to overcome this could not be obtained from National Instruments. The difficulties were further exacerbated by personnel commitments at Cranfield. The decision was therefore taken to employ a contractor to develop the data acquisition code in LabView. This meant that significant effort was put into developing a VisualBasic code which was used early on in the commissioning process, before it was replaced by the LabView code.

The electrical elements in the facility and the associated control system were both procured by PBL, and the ladder logic code used to operate the facility via the PLC was developed by G. Laird of PBL. Therefore, before the characterisation testing began, the author had to gain familiarity with the system, establish, verify, and document the operating procedures to be used in the facility (Herring, 2006). Another essential task carried out was to ensure that the both the soft and hard emergency stop systems operated effectively.

#### **4.1.3 Specification of 'wave' input parameters**

These parameters cause the PLC to move the flap so that the speed of the flap nominally follows a trapezoidal profile. In order to use the facility to evaluate the

performance of scaled test turbines, it is necessary to be able to define the parameter input values which will produce the flap movements which give the desired flowrate/time histories. The approach taken to achieving this was to develop the Matlab based code ‘profile’, which is described in Appendix F.

#### 4.1.4 Development of initial operating envelope

Evaluation of the operating envelope and definition of limitations is a critical part of the commissioning of any new test facility. Given the unique nature of the HydroAir test facility, the novel materials employed in its construction, its novel control system, and significant uncertainty with regard to the effectiveness of the sealing around the flap, an incremental approach was taken to developing the operating envelope.

The ‘profile’ program was used to define a datum input wave which had a nominal RMS volumetric flowrate of  $2.3\text{m}^3/\text{s}$  corresponding to the design point of the turbine, and a period of 7 seconds, which was chosen so as to have the flap sweeping less than half its maximum range. The actual wave period was determined by plotting the flap speed in DriveWindow. This was compared with the required period, and the acceleration parameter was adjusted until the two periods matched. The final input values for the datum wave are shown in Table 25.

Q	T	Speed	Accel	P1
2.3	7	686	11	9175

*Table 25 – PWG input parameters for datum wave*

This process was then carried out for a range of periods up to 15 seconds, which required the flap to use 96% of its movement. This exercise provided information regarding the correlation between the desired and actual periods of waves obtained by using the parameter values from ‘profile’, and verified that the control system and drive were moving the flap accurately over its range of movement.

Once a level of confidence had been gained in operating the facility and changing the input wave profile, a test was carried out to determine how square the input wave profile could be. This was determined by finding the maximum level of acceleration that could be used. The test was carried out by taking the datum wave profile and gradually increasing the acceleration, and observing the reduction in the wave period and the behaviour of the rig. The test was terminated at a maximum input acceleration of 56, when the period had reduced from 7 to 5.2 seconds, as the whole PWG began to shake. The duration of the acceleration/deceleration parts of the cycle ( $t_1$ ) for the datum wave was 1.17 seconds, whereas when the acceleration/deceleration was  $56\text{ rev/s}^2$  this was reduced to 0.29 seconds. The difference between the 2 profiles is shown in Figure 66.

Given that a true trapezoid profile is not achieved – so the maximum acceleration in speed is greater than shown - the test results showed that the drive could produce a remarkably rapid acceleration of the flap – albeit when there was very little resistance

in the system (i.e. little compression of the air). It was concluded from the test that the maximum level of acceleration that could be achieved was more than sufficient to meet the likely test requirements, but also that the maximum acceleration that should be input, without further structural analysis, was  $50 \text{ rev/s}^2$ .

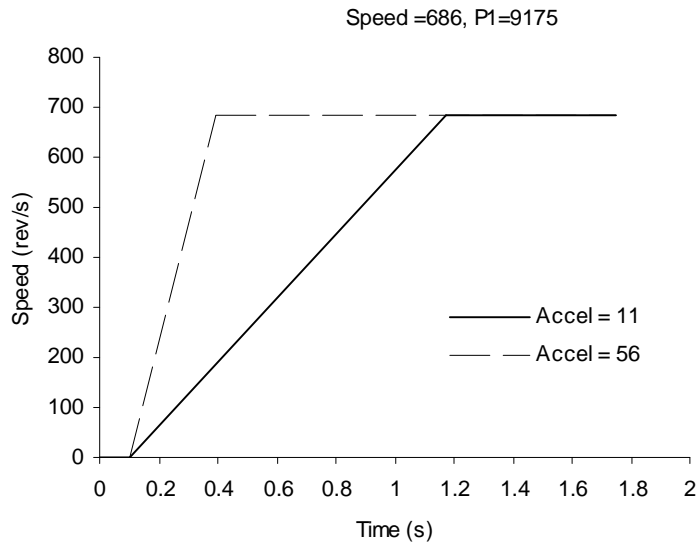


Figure 66 – Comparison of trapezoidal profiles for accelerations of 11 and 56

After the acceleration test had been completed an initial operating envelope was developed for nominal RMS flowrates of 2.3, 3.0, and  $3.6 \text{ m}^3/\text{s}$ . The data was taken after the flap had gone through a number of cycles to avoid initial transient effects. This process proved the robustness of the procedure used for determining the control inputs, and that the flap could be made to carry out the range of movements envisaged in the design specification, albeit with no real load. This exercise provided the basis for further developing the envelope with the porous plate, and then the turbine.

#### 4.1.5 Cycle Repeatability

A primary concern with regard to the subsequent testing which was to be carried out was the repeatability of the flap movements and conditions generated in the test facility, and so priority was given to establishing this.

The data was analysed by finding the mid-point of the flap movement from the flap encoder data, then finding the times when this occurred as the angle was increasing during the time history. This allowed the data could to be interpolated and a number of individual cycles, and the average cycle time, the standard deviations and range between minimum and maximum cycle times determined. This exercise was carried out for a range of flap oscillations using the VisualBasic data acquisition code. The results indicated that the periods of the flap cycles were very consistent, with small standard deviations and ranges. They also showed that the data was very smooth at 5.8 Hz, which was the maximum that could be achieved with the VisualBasic data

acquisition program<sup>3</sup>. Furthermore, the data did not indicate a growth in cycle variations as the time period was reduced from 8.7 to 4.8 seconds, but did appear to show a small growth in cyclic variations with flow rate, as indicated by the standard deviation and range values. The results indicated that the time period taken for the flap to execute its cycle was consistent to better than 0.025 of a second, based on the range, and that the average repeatability was better than 0.01 of a second. However, these findings needed to be validated through the analysis of data taken at a higher sample rate.

The cyclic repeatability of the flap movements was investigated further when the initial version of the LabView data acquisition code was installed. This allowed a sample rate of 100Hz to be used. In addition, the instrumentation arrangement was improved in that the flap encoder position was now read from the analogue output from the Protura encoder module, rather than its RS232 output. The flap cycles input are shown in Table 26, and the results of the cycle period and flap movement analyses in Table 27 and Table 28 respectively.

Q (m <sup>3</sup> /s)	Speed (rev/s)	DP	Accel (rev/s <sup>2</sup> )	P1 motor (degrees)	Flap demand (degrees)
2.3	686	31	8	11797	163.85
		32	11	11797	163.85
3.0	895	33	16	11968	166.22
		34	16	11968	166.22

Table 26 – Input parameters

Q (m <sup>3</sup> /s)	DP	No. of cycles	T Average (s)	T std dev (s)	T Range (s)
2.3	31	6	9.088	0.0100	0.025
	32	6	8.302	0.0057	0.017
3.0	33	8	6.819	0.0056	0.018
	34	8	6.815	0.0062	0.017

Table 27 – Results of cycle period analysis

Q (m <sup>3</sup> /s)	DP	No. of cycles	Flap demand (degrees)	Flap min (degrees)	Flap max (degrees)	Flap range (degrees)	Flap Average (degrees)	Demand-Average (degrees)
3.0	31	6	163.85	-0.68	163.60	164.28	164.00	-0.15
	32	6	163.85	-0.68	163.44	164.13	163.44	0.40
3.6	33	8	166.22	-0.70	165.81	166.51	165.81	0.41
	34	8	166.22	-0.70	165.83	166.53	165.83	0.39

Table 28 – Results of cycle flap movement analysis

<sup>3</sup> This low sample rate was due to difficulties in integrating the Visual Basic code with the DAQMX measurement task set up to run on the SCXI-1100. These difficulties, which could not be resolved even with assistance from National Instruments, led the development of a LabView based replacement code.

The results of the period movement analyses were consistent with the data acquired using the Visual Basic program, in that the maximum variation in period was less than 0.025 of a second, and the period was typically repeatable to better than 0.01 of a second or 0.15%.

Whereas the previous data appeared to show that the average actual flap movement were slightly less than demanded by about 0.05 degrees, the data from points 31-34 showed a tendency for it to be less than demanded by about 0.5 degrees. This could have been because the higher sampling rate (17 times greater), was providing a better indication of the actual movement of the flap. An error of 0.5 degrees on the movements demanded for data points 31-34 was an error of only 0.3%.

From the analysis of the flap movement data it was concluded that the period of the flap movement was typically repeatable to better than 0.01 seconds or 0.15%, and that the angular movement was typically short of that demanded by 0.5 degrees, or 0.3%.

#### **4.1.6 Sealing of PWG**

Just after the generator was fitted and coupled to the turbine it was observed that as the flap swept around the PWG the panels would flex, and strong jets of air could be felt issuing from the joints between them and also at places along the joins between the lid and base and the fibreglass panels. A calculation suggested that a significant mass of air could be leaking from the joints, and so tape was applied to seal along all the joints. In order to determine the effect of this exercise data points (281 and 285) were taken with the  $Q_{rms}=2.3/T=7$  wave profile before and after. Analysis of the data showed that although the maximum and minimum pressures recorded in the PWG were similar, there was a 9% increase in the volume of air that passed through the instrumentation planes. It was concluded from this that there was significant leakage from the joints between the fibreglass panels and they needed to be sealed with tape.

#### **4.1.7 Rig Adjustments**

It is to be expected that the initial commissioning of a new test facility will reveal the need for a number of adjustments and modifications, and this facility was no exception. Early in the characterisation testing the flap was seen to begin to 'wobble' when it changed direction. This was found to be due to the bolts securing it to the central column working loose. The remedial action taken was to apply Loctite to all the bolts and put spring washers under them. This didn't prove sufficient, however, and after a relatively short time the bolts were changed for higher specification ones which were done up to a torque of 100Nm.

Once the datum turbine was installed and the generator coupled, and profiles with nominal flowrates of  $Q_{rms}>2.3 \text{ m}^3/\text{s}$  were input, it was found that the bolts holding the lid and base on started to become loose. The initial action was to simply tighten them up, but this was unsatisfactory as they pulled down into the plywood. Washers were then put under the bolts but they too proved unsatisfactory, and so plates were made to go around the circumference of the lid which resolved this.

A further problem with the larger inputs was that the flap encoder started producing errors due to greater movement of the PWG structure, caused by the greater pressure changes within it. The resolution of this required 2 modifications. Firstly the frame across the top of the PWG was braced further to reduce flexure of the lid, and secondly a new bracket was made to hold the encoder head on the opposite side of the flap driveshaft. Once these modifications had been made a test was carried out in which short and long input profiles of incrementally increasing flowrates were input to establish the maximum operating input which was found to be a nominal  $Q_{rms} = 3.6 \text{ m}^3/\text{s}$ . This gave the final envelope for the facility with datum turbine installed as that shown in Figure 67.

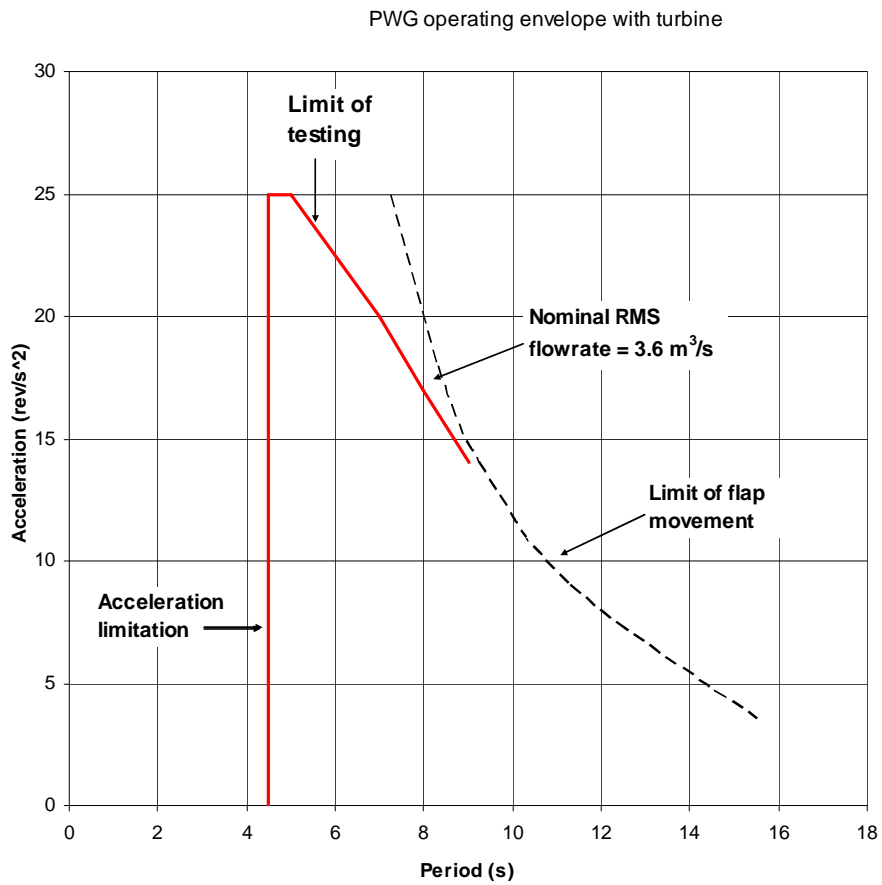


*Figure 67 – PWG test envelope with datum turbine installed*

## 4.2 Installation of Porous plate

### 4.2.1 Envelope

The second configuration of the rig was achieved by inserting the 1mm thick porous plate (3.3.6) between the two 1.5m long by 0.8m diameter duct sections (Appendix G, Table 63). Once the porous plate had been installed data was taken at a number of test points within the previously defined envelope. This data revealed significant noise on the pressure transducer signals. Eventually the SCXI 1100 card was found to be faulty. The problem was resolved by installing an alternative card, but in addition 800Hz filters were incorporated into the pressure transducer signal amplifiers. An error was also found in the LabView code which inserted additional blank data lines in the results.

Once the faults were cured data was taken over a range of conditions at 100Hz for periods of 3 minutes after the rig had been operating for a small number of cycles. The data was acquired by working from the low flowrate, long period conditions, up to higher flow rate and short period (i.e. with high flap acceleration) conditions, and the test facility envelope was expanded to include nominal 4.0 m<sup>3</sup>/s rms flow conditions as shown in Figure 68 .

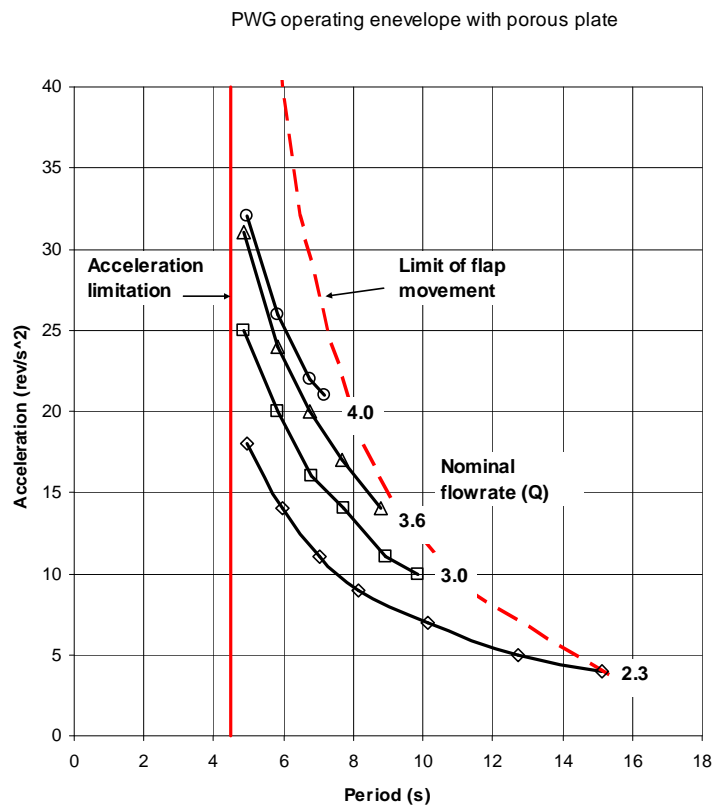


Figure 68 – PWG operating envelope with porous plate

## 4.2.2 Flow quality in PWG

The desire was that there would be very little total pressure loss as the air flow moved from the PWG into the transition section. If this was so then it was expected that the PWG static pressure and the NPL total outlet pressures would be very similar – when the flow was moving out of the PWG, similarly if the transition section was well designed, then it was expected that the PWG static and NPL total inlet pressures would be similar when flow was entering the PWG. When the data was analysed it was seen that there was remarkably close agreement between all 3 pressures (Figure 69), whether the flow was going out of or into the PWG, both at the lowest flow longest period condition ( $Q=2.3 \text{ m}^3/\text{s}$ ,  $T= 15.12 \text{ s}$ ), and at the highest flowrate, shortest period condition ( $Q=4.2 \text{ m}^3/\text{s}$ ,  $T= 4.93 \text{ s}$ ).

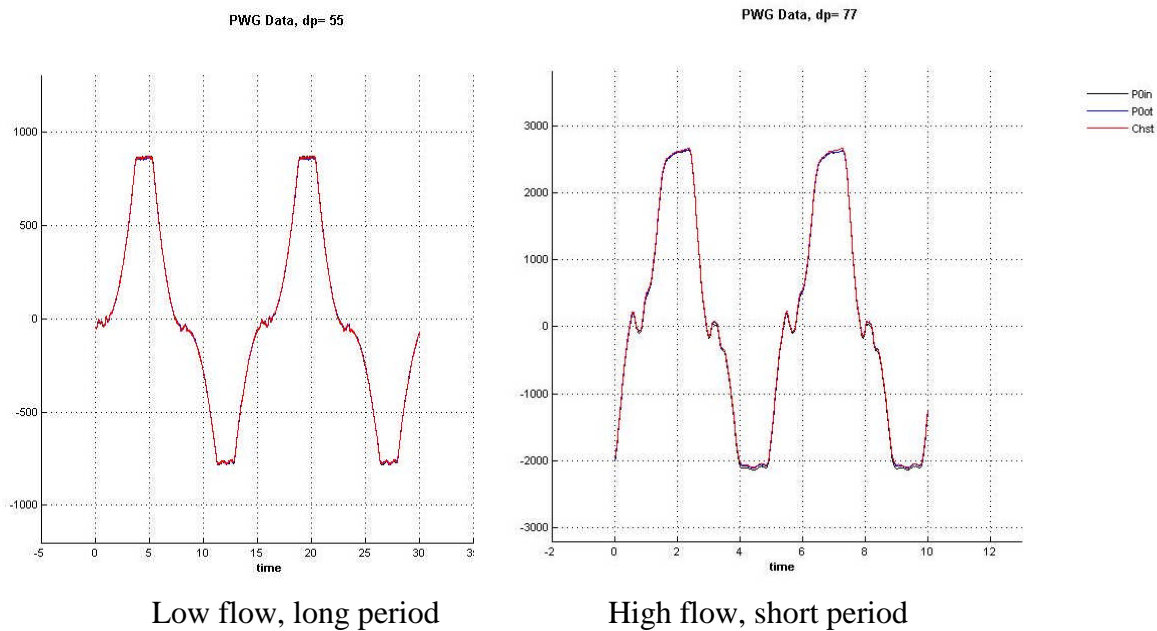


Figure 69 – Comparison of PWG pressures low flow, long period

This was not surprising because even at the highest flowrate the dynamic head was small. The cross-sectional area of the transition duct in the plane of the total pressure probes was  $0.7061 \text{ m}^2$ , which means at a flow rate of  $4.2 \text{ m}^3/\text{s}$  the axial flow velocity is  $6 \text{ m/s}$ , and the dynamic head would be:

$$\Delta p = \frac{1}{2} \rho v^2 = 22 \text{ Pa}$$

These results demonstrate that there are no major losses occurring at the inlet/outlet of the PWG. Furthermore, it is evident that the static pressure measurement in the PWG and the 2 total pressure probe measurements may be used to give a reliable indication of the total pressure in the PWG at any time. The measurements also demonstrated that the dynamic pressure in the duct was generally very small in comparison to the variations in total pressure, which could have an impact on the accuracy of the mass/volumetric flowrate calculations in the duct measuring sections.

Analysis of the data consistently showed that the positive pressure peak was significantly greater than the negative (as can be seen in *Figure 69*), but also that maximum and minimum pressures were very consistent for each nominal flowrate, although the periods varied. This can be seen in the data in *Table 29*, which shows that the pressure amplitudes reduced slightly as the wave period was reduced, but the largest reduction of 37 Pa for the 4.0 m<sup>3</sup>/s wave was only a change of 1.4%. As the amplitude variations at a given flow rate were small, the data was averaged and the variation in pressure amplitude within the PWG with flowrate was plotted, as shown in *Figure 70*.

Q (m <sup>3</sup> /s)	DP	Period (s)	PWG P max (Pa)	PWG P min (Pa)
2.3	55	15.12	908	-748
	56	12.71	908	-748
	57	10.13	908	-743
	58	8.13	906	-738
	59	7.03	906	-735
	60	5.95	903	-735
	61	4.95	901	-728
3.0	63	9.84	1544	-1246
	64	8.94	1544	-1244
	65	7.72	1539	-1241
	66	6.82	1544	-1230
	67	5.81	1528	-1223
	68	4.87	1526	-1217
3.6	69	8.78	2201	-1749
	70	7.70	2198	-1757
	71	6.75	2193	-1754
	72	5.81	2188	-1736
	73	4.84	2175	-1728
4.0	74	7.17	2683	-2147
	75	6.76	2672	-2145
	76	5.85	2649	-2132
	77	4.93	2646	-2119

*Table 29 – Maximum and minimum pressures for flow conditions*

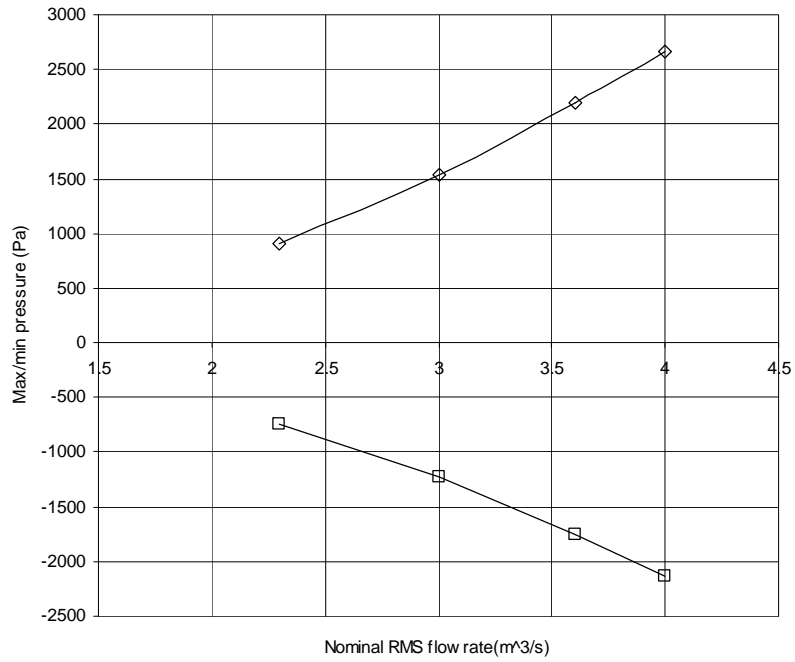


Figure 70 – Variation in PWG max/min pressure levels with RMS flowrate, for porous plate

Variation in squareroot of PWG pressure levels with peak flowrate

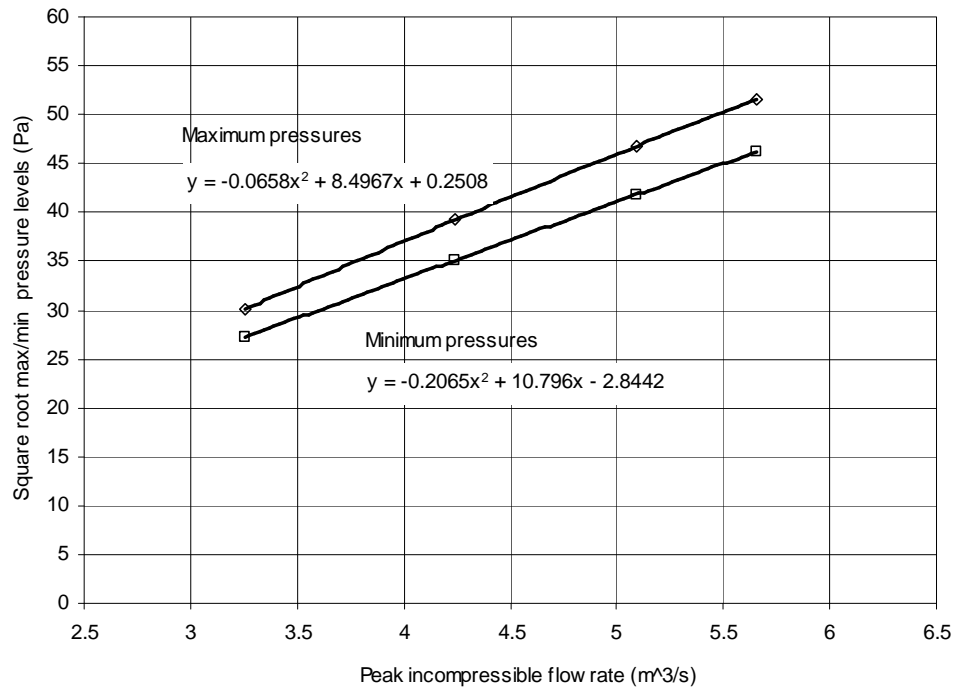


Figure 71 – Variation in PWG pressure amplitude with peak incompressible flow rate

If the overall loss coefficients of the system operating in its forward and reverse modes remained constant as the flowrate was varied (i.e the flow was incompressible), then it would be expected that plots of the square root of the pressure amplitudes against flow rate would be straight lines. This was seen to be the case when plots were made of the square roots of the absolute values of the maximum and minimum peak pressures against the peak flowrate based upon the flap movement (i.e. assuming incompressible flow), as shown in Figure 71.

One of the objectives of installing the porous plate was to enable an estimate of the mass/volumetric flowrate to be made which would give an indication of the leakage in the system. If there was no leakage in the system, and the flow was incompressible throughout, then the volumetric flowrate at any time would be equal to the rate of change of volume in the PWG produced by the movement of the flap. This means that we can define:

$$Q_{ideal} = \frac{dV_{PWG}}{dt}$$

which can be re-written in terms of flap position  $\theta$ , the radius and height of the PWG, radius of its central pillar as:

$$Q_{ideal} = \frac{d\theta}{dt} \cdot f_{vol} \quad \text{where } f_{vol} = \frac{1}{2} (R_{PWG}^2 - r_{pillar}^2) h_{PWG}$$

where  $R_{PWG} = 1.65$  m,  $h_{PWG} = 2.4$  m,  $r_{pillar} = 0.08425$  m.

$$\partial V = \partial \theta \cdot f_{vol}$$

$$\partial \theta = (\theta_{i+1} - \theta_i)$$

$$\partial t = (t_{i+1} - t_i)$$

$$Q_f = \frac{\partial V}{\partial t}$$

We can then determine the mass flow rate from a point-by-point calculation of density, based on the static pressure and temperature measured in the PWG.

$$\text{Density, } \rho = \frac{P_{PWG}}{R \cdot T_{PWG}} \quad \text{and so: } \dot{m}_f = \rho \cdot Q_f$$

The calculation of mass/volumetric flowrate through porous plate was made under the assumptions that the flow was incompressible, and that the 2 instrumentation rings were sufficiently far away from the porous plate that they record the static pressure drop across it. The actual distance between the static ports in the instrumentation rings and the porous plate was 1.555 m, which was much greater than the predicted

recovery distance of 0.125m. Hence, the volumetric and mass flow rates (Table 30) were determined as follows, where  $p_1$  and  $p_2$  refer to the averaged static pressures in the instrumentation planes 1 and 2 respectively, and the density was determined from the average static pressure and temperature measurements in instrumentation plane 1.

$$\Delta p = |p_1 - p_2|$$

$$v = \sqrt{\frac{2\Delta p}{\rho K_0}} \quad \text{where } K_0 = 34.7$$

$$Q_{pp} = v \cdot A \quad \text{where } A = \pi \cdot 0.4^2 = 0.50265 \text{ m}^2$$

$$\dot{m}_{pp} = \rho \cdot Q$$

Q (m <sup>3</sup> /s)	DP	Period (s)	Q rms Flap incomp	Q rms Flap meas	Qrms porous plate
2.3	55	15.12	2.42	2.21	2.15
	56	12.71	2.42	2.25	2.19
	57	10.13	2.42	2.31	2.28
	58	8.13	2.42	2.32	2.28
	59	7.03	2.42	2.37	2.31
	60	5.95	2.42	2.40	2.35
	61	4.95	2.42	2.41	2.37
3.0	63	9.84	3.15	3.12	3.03
	64	8.94	3.15	3.11	3.02
	65	7.72	3.15	3.18	3.09
	66	6.82	3.15	3.16	3.08
	67	5.81	3.15	3.19	3.11
	68	4.87	3.15	3.18	3.11
3.6	69	8.78	3.79	3.78	3.63
	70	7.70	3.79	3.83	3.69
	71	6.75	3.79	3.83	3.70
	72	5.81	3.79	3.82	3.70
	73	4.84	3.79	3.84	3.73
4.0	74	7.17	4.21	4.28	4.10
	75	6.76	4.21	4.24	4.07
	76	5.85	4.21	4.23	4.06
	77	4.93	4.21	4.20	4.05

Table 30- Calculated flowrates

A plot was made of the rms volumetric flowrates calculated from the flap movements and the static pressure drop across the porous plate. This showed a linear relationship between the 2 calculations, and that the mass flow rate through the porous plate was 96.8% that displaced by the flap. This suggested that the leakage area was:

$$A_{leakage} = 0.033 \cdot A_{duct} = 0.0166 \text{ m}^2$$

If it is assumed that the leakage occurs only around the flap seal, then the width of the gap  $h$  may be found:

$$A_{leakage} = 2 \cdot (1.56575 \times h) + (2.4 - 2h)h$$

assuming  $h$  is small, then:

$$h \approx \frac{A_{leakage}}{5.5315} = 0.003 \text{ m}$$

Whilst the porous plate was not a calibrated device for evaluating the mass/volumetric flow rate through the duct, the data indicated that the leakage between the PWG and the central portion of the duct was only 3.2%. In terms of area this was equivalent to a 3mm gap around the flap. These results showed that the leakage in the PWG was sensibly small.

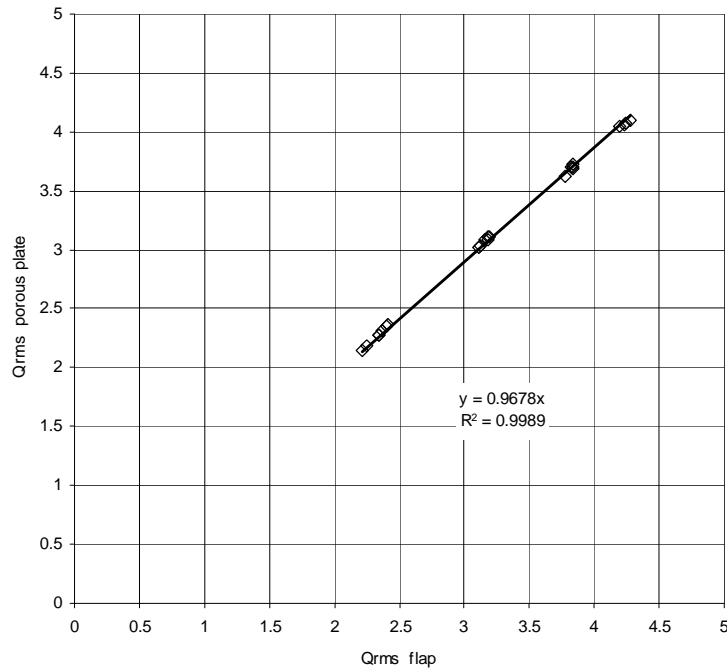


*Figure 72 – Relationship between volumetric flowrates calculated from flap movements and pressure difference across porous plate*

## 4.3 Determination of Mass/Volumetric flowrate

### 4.3.1 Uncertainties

The main objective of developing the HydroAir test facility was to enable the efficiency of the test turbine configuration to be determined from the calculation (see Appendix B):

$$\eta_{turbine} = \frac{\omega \tau}{Q \Delta P}$$

where,  $\omega$  = the rotational speed (rad/s),  $\tau$  = torque (Nm),  $Q$  = volumetric flowrate ( $\text{m}^3/\text{s}$ ), and  $\Delta P$  = the total-to-static pressure drop across the turbine (Pa). The accuracy of the resulting efficiency value is dependent upon the accuracy with which these terms are measured.

The measurements of the rotational speed and torque are provided by the output from the IML torquemeter, and their accuracies should be  $\pm 0.1\%$  for speed, and  $\pm 1.25\%$  for torque based on values of 20Nm and 850 RPM.

Based on a design point pressure drop of 3200 Pa, and a quoted accuracy of  $\pm 0.05\%$  full scale, then a pessimistic pressure measurement error of 40Pa, would equate to an error of 1.2%. In reality, the error is not so easily determined. The total pressure will have radial variations due to the presence of the boundary layers, there will also be circumferential variations, although these should be small. Wall static pressure measurements are inherently less accurate than total pressure measurements, due to the subtle effects associated with the geometry of the port, and the influence that disturbances in the flowfield may have on the measurement. The usual way of reducing the impact of these additional errors is to have a large number of total and static pressure measurements which are averaged. Unfortunately, the number of pressure channels available for doing this in the test facility was restricted to 2 total and 2 static pressure measurements, but the measurement error should be less than the pessimistic error, and assuming a uniform random distribution, the expected pessimistic error might be:

$$\varepsilon = \sqrt{\frac{1.2^2}{2}} = 0.8\%$$

The most difficult quantity to determine is the volumetric flow rate,  $Q$ , for a calibration was required. The usual process for determining the volumetric flowrate through a calibrated duct is to measure the dynamic pressure to determine the maximum axial velocity in the duct and then apply a calibration discharge coefficient ( $C_d$ ) for the duct so:

$$Q = v_{\max} \cdot C_d \cdot A_{duct}$$

It is expected that the area of the duct is accurately known, so the accuracy to which the volumetric flow rate can be determined depends upon the accuracy to which the discharge coefficient is known, and the accuracy to which the maximum velocity can be measured.

There are two ways of establishing the discharge coefficient: calibration against a standard flow meter, or derivation from a velocity profile, and it was the latter approach that was used in this work. Measurement of the discharge coefficient depends upon accurately measuring the velocity profile across the duct. The axial flow velocity at a given radial position is found by measuring the total pressure at the radius in question, and the wall static pressure, and determining the velocity from;

$$v = \sqrt{\frac{2\Delta p}{\rho}}$$

where the density is evaluated from  $\rho = \frac{p}{RT}$ , where  $T$  is the appropriate static temperature for the flow in the duct. Use of this procedure assumes that the static pressure is constant across the duct, and that there is no significant swirl component, or circumferential variation in the flow. The assumption of constant static pressure across the duct should be valid, as the annulus is parallel through the measuring section, and there no struts etc producing wakes ahead of the probes.

No measurements of the static pressure variation across the annuli were made, as this would have required the use of calibrated 3 or 5 hole pressure probes fitted with multiple transducers, which was not practical due to the limited number of transducer channels.

It was evident that the process of determining accurate discharge coefficients for the instrumentation planes, and the radial position at which the maximum dynamic pressure occurred, required the acquisition and processing of a lot of data. However, once these were it was anticipated that the flowrate at any time could be accurately determined from a relatively small number of measurements.

#### 4.3.2 Range of Calibration

The baseline turbine was sized for a operating flow range of flows of  $Q_{rms} = 1.77-3.11$  m<sup>3</sup>/s, which would give axial flow velocities in the range 19.1–33.6 m/s in the turbine annulus (area = 0.0926267 m<sup>2</sup>), but only 5.8-10.2 m/s in the measuring sections (area = 0.306305 m<sup>2</sup>). The objective of the calibration exercise was thus to obtain a calibration over this range of flows. However, given that the expected dynamic pressures were only in the range 15-65 Pa - which is nominally of the same order of magnitude as the uncertainty in the pressure measurements – it was evident that the utmost care would be required in acquiring and processing the data.

### 4.3.3 Transducer calibrations

The pressure transducers were calibrated against 20kPa range Furness FC0510 (Serial no. 9903149) micro-manometer calibrated to 0.25% of reading. The micro manometer was a differential device, and so a short tube was taken from the reference port into a box to ensure that the readings were not influenced by draughts/breezes within the test cell. Initially a 9 point calibration was carried out over the range -17kPa to 20kPa, but this was subsequently reduced to a 5 point calibration over the range  $\pm 10$ kPa. The pressures were set using a Druck DP140, and care was taken to ensure that the tubing was leak tight before the calibration data was taken. The transducer voltage output was logged by the NI SCXI interface. Care was taken to allow pressures to equalise properly when taking the measurements, as errors of even a very few Pascals in the calibration process would introduce significant bias errors into the data. The transducer outputs were seen to be linear over the range in all cases, and so the sensitivities were found from a least squares linear fit the calibration was only accepted if the coefficient of correlation was 1 to 4 decimal places.

### 4.3.4 Flow Uniformity

The amount of information required to accurately determine the volumetric flowrate through the rig depends upon the uniformity of the flow: the less uniform the flow is the more measurements are required, or the greater the uncertainty in the calculation.

If the flow was uniform then similar measurements at different positions in the instrumentation planes would be close to the average value. Plots of the differences in total and static pressures from the appropriate average values for each plane showed significant cyclic variations. When scaled plots of the average pressures were overlaid it was seen that the greatest differences from the average occurred around the zero flow conditions, whilst the minimum differences occurred at the maximum flow conditions. This is illustrated in Figures 73, 74, 75, and 76, in which the variations in the plane 1 total pressure are indicated for reference by 'mean p' (note scale is meaningless); the total pressures in plane 1 are: R1,R2,R3, and statics P1S1 to P1S6; whilst the total pressures in plane 2 are: R4,R5,R6 and statics P2S1 to P2S6. Figures 73 and 74 show the pressure differences for a nominal 7 second wave with an RMS flowrate of  $1.77 \text{ m}^3/\text{s}$ . Figures 75 and 76 are similar plots for a nominal 7 second wave with an RMS flowrate of  $2.3 \text{ m}^3/\text{s}$ .

The plots of the differences in the plane 1 total and static pressures in Figure 73, showed that the differences from the average were least when the total pressure was large and positive (which is the flow direction of interest in plane 1). When the flow rate was positive maximum the differences were in the range 5 to 10 Pa for the total pressures, and 5 to 15 Pa for the static pressures. The differences in the total pressures are smaller than those in the static pressures as might be expected. Figure 74 shows similar plots for the plane 2 pressures. On these plots the flow of interest is when the plane 1 total pressure is negative. A comparison between Figure 73 and Figure 74 showed smaller variations in both plane 2 total and static pressures than for plane 1. The range of differences in the total and static pressures was 0 to 5 Pa, and 5 to 10 Pa, respectively.

The plots in Figures 75 and 76 for the increased flow rate condition showed small increases in the levels of the differences for plane 1: 10 to 15 Pa for the total pressures and 20 to 25 Pa for the static pressures, and similar differences for the plane 2 pressures.

Overall, the examination of the pressure differences for 2 data points revealed consistent characteristics for each group of total and static pressure measurements. The plots did not indicate the presence of gross flow non-uniformities, but the differences did indicate the need to have a number of measurements, even for the total pressures. The data was taken with 3 total pressures and 6 static pressures in each plane and it may be concluded that although there is no evidence of large flow non-uniformities, due to the small pressure differences involved, it would be desirable to actually have more than 3 total and 6 static pressure measurements in each instrumentation plane.

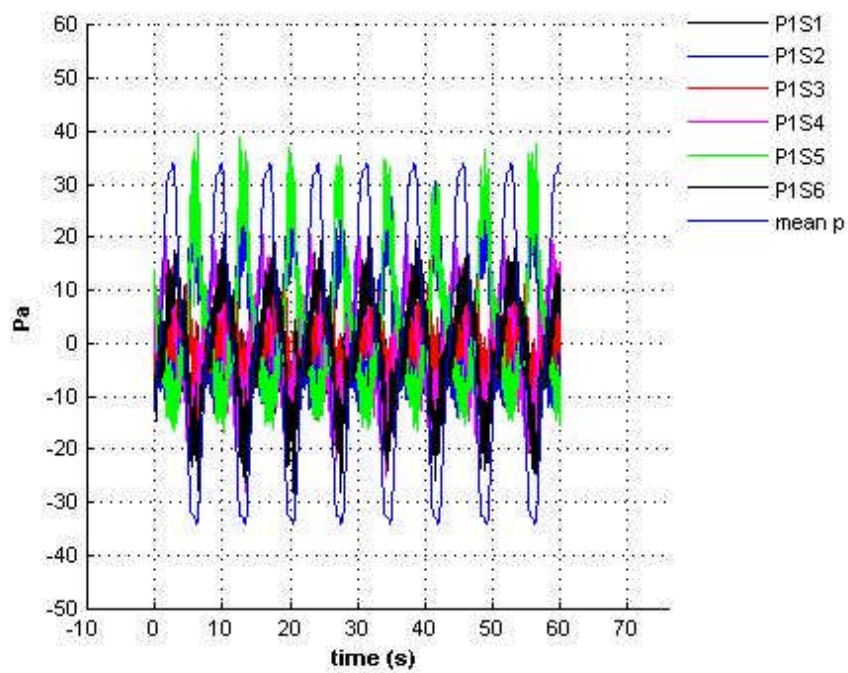
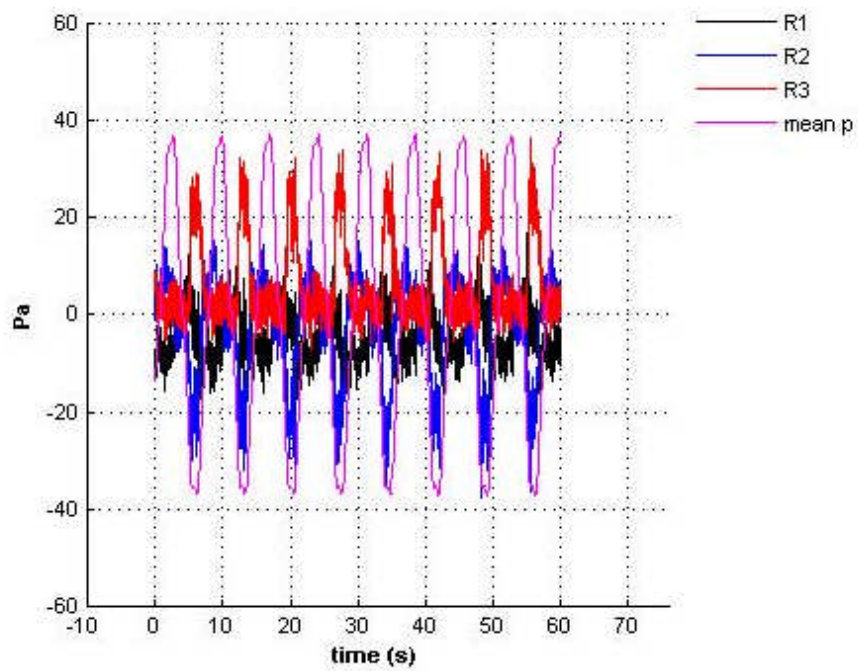


Figure 73 – Differences between total and static pressures and their averages for plane 1, data point 384

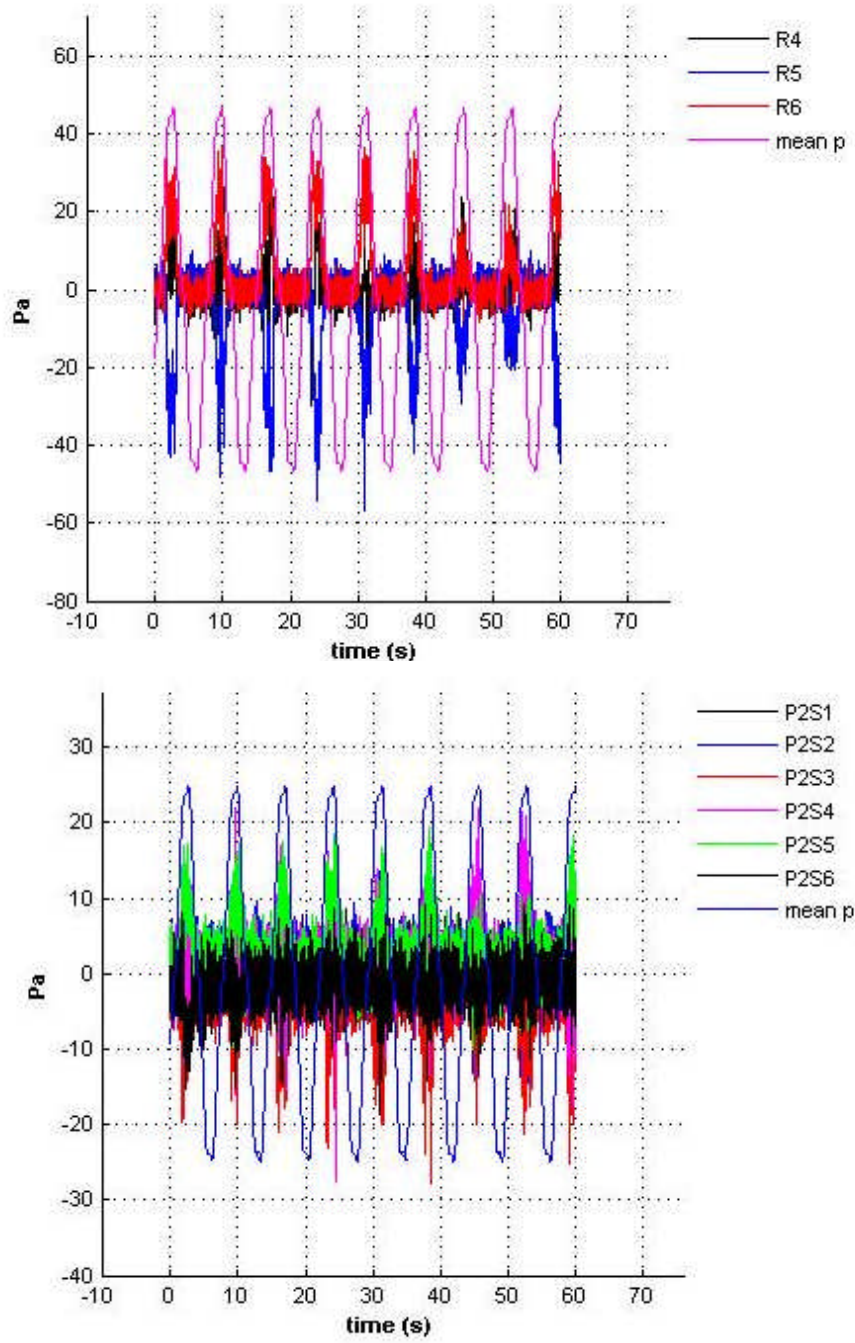


Figure 74 – Differences between total and static pressures and their averages for plane 2, data point 384

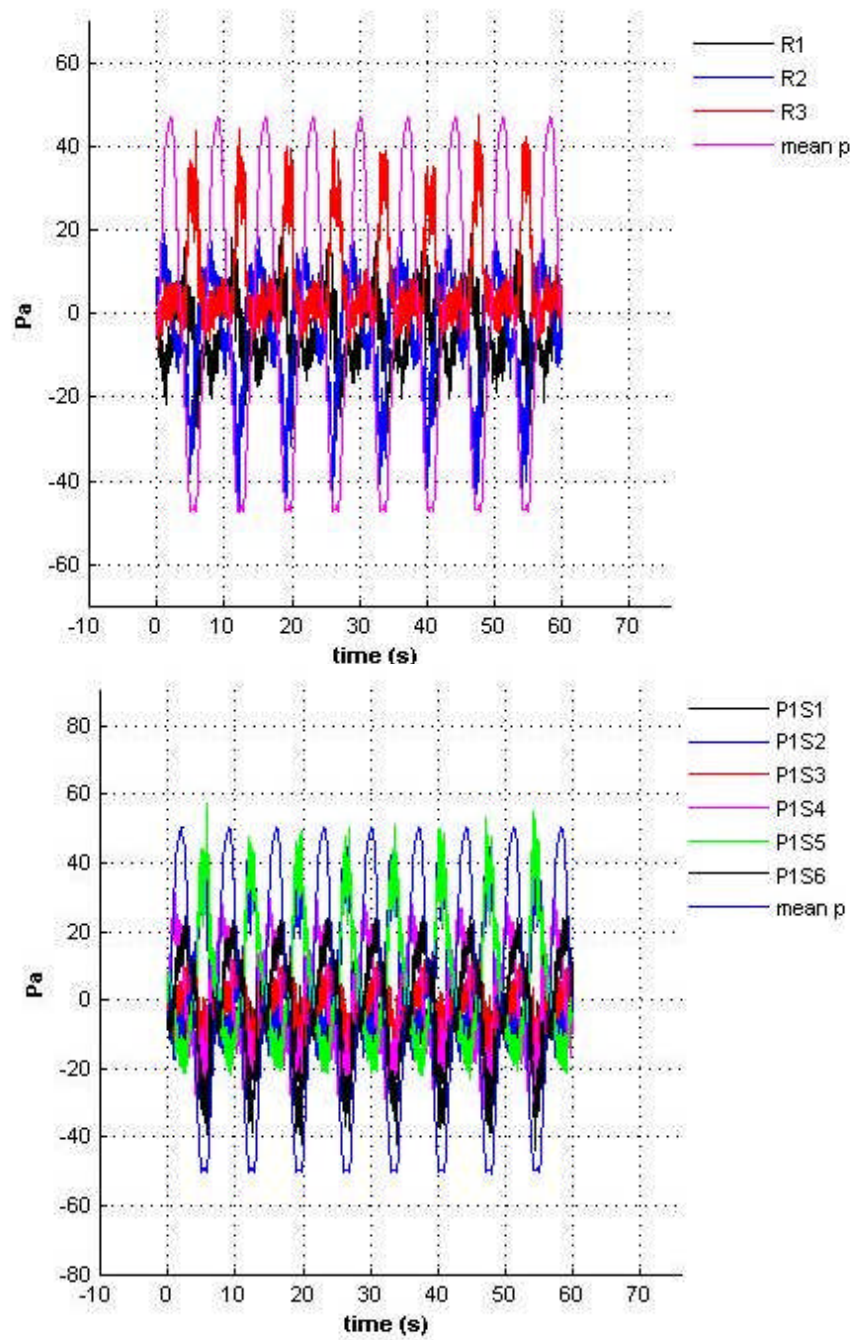


Figure 75 - Differences between total and static pressures and their averages for plane 1, data point 386

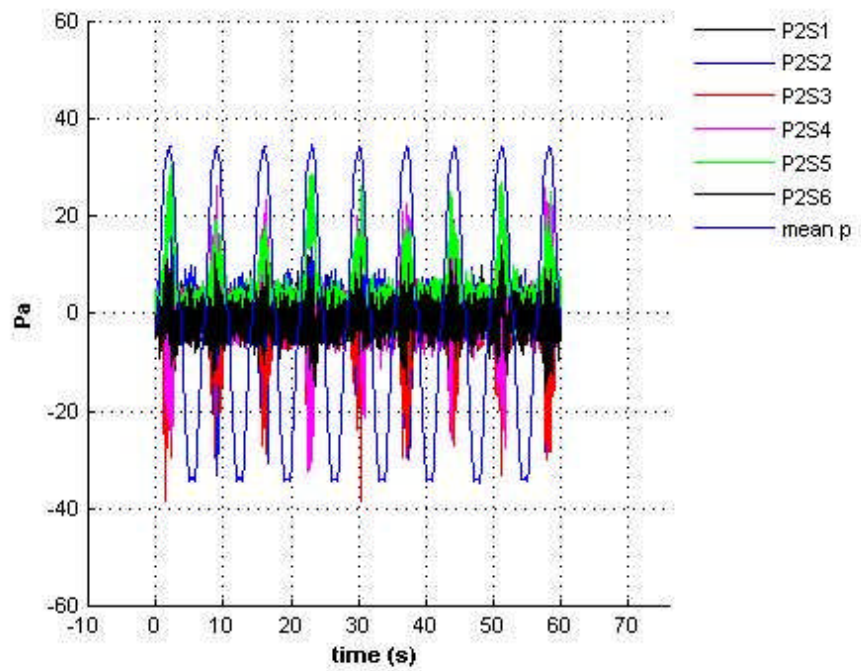
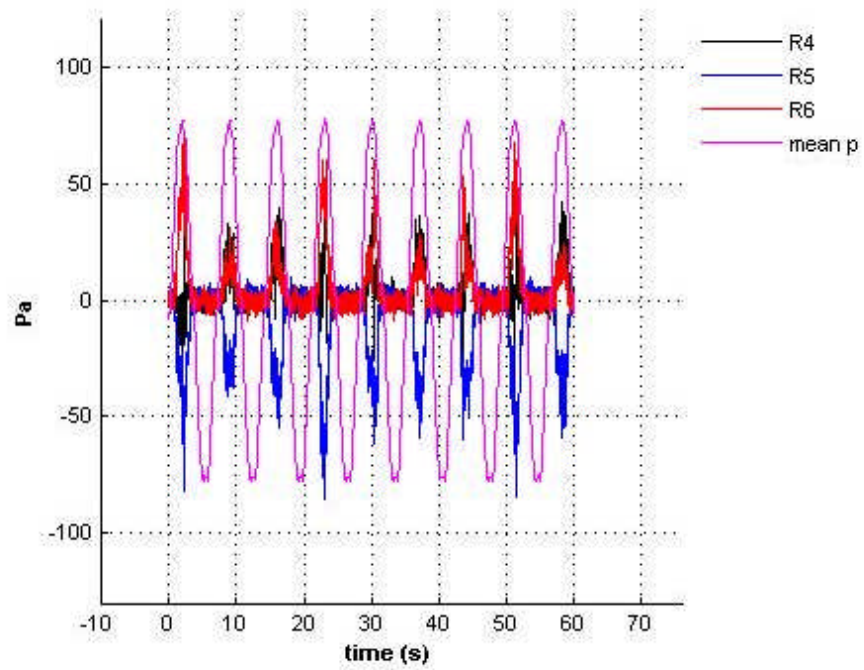


Figure 76 – Differences between total and static pressures and their averages for plane 2, data point 386

### 4.3.5 Transducer drift

The test procedures adopted attempted to strike a compromise between taking zeros on a sufficiently regular basis to minimise the impact of transducer drift on the data (which could easily be large given the low dynamic pressures involved), and running the rig for lengths of time which enabled reasonably steady conditions to be achieved.

The temperatures that were recorded when the zero data points were taken over a 3 hour test are shown in Figure 77. The plot shows how the temperatures throughout the rig rose with time whilst it was running, and fell as soon as the rig was stopped. It should be noted that the initial apparent fall in temperature P2T1 was the result of fixing a poor connection which was causing the thermocouple to read too high at the start of the test.

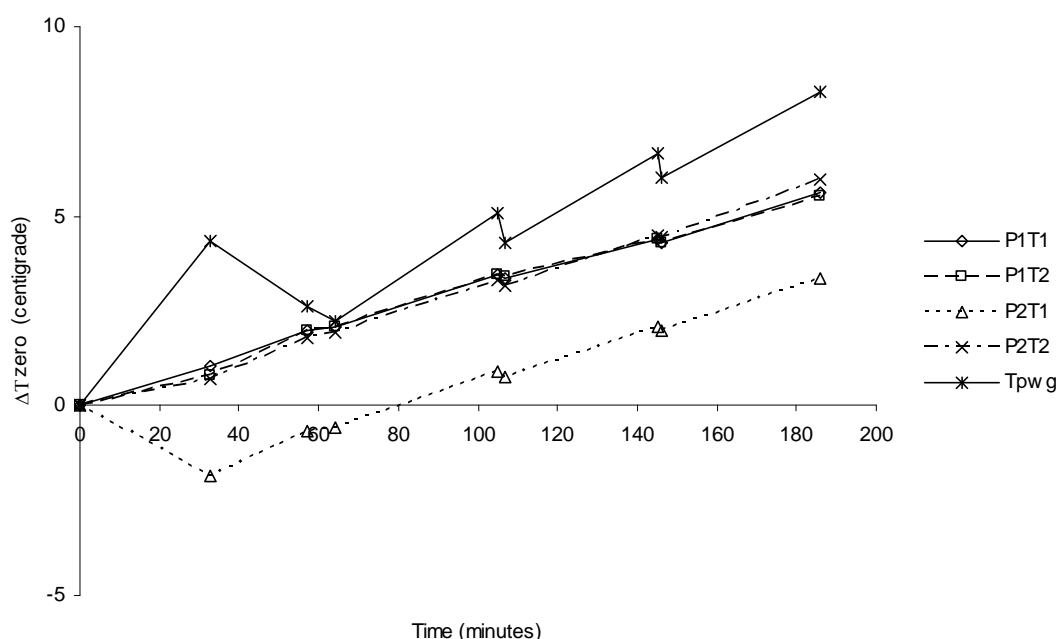


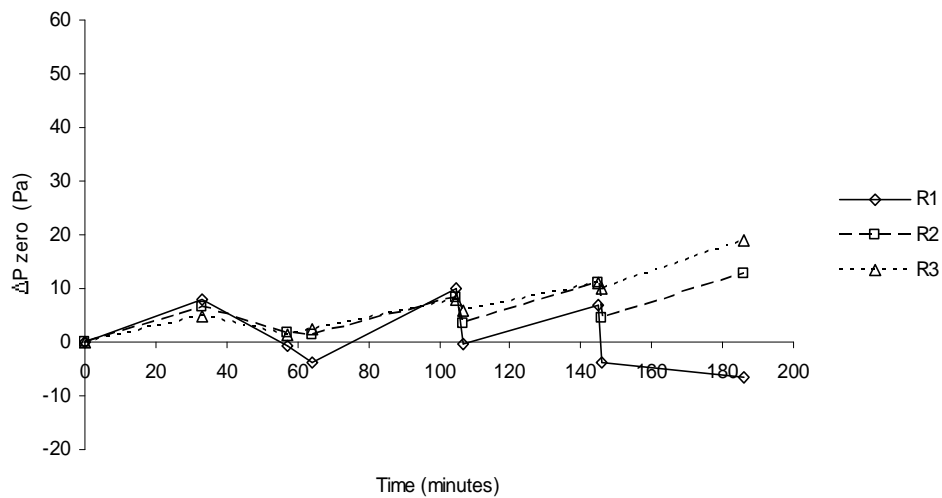
Figure 77 –Changes in rig temperatures during test

In addition to the temperature plot, plots were made of the changes in the zero readings of the pressure transducers as shown in Figure 78 (plane 1) and Figure 79 (plane 2). These plots showed how the pressure transducer zero readings reflected the changes in temperature: rising as the rig was run and falling as soon as the rig was stopped. All the data was plotted on the same scales, which immediately showed that:

1. there was up to 30 Pa drift in the transducer zeros throughout the test, with typical drifts in the range 5-20 Pa
2. there was a rapid drift as the once the rig was stopped
3. the drift of the transducers on the total pressure probes in plane 2 (Figure 79, R4, R5, R6), was significantly less than that of the other transducers.

If the drift was similar for all the transducers, then it would not have a great impact on the results as it is the *difference* between transducer readings that is measured. However, the drift in the plane 2 total pressure measurements was significantly less than the others by 5-15 Pa, which represented a sizeable proportion of the required measurement. Uncorrected this would lead to an increasing bias error in the plane 2 dynamic pressure measurement with time. This would mean that quite reliable measurements of dynamic pressure would be expected from instrumentation plane 1, but the dynamic pressure measurements from plane 2 would suffer from an increasing bias error with time. The plane 2 static data in Figure 79 has a bad data point for the P2S1 transducer, which demonstrates the need to have a significant number of measurements in order to minimise the effect of such points by averaging.

Change in zero reading plane 1 Rotadata probes 1-3



Change in zero reading with time plane 1 statics

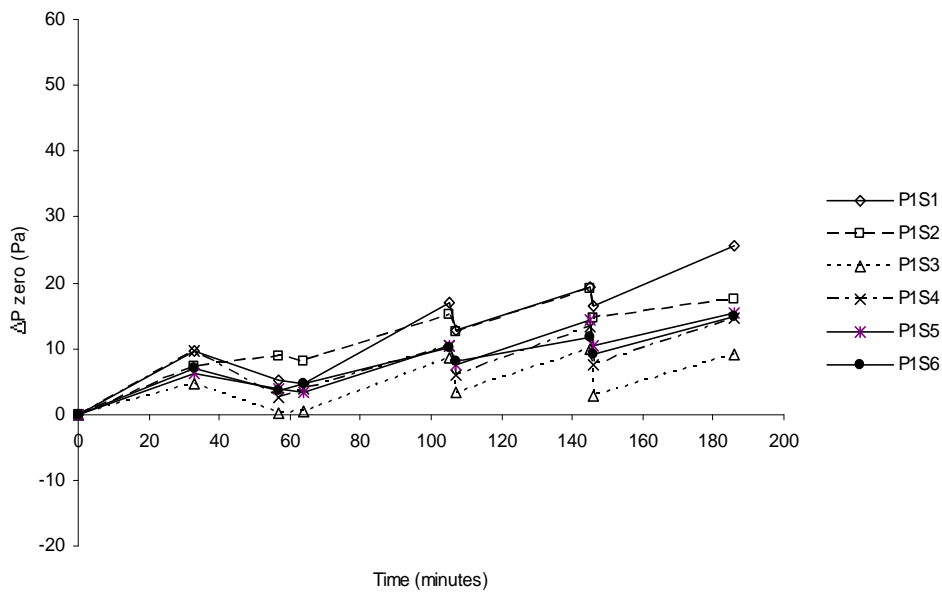
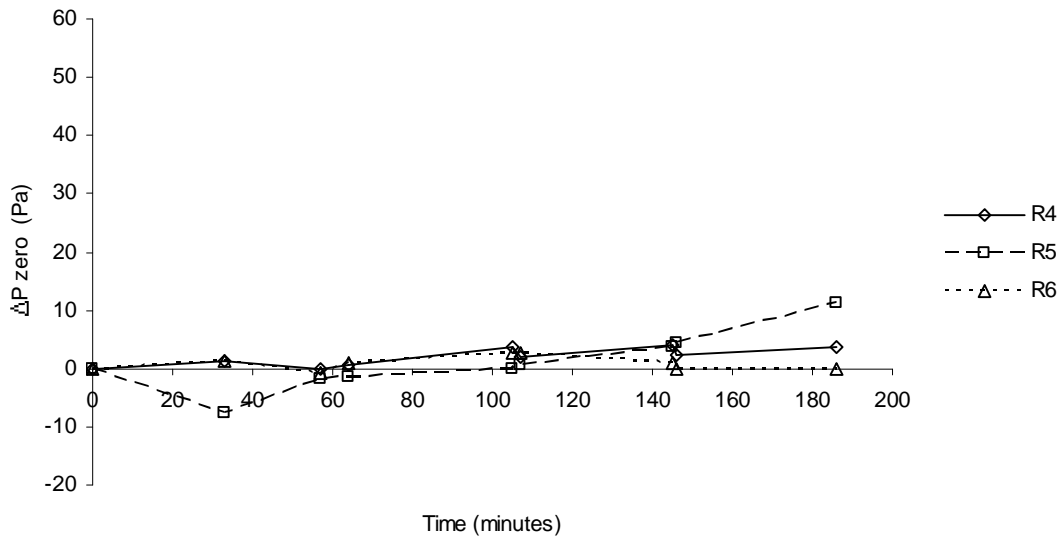


Figure 78 – Changes in plane 1 pressure transducer zero readings

Change in zero reading plane 2 Rotadata probes 4-6



Change in zero reading with time plane 2 statics

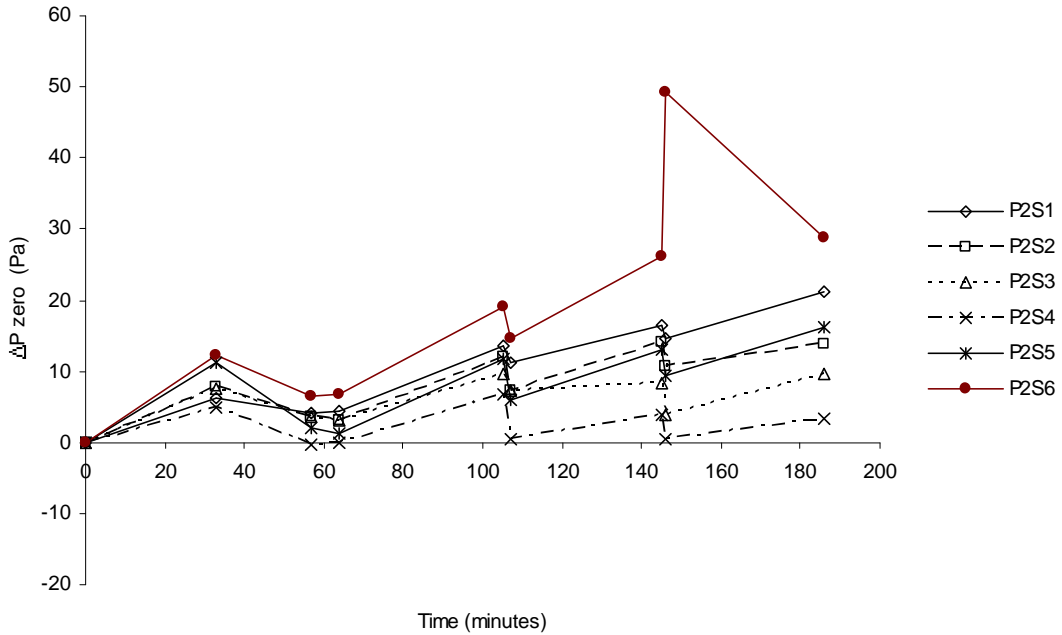


Figure 79 – Change in plane 2 pressure transducer readings

### 4.3.6 Impact of Transducer Drift

In order to determine the efficiency of the test turbine, it is necessary to firstly determine the volumetric flowrate. If the volumetric flowrate is determined from the instrumentation plane measurements, then there are two simple checks which can be made to establish that the calculations are sensible. The first is that the maximum instantaneous flowrate, or the integrated flow cannot be greater than the rate of change of volume or total change in volume of the PWG. The second is that the integrated mass flows through the 2 instrumentation planes should be the same, i.e. the outflow measured through plane 1 should be the same as the inflow measured through plane 2.

The impact of transducer drift on the results is illustrated in Figure 80 , which shows the averaged cyclic dynamic pressure variations recorded in the 2 instrumentation planes, for 2 data points for the same input wave, but taken 15 minutes apart. The data has been processed using a zero (data point 387) taken 8 minutes after data point 384. The input wave had a nominal rms flowrate of  $1.77 \text{ m}^3/\text{s}$ , and a period of 7 seconds.

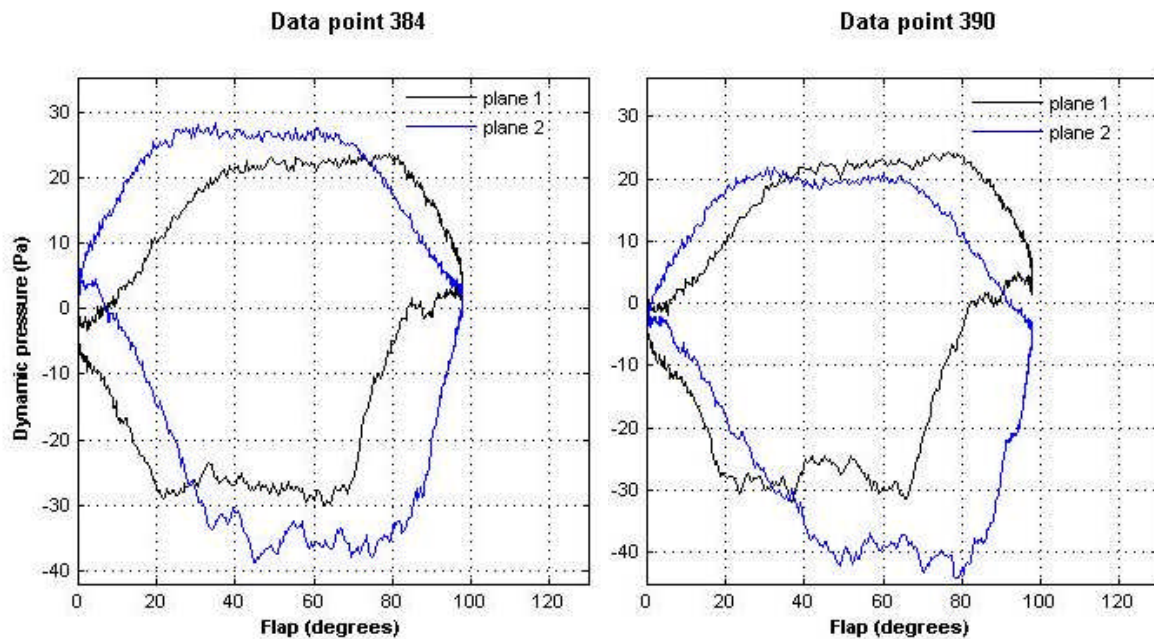


Figure 80 – Effect of pressure transducer temperature drift, data points 384 & 390

For the purposes of evaluating the mass flowrates/mass flows passing through the instrumentation planes it is only the positive values of dynamic pressure which are of interest. From Figure 80 it is immediately evident that there is a considerable difference in the positive areas under the curves for the plane 2 data at the 2 datapoints due to the drifts between the 2 points and the zero condition. This was confirmed by numerical integration using an assumed instrumentation plane discharge

coefficients of 1.0, as shown in Table 31 For comparison the ideal mass of air displaced by the movement of the flap (based on the temperature reading from the PWG) is also included.

Parameter	dp384	dp390	Difference (384-390) (%)
Total mass flow (flap) (kg)	7.092	7.081	0.15
Total mass flow plane 1 (kg)	6.515	7.527	15.5
Total mass flow plane 2 (kg)	8.208	5.245	36.1
Continuity error (%)	26	30.3	-

*Table 31 – Calculated mass flows*

The data in Table 31 showed large differences in the integrated flows and hence continuity. It also showed that whilst the greater variations were in the plane 2 calculations, there were also significant differences in the plane 1 calculations, and that the plane 1 calculation for datapoint 390 was not feasible. It was apparent that a process was required that enabled the transducer drifts to be removed. However, Figure 80 showed that at this flow condition the greatest positive dynamic pressure was only about 20 Pa, and that a 1-2 Pa difference in the level of the plane 1 dynamic pressures led to a 15% difference in integrated mass flow. It was thus evident that to have continuity maintained to within 5%, say, then the bias error in the dynamic pressure levels between the 2 planes had to be reduced to around 1Pa or better. It was decided that it was unlikely that such requirement could be achieved by attempting to derive and apply a calibration to the data. The alternative was to derive and apply a set of rules based upon what was physically happening to align the data.

The rules derived determine offsets to be applied to the data to ensure that when the flap reaches the ends of its movement the flowrate in the opposite direction is zero. In addition, after the offsets had been determined the data was smoothed by calculating a weighted average based on the 3 points either side of each point using the weights 0.125, 0.15, 0.15, 0.15, 0.15, 0.15, and 0.125. The results of applying this procedure to data points 384 and 390 are shown in Figure 81, and the re-calculated mass flows are shown in Table 32.

Parameter	dp384	dp390	Difference (384-390) (%)
Total mass flow (flap) (kg)	7.092	7.081	0.15
Total mass flow plane 1 (kg)	6.943	6.961	0.26
Total mass flow plane 2 (kg)	7.357	6.613	10.1
Continuity error (%)	0.2	10.1	-

*Table 32 - Calculated mass flows for corrected data, data points 384 & 390*

It should be noted that adjusting the level of the data in either plane affects the mass flow calculated in the other, as there was a small lag between the movement of the flap and the flow in the instrumentation planes.

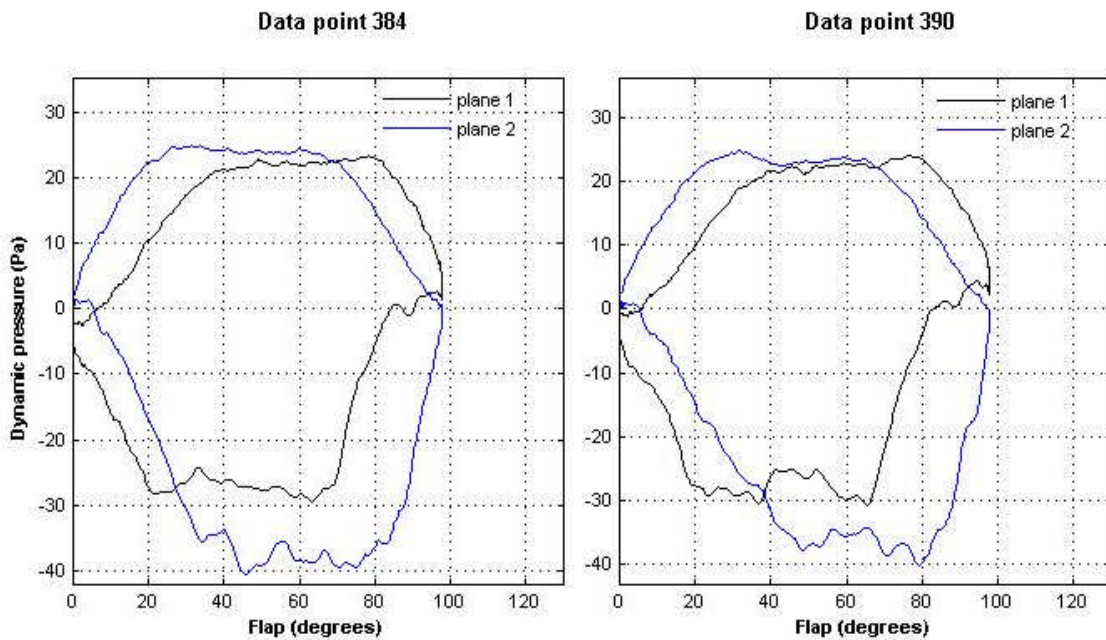


Figure 81 – Corrected dynamic pressure data for data points 384 and 390

Further experience led to a modification, whereby if the percentage difference in continuity between the two planes was greater than 7%, then the plane 2 offset was adjusted until the difference in continuity was less than 7%, it having been observed that the correction was generally an adjustment of the plane 2 data. The results of applying this method - which was used in the final processing of the data from the datum turbine - to data points 384 and 390 are shown in Table 33 and Figure 82.

Parameter	dp384	dp390	Difference (384-390) (%)
Total mass flow (flap) (kg)	7.092	7.081	0.15
Total mass flow plane 1 (kg)	6.701	6.976	4.1
Total mass flow plane 2 (kg)	6.667	6.895	3.4
Continuity error (%)	0.1	1.2	-

Table 33 – Calculated mass flows, final correction method, data points 384 and 390

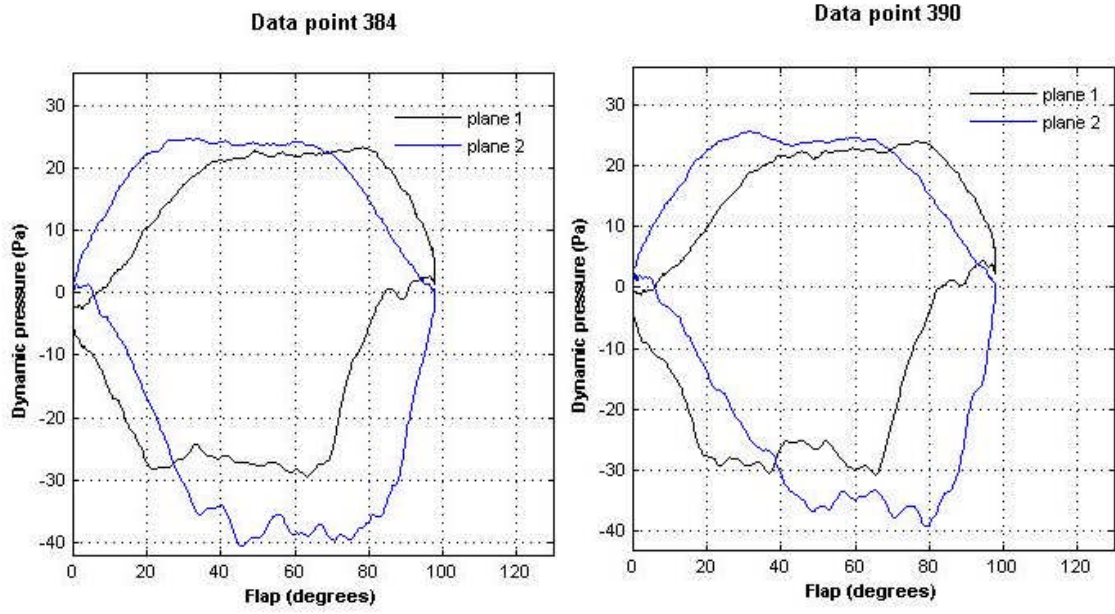


Figure 82 – Dynamic pressure data for data points 384 and 390 corrected by final method

## 4.4 Instrumentation Plane Discharge Coefficients

### 4.4.1 Procedure

Once a method had been established for correcting the data for temperature drift so that dynamic pressure data and hence flow velocity could be obtained with a reasonable degree of confidence, it was possible to collect data to determine the instrumentation plane discharge coefficients at the maximum flowrates associated with given input profiles.

The discharge coefficients for the 2 instrumentation planes were found by traversing the pitot probes radially across the instrumentation planes. The rig configuration was with the turbine installed. In order to obtain as accurate a calibration as possible the measurements made consisted of: 6 static pressure, 3 total pressure, and 2 temperature measurements in each instrumentation section. These numbers were determined by the number of transducer channels and Rotadata actuators available (which the pitot probes were mounted in).

The procedure after the first 2 traverses (see 4.4.2) was as follows: first a zero was taken with the flap stationary, then the desired wave was selected and the flap set in motion, and the probes were fully retracted. Then after 5 minutes running for the first traverse (or 2 minutes for subsequent traverses) the probes were moved in to the 99% height position (i.e. the position 99% of the way from the hub bullet to the casing) and the first data point taken. After this the probe was immediately moved inwards to the next radial position for the next data point. Each datapoint consisted of 1 minute of data taken at 100Hz sample rate. Data was taken at the following 21 radial heights: 99, 98, 97, 95, 90, 85, 80, 75, 70, 60, 50, 40, 30, 25, 20, 15, 10, 5, 3, 2, and 1%. At the completion of each traverse the rig was stopped and a zero taken.

### 4.4.2 Traverse data acquired

It was important to record data from a number of traverses to firstly establish whether consistent data could be acquired, and assuming it was, to then establish if the discharge coefficient calculated varied with either flowrate or wave period. A total of 10 traverses were made in all as detailed in Table 34. The results from the first two traverses showed the need for four additional radial points to be added, the time over which the data was taken to be increased from 30 seconds, to 1 minute to reduce the impact of 'noise' in the measurements, and that more accurate transducer calibrations were required. It was determined at this point that if the zero offset of a transducer was greater than  $\pm 50$  Pa then it would be re-calibrated. After an extensive transducer calibration exercise was carried out a further 8 traverses were made.

The data was processed by selecting a zero point for the traverse, and then finding the maximum positive dynamic pressure which occurred during the cycle in each plane. The data was checked to ensure that the maximum dynamic pressure occurred at a similar flap position at all radial points, and that spurious maximum values were not being found. Once the radial variation in maximum dynamic pressures had been found for each plane, the data was processed following the method described in Appendix H, to determine the coefficient of discharge (i.e. the ratio of the actual to the ideal

mass flowrate) at the maximum flowrate for the input profile in each plane. The results are shown in Table 35.

No.	Nominal $Q_{rms}$ ( $m^3/s$ )	Nominal Period (s)
1	2.3	7
2	2.3	7
3	1.77	7
4	2.0	7
5	2.3	7
6	1.5	7
7	2.3	7
8	2.65	7
9	2.3	5
10	2.3	9

*Table 34 – Nominal flowrates and periods of traverses*

Traverse	dps	$Q_{rms}$ ( $m^3/s$ )	T (s)	CD <sub>1</sub>	CD <sub>2</sub>
3	401-423	1.77	7	0.960	0.975
4	427-450	2.00	7	0.964	0.964
5	454-476	2.30	7	0.959	0.969
6	532-555	1.50	7	0.966	0.962
7	558-581	2.30	7	0.961	0.966
8	585-608	2.65	7	0.963	0.972
9	612-637	2.30	5	0.963	0.969
10	640-664	2.30	9	0.960	0.963

*Table 35 – Discharge coefficient values calculated from traverses*

A repeat traverse was taken for the  $Q_{rms} = 2.3 \text{ m}^3/s$ ,  $T=7 \text{ s}$  wave (Traverses 5 and 7), and the velocity profiles obtained in the 2 instrumentation planes are shown in Figure 83. The data were taken 8 days apart and show good repeatability in the profiles and CD values with differences of 0.002 and 0.003 in planes 1 and 2 respectively.

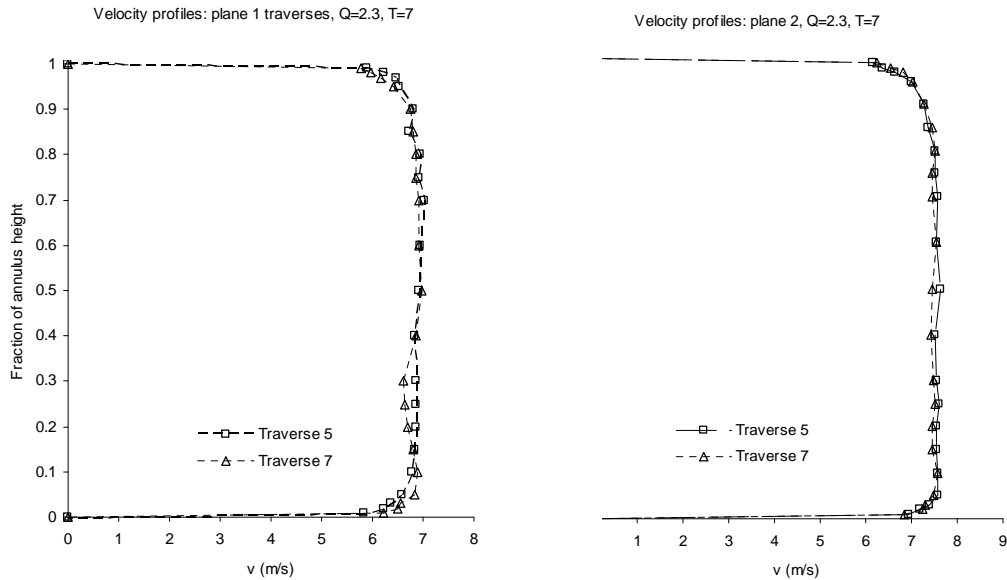


Figure 83 – Instrumentation section velocity profiles  $Q_{rms}=2.3 \text{ m}^3/\text{s}$

#### 4.4.3 Effect of flowrate on CD

The effect of changing the rms flowrate on the discharge coefficient was examined by comparing and plotting the data for traverses 3, 4, 5, 6, 7, 8.

The velocity profile data plotted in Figure 84 showed that the velocity levels increased with flow rate as expected, and that shapes of the velocity profiles in both planes remained similar. The derived values of discharge coefficient were all quite similar, and when plotted there was no observable trend that justified putting anything other than a best fit straight line through the data, particularly as it was expected that the scatter would increase as the rms flowrate was reduced. It was thus concluded that the discharge coefficients for the 2 instrumentation planes were constant for nominal rms flowrates of 1.5-2.65  $\text{m}^3/\text{s}$ .

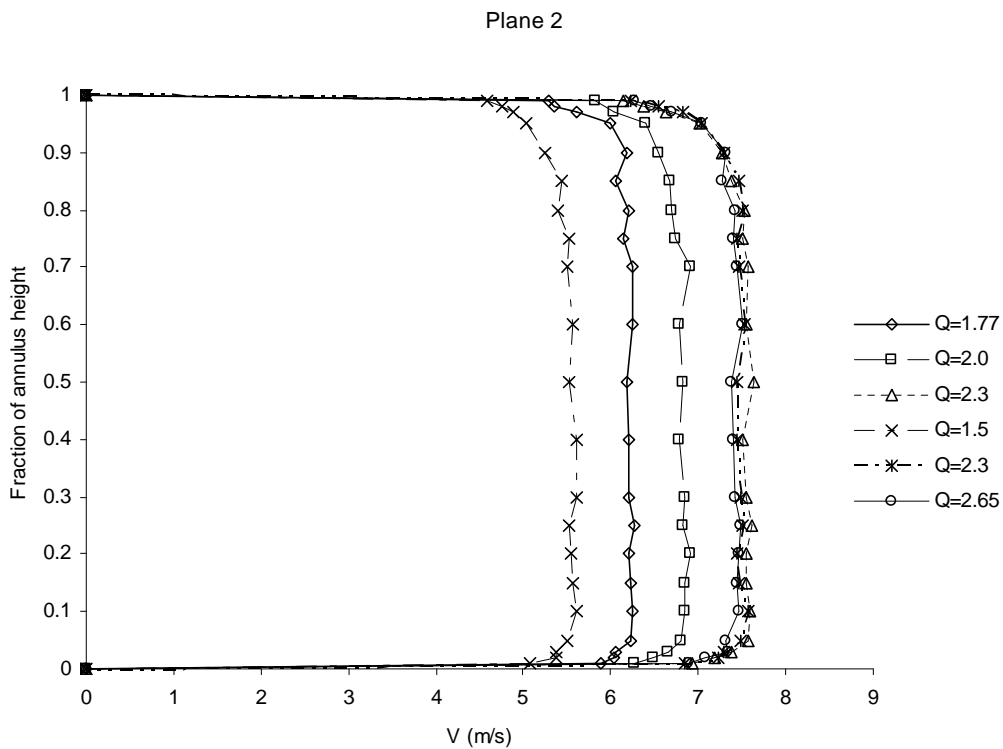
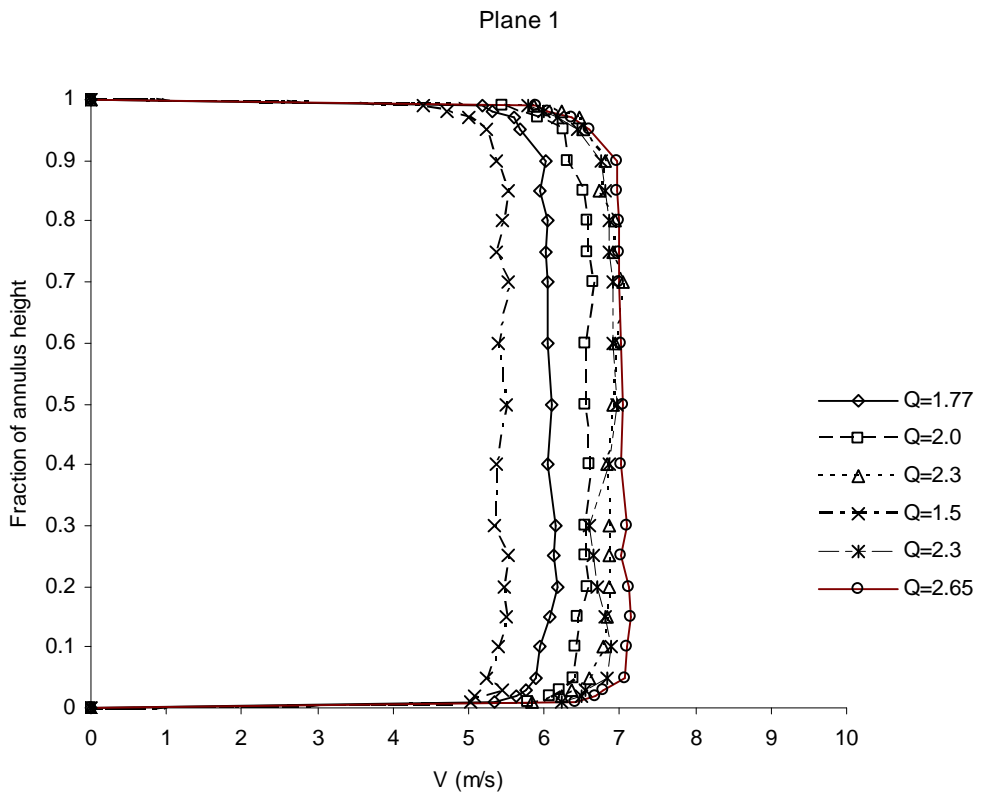


Figure 84 – Velocity profiles taken for cycles of  $Q_{rms}=1.77-2.65 m^3/s$

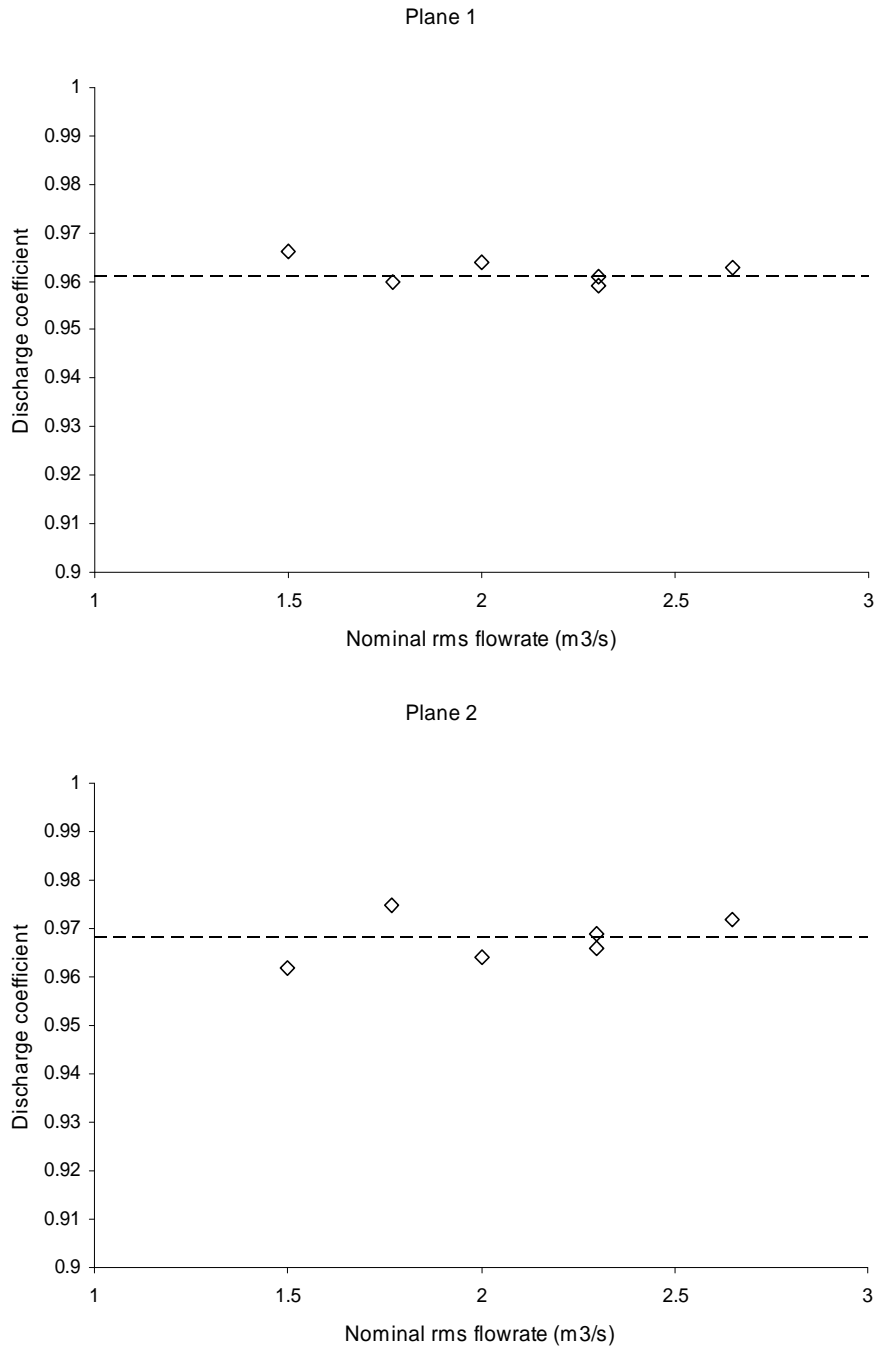
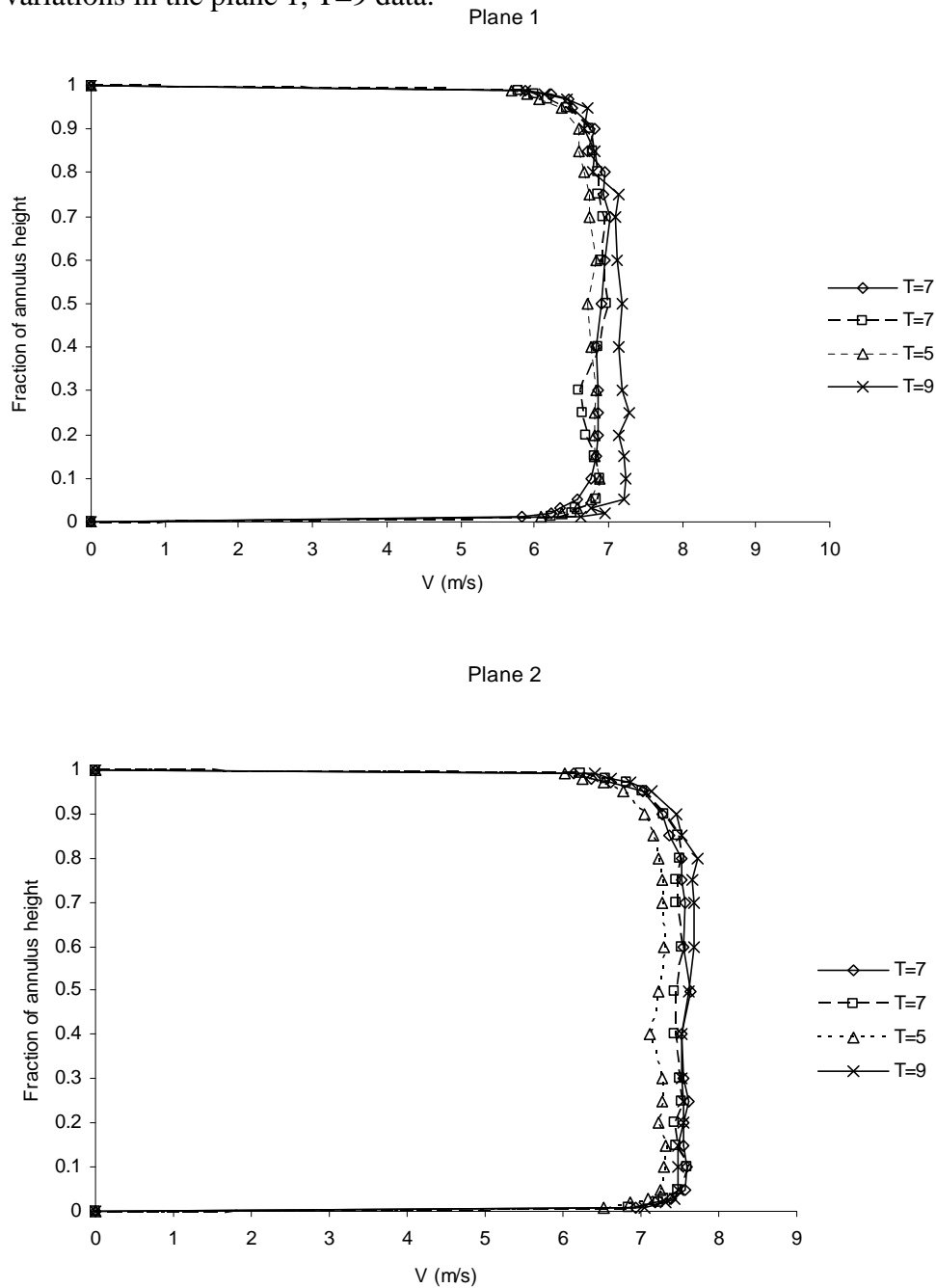


Figure 85 - Variation in derived discharge coefficient for rms flowrates of  $Q=1.5 - 2.65 \text{ m}^3/\text{s}$

#### 4.4.4 Effect of Period on CD

The effect of changing the period of the wave on the values of CD was examined by comparing and plotting the values for traverses 5, 7, 9, and 10. The velocity profile data for the 2 planes in Figure 86 generally showed good consistency despite the relatively large difference in cycle period from 5 to 9 seconds. Although the data for

plane 2 initially looked more consistent than that for plane 1, this was mainly because of the variations in the plane 1, T=9 data.



*Figure 86 – Velocity profiles for traverses taken at cycle periods of 5, 7, and 9 seconds*

The values of discharge coefficient calculated showed only very small differences and when plotted the differences were not judged sufficiently large - relative to the level of repeatability indicated by the traverse 5 and 7 data - to justify doing anything more than putting a best fit straight line through the points as shown in Figure 87. It was

thus concluded that the discharge coefficients for the 2 instrumentation planes were constant for cycle periods of 5 to 9 seconds.

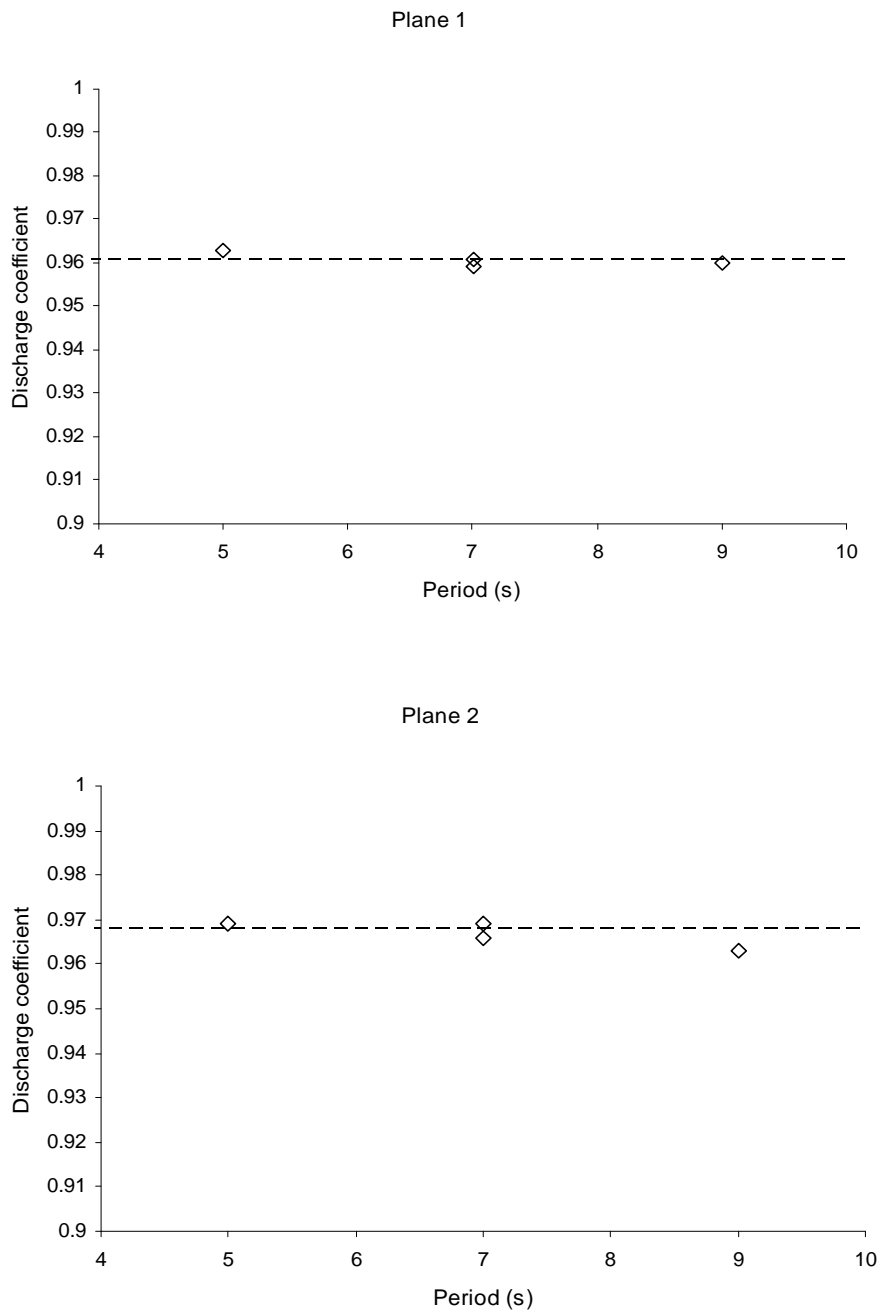


Figure 87 – Variation in discharge coefficients for traverses taken at cycle periods of 5, 7, and 9 seconds

#### 4.4.5 Final values of discharge coefficient

Analysis of the traverse data showed that the values of discharge coefficient for the two instrumentation planes were constant with both changes in cycle period and flowrate, for nominal rms flowrates of 1.5-2.65 m<sup>3</sup>/s and periods of 5-9 seconds. The

discharge coefficient data for the 2 planes was examined and the best fit values identified were: 0.961 for plane 1, and 0.968 for plane 2.

#### 4.4.6 Pitot probe position for measuring flowrate

In addition to the discharge coefficient for the 2 instrumentation planes, the total pressure probe has to be placed at the radial position where the maximum dynamic pressure will be measured in order to determine the mass/volumetric flowrate. The traverse data was examined to find these positions and they are shown in Table 36.

Traverse	Radial position of max q	
	Plane 1	Plane 2
3	0.2	0.65
4	0.7	0.2
5	0.7	0.25
6	0.25	0.1
7	0.5	0.1
8	0.15	0.25
9	0.1	0.15
10	0.1	0.8

*Table 36 – Radial positions at which maximum dynamic pressures were recorded*

The data did not reveal a constant radial position at which the peak dynamic pressure was recorded in either plane. However, analysis of the velocity profiles showed that they were very flat between 10% and 80% annulus height, except for a tendency for the dynamic pressure to fall slightly in the centre of the annulus. Overall, there was a bias for the peak values to occur in the lower 25% of the annulus, and the profiles were flattest in this region, therefore as it was impractical to change the probe positions with flow rate (and given the uncertainties probably incorrect), it was judged that a measurement of dynamic pressure at the 15% position in both planes should be used in conjunction with the discharge coefficient values to evaluate the volumetric/mass flowrate through the test rig.

#### 4.4.7 Mass/Volumetric Flowrate calibration

The analysis of the traverse data enabled a calibration to be derived for evaluating the mass/volumetric flowrate through the test rig which is shown in Table 37.

Plane	Discharge coefficient	Position of total probe (% from hub)
1	0.961	15%
2	0.968	15%

*Table 37 – Mass/volumetric flowrate calibration*

## **5. Design of Datum Turbine**

### **5.1 Turbine Design Point & Sizing**

#### **5.1.1 Objectives**

The objectives in the datum turbine sizing process were to:

1. Determine a rationale for selecting the design point for a turbine for use in an OWC power plant.
2. Define a test turbine that was approximately scaled in relation to that used in the LIMPET OWC facility.
3. To size the model turbine so that its design point was sensibly placed within the expected operating envelope of the test facility to achieve a useful range of turbine operating conditions.
4. To have pressure drop, axial flow velocity and torque data compatible with determining its efficiency to  $\pm 2-3\%$
5. Facilitate commissioning of the facility, i.e. there should be a good level of confidence in the performance predictions

The third point was critical to ensuring that sufficiently large transducer readings resulted at the design point that accurate measurements could be taken, whilst the range of useful test conditions that could be achieved was maximised. In addition, it was required that the blade Reynolds numbers achieved by the design would be  $\geq 2 \times 10^5$ , as defined in section 2.4.2.

The need to obtain good quality, accurate, data from the test rig was critical to being able to confidently comparing the measured performance with that predicted by the CFD analysis, and establishing a bench-mark for the CFD predictions and validating the design methodology and understanding of the characteristics of the turbine.

#### **5.1.2 Information used**

In order to scale the turbine with respect to LIMPET and pick a suitable design point, knowledge was required not only of the LIMPET facility dimensions, but also of the typical sea states and air flow rates associated with it. The basic dimensions of the LIMPET facility were given in (Queen's University Belfast, 2002). Information on the facility performance at various sea states was less readily available, but fortunately a number of spreadsheets were identified in the Marine Energy Challenge report (Webb et al, 2005), which appeared to contain information derived from LIMPET that was sufficient for the sizing exercise.

#### **5.1.3 Turbine Design Point**

Examination of the LIMPET OWC data showed that the most energetic wave condition occurred at  $H_s=3.5$ ,  $T_e=11.8$  and that the most frequent wave occurred at  $H_s=1.5$ ,  $T_e=9.5$  (Table 38). It was clearly desirable that the turbine achieved good efficiency at both these conditions, and so it was decided that the point  $H_s=2.5$ ,

$T_e=10.6$  between them should be taken as the full scale design point, i.e. the point at which it was desired the turbine achieved peak efficiency.

Hs v Te	5	6.2	7.3	8.4	9.5	10.6	11.8	12.9	14	15.1	16.2	17.4
0.5	220	1352	3877	8163	8367	6628	4454	2145	1281	519	131	132
1.5		5680	30303	76448	90992	87854	42340	29531	14991	5835	3534	1187
2.5			2551	33094	110398	138590	117548	78876	41642	16208	6545	
3.5					17083	88577	169764	123677	62783	31767	6414	
4.5						9762	50112	92001	83027	42010	10603	
5.5								15270	15504	15689		

Table 38– Sea state data Watts  $\times$  frequency for LIMPET

The most frequently occurring sea state point was of particular interest, as if the turbine characteristic was relatively flat selecting this lower wave condition might lead to greater overall efficiency, but this would depend on the turbine type used. There was insufficient information available, however, to undertake the trade-off study required to assess this at this point in the project. It is recommended that a study is carried out though to determine the possible benefit of designing the turbine to operate at the most frequently occurring wave condition.

### 5.1.4 Turbine sizing

Although the intention was to benchmark against the LIMPET turbine, its design point and true operating characteristics were not known. Therefore, it was assumed that the turbine used was a scaled version of the Setoguchi baseline design. At the design point this turbine would have a flow ratio of  $\phi = 0.2$  for maximum efficiency. If the basic geometric characteristics of the scaled device were taken to be similar to the LIMPET turbine, i.e.: diameter 2.3m, design speed 1050 rpm, hub/tip ratio 0.62, 7 blades. Then at the design point,  $U_{mid} = 115$  m/s,  $V_a = 23$  m/s, the area of the annulus  $A_{annulus} = 3.27$  m<sup>2</sup>, and the volumetric flowrate would be 75 m<sup>3</sup>/s.

From the data available, the computed range of wave input powers to the LIMPET facility were calculated as shown in Table 39, using the equation for the power of an ideal wave (Shaw, 1982):

$$P = \frac{\rho g^2 H_s^2 T_e}{64 \pi}$$

Hs v Te	5	6.2	7.3	8.4	9.5	10.6	11.8	12.9	14	15.1	16.2	17.4
0.5	13	16	19	22	24	27	30	33	36	39	42	45
1.5		144	169	195	220	246	274	299	325	350	376	403
2.5			470	541	612	683	760	831	901	972	1043	
3.5					1199	1338	1489	1628	1767	1906	2045	
4.5						2211	2462	2691	2921	3150	3380	
5.5								4020	4363	4706		

Table 39 – Calculated input powers (kW) for LIMPET for wave height/period conditions

If it was assumed that the capture efficiency was 0.8, then the total input power at the design point would be ~540 kW. It was recognised that this was a rather crude approach, but given that the operational characteristics of an OWC facility depend on the coupling between the specific turbine and chamber, and the primary objective was to enable the test facility to be sensibly sized, it was judged to be sufficient.

Definition of the representative full scale design point flow condition enabled a scaling spreadsheet to be set up which could then be used to determine the size and operating conditions to be achieved by the model in the test facility. The primary requirements were that the model would operate at the desired value of Reynolds number, whilst having high enough axial flow velocities and output powers to enable sensibly accurate measurements to be made, whilst keeping total input power and flap movement requirements within the achievable ranges.

Whilst the initial scaling spreadsheet was based on assuming that a Wells turbine was used, another one was constructed for an impulse turbine, as the literature review (Herring and Banks, 2007b) had identified that the desired Reynolds numbers were more difficult to achieve for impulse designs.

It was apparent that from the outset that it would not be possible to develop a facility capable of simulating the full range of conditions indicated in Tables 38 and 39 above. Consideration of how the required size of the PWG, input power, pressures and velocities varied with turbine size suggested that it should be possible to size the facility and turbine to achieve conditions representative of those indicated by the shading in Table 40. It can be seen that the design point is in the lower range of power inputs. This was done for 2 reasons, which were: to mitigate the risk that only very limited data could be gathered above the design point if the rig failed to perform as expected; and to ensure accuracy of the measurements as far as possible. The latter was a real issue, as it was expected the lower limit of input condition would be determined by an inability to compute sensible flow rates from the pressure measurements, but good quality data needed to be assured around the design point. Although not considered explicitly at this point, the maximum wave period that could be simulated in the facility would be limited by its volume.

Hs v Te	5	6.2	7.3	8.4	9.5	10.6	11.8	12.9	14	15.1	16.2	17.4
0.5	13	16	19	22	24	27	30	33	36	39	42	45
1.5		144	169	195	220	246	274	299	325	350	376	403
2.5			470	541	612	683	760	831	901	972	1043	
3.5					1199	1338	1489	1628	1767	1906	2045	
4.5						2211	2462	2691	2921	3150	3380	
5.5								4020	4363	4706		

*Table 40 – Envelope of full scale conditions to be simulated in test facility*

The analysis led to the definition of a range of full scale input powers against which the datum turbine would be designed. From these a second spreadsheet was constructed which enabled the variation in powers, pressures and velocities that would be obtained in the test facility with respect to various assumptions of turbine scale and design point rotational speed to be examined via the non-dimensional performance

parameters. The scale turbine assumptions and final spreadsheet results are shown in Tables 41 and 42 and the process is described in Appendix C.

Parameter	Value
Scale	0.23
Diameter	0.6 m
Hub/tip ratio	0.82
RPM	850
Flow ratio	1.03

Table 41 – Model size, design point speed and flow ratio

Power input full scale	RPM full scale	U full scale	$\epsilon$	U <sub>model</sub> (m/s)	P input model (W)	V <sub>a</sub> model (m/s)	Q model (m <sup>3</sup> /s)	$\Delta p$ (Pa)	RPM model	$\psi$ ( $\eta=100\%$ )
1500000	401.9	46.5	4.604	34.3	20586.7	35.29	3.27	6297.3	1198.6	4.47
950000	345.1	39.9	4.604	29.4	13038.3	30.31	2.81	4644.2	1029.3	4.47
535000	285.0	33.0	4.604	24.3	7342.6	25.03	2.32	3167.1	850.0	4.47
400000	258.7	29.9	4.604	22.1	5489.8	22.72	2.10	2609.0	771.5	4.47
250000	221.2	25.6	4.604	18.9	3431.1	19.42	1.80	1907.2	659.6	4.47

Table 42 – Resulting variation in model and test facility parameters with full scale input power

Once an acceptable solution had been found the calculations were checked by constructing a final spreadsheet relating model and full scale values, which included an evaluation of the model rotor chord necessary to obtain the minimum desired Reynolds number; this is shown in Table 43.

If we wish to match Strouhal number in the testing, then:

$$T_{\text{model}} = \frac{V_{aFS}}{V_{a\text{ model}}} \cdot \frac{L_{\text{model}}}{L_{FS}} \cdot T_{FS}$$

or,

$$T_{\text{model}} = \frac{U_{\text{midFS}}}{U_{\text{mid model}}} \cdot \frac{L_{\text{model}}}{L_{FS}} \cdot T_{FS}$$

Then from Table 43:

$$T_{\text{model}} = 0.314 \times T_{FS}$$

Parameter	Model	Full Scale
Scale	1.00	4.33
Tip Radius (m)	0.3	1.3
Hub/tip	0.82	0.7
Rmid	0.273	1.105
Annulus area (m2)	0.093	2.708
Chord	0.117	0.508
Blade height (m)	0.054	0.390
m $\dot{m}$	2.78	110.37
Q	2.32	91.98
delta P	3167.0	5833.1
Power Input(W)	7347.4	536887.4
RPM	850.0	285.0
Umid	24.3	33.0
Va	25.0	34.0
$\phi$	1.03	1.03
$\varepsilon$	4.607	4.607
$\psi$	4.469	4.469
Re	2.00E+05	1.18E+06

*Table 43 – Comparison of scaled model and full size turbine parameters*

The limitation on achieving similarity in  $St$  is set by the maximum accelerations and velocities which the flap can attain in the PWG. If the minimum wave period that can be simulated is 5 seconds, then the shortest full scale wave period that could be correctly simulated with respect to  $St$  would be a wave of approximately 16 seconds.

## 5.2 Development of Datum Turbine design

### 5.2.1 CFD analyses of baseline designs

In order to demonstrate that a new turbine solution is better than its predecessors, there is a need to be able to perform accurate comparisons between experimental and theoretical results, and with the work of others. As it was not practical to re-create the experimental work of others in the HydroAir test rig, it was considered important to carry out some CFD analyses of designs produced by others and compare the results with those in the literature to establish a level of confidence in the ability of CFD simulations to capture the physics of the problem, and obtain an initial ‘calibration’ for the subsequent design process and set a bench mark against designs could be compared<sup>4</sup>. Two additional objectives were to produce turbine characteristics for use in ‘wave-to-wire’ simulations to compare the relative efficiencies of turbines when subject to a range of wave spectra that couldn’t be obtained in the test facility, and secondly, to define the conventions and analysis process used within the project to overcome the lack of consistency evident in the literature, and ensure that like was compared with like.

As the literature had revealed a large number of experimental studies on both Wells and impulse turbines conducted by Setoguchi and his team at Saga University. It was decided to select a baseline Wells and impulse turbine design from these for CFD analysis, which could be compared with the experimental results obtained by Setoguchi. Details of the chosen geometries chosen, and a summary of the results obtained from the simulations carried out by Banks (Banks, 2005b; Banks, 2005a) is given in Appendix I.

The results of the simulations were processed to obtain turbine characteristics in terms of the input power coefficient, torque coefficient and efficiency using the same non-dimensional groups as Setoguchi. From the subsequent comparison with Setoguchi’s experimental data it was concluded that CFD would be expected to over-predict the input power coefficient of Wells turbine, or an Impulse turbines with guide vanes, with the difference generally increasing with flow ratio, and being greater for the Wells turbine than the impulse turbine with guide vanes.

The CFD simulations were probably optimistic, in that the actual inlet flow conditions would be less perfect than in the simulations and the simulations did not include representation of a hub bullet, and the inlet sections in the CFD were probably not long enough to have fully developed boundary layers. Overall, it was concluded that there are likely to be significant errors in the efficiency characteristics derived from CFD simulations of either Wells turbines or Impulse turbines with fixed guide vanes due to the large flow separations which are present over a wide range of flow conditions for both turbines. However, in using CFD to develop new turbine designs it is necessary to assume firstly that if the CFD indicates a relative advantage in one

---

<sup>4</sup> The use of a meridional flow solver was not considered worthwhile, as the accuracy of these depends upon the blade row loss coefficients and 3-dimensional flow corrections incorporated, and appropriate data was not available for the guide vanes used by Setoguchi and for the highly-off design flow conditions of the downstream guide vane row in particular.

design over another then this is likely to be correct, although the magnitude may be wrong, and it was the case that the simulations for both turbines predicted the general trends although the magnitudes were wrong. The results produced indicated that the performance trends were likely to be more accurate for an impulse turbine with guide vanes than a Wells turbine. The other aspect of interest is whether the performance characteristics of the turbines are predicted sufficiently accurately to use in system simulations to assess the relative merits of designs and focus attention on detailed design. It was readily apparent that the predicted characteristics for the Wells turbine were not accurate enough in level or shape to feed into system simulations, it would be better to use experimental data from the literature, and only use CFD derived characteristics in the last resort. The characteristics for the impulse turbine had the correct shapes, and were wrong only in level, which was pessimistic, so use of the CFD performance characteristics in system simulations could be countenanced in the design process, on the basis that the trends should be correct and the predictions pessimistic. However, more comparisons are required to fully justify this. It is therefore concluded that CFD may be used to evaluate the relative merits of new turbine designs with reasonable confidence, but CFD characteristics for Wells turbines are too inaccurate for use in system performance calculations, and CFD characteristics for impulse turbines with fixed guide vanes should only be put into system performance calculations for the purpose of informing the design process. It is recommended that more comparisons between CFD predicted characteristics and experimental data from impulse turbines with fixed guide vanes are carried out.

### **5.2.2 Choice of datum turbine type**

The conclusion from the project literature review was that even complex fixed geometry Wells turbine configurations would not deliver the conversion efficiency required for HydroAir, and that a variable pitch solution and/or a different type of turbine was required (Herring, 2005).

The literature review revealed that the impulse turbine solution offered a number of advantages over the Wells turbine. Its drawback was that if fixed guide vanes were used these caused a large loss in performance. However, if these losses could be significantly reduced then the potential would exist to achieve a more favourable device than the Wells turbine. On this basis it was decided that the datum turbine that to be tested in the HydroAir test facility should be an impulse design that was predicted to have a performance comparable with the impulse turbine design tested by Setoguchi et al previously selected as the baseline impulse turbine design for CFD analysis.

### **5.2.3 Aerodynamic specification**

The method employed to determine the aerodynamic specification for the datum turbine followed a conventional mean line approach which was set up as a Matlab program 'Impulse' (see Appendix J). In doing this account was only taken of the inlet guide vanes and rotor rows, and the outlet guide vane row was neglected as in the ideal case the outflow would be essentially axial. The design pressure drop across the

turbine was initially taken as that from the spreadsheet, but recognising that this would have to be adjusted when the guide vanes were added.

In addition to determining the flow angles which needed to be obtained a relationship was required to determine the number of blades that should be used in each row. This was based on the ‘optimal’ space/ axial chord relationships derived by Zweifel:

$$\text{Nozzle space/chord ratio} = 1.25 \sin(2\alpha_2)$$

$$\text{Rotor space/chord ratio} = \frac{1}{2.5 \sin(2\beta_2)}$$

#### **5.2.4 Basic design of rotor and guide vane blades**

At the outset of the work there was no history of impulse turbine design in the group at Cranfield, and no pre-existing programs for developing the appropriate blade geometries. The Matlab ‘Impulse’ was therefore developed to include routines which would define the geometries of the guide vane and rotor blades, and output them as ‘.curve’ files which could be directly imported into the CFX CFD package for analysis.

The need to develop both a process and an understanding of the nature of the flow meant that the approach adopted was to begin with the simplest solution and refine it in the light of results obtained from CFD analyses. The first step was thus to carry out some analyses of single guide vane and rotor row geometry to develop the design process and verify that geometries had sensibly high performance predictions, before predictions were made for configurations with outlet guide vanes. In order to have a reference for the Cranfield results a characteristic was produced for the Setoguchi baseline impulse design without the outlet guide vane row. The results (Figure 88) showed an increase in predicted peak total-to-static efficiency from 32% to 54%. As expected the difference was greatest at the no OGV peak efficiency point, where the outlet flow from the rotor was virtually axial. The difference decreased at off-design conditions, particularly at high flow ratios as the downstream guide vane incidence to the rotor outlet flow actually reduced.

For simplicity, the initial blade geometries were created with sharp leading and trailing edges. The initial guide vanes were created by using circular arcs (Figure 89), but these were found to be inadequate for producing the desired degree of turning and pressure drop. The pitch-wise variation in static pressure at the guide vane outlet is clearly evident in Figure 89 (note: simulation was carried out for a single passage).

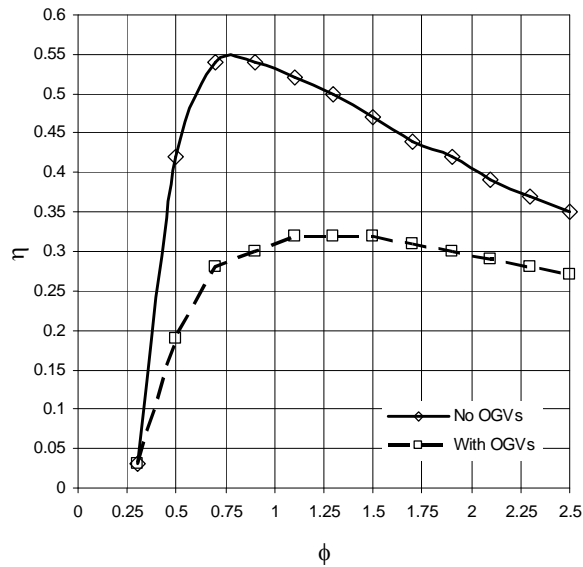


Figure 88 – Effect of adding OGV on performance of Setoguchi baseline design

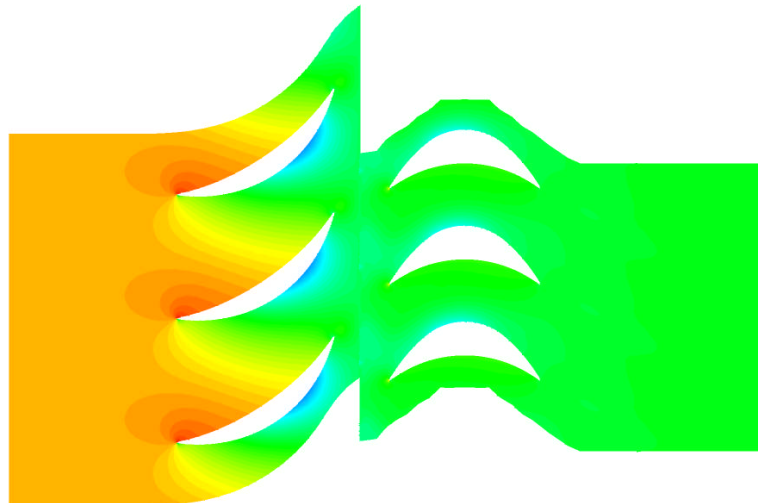
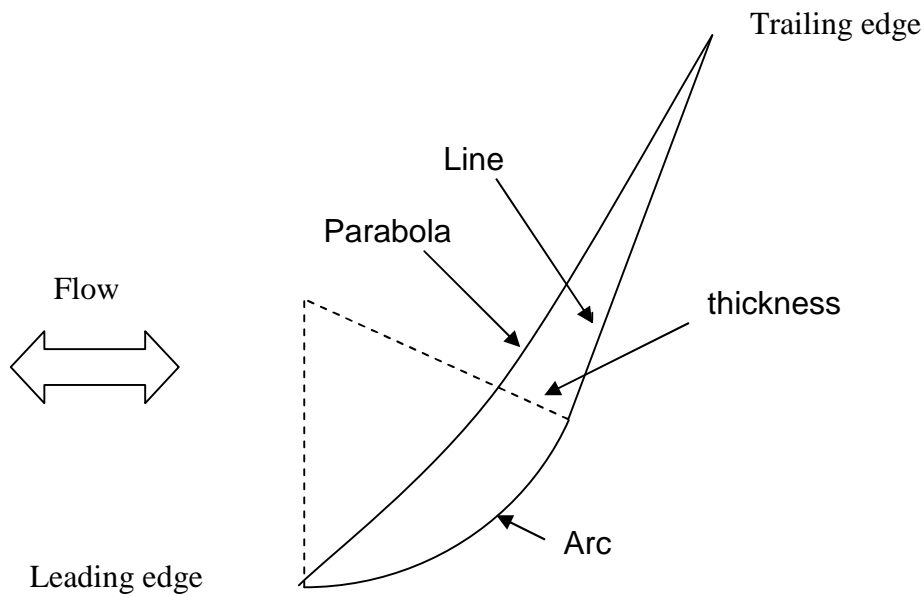


Figure 89 – Static pressure distribution around stage with circular arc guide vanes (Banks)

The circular arc guide vanes were replaced with what were referred to as ‘hockey sticks’. On these the suction surface was defined by a circular arc which was then extended by a straight line. The pressure surface was then specified by a parabolic fit through the suction surface leading and trailing edge points and a point of maximum thickness perpendicular to the end of the circular arc, as shown in Figure 90. For the sake of clarity in discussing the guide vane flows, it is helpful to define the end of the profile that is aligned with the axial flow direction as the ‘leading edge’, and the other

end as the trailing edge, and this convention will be used throughout the remainder of this thesis. This approach was taken rather than using standard sections due to the need to develop a fundamental understanding of the flows, develop a turbine geometry creation program, and because it was anticipated that the target performance levels ultimately sought would not be achieved by the use of standard blade sections.

This approach coupled with the development of the rotor geometry, led to a peak total-to-static efficiency of 68% (80% total-to-total) as shown in Figure 91, with the stage geometry shown in Figure 92. The improvement in the guide vane exit pressure distribution is clearly evident.



*Figure 90 – Geometry of 'Hockey stick' guide vane*

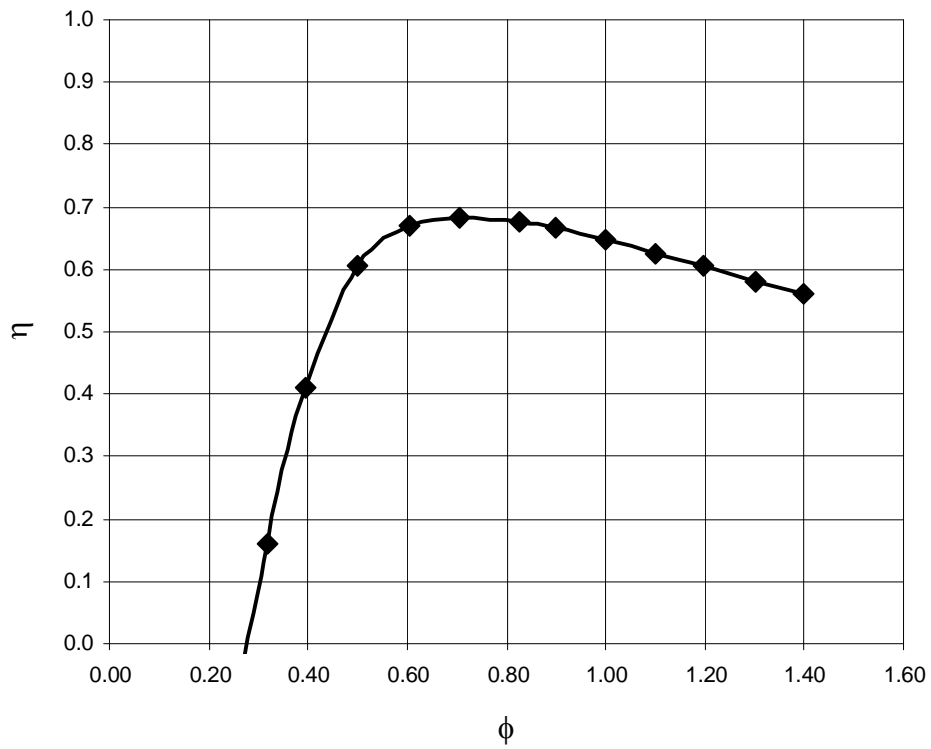


Figure 91 – Predicted characteristic for turbine with ‘Hockey stick’ guide vanes

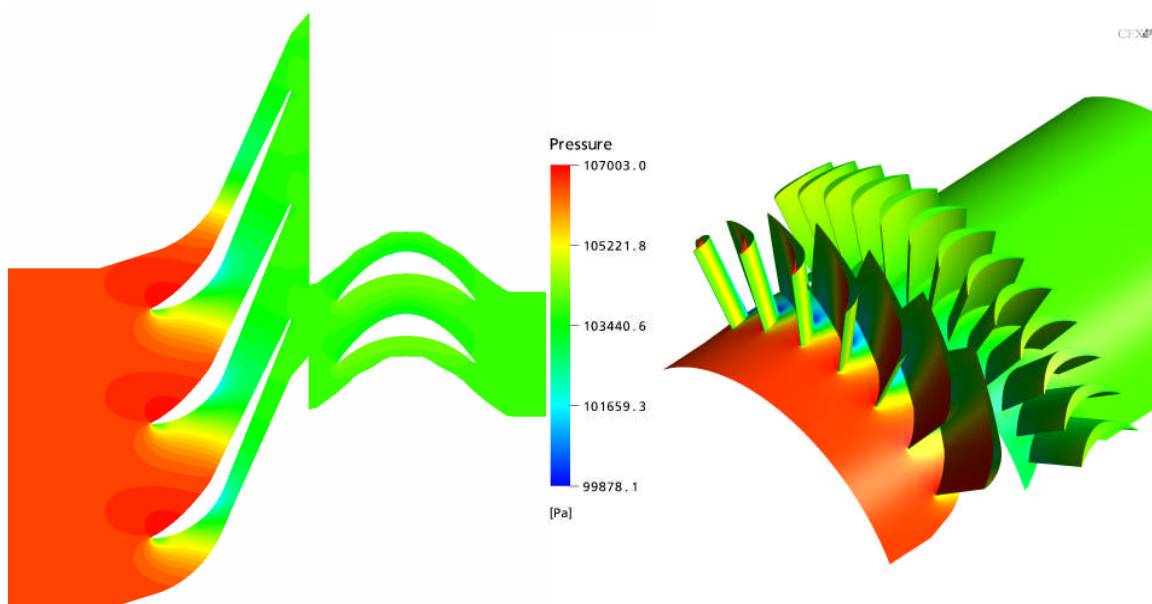
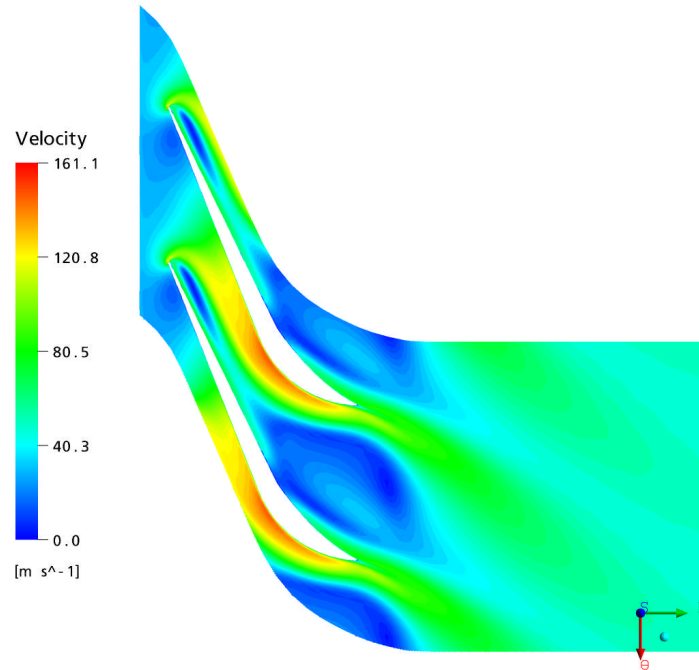


Figure 92 – Static pressure distribution through stage with ‘Hockey stick’ guide vane (Banks)

Once the above result had been obtained the geometry was modified to include the downstream guide vane, and the characteristic was re-calculated. This resulted in the pressure drop more than doubling, and the peak efficiency falling to less than 30%. The reason for this could be seen in a velocity plot for the OGV row (Figure 93)



*Figure 93 – Flow separation on Hockey stick guide vanes operating as OGVs (Banks)*

It was evident that although the hockey stick guide vane appeared better than the plate guide vanes used by Setoguchi et al in a uni-directional arrangement, it led to worse performance in the bi-directional arrangement. This amply demonstrated that an inlet guide vane design that produced a good turning effect and large pressure drop, was likely to be a very poor design for use in a bi-directional arrangement. The challenge was to develop a guide vane design that performed reasonably well as an inlet guide vane, whilst keeping the losses when it was an outlet guide vane down to a reasonable level.

Up to this point the geometries had been produced with sharp leading and trailing edges, which were clearly impractical, and so a routine was developed to crop the sharp edges back to a point where a specified radius could be produced. It was also evident that the design of the rotor could be improved. The developments in rotor blade profile to that used in the datum design are described in Appendix K for clarity, as obtaining an effective rotor design was a much simpler process than obtaining a good guide vane design.

## 5.2.5 Development of Geometry of Datum Turbine

Once the Matlab aerodynamic specification and geometry generation code had been developed to enable the geometry of the three blade rows to be produced with leading and trailing edge radii applied, it was possible to conduct a systematic analysis to define a geometry for the datum turbine which matched the specification in terms of

flow ratio and pressure drop and achieve a predicted efficiency at least comparable with the Setoguchi baseline design. As indicated in 5.2.4 the primary challenge was to determine a suitable guide vane geometry.

At the outset of the design process the idea with the greatest potential for significantly enhancing the performance of the fixed geometry impulse turbine was to apply boundary layer blowing to the down stream guide vanes to reduce/prevent separation. It was therefore decided that it should be ensured that this could be applied to the guide vanes if desired. This meant that the guide vane profiles had to be sufficiently thick that it was possible to duct air through them and form an outlet nozzle/slot. In consultation with PBL it was decided that the minimum thickness of trailing edge in which a blowing slot could realistically be installed for testing in the test facility was 4mm, and so this was designed into the guide vane at the outset.

The datum turbine design process started from the ‘Hockey stick’ geometry. In order to reduce the extent of the losses that occurred in the downstream guide vanes it was evident that the blockage they presented to axial flow needed to be reduced. It was also evident that the extent of the separation was enhanced by the diffusion that occurred in the guide vane passage. It therefore appeared that the circumferential length of the guide vane needed to be reduced to the minimum length that could produce a uniform inlet flow to the rotor, and that the rate of diffusion in the guide vane row should be reduced. Examination of the solutions produced for the airfoil geometry of Setoguchi et al showed that it had a region of separation at its leading edge (indicated as ‘A’ in Figure 94) and significant exit swirl, both of which could perhaps be reduced by careful design.

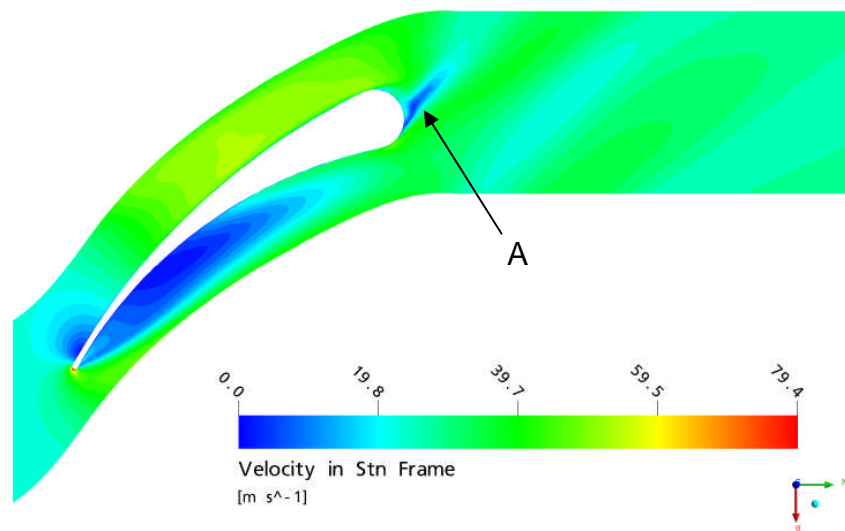
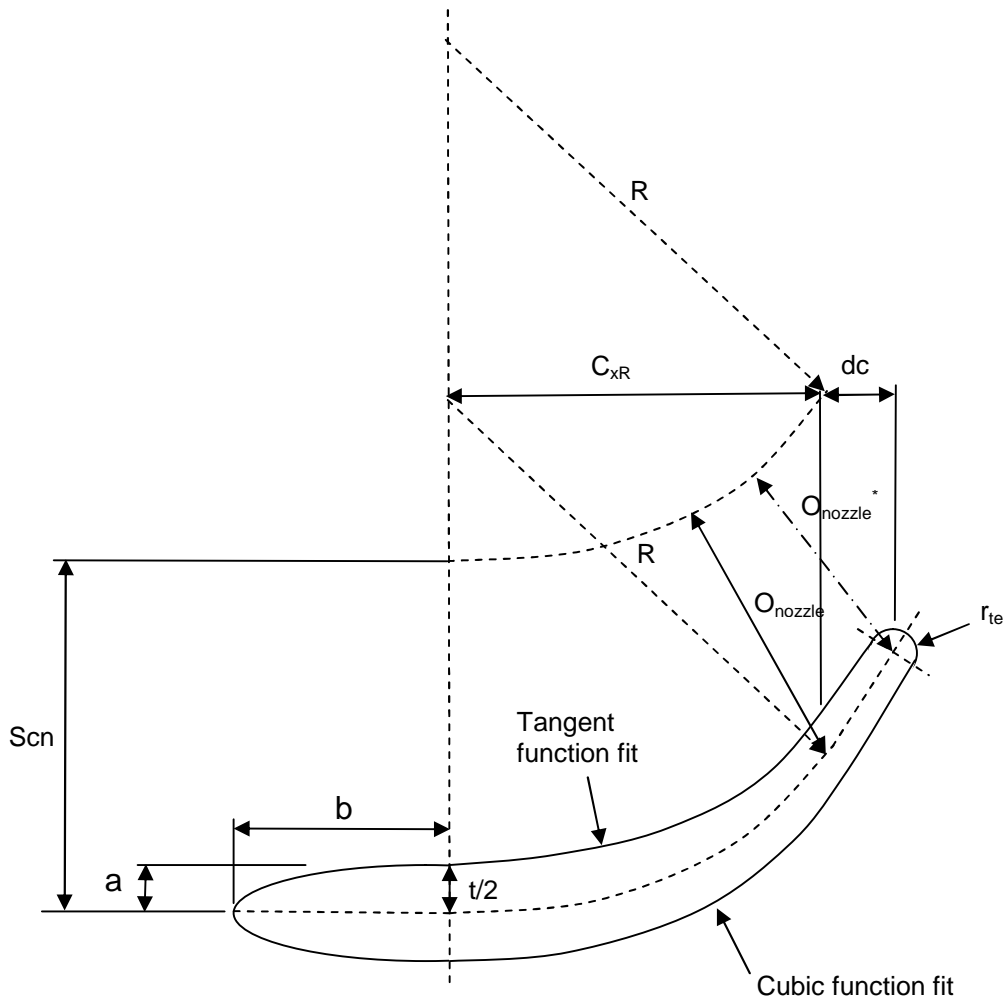


Figure 94 – Separation on airfoil guide vane

In order to enable a wide range of guide vane blade geometries to be evaluated in a reasonable time, and to discover the most beneficial design features, it was decided to carry out CFD evaluations in a pseudo 2-D way. This was done by creating a grid 2

cells thick around a thin slice through the blades at mid-span with free-slip boundary conditions on the end-wall surfaces. The initial results were relatively disappointing with peak efficiency below 35%, whereas the predicted efficiency of Setoguchi's airfoil impulse turbine was 39%. Nevertheless, the effects of a number of geometric features on performance were then assessed by creating a guide vane section consisting of 3 parts.



- a,b parameters to define leading edge ellipse
- dc trailing edge extension distance (fraction of distance  $C_{xR}$ )
- $O_{nozzle}$  distance used to determine maximum thickness of profile
- R radius of camberline arc
- $r_{te}$  radius applied to trailing edge
- Scn space between guide vanes
- t maximum thickness of section

Figure 95 - Geometric definition of guide vanes

When the guide vane section was created, the central section was defined first from the amount of turning required and the axial chord. Then a trailing edge extension was added, and then an elliptical nose was added. This process was implemented in a non-dimensional manner to simplify the coding and the final profile was then scaled to obtain a section with an axial chord that would give a design point Reynolds number of  $2 \times 10^5$  in the test facility. The final geometric definition of the guide vanes is shown in Figure 95.

Trailing edge extensions of  $dc = 0.1-0.2 \times C_{xR}$  were evaluated, and elliptical noses with semi axis ratios of  $b/a = 1-9$ , as well as asymmetric elliptical noses (i.e. nose was formed by using 2 ellipses of different  $b/a$  ratios). The progression in terms of efficiency predicted by the pseudo-2-D solutions is shown in Figure 96.

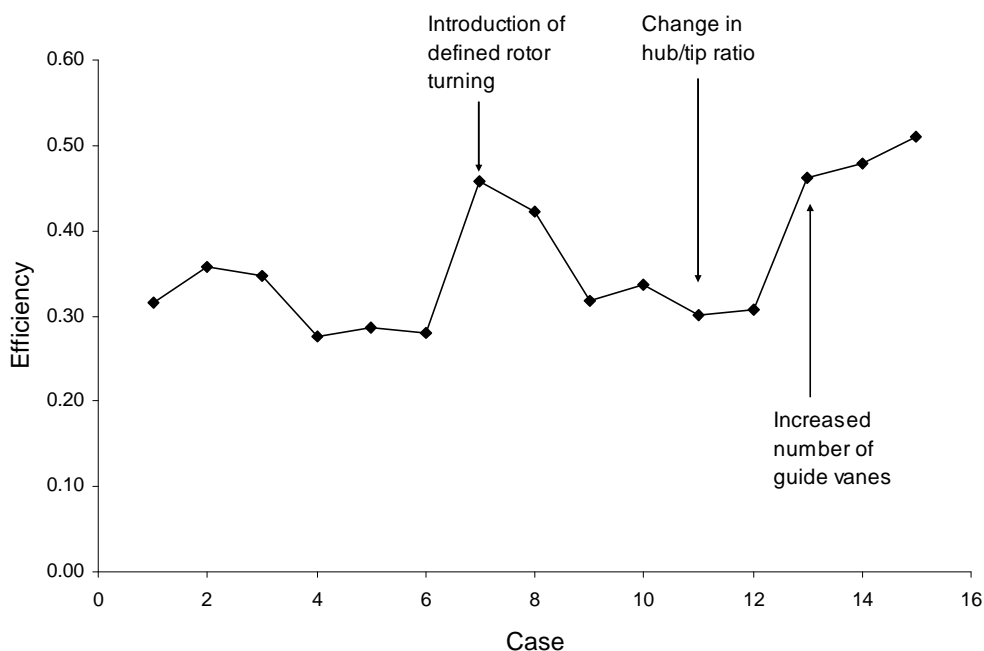


Figure 96 – Progression of efficiency results for pseudo-2-D simulations

A number of critical points are indicated on Figure 96 which had a greater impact on the results than the modest geometric changes that were made. The first thing was that it was found that if the rotor turning angle was increased by a modest amount above that determined by the mean line calculation then the performance improved significantly. This was attributed to the exit flow being over-turned which actually reduced its incidence onto the downstream guide vanes, and so reduced losses.

The second highlighted feature occurred when it was decided to change the design flow ratio from 0.8 to 1.0, which was again expected to improve performance by reducing flow incidence onto the downstream guide vanes. The knock-on effect of this was that to accommodate the change in design flowrate, and still achieve a sufficiently high design point blade Reynolds numbers, it became necessary to

increase the hub/tip ratio from 0.7 to 0.82. At this point the basic design of the blading was becoming fairly determined, with only small changes being made to smooth out undesirable features in the geometry and achieve the required power input and pressure drop characteristics. The final significant factor was that examination of the predicted flowfields showed poor matching between the rotor and its inlet flow which suggested that there were too few inlet guide vanes. The number of guide vanes was therefore increased from the number calculated using Zweifel's correlation (from 24 to 28) and consequent improvements in matching and performance were seen.

It had been expected that the 2-D simulations would predict efficiencies a few percent higher than full 3-D simulations, but that the performance differences would be reasonably consistent. This proved not to be the case. When 2-D and 3-D results were compared for 2 reasonably similar blade designs a difference of more than 10% was seen. Such a difference was thought to be too great to confidently infer the likely 3-D performance from a 2-D simulation. It can be seen from Figure 96 that the final predicted efficiency was 51%, which did not appear credible, given the rather small changes that were apparently required to go from a 30% design to a 50% design.

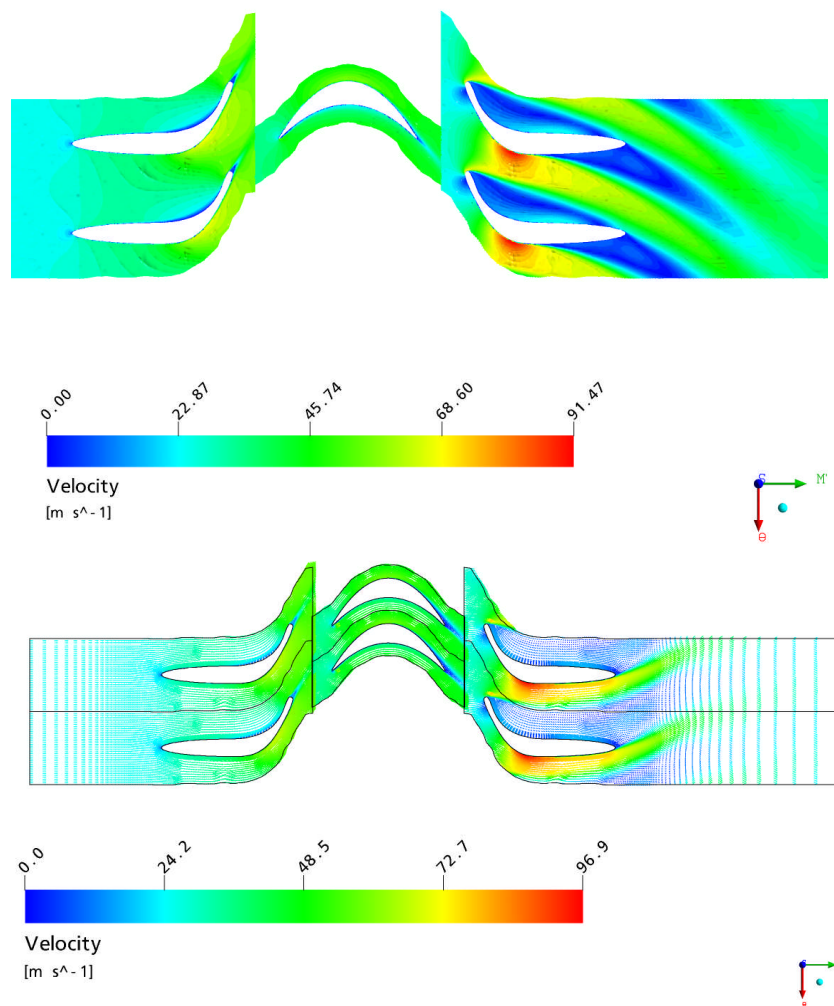


Figure 97 – Two types of pseudo-2-dimensional solution

One factor in accounting for the differences in the results was the lack of any representation of the end wall boundary layers and rotor tip flow and associated 3-dimensional effects. Even so, the differences observed suggested that perhaps there was another factor. As a first step in investigating the differences a second independent calculation was carried out for the final geometry. This second calculation also resulted in a predicted efficiency of 51%, but the flow pattern on the downstream guide vanes was quite different as shown in Figure 97. This was interpreted as an indication that there was probably some fundamental unsteadiness in the solution. This would not be surprising given the large region of separated flow that the problem contained.

The next step was to carry out a 3-D simulation of the geometry. This yielded a predicted efficiency of 41%, suggesting that there were significant viscous and 3-D flow features that were not being captured by the pseudo 2-D simulation. The efficiency of 41% was marginally greater than the peak efficiency predictions obtained for the Setoguchi baseline and airfoil geometries, and so a characteristic was produced (Figure 98).

Examination of the 3-D solution for the final design showed that, as might be expected given the high hub/tip ratio, the flow was highly 3-D. It was seen that the strength and magnitude of the separation over the downstream guide vane increased quite markedly in going from hub to tip. This appeared to be the result of the spanwise change in  $Va/U$  from 0.94 at the hub to 1.14 at the tip. This suggested that relatively modest changes in  $Va/U$  could have a significant effect, and that spanwise changes to the blade design (i.e. a 3-D blade design) could also be beneficial. It has to be remembered that the hub/tip ratio used here is artificially high in order to enable the desired Reynolds numbers to be achieved. This will have a negative impact on performance and the literature review indicated that a hub/tip ratio of 0.6 is actually desirable.

It was concluded from the above results that:

1. Whilst pseudo 2-D CFD analyses can assist in identifying beneficial design features for the impulse turbine with inlet and outlet guide vanes problem, they provided a poor indication of the likely 3-D efficiency.
2. The high hub/tip ratio required for the datum turbine, coupled with the spanwise variation in local flow ratio led to highly 3-D flow around the outlet guide vanes.

Furthermore it is recommended that:

1. Further work is carried out to establish if the highly 3-D flow observed around the outlet guide vanes for the high hub/tip ratio case remains at more representative hub/tip ratios when spanwise changes in flow ratio are greater.

2. Further work is carried out to investigate whether the introduction of lean and sweep into the design of the guide vanes can reduce the 3-D flow effects and increase performance.
3. An analysis is carried out to determine the performance of the turbine when scaled to full size with a hub/tip ratio of 0.6.

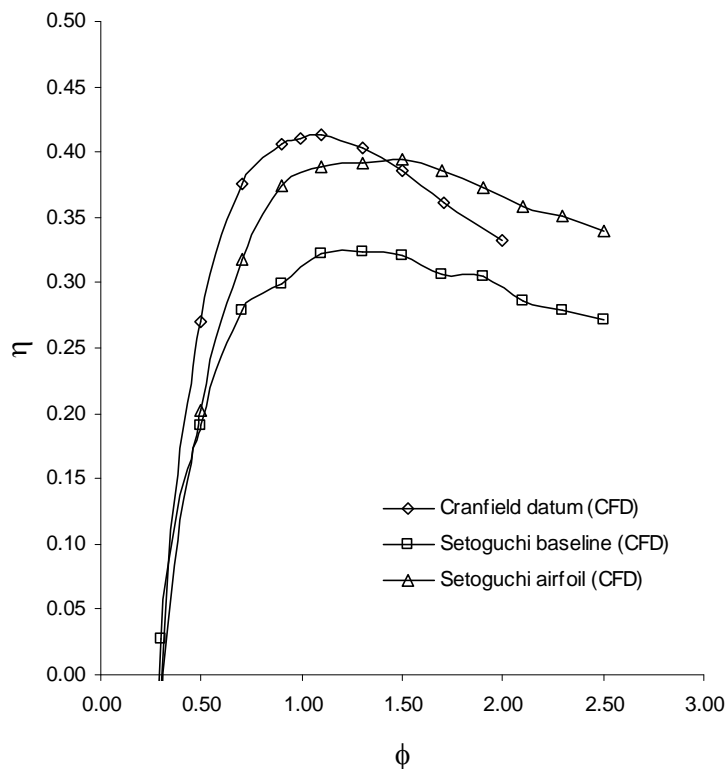


Figure 98 – Comparison of predicted efficiency of Cranfield datum turbine with geometries of Setoguchi et al.

### 5.2.6 Design Characteristics of HydroAir Datum Turbine

Although there were further changes to the guide vane geometry that could have been explored to improve performance, the project schedule required that a design was taken forward into manufacture. As a design had been found whose performance was predicted to be better than both the baseline and airfoil designs of Setoguchi et al, this fulfilled the design objective for the datum turbine and so it was decided that this design should be developed for manufacture. It should be noted, however, that whilst the distance  $O_{\text{nozzle}}$  was used to define the thickness of the blade section in the developmental process this approach is not expected to be the best. It is believed that performance can be significantly improved if the cross-sectional area of the passage can be kept virtually constant so that the diffusion occurs along the elliptical leading edge, this would be better achieved by using the distance  $O_{\text{nozzle}}^*$  indicated in Figure 95. It is recommended that effect of producing a guide vane geometry with a constant area passage and diffusion only around the leading edge is investigated.

The final geometry used was unchanged except that the rotor blade sections were stacked on a radial axis in the plane of the centre of the pressure surface, rather than the section centroid. This stacking axis was chosen because it followed conventional practice at PBL, and facilitated manufacture of the turbine blisk. Calculation showed that choice of the stacking axis made no significant difference to the predicted performance within the anticipated level of uncertainty. The guide vane sections were stacked on a radial axis at their leading edges, which again facilitated manufacture.

The final part of the design was to define 6 positions for the incorporation static pressure ports into an instrumented blade, which was to be produced by a rapid prototyping process. The ports were sited at the mid-radius of the blade at positions on the surface selected by analysing the outputs of the CFD analyses to determine positions where significant changes might be recorded. Although only a small number of ports could be used (due to the limited number of pressure transducers that would be available), it was hoped that these might provide some information to validate the CFD analyses and perhaps more importantly indicate whether there was any large scale unsteadiness in the flow field on timescales shorter than the period of flow oscillation. The geometry and axial positioning of the datum turbine blades is shown in Figure 99.

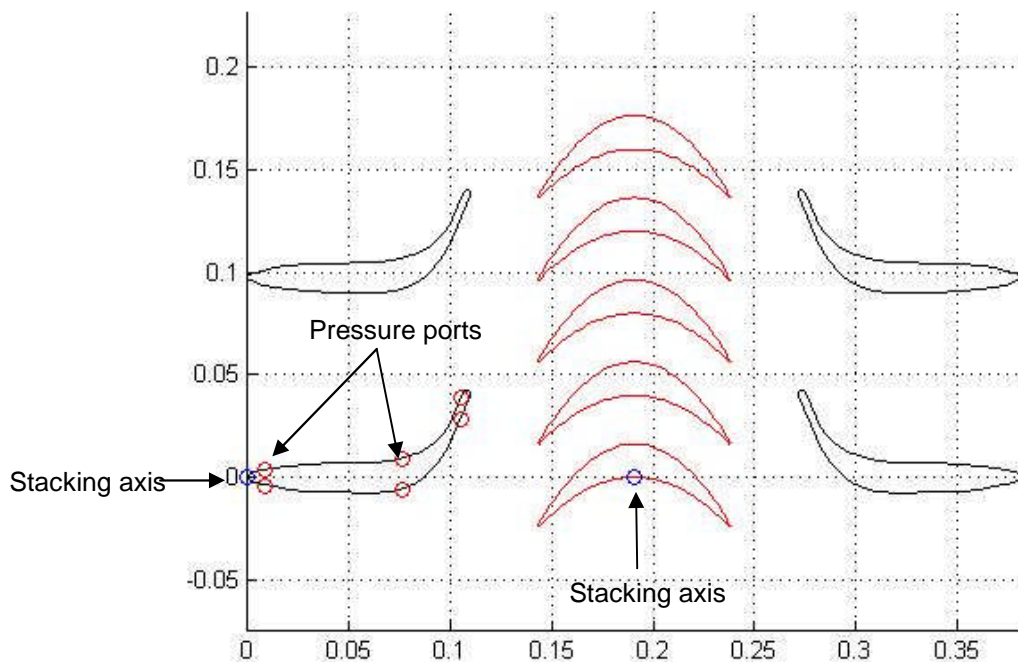


Figure 99 – Geometry of datum turbine (2-D view)

A comparison of the design point values derived in the scaling exercise and those obtained for the design point 3-D CFD prediction are given in Table 44. The table shows that the pressure drop obtained for the datum design was somewhat higher than

specified. This was introduced in moving from the pseudo-2-D simulations to the 3-D simulations. The design pressure drop was matched in the 2-D simulation, but increased when the 3-D analysis was carried out. This was not seen as a problem in terms of input power, and eased the measurement problems with regard to pressures and output power.

Parameter	Spreadsheet	3-D CFD
Flow rate (m <sup>3</sup> /s)	2.3	2.25
Pressure drop (Pa)	3170	3757
V <sub>a</sub> (m/s)	25.0	25.0
Output power (kW)	2.8	3.6

*Table 44 – Comparison of spreadsheet and CFD design point values*

The design characteristics obtained for the datum turbine are given in Table 45. The overall length calculated for the turbine, from the leading edge of the upstream guide vane, to trailing edge of the downstream guide vane, was 381.39 mm.

#### General

Parameter	Value
Casing diameter	0.6m
Hub/tip ratio	0.82
Axial gap between blade rows <sup>1</sup>	0.03305 m
Annulus height	54 mm
Annulus area	0.09263 m <sup>2</sup>
Design mass flow	2.76 kg/s

<sup>1</sup>The axial gap between the blade rows = 0.3 × (guide vane axial chord)

#### Guide Vanes

Parameter	Value
No. of guide vanes	28
Guide vane turning angle	67.18 deg
Axial chord	110.16 mm
Section t/c	12.56%
Design Re	2.15 × 10 <sup>5</sup>
Trailing edge thickness	4.12 mm
Stacking axis	Leading edge

### **Rotor**

Parameter	Value
RPM	850
No. of rotors	43
Relative inlet flow angle	70 deg
Axial chord	94.97 mm
Tip clearance	1 mm
Design Re	$2.37 \times 10^5$
I.e. & t.e. radii	0.52 mm
I.e. ellipse	8:1
Stacking axis	Centre of pressure surface

*Table 45 – Design Characteristics of HydroAir Datum turbine*

In comparison to the designs of Setoguchi et al, the datum turbine design had larger turning angles on both the guide vane and rotor: 67.18 and 70, as opposed to 60 and 60 respectively. In conventional terms this would mean that the datum turbine was designed to have a relatively higher stage loading coefficient and lower design flow ratio than the designs of Setoguchi et al.

## 6. Oscillating flow simulation program

### 6.1 Fundamental equation

The literature revealed that previous researchers developed simulation programs which used steady flow characteristic data to predict the performance of turbines under pseudo-sinusoidal or irregular flow conditions. Access to such a tool in the HydroAir project was very desirable – if not essential - in order to have both an expectation of what should be measured in the test facility and to carry out investigative analyses to understand the interaction and effects of changes in system components.

The simulation program developed by Setoguchi et al was a simple model which solved the equation of motion for an OWC, in which the system was driven by defined wave input. the basic equation being:

$$\frac{d}{dt} \left( \rho_s h A_c \frac{dh}{dt} \right) = [\rho_s g (H - h) - \Delta p] A_c$$

where  $H$  is the incident wave height,  $h$  is the wave height in air chamber,  $\rho_s$  is the density of sea water,  $A_c$  is the cross-sectional area of air chamber, and  $\Delta p$  the gauge pressure in air chamber. The basic model assumed that the flow was incompressible, although Thakker et al (Thakker et al, 2005) modified it to allow for compressibility.

Freeman developed a different approach for the HydroAir system simulation program. This considered what happened to the volume of gas which was contained within a piston with an outlet which leads to solution of the equation:

$$\frac{\partial p}{\partial t} = \frac{1}{V} \left[ \gamma p A_c \frac{\partial h}{\partial t} - a^2 \dot{m}_T \right]$$

where  $V$  is the volume of the gas in the piston at any time, and  $\dot{m}_T$  is the mass flowrate passing through the turbine which is in the outlet airflow. The derivation of the equation is given in Appendix L.

Both of the formulations presented above assume that the flow can be assumed to be quasi-steady, and so steady flow turbine performance characteristics can be used to predict the turbine behaviour under oscillating or irregular flow conditions.

### 6.2 Developed Program

The author developed an initial Matlab code written by Freeman for a device with a Wells turbine type characteristic, into the code ‘OWCsimgui2’ with graphical user interface which allowed the user to select a number of turbine characteristics and input ‘wave’ types. However, the code was primarily developed to enable simulations

of the performance of a test turbine in the test facility to be carried out. The option was put into the program to either determine the efficiency of a turbine operating with a given input wave at one specified rpm, or to produce a characteristic by calculating its efficiency for a range of different rpms. To this end the PWG control parameter program ‘profile8’ (Appendix F) was modified to produce a suitable output file representing the test flap movements for any specified test condition which could be used to drive the simulation program. Some of the plots that are produced from the program for a simulation of the datum turbine running at 850 rpm are shown in Figure 100 . The effect of the trapezoidal profile on flow rate is clearly evident. The simulation shown and those referred to the analysis of the datum turbine data were conducted allowing for the additional volume of the duct which is not swept by the flap.

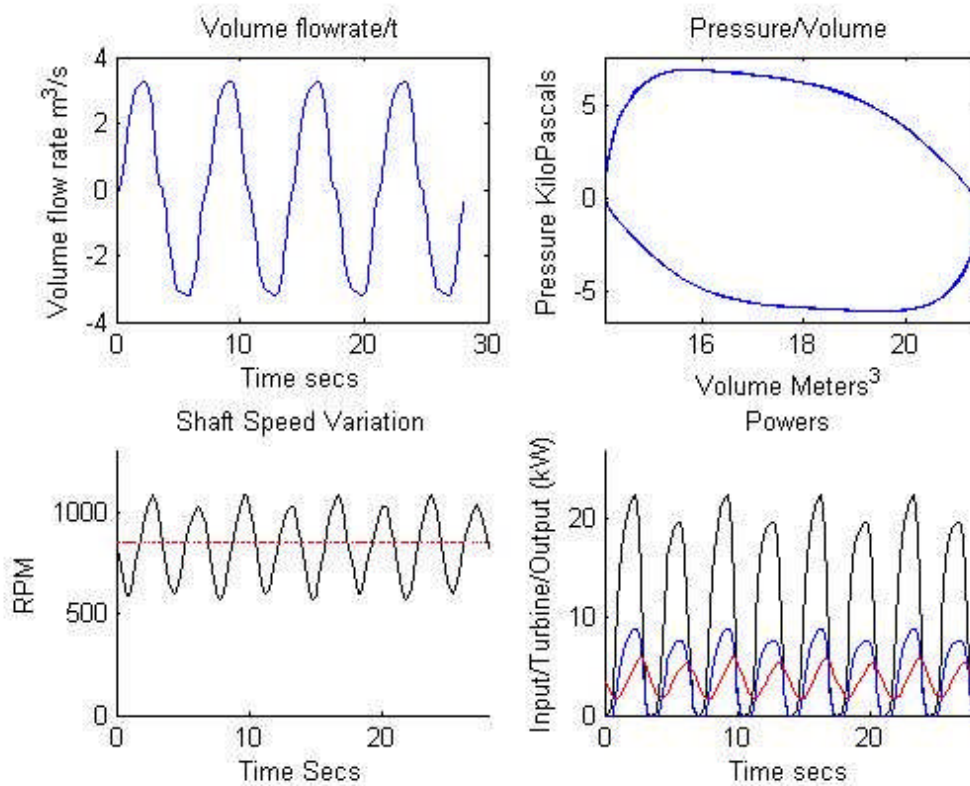


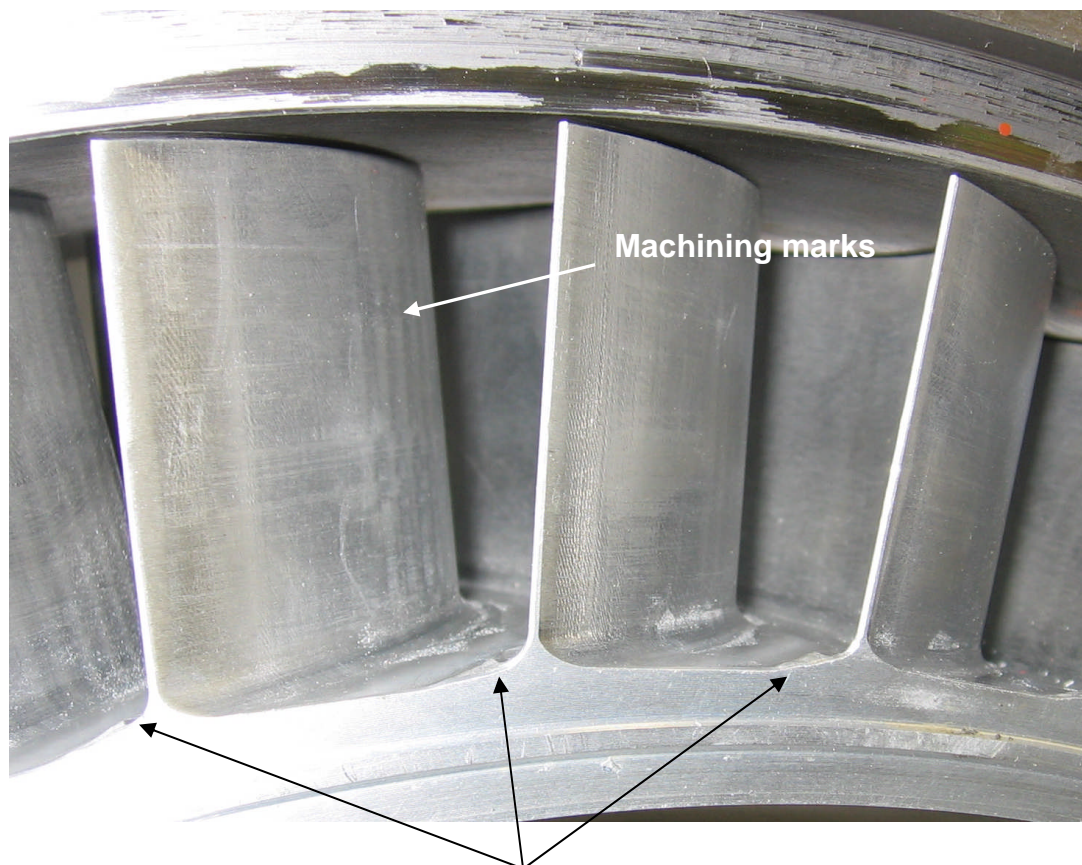
Figure 100 – Simulation of  $Q_{rms}=2.3$ ,  $T=7$  profile and datum turbine at 850 rpm

## 7. Testing of Datum Turbine

### 7.1 Installation of Turbine

#### 7.1.1 State of manufactured turbine

Before the turbine test module was installed in the rig an examination was made of the rotor to assess how it compared to the design specification. The tip clearance around the rotor blades on the side furthest from the PWG was measured using feeler gauges. The tip clearance was found to be ~0.45mm at top-dead-centre, which reduced around both sides to 0.22mm at bottom dead centre. This indicated a tip clearance of 0.4-0.8% blade height, which was considerably smaller than the 1.85% (1mm) tip clearance assumed in CFD simulations. This would be expected to help improve the performance. Unfortunately, it was also observed that there was a large machining 'step' in the blade passages on the turbine hub (Figure 101). This step had a width of around 4mm and a height of around 1mm, and would not improve the performance. In addition, the rotor blades had not been polished, and the machining marks were clearly visible. Ideally, there would have been no steps or machining marks, as these introduce uncertainty into comparisons made with the aerodynamically smooth blades assumed in the CFD predictions.



**Machining step**

*Figure 101 – Finish and machining steps on rotor blisk*

### 7.1.2 Turbine inertia and break-out Torque

A calculation was made of the total inertia of the turbine rotor and its drive train, with and without the generator connected. The inertia of the rotor blades was calculated in the Matlab blade design program, the rest of the information was taken from the appropriate drawings and manufacturer's information. The values obtained are shown in Table 46.

Item (in sequential order)	Inertia (kgm <sup>2</sup> )	Comments
Rotor	0.64182	Density = 2720 kg/m <sup>3</sup>
Shaft GW/2/42740	0.00540	Density = 7850 kg/m <sup>3</sup>
Torquemeter coupling	0.02140	Manufacturers value
Torquemeter	0.00125	Manufacturers value
Torquemeter coupling	0.02140	Manufacturers value
RAN 38 SA 1 HS right angle gearbox	0.00504	Manufacturers value
Drive shaft GW/2/42739	0.00124	Density = 7850 kg/m <sup>3</sup>
Half of generator coupling	-	
<b>Total inertia without generator</b>	<b>0.69755</b>	
Half of generator coupling	-	
Generator	0.37000	Manufacturers value
<b>Total inertia with generator</b>	<b>1.06755</b>	

Table 46 – Rotor drive train inertia

Based on the definition used by Setoguchi, the non-dimensional inertia of the turbine and its drive train is:

$$X_I = \frac{I}{\pi \rho_a R_{mid}^5} = 183$$

Before the turbine module was fully installed a measurement was made of the break-out torque required to just get it to move. This was done by screwing a threaded bar into one of the 3 taped holes close to the centre of the turbine blisk, and then gradually increasing a mass suspended from this until the turbine began to just rotate very slowly. The distance from the centre of the blisk to the centre of the shaft was 77mm, and the mass required to just rotate the turbine (including the mass of the shaft) was 2.11 kg. The applied torque was thus 1.594 Nm.

Once the turbine had been installed, data was taken with the generator dis-connected which included taking the rotor up to speed then stopping the flap, and recording the run down of the rotor. This data was used to check the measurement of the break-out torque and the inertia.

Examination of the how the rotor came to a stop showed that when the speed diminished to zero the torque was around 1.5 Nm, as shown in Figure 102. The final 'hump' in the torque trace peaked at 1.6 Nm, and is probably the result of the rotor rocking as it comes to rest in its bearings. It can thus be concluded that break-out torque of the rotor without the generator connected was 1.6 Nm.

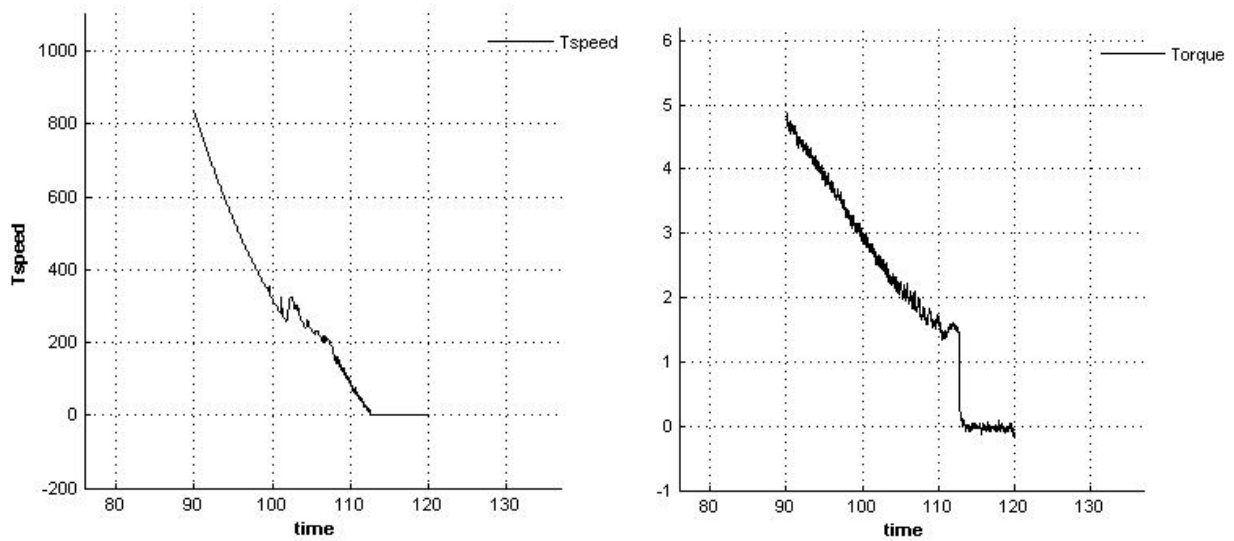


Figure 102 – dp182 run down of rotor speed and torque from datum wave profile

### 7.1.3 Noise Measurements

When the first run with the turbine fitted took place it was immediately apparent that there was a large increase in the perceived noise level above that experienced with the empty duct and porous plate configurations. Noise measurements, primarily for the purpose of establishing whether ear defenders should be worn whilst running the rig with the turbine fitted, were thus made using a CEL 328 instrument. The weather conditions under which the measurements were taken were overcast, with only a light wind in front of the test house. For the purposes of the assessment a profile was selected towards the lower energy end of the possible running conditions, and close to ‘typical’ conditions. The chosen wave had a nominal rms flowrate of  $2.3\text{m}^3/\text{s}$ , and period of 8.13 seconds.

The measurements were made at a number of points as indicated in Figure 103. In Figure 103 the base of the arrow indicates the approximate position of the measurement, whilst its direction indicates the direction in which the microphone was pointed whilst making the measurement. The results are shown in Table 47

Position	Description	LEQ (dBA)	Peak (dBA)	SPL (dBA)
A	By ACS800	87	-	-
B	By rotor casing	-	-	95
C	At control desk	90	107	-
D	In front of outlet diffuser	97	117	-
E	By roller door	86	-	-
F	In road	75	-	-

Table 47- Noise measurement results

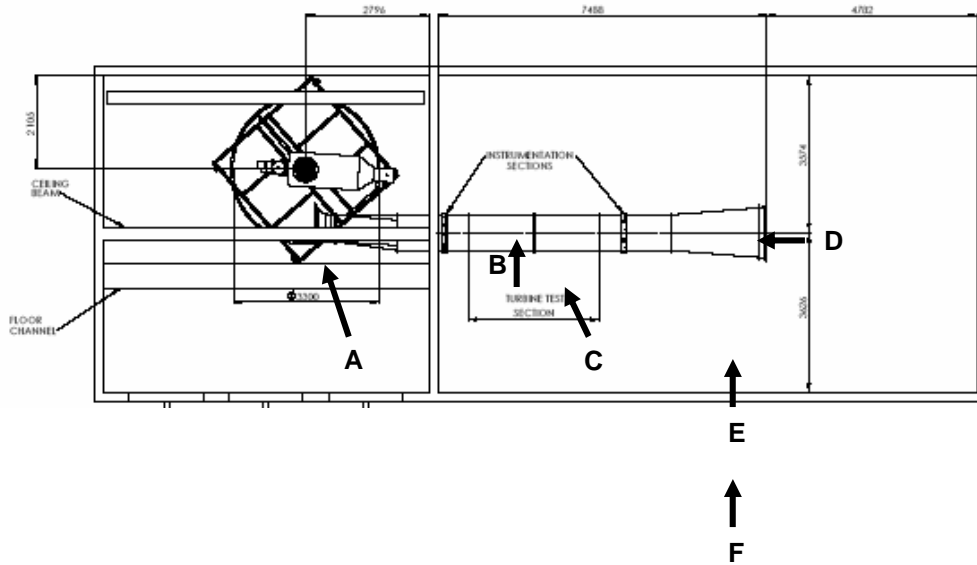


Figure 103 – Positions of noise measurements

From the data taken it was concluded that ear defenders should be worn at all times when running the rig.

#### 7.1.4 Test Condition Noise Measurements

When the turbine performance data was taken, noise measurements were taken at the no-load and maximum load points, for the shortest and longest periods, for each flow rate condition. The measurements were made using the CEL 328 mounted on a tripod so that the microphone was on the centreline of the turbine, 1m from the end of the outlet diffuser (i.e. at point 'D' in Figure 103). The background noise level measured when the PWG, all instrumentation except for the SCXI chassis, and both heaters in the 2-3 Link were turned 'off', was generally 50 dB(A), with peaks up to 59 dB(A).

The measurements made were of the 'A' weighted SPL, and the highest linear octave reading at each test condition. The SPL reading was taken with the response set to 'fast'. The measurements showed that:

1. The noise contained broadband and discrete frequency components.
2. The range of SPLs varied from 94 to 108 dB(A).
3. The greatest sound level occurred on the exhalation part of the cycle.
4. The 500Hz octave band, was the band in which the highest sound levels were recorded throughout the testing.
5. The recorded levels were less at full load than at no-load.

Qualitatively, the perceived sound was quite different at no-load conditions to full load conditions, and between small flow rates and high flowrates. At the low flow rate/fully loaded conditions the observer was most aware of a distinct 'whistling' at

the low flow points when the flap reached the end of its movement, whereas at higher flow rate/shorter period conditions the sound was that of a rushing of air which rose and fell in a similar way to the sound of waves on the sea shore. A summary of the measurements is given in Table 48.

A noise level of 108 dB(A) is comparable to that produced by a pneumatic hammer, and can be experienced without protection for under half an hour. The measurements taken were only for indicative levels, as they will have been affected by reflections from the walls and surrounding equipment.

The fact that the octave with the highest sound level component in was always the 500Hz one indicated that the most dominant component was probably associated with the blade passing frequencies (BPFs), or blade interaction frequencies. The range of test rpms was 500-1800, which would have given BPFs of 350-1300Hz.

Nominal rms Flowrate (m <sup>3</sup> /s)	SPL		500 Hz Octave band	
	No Load (dBA)	Full Load (dBA)	No Load (dB)	Full Load (dB)
3.0	108	106	100	95
2.65	106	104	98	94
2.3	103	101	96	95
1.77	97	94	92	90

*Table 48 – Sound levels recorded during Datum turbine testing*

In general, it is expected that the noise levels associated with turbomachinery reduce as the design point is approached, perhaps by 5-10 dB (Wright, 1999). However, the measured differences between the unloaded and fully loaded condition – which was reasonably close to the design point – was only 2-3 dB. This was almost certainly because there was always a set of guide vanes which were operating highly off-design and introducing turbulence into the flow, however, the noise reduced at the high load conditions because more kinetic energy was taken out of the flow.

The overall levels recorded may have been influenced by the specific design of the facility: the particular dimensions and material of the inlet/outlet duct, for example. There will also have been an effect due to reflection of sound from the surrounding walls and equipment which will have reduced the degree of attenuation at the microphone.

Calculations made by Pervier (Pervier, 2006) based on empirical methods for predicting fan noise and an ESDU noise prediction code, predicted noise levels of 90-105 dB at the 1m position. In addition, his predictions showed that full scale noise levels would be 10-20dB greater than those at model scale. This would indicate peak full scale, high flow rate noise levels comparable to those associated with Concorde, which may not be acceptable with regard to location and environmental considerations.

From the observations and results, it was concluded that the measured sound pressure levels were as great as the highest predictions, and that full scale noise levels could exceed 120dB(A). It is therefore recommended that further work is carried out to obtain a better understanding of the cyclic noise profile, with a view to determining to what degree the measured levels are specific to the facility, and whether consideration needs to be given to developing a design with a reduced noise signature.

## 7.2 Performance Data

### 7.2.1 Test Conditions

The performance of the datum turbine was evaluated over the range of nominal flowrates and flap periods indicated in Table 49. The maximum periods that could be obtained were limited by the range of flap movement in the PWG. Preliminary work showed that for wave periods greater than 10s the calculated profile parameters resulted in flap oscillations which were significantly longer than required. This was apparently due to the accelerations being too small, and so tests were done to establish the acceleration values required to give the desired wave periods. The profile parameters for all the conditions used are given in Appendix M.

Nominal rms flowrate (m <sup>3</sup> /s)	Period (s)					
	5	7	9	10	12	14
1.5	✓	✓	✓	✓	-	✓
1.77	✓	✓	✓	✓	-	✓
2.3	✓	✓	✓	✓	-	✓
2.65	✓	✓	✓	✓	✓	-
3.0	✓	✓	✓	✓	-	-

*Table 49– Matrix of performance test conditions*

### 7.2.2 Precautions in Testing

Two particular precautions were taken to assure the quality of the test data. The first was to turn off the heating fan in the 2/3 link that was close to the instrumentation ring furthest from the PWG. This was because it was found that if this was on, it produced a temperature differential between the top and bottom of the instrumentation ring of about 3°C. The effect of this temperature differential on the pressure transducer and thermocouple outputs, combined with transducer drift during testing, was such that a meaningful determination of efficiency could not be made.

The second precaution was to look at the tare outputs of all the instrumentation before starting the test. In the first instance this was to look for anomalies, but in addition, if the output of any pressure transducer was showing more than  $\pm 50$  Pa, then that

transducer was re-calibrated before starting the test. This meant that a large number of transducer calibrations were carried out during testing, due their temperature sensitivity. In the test period the outside temperature ranged from quite mild conditions of up to 14°C, down to sub-zero conditions. In order to try to keep the conditions in the test house as constant as possible, all the testing was carried out with the doors closed, and the thermostat on the remaining heater in the 2/3 link was set to ~14°C.

Before the acquisition of the test data for the datum turbine was begun a check was made of the repeatability of the data. This was done by comparing data taken on 24 Nov 06 with data for a similar set of test points taken on 8 Jan 07. Both sets of data were taken using the 'direct' mode on the MV3000. The set-up of the MV3000 differed from that used when acquiring the actual datum performance data, in that a lower turbine speed limit of 65% of 1498 rpm, i.e. 974rpm was set, below which power would not be taken. In addition, when the January data was taken the power take off could only be increased in integer values, leading to an increasingly non-linear spacing of points as the flow ratio was increased. The results in Figure 104 showed good repeatability, even though the data were taken some 7 weeks apart. The ambient temperature and pressure were similar on both occasions.

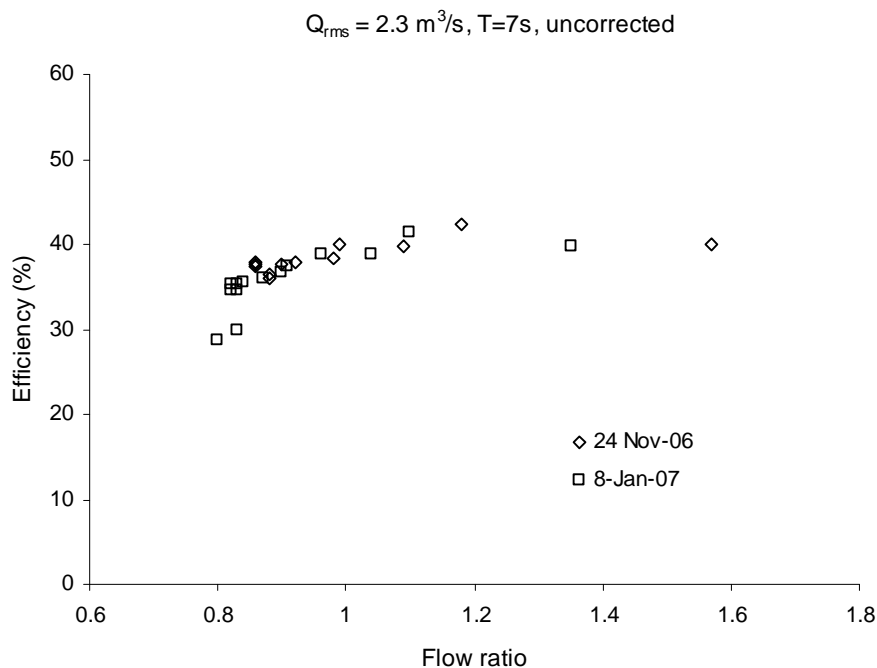


*Figure 104 – Test data repeatability*

### 7.2.3 Test Procedure

The procedure used to acquire the performance data at each test condition was as follows: first a zero point was taken just before the PWG started generating the desired profile. Once the PWG was operating, 3 minutes was allowed for the turbine to run up to speed and a steady repeating flow condition to be established. A ‘no load’ point was then taken before the MV3000 converter was switched on.

At the time of the tests the MV3000 could only be operated in its ‘Direct’ mode, in which the user specified a fixed percentage of the generator rated power to be taken off the rotor. The generator Fixed Flux Limit (Parameter 12.23) was set to 40% throughout the testing. The MV3000 software was modified (in response to a request by the author) just before the performance data was taken to enable non-integer percentages of power take-off to be used to facilitate better resolution of the characteristic. Once the MV3000 bridges were ‘on’, and it had synchronised with the generator, the speed reference was set to zero, and the Direct take-off set to 1%. One minute was then allowed for the conditions to settle before a 1 minute datapoint was taken at 100Hz samplerate. The power take-off was then incremented up and the procedure repeated. The increments used depended upon the energy in the profile, and were gradually reduced as more power was demanded due to the non-linear change in rotor speed produced. The process was continued until a point was reached where the turbine speed simply decayed towards zero. The MV3000 was then turned off, and the motion of the flap halted, and a final zero taken when the rotor came to rest.

Once the data had been acquired it was processed using the Matlab data reduction code ‘PWGgui’ which had been developed during the rig commissioning process. In order to avoid introducing any bias due to temperature changes during the testing process as far as possible, the data was reduced twice using the start zero and the end zero, and then averaged to give the final results.

### 7.2.4 Windage and bearing losses

In order to determine the true aerodynamic efficiency of the test turbine it is important to determine the windage and bearing losses as a function of rotor rotational speed, as these reduce the shaft power output:

$$\bar{P}_{shaft} = \frac{\omega}{t_1} \int_0^{t_1} [\tau_{aero}(\omega, q_t(t)) - \tau_{losses}(\omega)] dt$$

The power required to overcome the losses as a function of rotational speed can be determined by getting the turbine running, then stopping the power input to it, and recording the decay in rotational speed. If the inertia of turbine and drive are known the power required to overcome the losses at any speed can then be determined from:

$$P_{losses}(\omega) = I\omega \frac{d\omega}{dt}$$

The gross power extracted by the rotor is then:

$$P_{gross}(\omega) = \omega \tau_{shaft} + P_{losses}(\omega)$$

The power required to overcome windage, blade drag, and bearing losses as a function of rotational speed for the datum turbine was determined by getting the rotor speed up to around 1700 rpm under no load, using the nominal  $Q_{rms} = 3.0/T=7$  flap movement profile. The motion of the flap was then stopped and the decay in rotor speed recorded as shown in Figure 105. The following procedure was then used to determine  $P_{Losses}(\omega)$ .

A parabolic fit was made to the variation in rotational speed between  $t=19$  and  $t=41$  seconds where there was a smooth variation in speed. This enabled a smooth function for  $d\omega/dt$  to be immediately derived, and a series of 25 values for the variation in power loss between  $t=19$  and  $t=41$  to be calculated, using the previously calculated turbine and drive train inertia value of  $I=1.07 \text{ kg m}^2$ . A parabolic fit to the variation of power loss with rotational speed was then determined which gave:

$$P_{losses} = 0.0262\omega^2 + 4.3510\omega - 93.7668$$

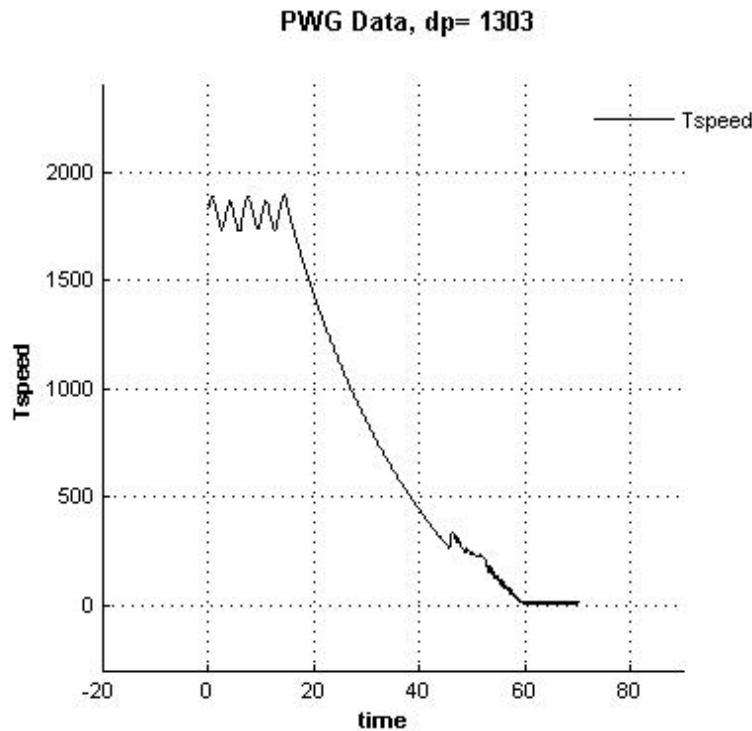


Figure 105 – Rotor speed decay

It can be seen from Figure 105 that this relationship would not be valid for speeds below 300 rpm, when there is an increase in noise and an apparent discontinuity which causes the rotor to accelerate. The latter might possibly be due to some free-play within the drive system, however, it was ascertained from the manufacturer that

it might be necessary to fit a R-C filter in series with the frequency to voltage converter to obtain a smooth output at low speeds. It is therefore recommended that the low speed output of the frequency to voltage converter is measured to determine whether a filter is required.

Application of the derived windage correction showed that it was relatively large. For example, when applied to the data for the datum test condition of  $Q_{rms} = 2.3 \text{ m}^3/\text{s}$ ,  $T=7 \text{ s}$ , the windage correction varied from 20% to 50% of the calculated shaft power between the fully loaded and no load conditions.

The assumption was made that once the flap stops moving the flow through the turbine is zero, which should be reasonable. However, it is recognised that the derived correction is not ideal as it includes the aerodynamic drag of the blades, which increases the shaft power and hence derived efficiency. Ideally, the windage and bearing losses would be determined as a function of flow ratio with the rotor blades removed, but this is very difficult to achieve in practice. The effect of the differences between the ideal and adopted practices should not usually be great, however, the magnitude of the derived correction suggests that further work should be done to determine the impact on the data of the compromises made. One possible course of action is to estimate the blade drag at zero flow from CFD simulations, but consideration should also be given to making a bladeless rotor hub and using the MV3000 to run the generator as a motor to motor the hub up to speed so that the bearing and windage losses can be determined accurately.

### 7.2.5 Hysteresis

A significant hysteresis effect had been observed in earlier testing when there was no load on the turbine, and so data was taken to see whether this remained when the rotor was operating under load. Analysis of the data (Figure 106) showed that there was no significant hysteresis.

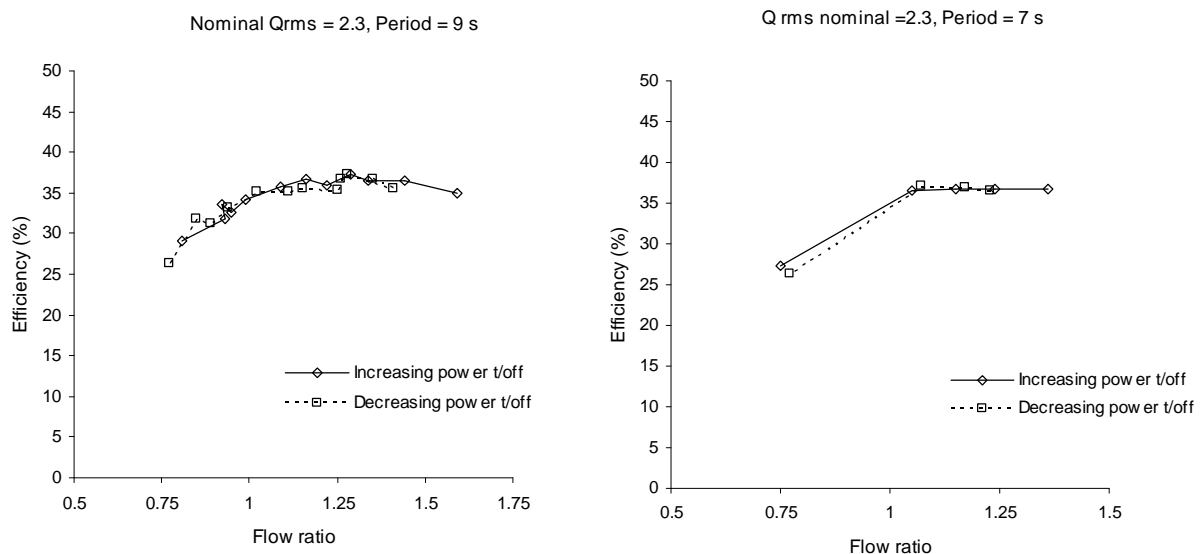


Figure 106 - Hysteresis evaluation data

## 7.2.6 Actual RMS Flowrates

The extent to which conclusions could be drawn from comparing the data from the various test conditions depended upon the input profiles forming a consistent set, i.e. consistent flowrates needed to be obtained. The reduced test data was thus examined to establish how consistent the calculated rms flowrates were. The data (Figure 107 and Figure 108) showed reasonably consistent values for changes in both flow ratio and profile period for all 4 nominal flowrate conditions, although there was a consistent trend in the calculated flowrates to increase with flow ratio. The magnitude of this linear increase was  $\sim 0.2\text{-}0.25\text{ m}^3/\text{s}$  and was similar for all the flow rates.

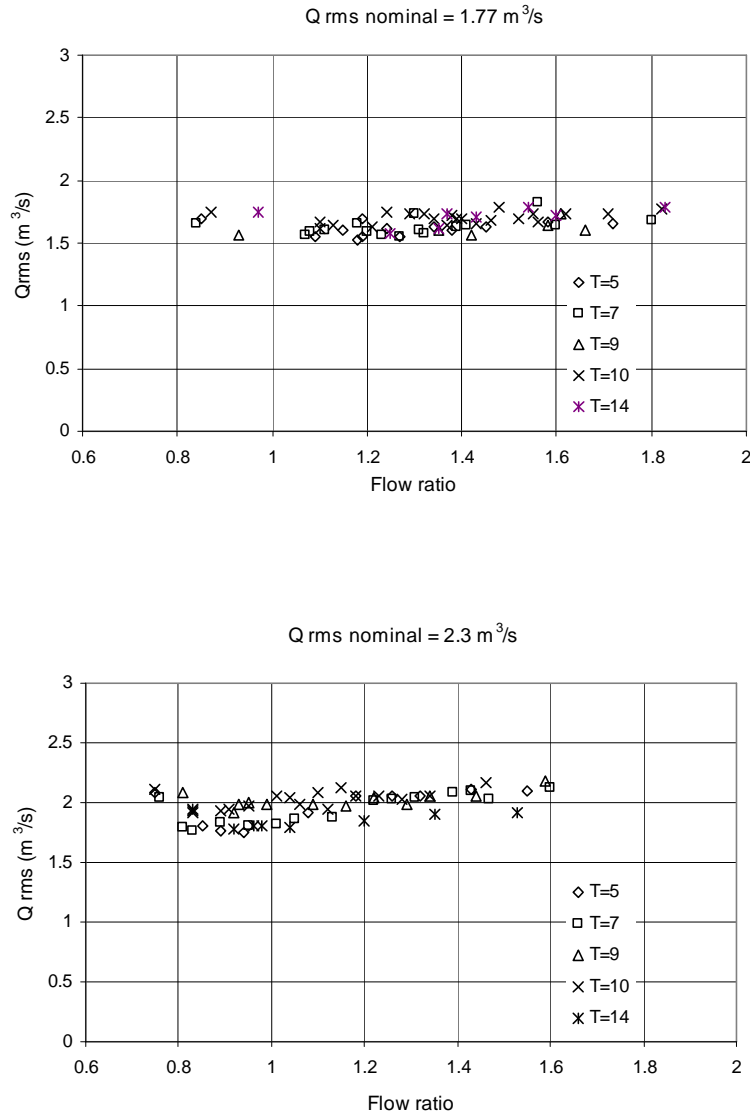
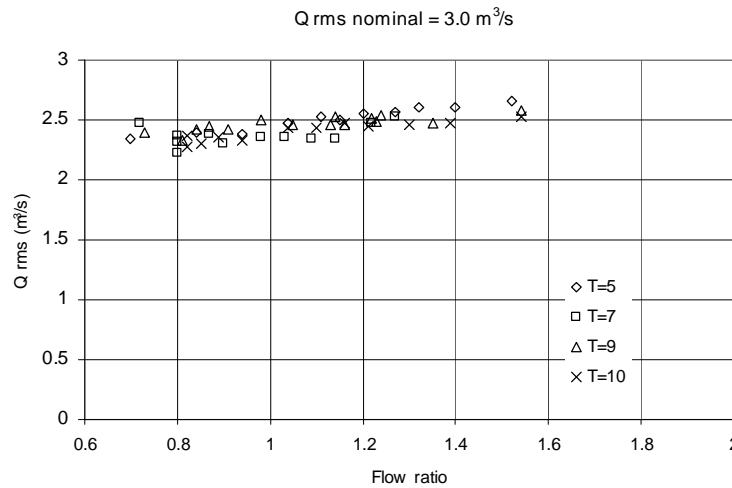
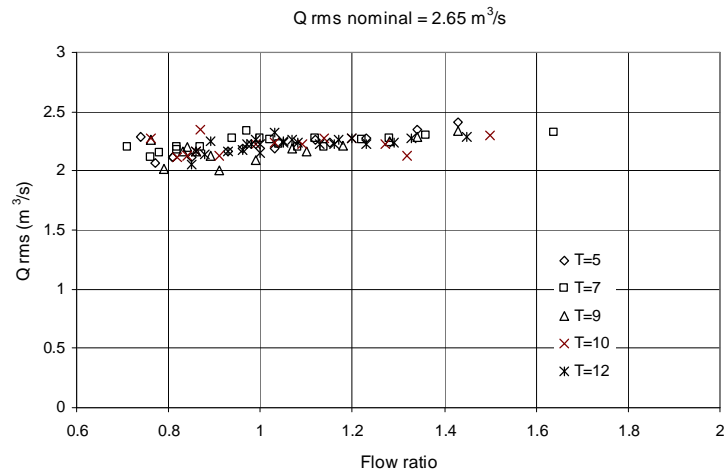


Figure 107 - Calculated rms flowrates for nominal rms flowrate of  $1.77\text{m}^3/\text{s}$



*Figure 108 – Calculated rms flowrates*

Although the scatter for the range of profile periods was  $\sim 0.25 \text{ m}^3/\text{s}$  the scatter within the data for each period was typically rather less than this, as shown in Figure 109. It was a consistent feature that the calculated flow rate for the ‘no-load’ point was significantly higher than subsequent low load condition points. The reason for this was not obvious.

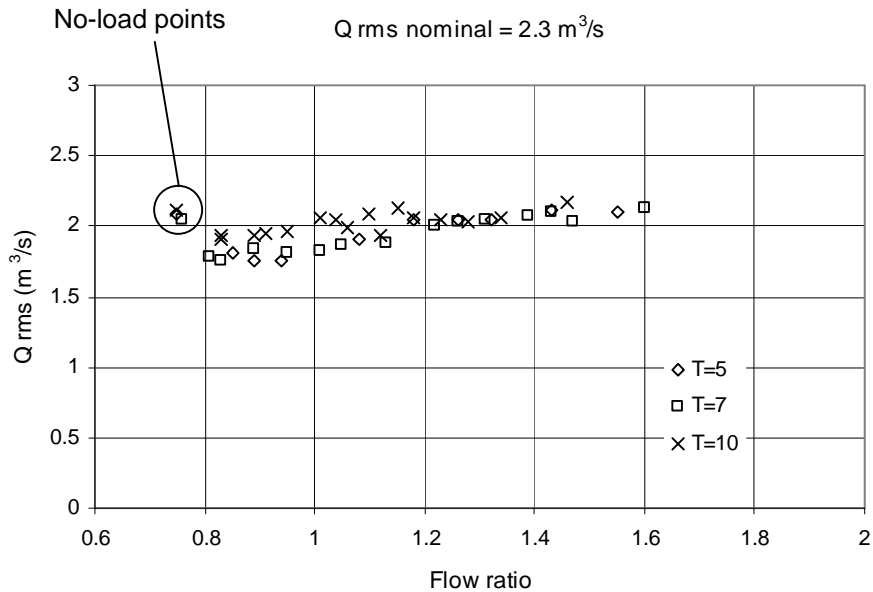


Figure 109 – Scatter in calculated rms flow rate data

Given the very small measurements of pressure difference that the evaluation of the volumetric flow rate depended upon, and the reduced number of instrument plane measurements that were used whilst taking the performance data, it was judged that the data obtained was as accurate as could reasonably be expected.

Given that the data showed that different profiles had been input which produced similar rms flowrates, it was desirable to establish the relationship between the specified and actual rms flow rates. The data for the 5, 7, 9, and 10 second profiles for each flow rate was therefore averaged and plotted. The longer time period data was neglected as it was both less complete and more variable. The resulting points are shown plotted in Figure 110, together with a linear fit through them which indicates the relationship:

$$Q_{rms\ actual} = 0.647Q_{rms\ specified} + 0.4978$$

It can be seen that the plot shows that it would be expected that the actual flowrate would match the specified at  $Q_{rms} = 1.5 m^3/s$ . This was the minimum level of flowrate that it was thought possible to measure using the instrumentation plane pressures, and so flowrates at or below this would be determined from flap displacement measurements. Application of the above relationship gives the values of actual rms flowrates obtained in the tests shown in Table 50.

$Q_{rms\ specified}$	$Q_{rms\ actual}$
1.77	1.64
2.30	1.99
2.65	2.21
3.00	2.44

Table 50 – Specified and actual rms flowrates

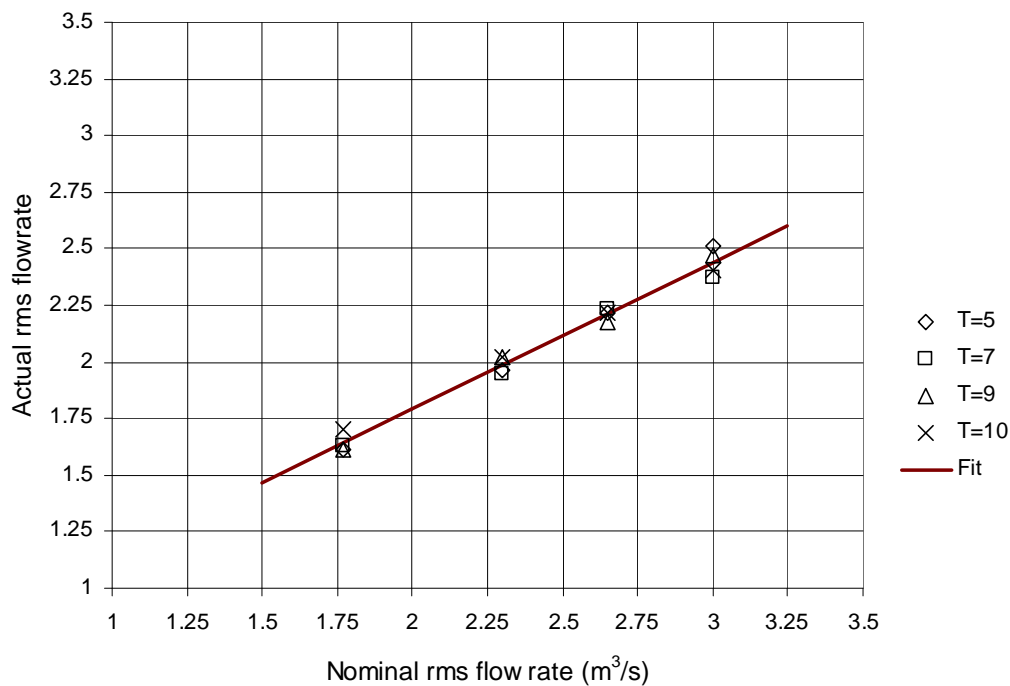


Figure 110 – Relationship between actual and specified rms flowrate

From the foregoing analysis it was concluded that over the range of test conditions:

1. the consistency in the calculations of volumetric flow rate indicated that their accuracy was as good as could reasonably be expected
2. the low scatter in the calculated flow rates made them acceptable for verifying the characteristics of the input profiles.
3. there was a linear relationship between the actual and specified rms flowrate.

However, it is also recommended that further work is undertaken to determine the reason for the variation in calculated flowrate with flow ratio, and the reduction from the no-load point in particular.

### 7.2.7 Range of flow ratios obtained

It was expected at the outset of the testing that as input profiles of higher rms volumetric flow rate were used that it would be possible to obtain data to ever increasing flow ratios. However, the reverse proved the case, as can be seen in Figure 111, as the rms flow rate was increased, the minimum rpm that could be achieved by gradually increasing the power take-off also increased. The points plotted are the average of the average minimum rpms for each of the periods, at the four different input flowrates.

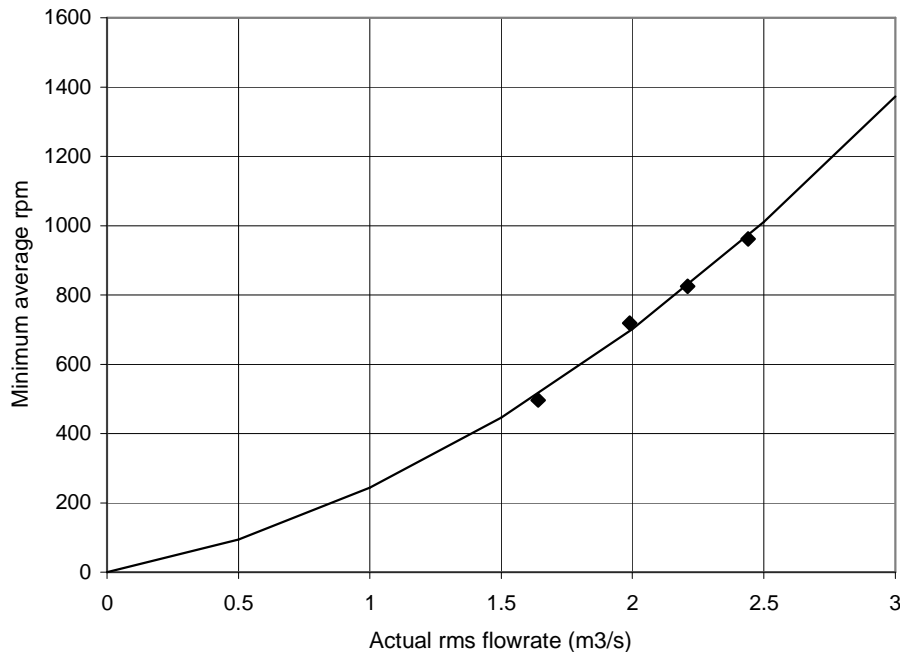


*Figure 111 – Variation in minimum average rpm achieved with actual rms flow rate*

The parabolic fit to the data in Figure 111 suggests that as the minimum rpm is a function of both  $v_a^2$  and  $v_a$ , part of the reason for this could be a growth in aerodynamic losses.

### 7.2.8 Instrumentation related observations

Two observations were made during the testing that may indicate the need for additional instrumentation.

The first observation was that when the turbine was operating close to its fully loaded condition, and the rpm was dropping down to values below 500 rpm, it was observed that as the rotor accelerated up the whole front section of the rig (i.e. the section that may be wheeled away to access the rotor) would visibly ‘shudder’. This appeared to happen as the rotor passed through 500 rpm – but the update rate on the display made this hard to judge. This showed that there was a rig natural frequency around 500 rpm. This did not have any harmful effect on the operation of the rotor in the datum build,

however, this may become critical for the proof-of-concept turbine arrangement (section 9), in which the rotor will have a greater overhang. It is therefore recommended that consideration is given to the fitting of an accelerometer/strain gauge to the turbine casing of the proof-of-concept build to enable vibration to be monitored. It is also recommended that the rpm display is modified to provide a moving needle indication with a high update rate.

The second observation made was that after an extended period of running the outer casing of the rotor was warm to the touch, this was to be expected given the temperature rises recorded by the thermocouples in the instrumentation rings. For example, when data was recorded at the highest test flowrate the temperatures rose from 15°C to the 24-28°C shown in Figure 112. These temperature changes were due to heating of the air in the PWG, much of which probably resulted from frictional heat generated by the seals around the flap rubbing on the walls as it moved back and forth. If the torquemeter also underwent this magnitude of temperature rise, then it is probable that a temperature correction should be applied to its reading. Figure 112 also shows that the thermocouple in the PWG (ChT) should be shielded to provide a more constant output.

It is therefore recommended that a thermocouple is installed to monitor the temperature of the torquemeter, and that the manufacturer be approached with regard to determining the temperature correction that should be applied, and that the PWG thermocouple is installed in a suitable probe.

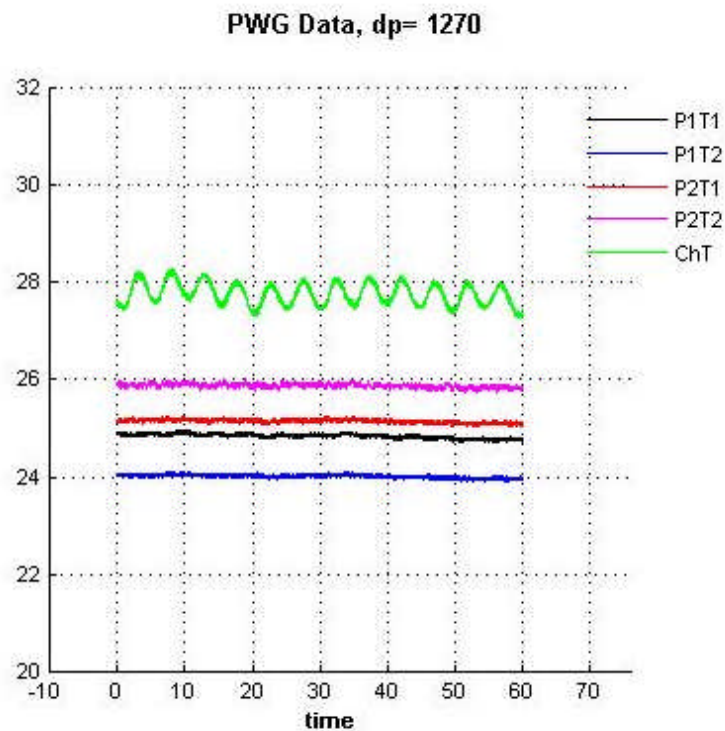


Figure 112 – Thermocouple readings at end of testing with  $Q_{rms}=2.44 \text{ m}^3/\text{s}$

The final observation made, was that it was very difficult from the instrumentation information displayed to determine whether the measured shaft power correlated with the information displayed on the MV3000 HMI. This problem would be greatly eased if the LabView code was modified to provide a strip indicator, with high update rate, that displayed a calculation of the instantaneous shaft power.

### 7.2.9 Starting Characteristic

The starting characteristic of the datum turbine was recorded over a range of nominal flow conditions covered by the test matrix from low to high flow rates and short to long periods. The starting characteristic was seen to be similar in all cases: the turbine went from zero to approximately 80% of its average steady oscillating flow running speed in ~4 periods, thereafter it's speed continued to asymptote slowly to its steady oscillating flow condition over the next minute or so. This behaviour was similar to that recorded by Setoguchi et al (Figure 27), which was to be expected as the non-dimensional inertias were quite similar, that of the datum turbine being  $X_I=183$ , whilst Setoguchi's was 206.

### 7.2.10 Performance Data

The data gathered for each of the input profile conditions was reduced to derive the efficiency over a cycle based on:

$$\eta = \frac{\int_0^T \omega \tau_{shaft} dt + \int_0^T P_{losses}(\omega) dt}{\int_0^T Q \Delta p dt}$$

and the flow ratio at each point was calculated as:

$$\phi = \frac{v_{a \max}}{\bar{U}_{mid}}$$

where  $\bar{U}_{mid} = \frac{1}{T} \int_0^T U_{mid} dt$

This formulation of  $\phi$  is the most appropriate as due to the oscillatory nature of the air flow the variations in  $v_a$  and  $U_{mid}$  are out of phase with each other.

Data was gathered for all the points in Table 49 except those for a nominal rms flowrate of 1.5 m<sup>2</sup>/s. Data could not be gathered at this condition because when this was attempted at both 5 and 14 second periods, the action of engaging the MV3000 to the generator caused the turbine to stop. Once the data had been reduced using 'PWGgui' plots of the variation in efficiency with amplitude (rms flow rate) and

period were produced. This reduced data, together with the characteristic predicted by the simulation program are shown in Figure 113 and Figure 114.

Analysis of the data suggested that there was a drop in efficiency as the period of oscillation of the flap increased, but that this variation was not that much greater than the scatter in the data. However, at the lower rms flow rates there did appear to be a reasonably clear distinction between the data taken at 5 and 7 seconds, and the data taken at longer periods for all except that at the highest flowrate. This has been highlighted in Figure 113 and Figure 114 by the use of filled symbols for the 5 and 7 second data.

Two possible problems were identified in the data. Firstly, the differences between the  $T=5$  and  $7$  data and  $T=9,10$ , and  $14$  data at  $Q_{rms}=1.99$  did not appear entirely credible, the shorter period data having a bulge between flow ratios  $0.8-1.2$  whose peak efficiency exceeded that predicted by the simulation. Secondly, it appeared that there was a bias error in the  $Q_{rms}=2.44$ ,  $T=7$  data.

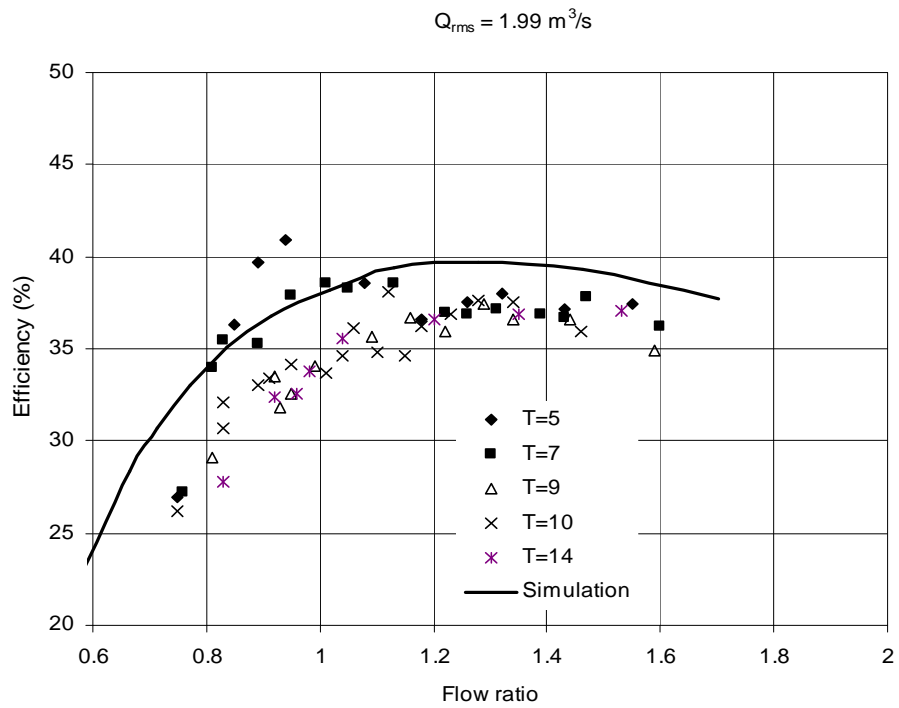
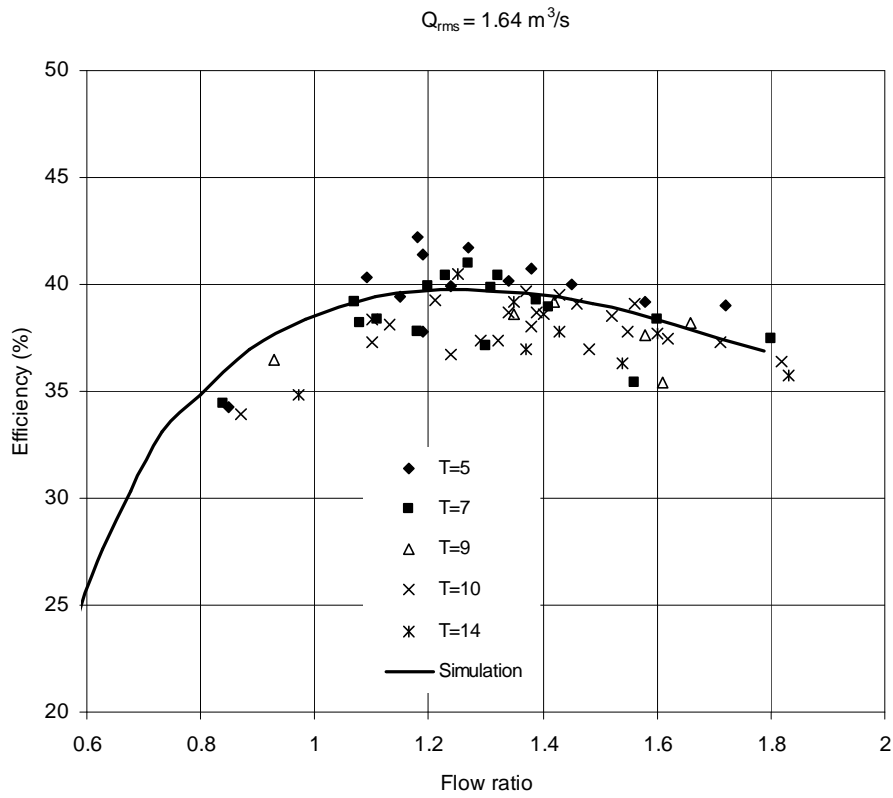
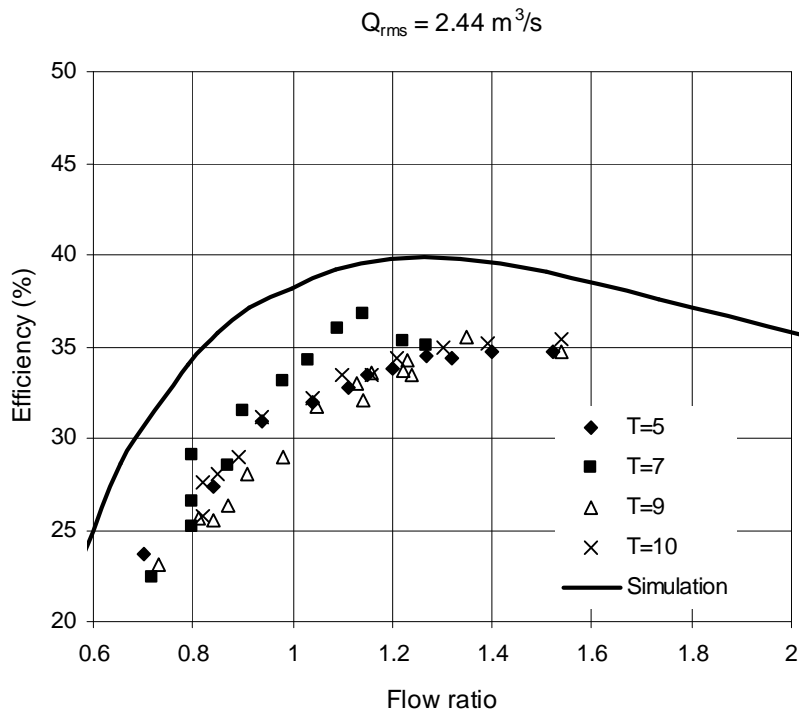
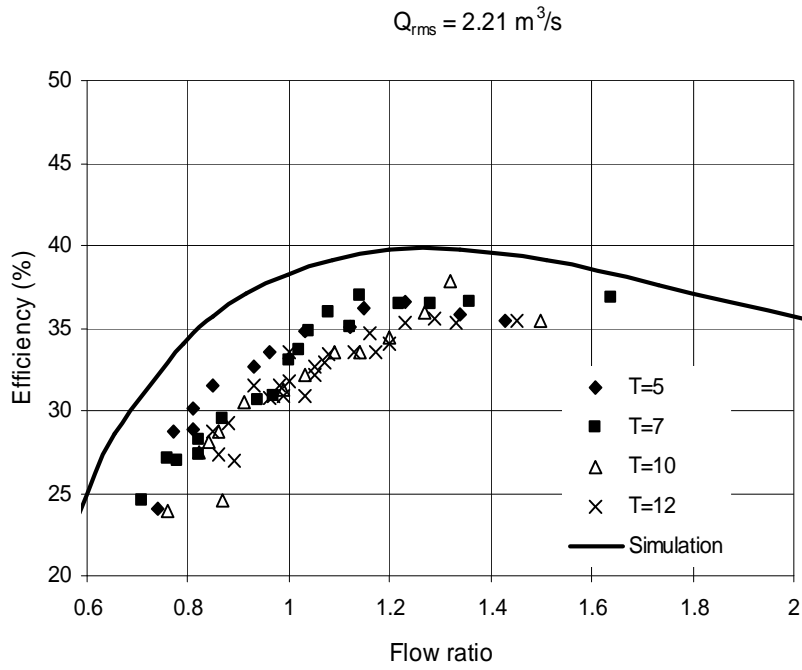


Figure 113 – 1.64 and 1.99  $\text{m}^3/\text{s}$  data



*Figure 114 – 2.21 and 2.44 m<sup>3</sup>/s data*

A closer examination of the  $Q_{rms}=1.99$ ,  $T=5$  data was made to establish whether the efficiency bulge was real effect, or not by seeing if the variation in turbine efficiency was reflected in changes in the pressure, calculated fluid power in the PWG, and changes in the rotor speed and torque. The trends in all parameters were seen to be smooth, except for the calculated volumetric flow rate. As it was known that the flap movements were very repeatable, and a constant profile was maintained for each time period condition, it was not expected that the rms flow rate would vary significantly at a given test condition. It was therefore concluded that apparent variation in efficiency was a result of errors in the calculated volumetric flowrate: the highest efficiency point coinciding with the lowest calculated volumetric flow rate. In order to reduce these errors, the efficiency and flow ratio values for each data point were corrected to the average calculated rms flowrate for the particular flow rate/time period condition as follows:

$$\eta_{corr} = \eta \cdot \frac{Q_{rms}}{\bar{Q}_{rms}}$$

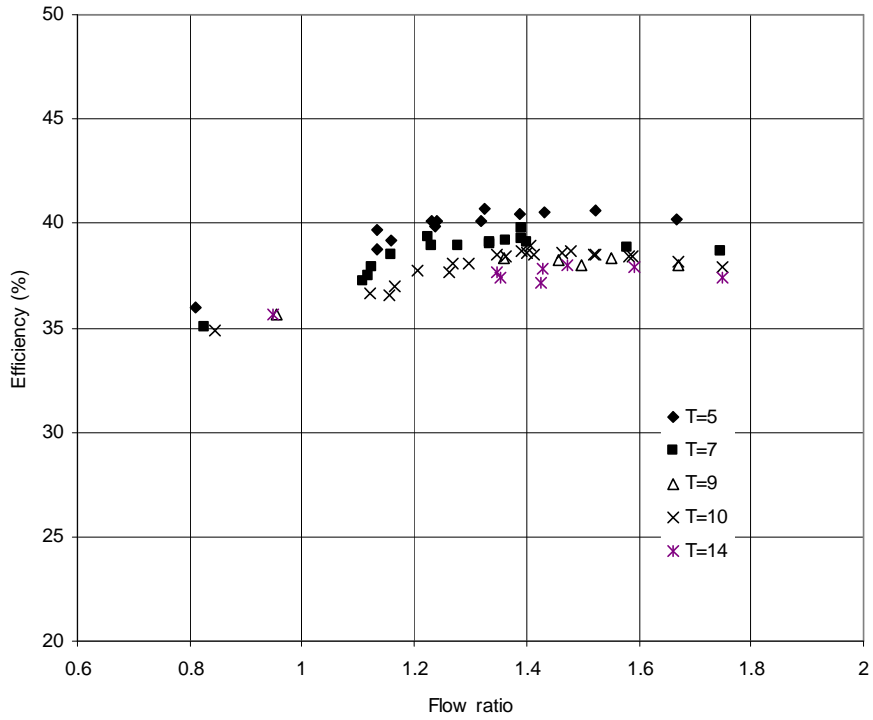
$$\phi_{corr} = \phi \frac{\bar{Q}_{rms}}{Q_{rms}}$$

This correction significantly reduced the scatter in the data generally, and removed the bulge in the  $Q_{rms} = 1.99$  data, as shown in Figure 115 and Figure 116. However, the apparent bias in the  $Q_{rms} = 2.44/T=7$  data remained, and so this was neglected in the subsequent curve fitting exercise.

The corrected data was examined, and a clear trend for efficiency to reduce as profile time period increased was seen for the  $Q_{rms} = 1.64$ ,  $1.99$ , and  $2.1 \text{ m}^3/\text{s}$  data. However, the efficiency versus flowrate characteristic was independent of profile period for  $Q_{rms} = 2.44 \text{ m}^3/\text{s}$ . It was thought most useful to curve fit the shortest and longest period data for each rms flow rate, using the remaining data as a guide to judge the appropriateness of the curve fits. For the  $Q_{rms}=2.44$  condition, a single curve was derived using all the data. The derived curve fits are shown in Figure 117 and Figure 118.

The curve fits showed that below the maximum rms flow rate, the maximum decreases in efficiency with increasing period varied from 2.2 to 2.9 %, for flow rates of 2.21 and 1.64  $\text{m}^3/\text{s}$  respectively. A comparison between the curve fits and the predicted characteristic showed that the measured peak efficiency was achieved at a flow ratio of  $\phi=1.4-1.5$ , rather than the 1.25 predicted by the simulation.

$Q_{rms} = 1.64 \text{ (m}^3/\text{s) - corrected}$



$Q_{rms} = 1.99 \text{ (m}^3/\text{s) - corrected}$

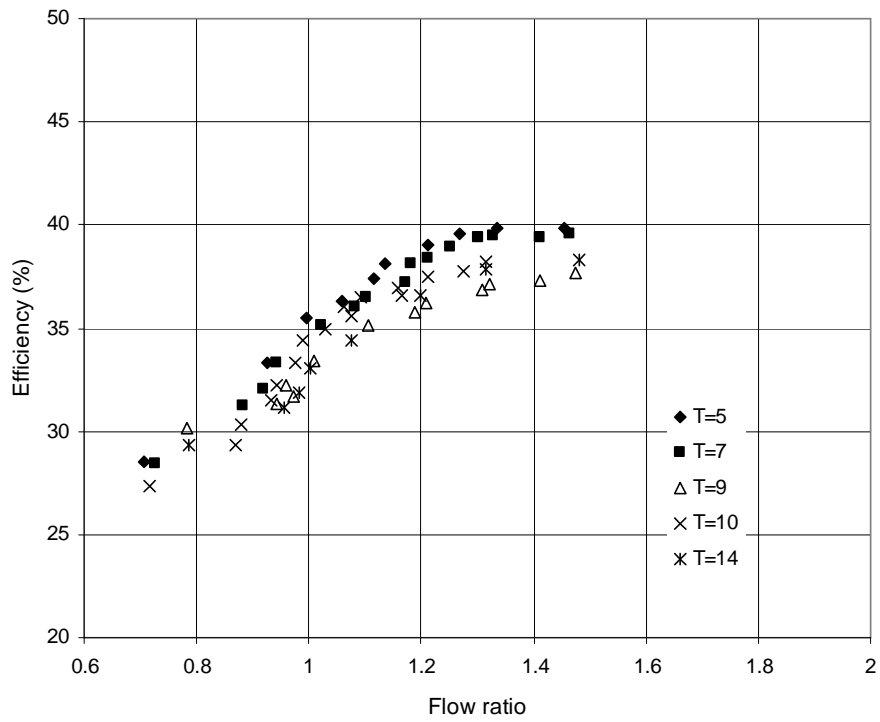
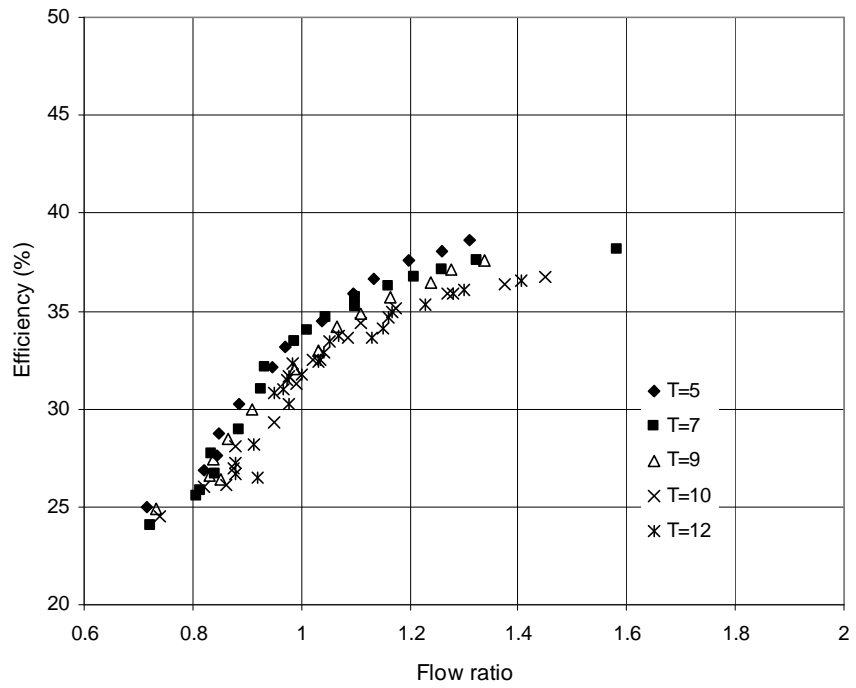


Figure 115-  $Q_{rms} = 1.64$  and  $1.99 \text{ m}^3/\text{s}$  corrected data

$Q_{rms} = 2.21 \text{ (m}^3/\text{s) - corrected}$



$Q_{rms} = 2.44 \text{ (m}^3/\text{s) - corrected}$

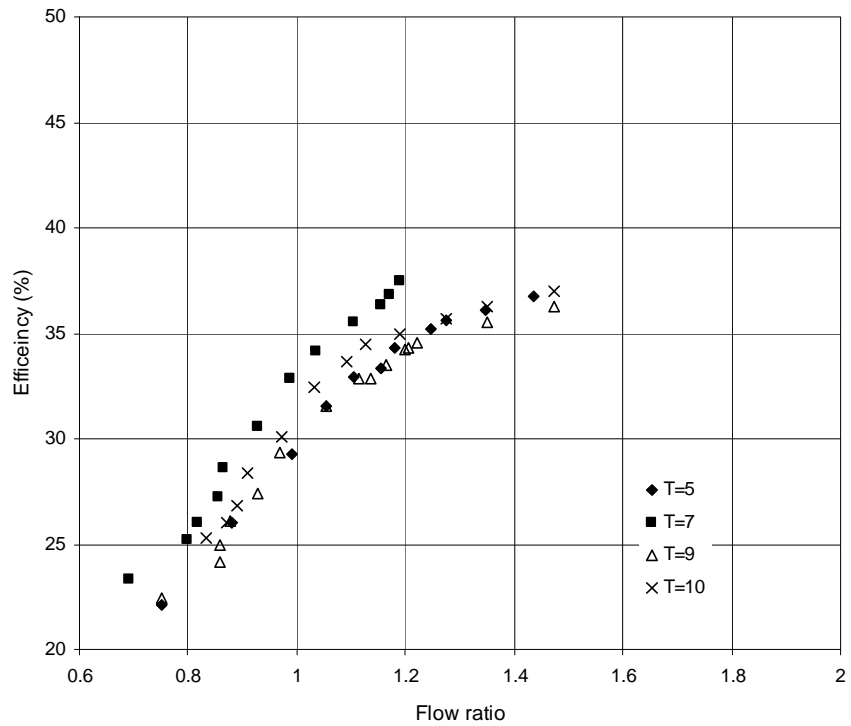


Figure 116 –  $Q_{rms} = 2.21$  and  $2.44 \text{ m}^3/\text{s}$  corrected data

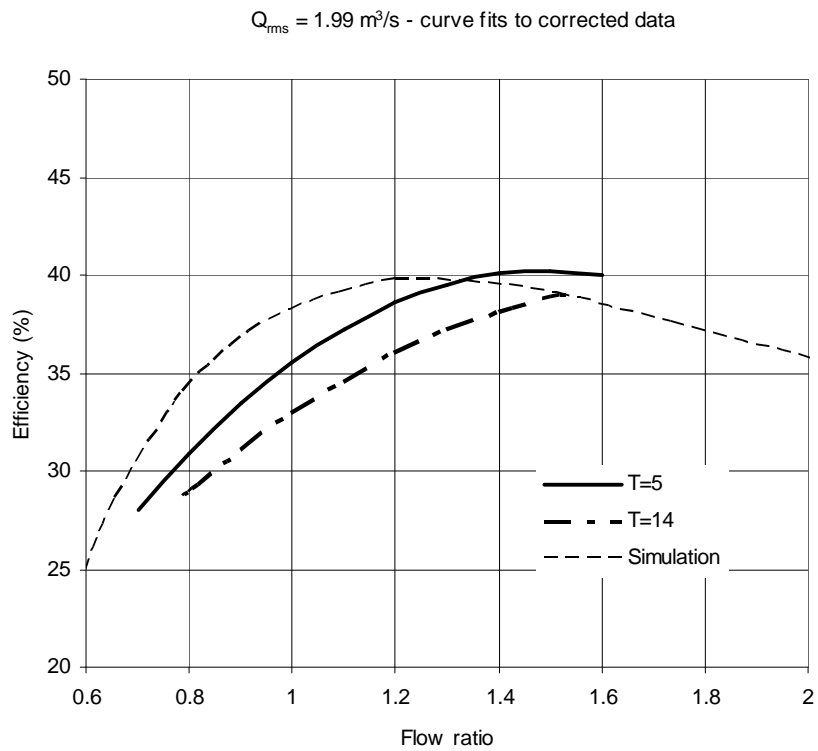
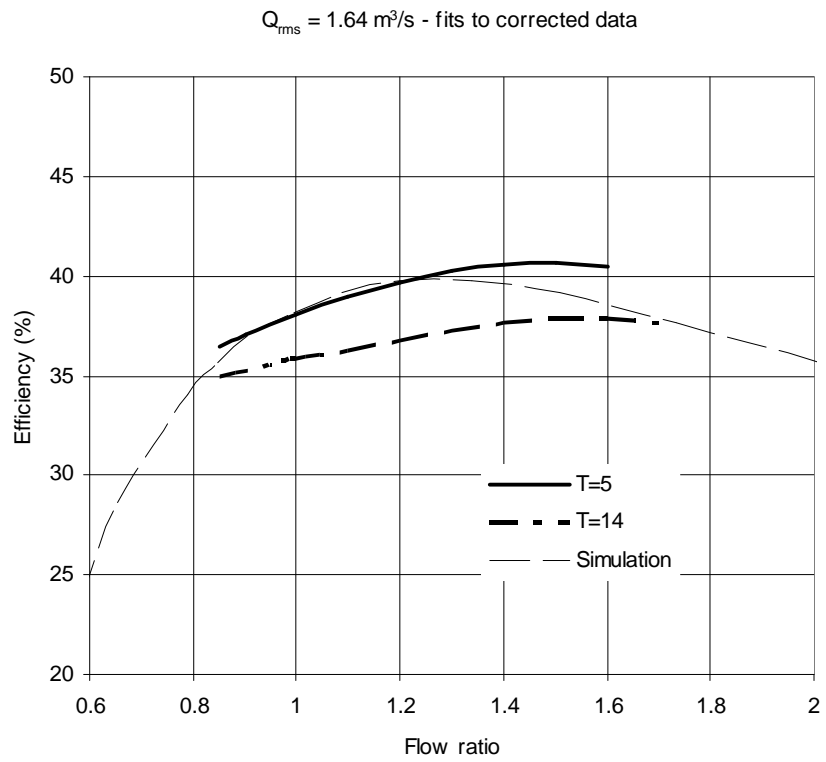
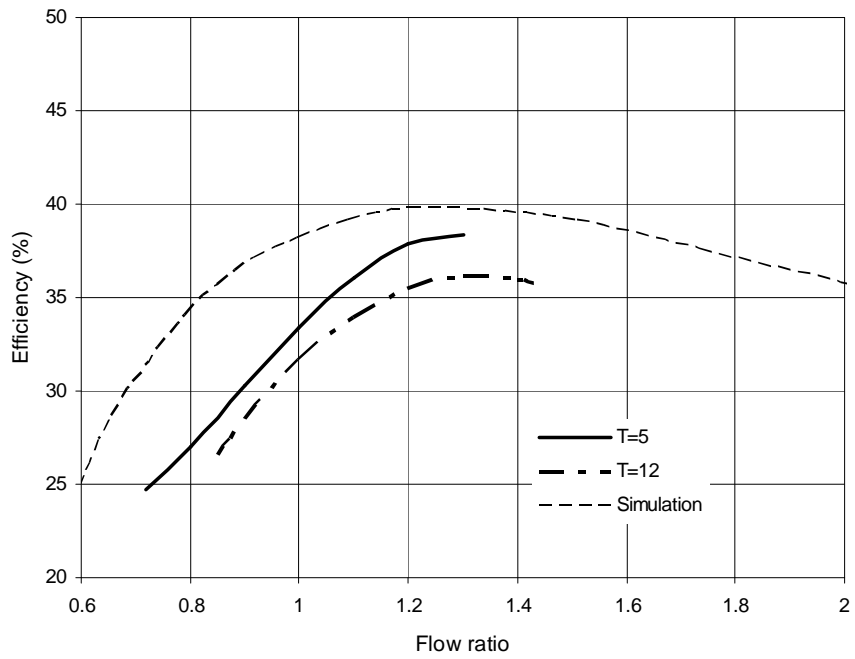


Figure 117 – Datum turbine performance data  $Q_{rms}=1.64-1.99 \text{ m}^3/\text{s}$

$Q_{rms} = 2.21 \text{ m}^3/\text{s}$  curve fits to corrected data



$Q_{rms} = 2.44 \text{ m}^3/\text{s}$  - curve fit to corrected data

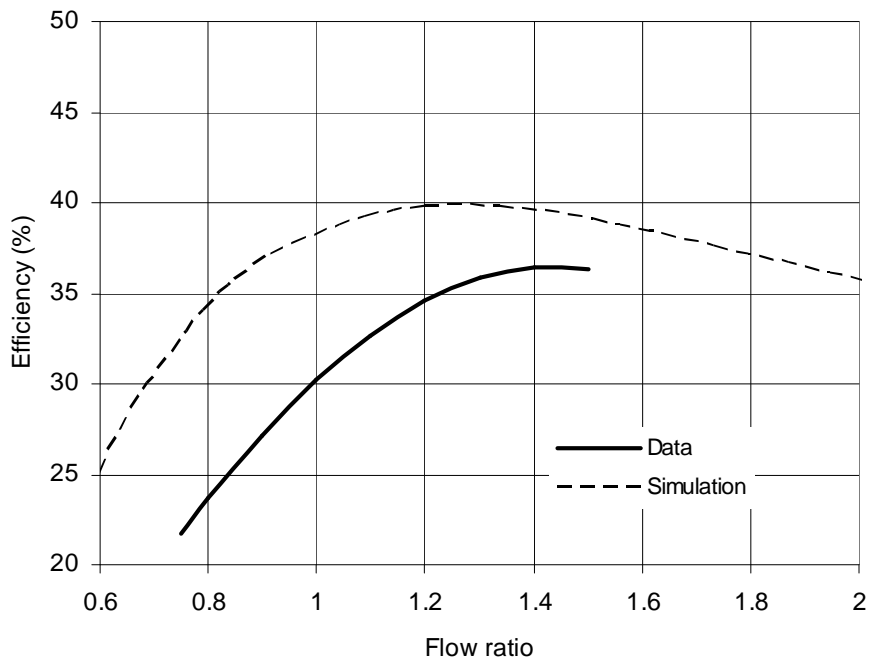


Figure 118 – Datum turbine performance data  $Q_{rms} = 2.21$  and  $2.44 \text{ m}^3/\text{s}$

### 7.2.11 Discussion of results

The plots in Figure 117 indicated peak efficiency values slightly greater than the simulation, and the  $Q_{\text{rms}}=1.77$  data appeared to show a rather slower drop off in efficiency with reducing flow ratio than might have been expected. These results should not be accepted too readily, as this data was approaching the lower limit and significant errors could easily be present due to the small pressure differences involved. It should also be noted that whilst the scatter in the derived results was low (typically less than 0.5%), a significant bias error could be present due to the sensitivity of the evaluation of efficiency to the calculated flowrate. For example, if the actual flow rate is  $2.0 \text{ m}^3/\text{s}$ , but the calculated value is  $2.05 \text{ m}^3/\text{s}$ , then the efficiency changes by 3% - which is very significant in terms of the final results. However, this would be acceptable, as it must be remembered that the instrumentation system was constructed on the basis of an accuracy of  $\pm 2\text{-}3\%$  as being the best achievable.

Overall, the curve fitted data indicated that as the rms flowrate was increased from  $1.77$  to  $2.44 \text{ m}^3/\text{s}$  the peak efficiency fell by  $\sim 3.7\%$ . It also showed that the efficiency tended to drop away more rapidly as flow ratio was reduced, and that the maximum flow ratio that could be achieved also reduced. The probable explanation for the drop in efficiency with increasing flow rate, and reduction in maximum achievable flow ratio (and increase in minimum rpm), is that as the flow rate and ratio are increased the axial velocity increases, but the pressure losses increase with square of the axial velocity. This means that at higher flow rates the effective resistance increases, and the useful work is reduced, producing a reduction in efficiency.

A comparison between the test data with the simulated characteristic, showed that the peak efficiency was achieved at a flow ratio of around  $\phi = 1.5$ , rather than  $\phi = 1.3$  as predicted by the simulation. A possible reason for this is that the boundary layers are significantly thicker in the actual turbine than in the CFD simulation causing the local flowrate over a significant proportion of the span (particularly given the high hub/tip ratio) to be reduced. It is very likely that the actual boundary layer thickness is considerably more than the CFD simulations, in which the growth was only from the inlet plane i.e. 2 blade chords, whereas there is a considerable length of duct leading to the turbine in both flow directions. The velocity profiles recorded in the instrumentation sections indicated boundary layer thicknesses of 2-3 mm. If the growth of a turbulent boundary layer on a flat plate is considered (Figure 119) then it can be seen that it is conceivable that, particularly on the PWG side of the turbine (on which the instrumentation ring is 1.64m from the turbine), the boundary layer thickness could develop to 50% or more of the blade height.

The results showed that for a given profile flow rate, the efficiency tended to reduce as the profile period was increased. This should not happen in the ideal situation. Examination of the data for points of 5 and 14 second periods,  $Q_{\text{rms}}=2.21 \text{ m}^3/\text{s}$  showed that their variations in flowrate with non-dimensional period (i.e.  $t/T$ ) were different as shown in Figure 120. The data showed that at the longer period the peak flow rate

condition was not maintained in the way it was for the shorter period, and as the output of useful work is biased to the high flow condition the overall efficiency at

longer period is reduced. This said further analysis should be carried out to understand why the flow peak is not maintained at long periods in the way that it is at short periods. This loss of performance at long periods is not too serious, as is testing at short periods that provides the most representative data, as the non-dimensional frequency (Strouhal number) is closer to reality.

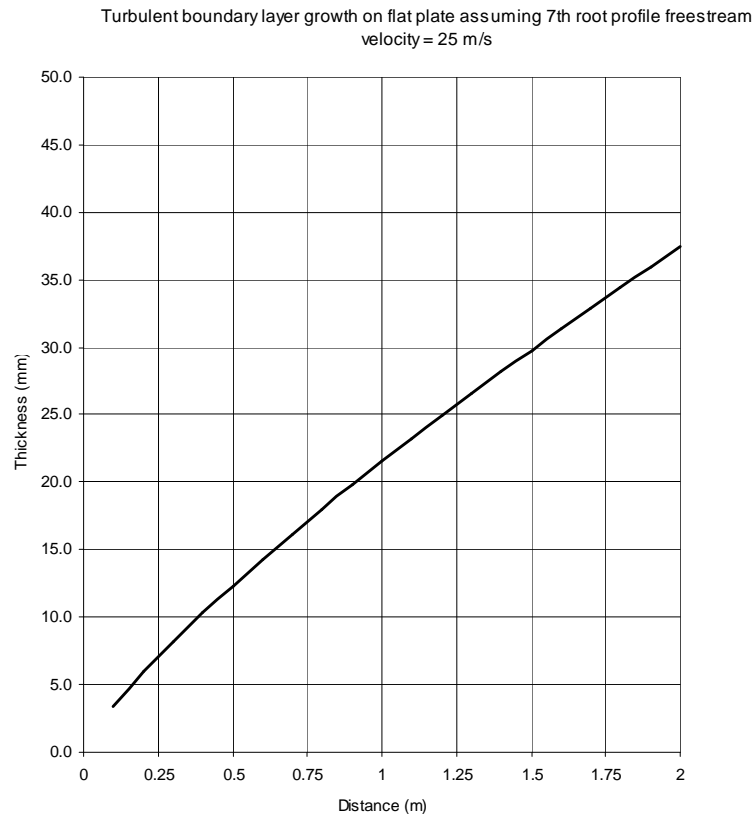
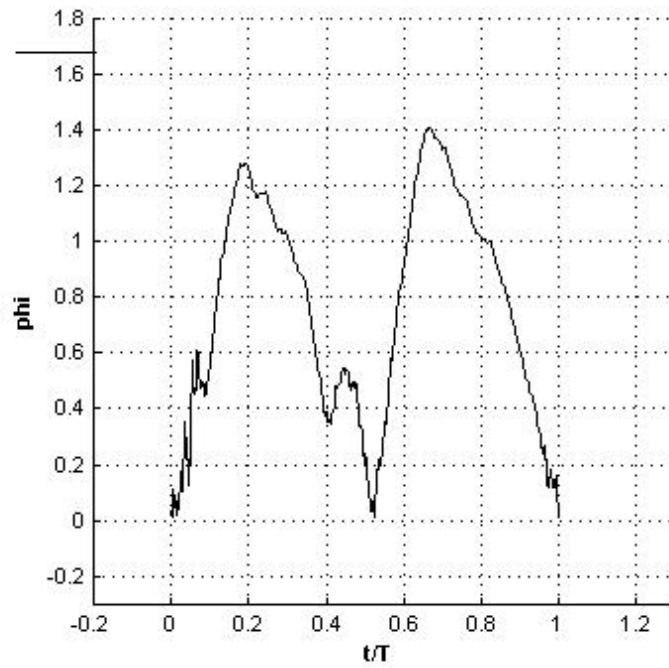
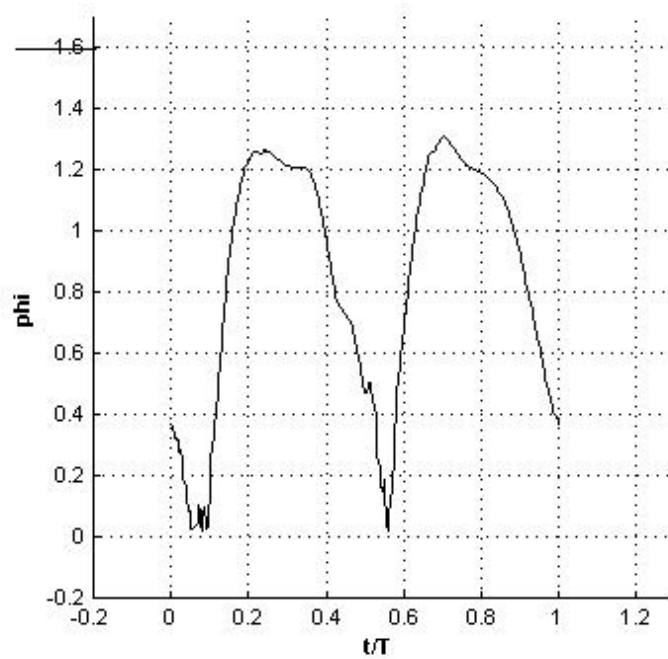


*Figure 119 – Growth of turbulent boundary layer*

There is a need to understand the (time varying) extent and characteristics of the boundary layers entering the test turbine with regard to relating the performance of a turbine tested in the test facility to that a full scale device would achieve. Given that the flow ratio at which the peak efficiency is achieved may have a significant impact on the productivity of a real device, there is a need to understand whether boundary layer development is affecting this point in the test facility. It is concluded that the flowratio for peak efficiency was  $\phi=1.5$ , 0.2 higher than predicted, and it is recommended that further tests are carried out to determine the characteristics of the boundary layers entering the turbine by taking boundary layer measurements using hot wire probes, for example.



T=14 seconds



T=5 seconds

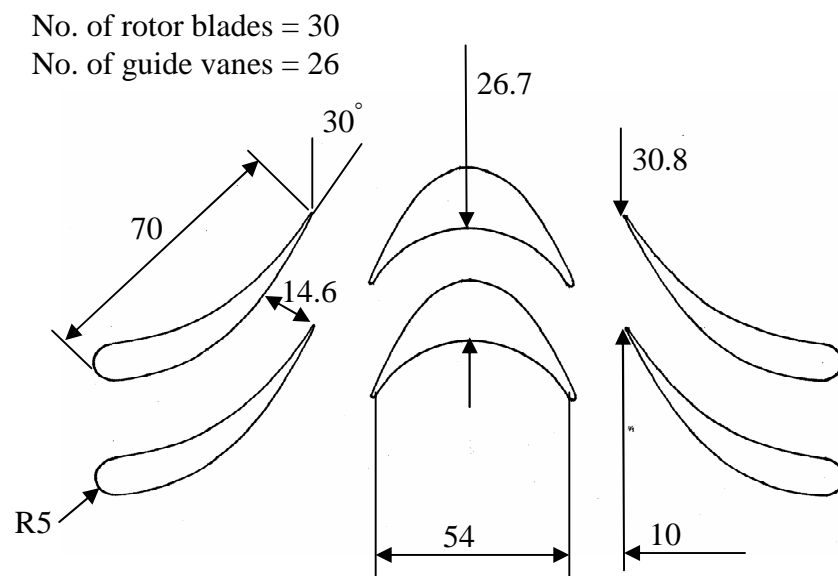
Figure 120 – Comparison of flowratio/period characteristics of 5 & 14 second waves

## 8. Development of Concept for Advanced Turbine

### 8.1 Evaluation of Guide Vane Blowing

#### 8.1.1 Concept

One of the most promising ideas for producing a step change in the performance of an impulse turbine without going to variable geometry was to apply boundary layer blowing to reduce, or preferably remove the separation that occurred on the downstream guide vanes. This was attractive because, as the flow control was required on the downstream guide vanes, it was thought that it might be possible to use the pressure drop across the inlet guide vanes to create a passive blowing system. As stated in section 5.2.5 the guide vane geometry was developed with the idea of installing blowing in mind. However, the initial study into the effectiveness of blowing was carried out by Banks (Banks, 2006) using the ‘airfoil’ geometry of Setoguchi et al (Figure 121) as the author was developing the datum turbine design.



All dimensions in mm

*Figure 121 - Geometry of impulse turbine with airfoil guide vanes (Setoguchi et al, 2001)*

The objective of the initial study was to determine if CFD analysis indicated that the flow could be made to remain attached by the use of a suitably directed air jet, and what efficiency benefits might result in relation to the mass flow and momentum impulse required to achieve this. It was evident that the geometry of the airfoil guide vanes used by Setoguchi et al was not well suited to actually incorporating air jets in reality – even allowing for the fact that it could be scaled up by a factor of 5-10 times in a full scale installation. This was because not only was the airfoil ‘trailing edge’

where the blowing was required very thin, but the section remained very thin up to around the mid chord point. It was thus planned to carry out further simulations with a guide vane design more suited to the installation of air jets if the initial results proved promising, and to begin to answer the questions:

- Where should the blowing be located?
- How much mass flow should be used?
- What angle should the jet be at?
- Should there be more than one jet?

### **8.1.2 Computational mesh**

The datum turbine design process had shown that there were significant 3-dimensional flow features associated with the downstream guide vane. This meant that it was decided to undertake the blowing study as a full 3-dimensional simulation of all 3 blade rows, rather than a more simple 2-dimensional study, as might have been expected. The analysis undertaken was only to assess the potential value of the technique - rather than to actually design a system – and so the blowing ‘slot’ was not explicitly modelled. Instead, for convenience, a surface region was defined on the blade over which an inlet boundary condition was defined. Cartesian velocity components were then specified to allow a parametric study based upon the mass flow rate and direction of the injected flow to be conducted.

The upstream and downstream guide vanes were meshed using ICEM CFD-10 with hexahedral H-type grids incorporating O-grids around the vanes themselves. A  $y^+$  value of 1 was specified to define the first cell height (based on a Reynolds number of  $1 \times 10^6$ , taking the blade chord as the characteristic length) with an expansion ratio of 1.2. A larger number of cells were concentrated around the airfoil ‘trailing edge’ and the blade surface of the outlet guide vane in an effort to capture the flow physics in the injection region more accurately. This meant that the IGV mesh contained approximately 280,000 nodes, and the OGV mesh approximately 525,000.

The rotor was meshed using ANSYS TurboGrid 10.0 with an H/J/L grid topology specified, and included an O-grid around the blade. The tip gap was also modeled by means of a non-matching H-grid in the tip region, with the tip gap specified as 1mm. Values used for  $y^+$ , expansion ratio and minimum face angle were all the same as for the guide vane meshes. The rotor blade mesh contained approximately 260,000 grid points. The inlet and outlet domains were extended upstream and downstream respectively to ensure the results were not distorted by inlet/outlet proximity. The complete domain, showing connectivity is shown in Figure 122.

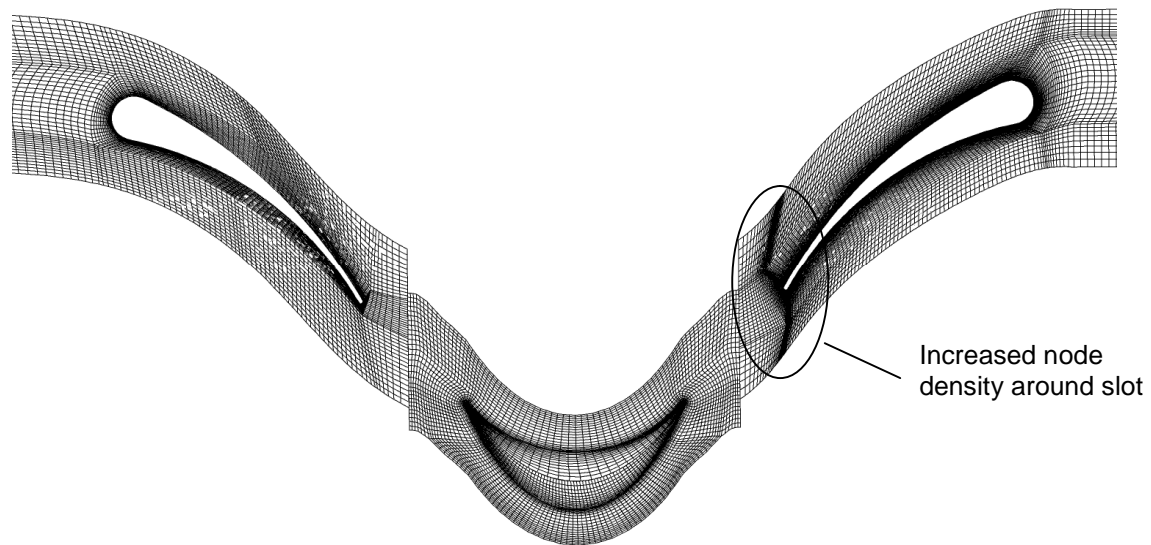


Figure 122 - Plot of complete domain showing connectivity (extended inlet and outlet not shown). (Banks, 2006)

### 8.1.3 Boundary Conditions

A summary of the problem boundary conditions is given in Table 51.

Parameter	Value
No. of Guide vanes	26
No. of Rotor blades	30
Tip radius	150 mm
Hub/Tip ratio	0.7
Tip gap	1 mm
Turbine rotational speed	1900 rpm
Inlet velocity ( $U_1$ )	$17.7 \text{ ms}^{-1}$
Outlet average static pressure	101325 Pa
Slot velocity	See Table 2

Table 51 – Problem boundary conditions

In order to establish confidence in the quality of the CFD solutions a number of CFD simulations were made over a range of flow ratios to obtain a predicted *steady flow* efficiency characteristic which could be compared with the experimental data presented by Setoguchi et al (Setoguchi et al, 2001). The results, plotted in Figure 123, show that best agreement was obtained at a flow ratio of  $\phi=0.7$ . It was therefore decided to take this as the reference flow condition for the investigation of the effect of blowing, although the total-to-static efficiency here was only 31.9 %, whereas the peak obtained in the experiment was 37.9%. A further consideration was that, if the blowing was to be of benefit in reality it would have to be equally effective at off-design conditions as at the peak - particularly at low flow ratio conditions, due to the

oscillatory nature of the flows, and so a lower than peak flow ratio was considered quite acceptable for the study.

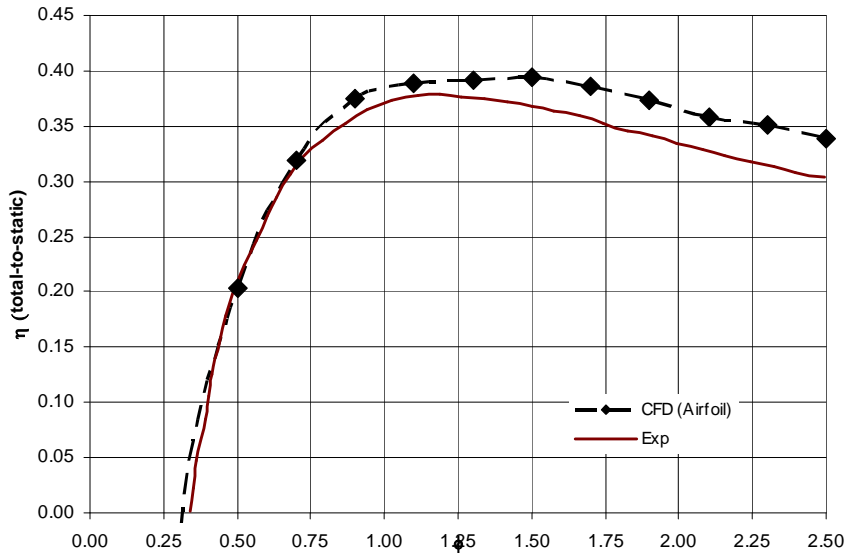


Figure 123 - Comparison of experimental and predicted efficiency characteristics for baseline turbine design

Since very little information on such schemes as that under study was available in the literature, it was decided to employ what ‘best practice’ advice available, which was taken from the work of Culley et al (Culley, Bright, Prahst, and Strazisar, 2004). This suggested that the jet should be located just downstream of the separation onset, and that the jet angle should be approximately 30° to the airfoil surface. The nature of the geometry meant that there was likely to be little error in identifying the point of separation using CFD, and so determination of a suitable point for fluid flow injection just downstream of the airfoil ‘trailing edge’ (identified as the point ‘A’ in Figure 124), from a flow solution calculated without blowing was straightforward.

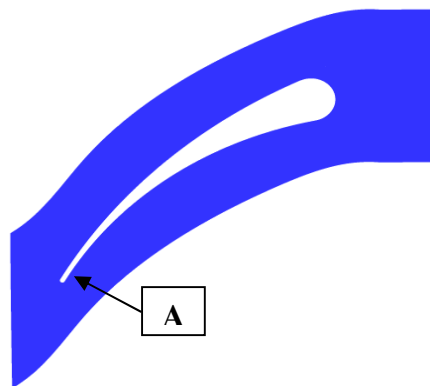


Figure 124 - Location of the slot used to blow air from (Banks)

The ‘slot’ modelled to provide the jet was defined as being 0.4mm wide, and extended along the full blade span from hub to tip. A slot width of 0.4mm was chosen as this was the minimum width that it was likely to be possible to incorporate into a test model. This meant that the ratio between the length of surface between the slot and the leading edge of the airfoil (L), and the slot width h, was L/h=175.

In order to demonstrate the potential effectiveness of flow control, it was necessary to investigate the mass flow and momentum impulse required. To this end, simulations at a range of jet velocities were carried out as detailed in Table 52. The simulations were run in CFX -10 using the shear stress transport turbulence model. Convergence was typically achieved after about 100 iterations, although only to a level of about  $10^{-4}$ . This lower than usual level of convergence was not particularly surprising, as most of the flow simulations contained quite large separations, and previous simulations in the project suggested they contained a considerable amount of unsteadiness. This said, the all the global imbalances were below 0.01% for all the cases.

### 8.1.4 Results

The 3-dimensional CFD simulation results obtained for the single slot blowing are shown in Table 52. The results are expressed in terms of the parameters used by Culley et al (Culley et al, 2004), i.e. the momentum coefficient, velocity ratio, mass flow ratio and total to static efficiency (see Appendix B), where, the momentum coefficient was defined as:

$$C_{\mu} = \frac{2h}{L} \left( \frac{U_{jet}^2}{U_1^2} \right)$$

The results in Table 52, and the plot of performance improvement with impulse coefficient in Figure 125, demonstrated that the CFD analysis predicted that the concept of bringing about improved efficiency by means of blowing was a valid one. All of the simulations carried out showed a rise in efficiency over that achieved without blowing (baseline 31.9%).

$C_{\mu}$	$U_{jet}/U_1$	$m_{jet}/m_1$	$\eta$	$\Delta\eta$
0	0	0	31.9%	0
0.079	2.69	0.0091	32.4%	0.5%
0.179	4.06	0.0137	33.3%	2.4%
0.321	5.44	0.0182	35.5%	3.6%
0.504	6.81	0.0228	37.1%	5.2%
0.728	8.19	0.0273	37.8%	5.9%
0.992	9.56	0.0319	38.7%	6.8%
1.297	10.93	0.0364	39.5%	7.6%

*Table 52 - Results of single slot blowing*

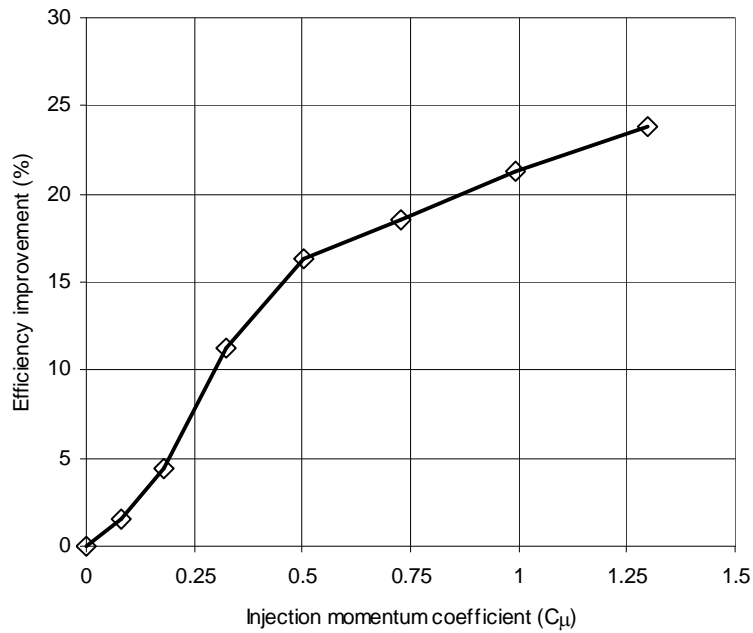


Figure 125– Sensitivity of performance improvement to injection momentum

Qualitative examination of the solutions showed that the improved efficiency resulted, as expected, from the jet reducing the extent of the flow separation in all cases, and at the highest flow rates effectively preventing any separation. This is demonstrated by the comparison shown in Figure 126, which shows that elimination of the separated region was predicted due to the presence of the jet. The effect of the jet is shown more graphically in Figure 127, which is a streamline plot of the trailing edge region of the OGV. This shows how the flow is predicted to remain attached, despite the highly adverse angle at which it encounters the vane.

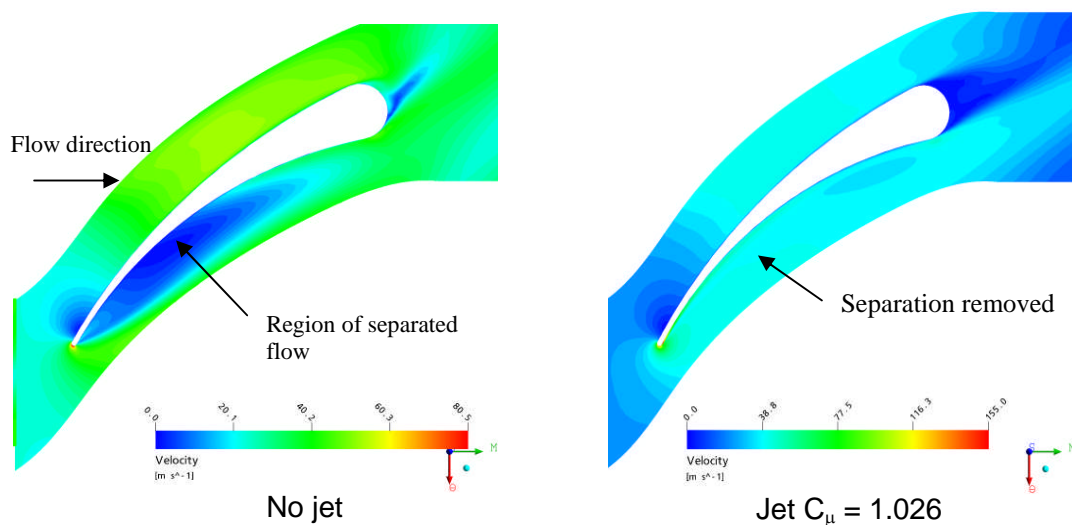


Figure 126 - Velocity contour plots around OGV without and with jet (Banks)

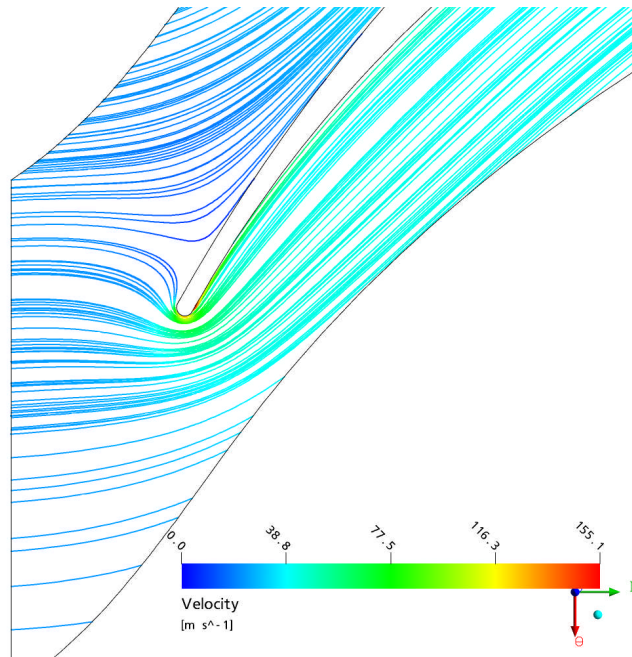


Figure 127 - Streamline plot around OGV trailing edge for  $C_{\mu} = 1.026$  demonstrating attached flow (Banks)

To assess whether there was a net benefit or loss due to the addition of the blowing mass flow, the reduction in pressure drop across the turbine relative to the baseline pressure drop was computed for all values of jet mass flow, and divided by the original pressure drop without blowing. These values were then plotted against the corresponding ratio of jet mass flow rate to freestream mass flow rate, and the results are shown in Figure 128.

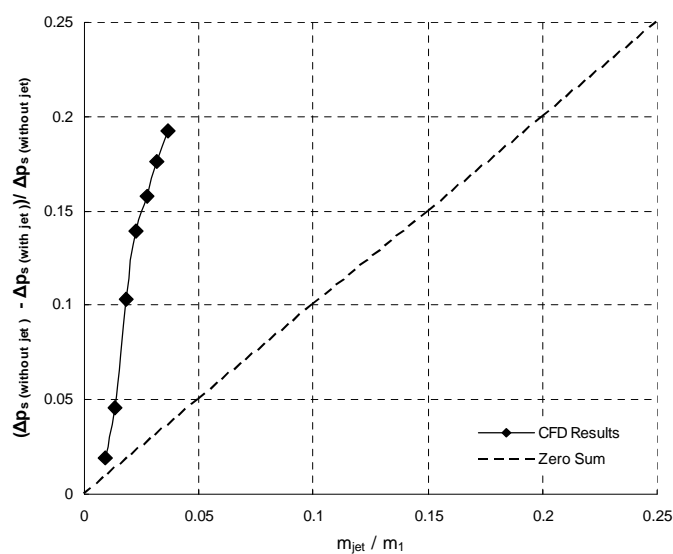


Figure 128– Graph of massflow ratio against pressure drop reduction ratio

The 45° line in Figure 128 indicates a zero net benefit i.e. the mass flow required to bring about a 1% reduction in pressure drop creates a 1% reduction in work done. Values above the line in Figure 128 indicate a net benefit from injecting mass to provide flow control, while values below the line indicate that the benefit is outweighed by the cost. The resulting plot showed a large benefit for the range of mass flows calculated, although the benefit from increasing the slot mass flow (or impulse coefficient, as shown in Figure 125) reduced when the jet mass flow was more than 2.3% of the freestream mass flowrate (or the impulse coefficient was greater than 0.71).

### 8.1.5 Further Analyses

The encouraging results obtained from the study conducted using the Setoguchi airfoil geometry, led to some further analyses based upon the geometry of the datum turbine. It was noted in section 5.2.5 that the guide vane geometry was developed with the possible desire to install a blowing system in mind, and so the trailing edge of the guide vanes was made 4.2mm thick. In addition, the width of the simulated jet was increased to a more realistic 0.6mm.

The same approach was applied to the simulation of the jet and the setting up of the computational grids as for the Setoguchi geometry. In all simulations were carried out with jets at 4 locations designated A-D and shown in Figure 129.

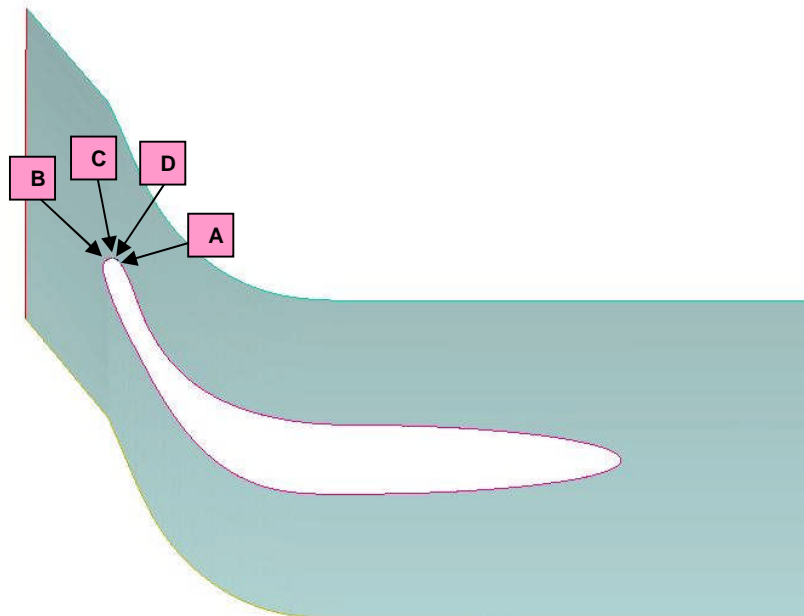


*Figure 129 – Locations of simulated jet (Banks)*

The jet was initially located at position ‘A’, just downstream of the separation onset in the flow solution calculated without blowing. Simulations were carried out at two different jet velocities, but maintaining the same jet angle. The jet location was then moved to position ‘B’. This was done to get it as close as possible to the point of separation in an effort to suppress it completely. In this position the jet angle and velocity was varied. Finally, a third position ‘C’ was tried, which was between the first two, at which one calculation was made. The boundary conditions for the analyses were the datum turbine design point conditions, i.e. those which gave  $\phi = 1.0$ , and  $\eta = 41.1\%$ . The results for the analyses are given in Table 53. It can be seen that blowing at position ‘A’ resulted in a net loss, believed to be due to the slot being too far downstream of the point of separation. The best result was for case B2 which gave an 8.3% increase in efficiency from a jet of 1% of the bulk mass flow rate.

Case	Jet angle (deg)	$C_\mu$	$U_{jet}/U_1$	$m_{jet}/m_1$	$\eta_s$	$\Delta\eta_s$
No jet	0	0	0	0	41.1%	0%
A1	-45	0.176	4.13	0.0104	38.0%	-3.1%
A2	-45	0.397	6.20	0.0157	38.9%	-2.2%
B1	-16	0.213	4.54	0.0038	44.6%	3.5%
B2	-13	0.540	7.23	0.0104	49.4%	8.3%
C	-25	0.480	6.82	0.0188	45.4%	4.3%

*Table 53 – Results Single slot blowing on datum turbine guide vane*

A comparison of the results in Table 53 with those in Table 52, showed that the result for B2 was significantly better than the best improvement obtained for blowing on the Setoguchi geometry: 8.3% for 1% mass flow injection and  $C_\mu=0.54$ , as compared to 7.6% from 3.6% mass flow injection and  $C_\mu=1.83$ .

In addition to the single jet simulations above, it was decided to investigate whether multiple jets might achieve a greater effect with lower momentum input. To determine this, 3 further cases were run with 2 jets located at positions ‘B’ and ‘D’, with different mass flows. Jet ‘B’ was angled at -16 degrees to the axial, and jet ‘D’ at -42 degrees. The results in Table 54 showed that using two slots did produce greater improvements, but when the positive results from the single and double slot blowing were combined it was seen that, for the limited cases run, using multiple slots did not lead to a lower injection momentum coefficient for a given improvement. In fact the results indicated a linear relationship between efficiency and injection momentum coefficient (Figure 129). Nevertheless, the maximum improvement of 14.2% from injection of 2% bulk mass flow was very significant, and the improvements were seen to be substantially better than for the Setoguchi airfoil geometry.

Case	$C_\mu$	Slot B $U_{jet}/U_1$	Slot B $U_{jet}/U_1$	$m_{jet}/m_1$	$\eta_s$	$\Delta\eta_s$
No jet	0	0	0	0	41.1%	0%
M1	0.789	6.19	6.17	0.0195	52.3%	11.2%
M2	0.904	7.52	7.52	0.0191	55.3%	14.2%
M3	0.505	4.94	4.94	0.0156	48.9%	7.8%

*Table 54 – Results for double slot blowing on datum turbine*

Although no peak in efficiency due to injected momentum was indicated by the double slot results, the amount of additional benefit that might be obtained by further increases in injection momentum coefficient might be limited. This is because at the highest value used the flow on the guide vane was substantially attached along the full length of the guide vane.

### **8.1.6 Discussion**

The results obtained above have predicted that blowing may be used to effectively remove the separation that occurs on the downstream guide vanes of a fixed geometry OWC impulse turbine arrangement. Moreover, the results have shown that the injection momentum required is significantly influenced by the choice of injection location and by the guide vane geometry, such that relatively small changes in injection position or guide vane design can lead to large increases in the effectiveness of blowing.

The best result achieved produced almost 35% improvement in performance from an injection mass flow of 2%. Although the velocity ratios of the jets appeared relatively high at 7.5, this only represented a nozzle pressure ratio of 1.17, or a pressure difference of 20kPa. If the efficiency continued to increase as shown in Figure 130 then 60% efficiency could be achieved by injection of 3% additional mass flow. This is a level of performance which would begin to have a large impact on the economic viability of OWC plants.

The cases calculated so far have shown a significant performance benefit due to blowing at the off-design flow condition of  $\phi = 0.7$  for the airfoil geometry and at the datum turbine design point. Further calculations are required to verify that similar benefits are obtained for a particular geometry across the flow range.

Whilst the CFD results are very encouraging, they do have to be treated with some caution for 2 reasons. The first is that, as noted previously, the testing undertaken in the Saga University facility the maximum Reynolds number achieved was only  $0.4 \times 10^5$ . The second, more important factor, is because of the limitations inherent in the boundary layer modelling in the present CFD computations. Fundamental theoretical and experimental work on the re-attachment of 2-dimensional jets onto inclined flat plates presented by Newman (Newman, ) supports the use of a jet angle

of 30 degrees to achieve rapid flow re-attachment. However, it also suggests that the entrainment mechanism which leads re-attachment is dependent upon Reynolds number calculated as:

$$Re = \sqrt{\frac{(P - p_{\infty})h^2}{\rho v^2}}$$

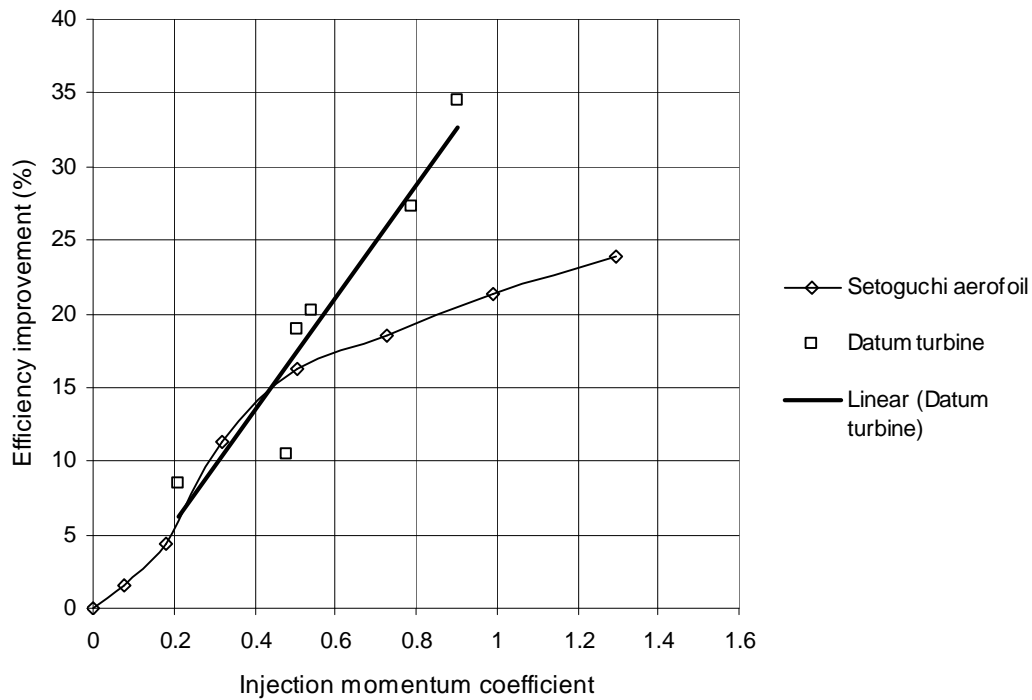


Figure 130 – Sensitivity of performance to injection momentum

The work of Bourque cited by Newman (Newman, ), suggested that the entrainment behaviour was independent of Re, for values of  $Re > 5 \times 10^3$ . Evaluation of Re for cases calculated gives maximum Re of only  $3 \times 10^3$ . This indicates a need for further analysis and experimental data to validate the physics of the simulations, and to determine the magnitude of scale effects that would be associated with testing at the scale of the baseline turbine configuration, and whether there is a need for the blowing concept to be validated by testing at a larger scale. The lower than usual level of convergence due to suspected fundamental unsteadiness, also indicates a need for experimental data to verify the true nature of the flow. The issue of fundamental unsteadiness, and need for an understanding of how the blowing system would perform in irregular flow conditions, means that the experimental data should perhaps ideally be acquired in the HydroAir test facility which would enable representative irregular oscillating flow conditions to be produced and measured, but more fundamental work is required before going to the complexity and expense that this would involve.

In order to carry the work further, there is a need to carry out further analyses to determine how guide vane design influences blowing performance. Consideration also needs to be given to the practicality of implementing the technique. Although good results have been obtained with thick guide vanes, the complexity and losses involved in creating a full scale system may be prohibitive. The fact that the separation occurs on the downstream guide vanes means that the pressure drop across the upstream guide vane rows may be used to pump the required mass flow to the downstream ones, or used to minimize the amount of additional work input required to raise the total pressure to the level required. If no loss is assumed in passing the mass flow to the downstream guide vane, the pressure drop across the datum turbine is only sufficient to provide a jet velocity of  $U_{jet}/U_1 \sim 4$ . The assessment of the benefit of blowing has not so far considered the additional work that would have to be done to provide the simulated jet velocities. A simple analysis was carried out for the best case obtained so far, i.e. the double slot case 'M2' in table 54, which gave an efficiency of 55.3%. Firstly, the nozzle pressure ratios required to produce the jet velocities based on the exit static pressure were determined, which enabled the volumetric flowrates to be calculated, and hence the additional QAP associated with the jets to be determined. The ideal work required to compress the air in the jets from the inlet conditions to the required nozzle total pressure was then calculated. When this was added into the efficiency calculation it was seen that the efficiency had dropped to 46% - a 5% net gain, but 2/3 of the reduction was due to the additional QAP terms, rather than the additional work. It might be that the use of a (more complex) pulsed jet system could reduce both the mass flow and work input required. Further work is required to assess the impact of the probable duct losses and compression required to get the higher jet velocities. In addition there is a need to consider the likely degradation in system performance due to environmental effects.

From the analysis that has been carried out, it is apparent that there are many guide vane geometries, slot locations, and jet conditions that could be evaluated. This means that the problem of finding the most appropriate guide vane and of jet arrangement might be well suited to application of an optimisation process

The representation of the slot in the present CFD analyses was highly idealised, and further development of the concept will have to consider the design of a slot which is less than full span, and the geometry of the ducting within the blade and of the slot itself, required to produce the uniform spanwise jet at the desired angle. There is some scope for considering different slot widths, but the slot width chosen is likely to be largely driven by manufacturing considerations (particularly for model testing), rather than relative effectiveness, as the jet velocity has a far greater impact on the impulse coefficient obtained.

### **8.1.7 Summary**

There are a number of conclusions which may be drawn from the work carried out so far:

- CFD analysis predicts that blowing may be used to effectively remove the separation that occurs on the downstream guide vanes of a fixed geometry OWC impulse turbine arrangement
- The effect of the injected mass flow is significantly influenced by guide vane geometry and jet location.
- For the 2 geometries analysed re-attachement and improvements in efficiency of 25% and 34.5% were obtained by the addition of 3.6% and 2% additional mass flow respectively.

The work carried out so far has indicated a need for the following further work:

- There is a need to verify that the predicted benefits of blowing are maintained across the operating range of the turbine.
- There is a need to consider how the predicted benefits are affected by a more detailed analysis of the additional work required to provide the jet velocities simulated, and whether it is practical to provide these in reality.
- There is a need to consider whether pulsed jets could be more efficient than steady ones.
- Experimental data is required to verify the accuracy of the present CFD analysis, and to assess the magnitude of scale effects associated with testing blowing configurations at sub-scale.
- There is a need for testing of the concept initially in a cascade type arrangement, and then in a facility that enables the fundamental unsteadiness of the flow to be assessed, and how the benefits of blowing would be affected by real irregular oscillating flow conditions.
- The possible degradation in system performance due to environmental effects needs to be considered.

## 8.2 Varying Radius Duct Concept

### 8.2.1 Physical Basis

The problem with the basic impulse turbine configuration with fixed guide vane rows on either side of the rotor, is that large scale flow separations occur in the downstream guide vane row. The predicted extent of the flow separation at the *peak efficiency* condition for the datum turbine geometry is shown in Figure 131.

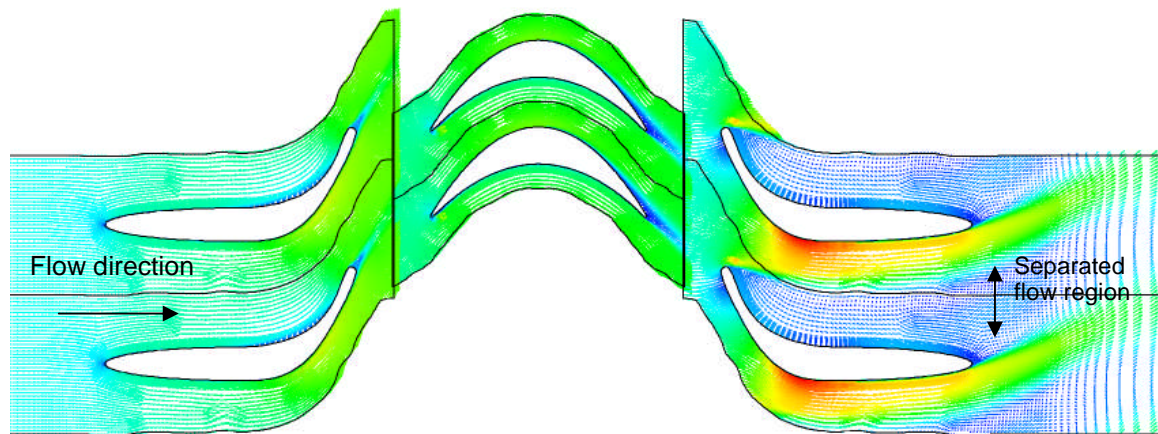


Figure 131 – Velocity vectors for datum turbine geometry,  $\phi = 1.0$

These flow separations occur because the guide vanes are not aligned with the rotor exit flow, and cause the pressure drop ( $\Delta p$ ) to increase by more than a factor of two compared to a conventional uni-directional arrangement. This means that the efficiency of the turbine is greatly reduced as:

$$\eta = \frac{\omega T}{Q \Delta P}$$

In order to improve the performance of the turbine a means must be found to prevent the flow separation that occurs, or to reduce the total pressure loss associated with the downstream guide vane row.

In the design of pipe systems it is usual to carry out the analysis using loss coefficients, where the loss coefficient of any component in the system is defined by:

$$\text{Loss coefficient, } K = \frac{\Delta P}{\frac{1}{2} \rho v^2}$$

where  $\Delta P$  is the total pressure drop across the component,  $v$  the inlet velocity to the component, and  $\rho$  the density of the fluid. When the flow may be considered to be incompressible, then  $K$  is replaced by  $K_0$  the loss coefficient in incompressible flow, and the total pressure drop may be replaced by the static pressure drop  $\Delta p$ . The CFD analyses conducted in defining the datum turbine showed that the flow may be assumed to be incompressible, and so if we consider the downstream guide vane row to simply be a system component, then the static pressure drop across it can be expressed as:

$$\Delta p = \frac{1}{2} \rho v^2 K_0$$

where  $K_0$  is the constant loss coefficient for the downstream guide vane row. Hence it can be seen that:

$$\Delta p \propto v^2$$

This means that if the velocity of the flow through the guide vane row is reduced then this results in a much larger reduction in the pressure loss.

In order to maintain continuity if the area of the flow annulus is increased then the velocity of the flow through the guide vanes will be reduced. One way of doing this is to keep the blade heights the same but to move them outwards to a greater diameter, so the 2 rows of guide vanes are placed at a greater radius than the rotor, and geometry of the flow annulus is as shown in Figure 132.

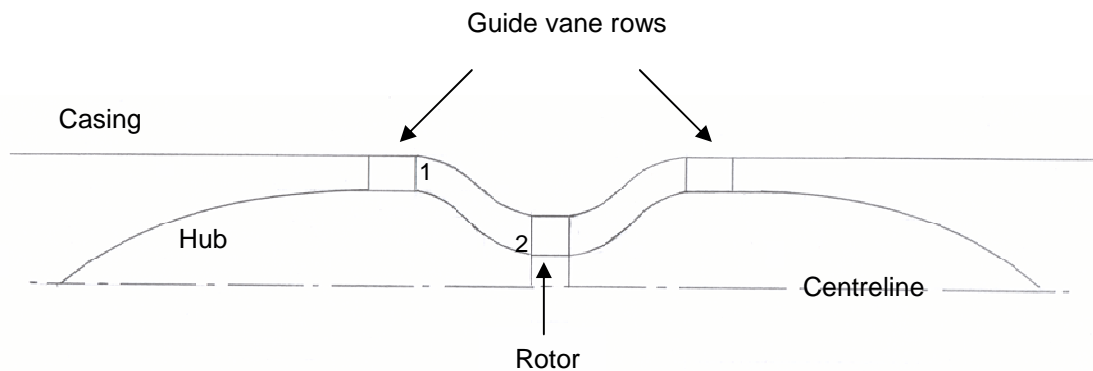


*Figure 132 -Flow annulus geometry for offset guide vane rows*

If the annulus between the outlet of the inlet guide vane row and the inlet to the rotor are considered (points 1 and 2 in Figure 132) then there must be both continuity of flow and conservation of angular momentum (ignoring frictional and viscous effects), i.e. in any axial plane:

$$\begin{aligned} \dot{m} &= \text{constant} \\ \omega r &= \text{constant} \end{aligned}$$

If we consider the equation of continuity, then this may be re-written as:

$$\begin{aligned}\dot{m} &= \rho v A \\ &= \rho v (2\pi r h)\end{aligned}$$

where  $r$  is the mean radius of the blade row, and  $h$  is the blade height. If the blade height is the same at planes 1 and 2, and the flow is incompressible then:

$$v_1 r_1 = v_2 r_2$$

Now,  $\omega_1 r_1 = \omega_2 r_2$ , and substituting for  $r_1$  and  $r_2$  gives:

$$\frac{v_1}{\omega_1} = \frac{v_2}{\omega_2}$$

This shows that the ratios of the axial and whirl components of velocity are the same at both  $r_1$  and  $r_2$ . This means that if the guide vanes are moved out to a greater mean radius than the rotor blades without changing the blade height the axial velocity will be reduced, but the vector triangles for the blade design will remain the same.

It is expected that if the mean radius of the guide vane rows is increased from  $r$  to  $r'$ , then the pressure drop associated with the downstream guide vane row will be reduced from  $\Delta p$  to  $\Delta p'$  according to the relationship:

$$\Delta p' = \left(\frac{r'}{r}\right)^2 \Delta p$$

Hence, if  $r'$  is twice  $r$ , then the pressure loss in the guide vane row will be reduced to a quarter of its previous level. The actual benefit would be expected to be less than this due to the losses caused by viscous effects, nevertheless, it would still be expected to be quite significant.

The simple analysis presented above, suggested a physical basis for a turbine arrangement which would have significantly better performance than the impulse turbines with fixed guide vane rows which had been studied by other researchers. However, it said nothing about the geometry of the ducts – and their associated losses - required to link the offset guide vane and rotor blade rows and the real limitations on performance which would exist. What was evident was that it was worth undertaking a CFD study to assess the benefits of this novel concept. It is to be noted that this approach does not lead to an improvement in the flow through the downstream guide vanes, it merely reduces the impact of the poor flow on the overall performance.

### 8.2.2 Initial test case

The novel nature of the concept meant that there was no design guidance available in the literature with regard to determining the geometry for the varying radius ducts and the maximum amount of radial offset that could be used. The initial approach taken to assessing the validity of the concept was therefore to select a target performance that represented a significant improvement, but that was associated with ostensibly modest duct geometries that would not be expected to lead to problematic flow conditions. It was thus assumed that the datum peak efficiency performance was 40%, and that it was desired to develop a turbine geometry with varying radius ducts that would have a peak efficiency of 60% with the same input flow. This meant that (ignoring other losses) the overall pressure drop across the turbine would have to be reduced to:

$$\Delta P'_{device} = 0.66 \Delta P_{device}$$

where  $\Delta P$  is the total-to-static pressure drop. However, for the purposes of evaluating an initial test case, it is assumed that as the inlet velocity is low (25 m/s at the design point) the total-to-static pressure drop can be replaced by the change in static pressure, and that the additional duct losses will remain small in comparison to the losses across the downstream guide vanes, so splitting the static pressure drop across the inlet guide vane and rotor ( $\Delta p_{turbine}$ ), and the outlet guide vane rows ( $\Delta p_{OGV}$ ) we have:

$$0.66 = \frac{\Delta p_{turbine} + \Delta p_{OGV'}}{\Delta p_{turbine} + \Delta p_{OGV}}$$

If it is now assumed that for the datum configuration  $\Delta p_{OGV} = \Delta p_{turbine}$  (as the pressure drop was seen to over double when the outlet guide vanes were added, section 5.2.4), then:

$$\Delta p_{OGV'} = 0.33 \Delta p_{OGV}$$

and

$$\frac{v_2}{v_1} = \sqrt{0.33}$$

and

$$r_2 = \frac{r_1}{0.58}$$

It was decided to utilise the HydroAir datum turbine geometry as the test case. The mean radius of this was 0.273m, and so the new mean radius required for the guide vanes was 0.471m (this equated to a radial displacement of  $h_r = 3.6$  blade heights).

Once the blade geometry and offset required had been selected, the ducts to link the blade rows had to be defined. It was decided that the connecting duct would be defined between the guide vane blades and rotor blades without incorporating

additional parallel flow sections at the inlets/exits of the blade rows, but that a smooth change in radius was required. The approach taken was thus to join the mean radii of the blades rows with a Cosine function, and to maintain a constant radial height along the duct. The radius of the mean line along the duct was thus defined by the function:

$$r = r_{mid1} + \frac{h_r}{2} \left( 1 + \text{Cos} \left( \frac{\pi x}{L} \right) \right)$$

where  $L$  was the axial length of the duct, and  $r_1$  was the mean radius of the rotor. The initial axial length of the duct was chosen to be  $h_r = 4$  blade heights. The final consideration was to extend the annulus geometry upstream and downstream by  $1 \times$  axial blade chord, and downstream by  $2 \times$  axial chord of the guide vane to ensure that the inlet and outlet boundaries were sensibly far away in the 3-dimensional CFD analysis. The choice of these parameters gave the duct geometry illustrated in Figure 133, in which the guide vane hub casing geometry is shown in black, the rotor hub casing geometry in green, and the blade sections in blue. The other factor that needed to be considered was that as the mean radius of the guide vane rows was increased, the number of guide vanes needed to be increased to maintain the same space/chord ratio, and this was done according to the relationship:

$$n'_{\text{guide vanes}} = \frac{r'}{r} n_{\text{guide vanes}}$$

The initial CFD results were encouraging, corresponding closely to expectation, and so a number of further CFD calculations were carried out to see how the efficiency varied as the radius of the guide vanes was varied, but the axial length of the duct was kept constant. These analyses were carried out by Davin (Davin, 2006). The results plotted in Figure 134 showed that the variation in efficiency was parabolic, with a peak of 57.3% for a radial offset of  $4h$ .

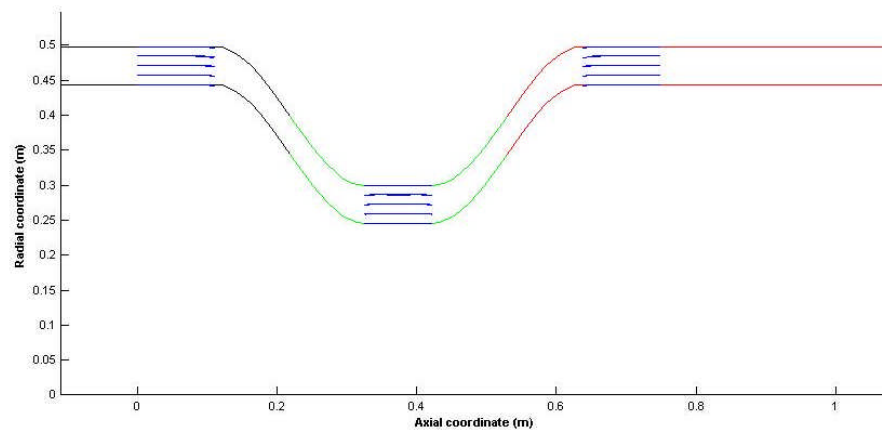
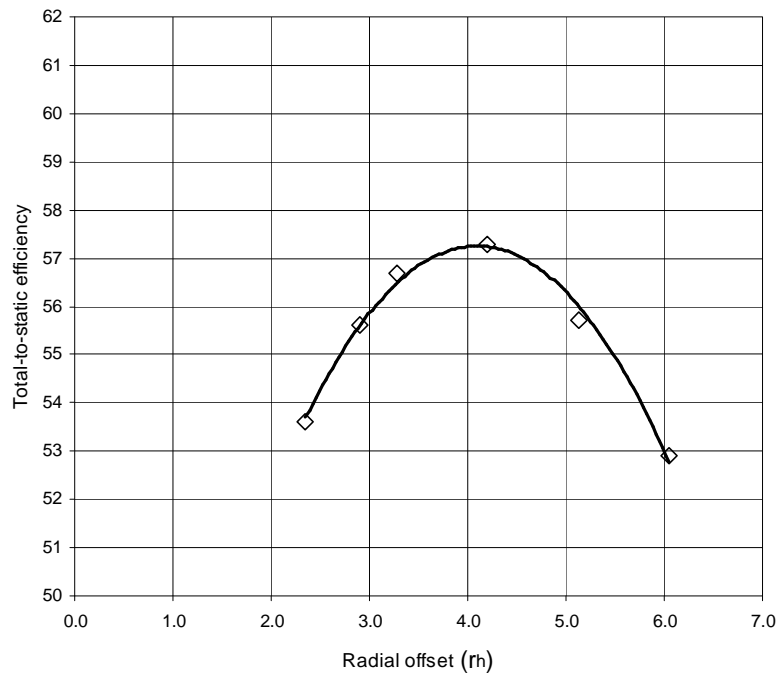


Figure 133 – Initial geometry for datum blade design with varying radius duct,  $h_r = 3.6$ ,  $h_r = 4$



*Figure 134 - Variation of efficiency with guide vane radial offset for axial duct length of 4h*

### 8.2.3 Improved duct geometry

The 3-dimensional CFD results obtained for the turbine incorporating the initial duct geometry were very encouraging, but they showed that further work was required to determine if a duct geometry could be found that would enable the target peak efficiency of 70% (Herring and Banks, 2007b) to be achieved. It was intuitively apparent that better flow uniformity and hence better overall duct performance might be achieved, if the duct walls were kept at a constant distance apart relative to a line perpendicular to the duct centreline. The duct geometry code was thus modified to produce the new geometry, which is shown in Figure 135, and may be compared with that in Figure 134.

When the previous cases were re-computed with the duct geometry a significant benefit was seen, with a predicted increase of 3.3% for the optimum offset of 4h as shown in Figure 136. From these results it was concluded that the new duct geometry would be used as the basis for all further work in developing the concept.

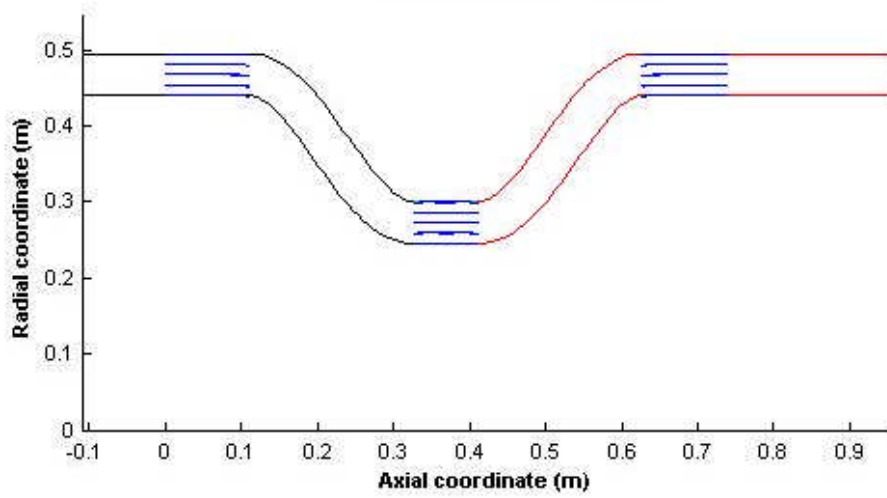


Figure 135 – Modified duct geometry

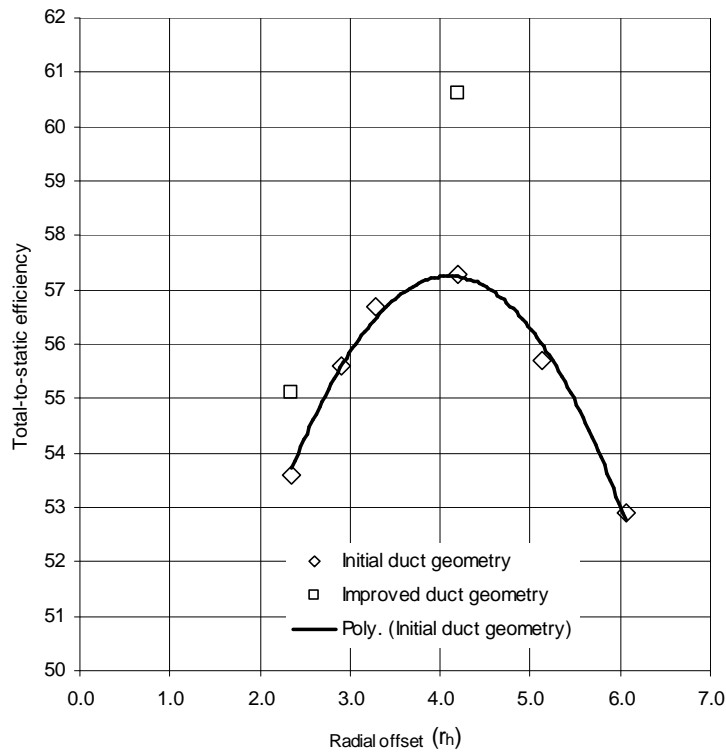


Figure 136 – Effect of modifying duct geometry for axial duct length of  $4h$

### 8.2.4 Increasing Efficiency by increasing duct length & offset

Once the improved duct geometry had been validated by the CFD analyses, an examination of the effect of changing both the axial length and radial offset was begun. This quickly led to a predicted efficiency of 65.5% for a duct length of 5h with radial offset of 6h. At this point it was deemed prudent to produce an efficiency characteristic for the geometry over a range of flow ratios, in order to reveal any problems with the concept at off-design conditions or in the methodology adopted in constructing the CFD model. A comparison of the computed characteristic with that predicted for the HydroAir datum turbine configuration is shown in Figure 137.

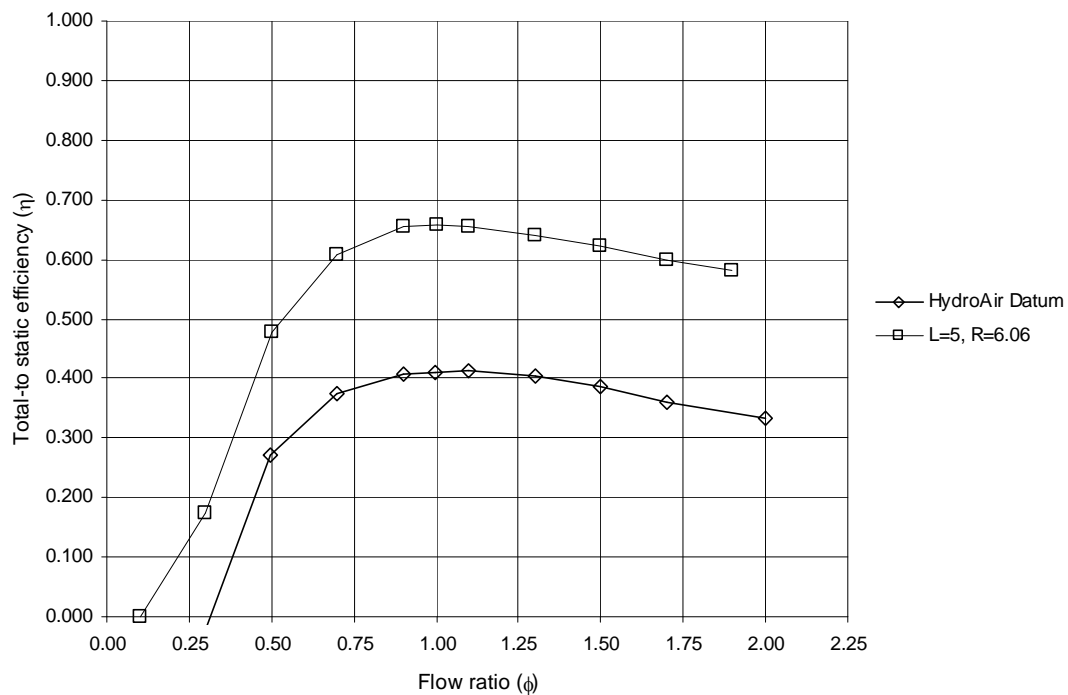


Figure 137 – Efficiency characteristics for datum configuration & configuration with varying radius ducts

Figure 137 shows that that the shape of the characteristic has remained the same - as might be expected, as the blade profiles and space/chord ratios are unchanged - and that the level of performance has simply been raised across the flow range. However, it also indicates a modest expansion of the flow range at the low end. On the basis of the results in Figure 137, it was concluded that the concept remained valid and that the quality of the CFD results was consistent and sensible.

Once confidence was established in the characteristic results, a series of solutions were calculated to determine the variation in efficiency with guide vane radius for a duct length of 5h. The results of these calculations are shown in Figure 138. As with the results for the duct length of 4h, it was seen that the results had a parabolic profile, with the maximum calculated efficiency of 68.9% occurring at a radial offset of 8.83h.

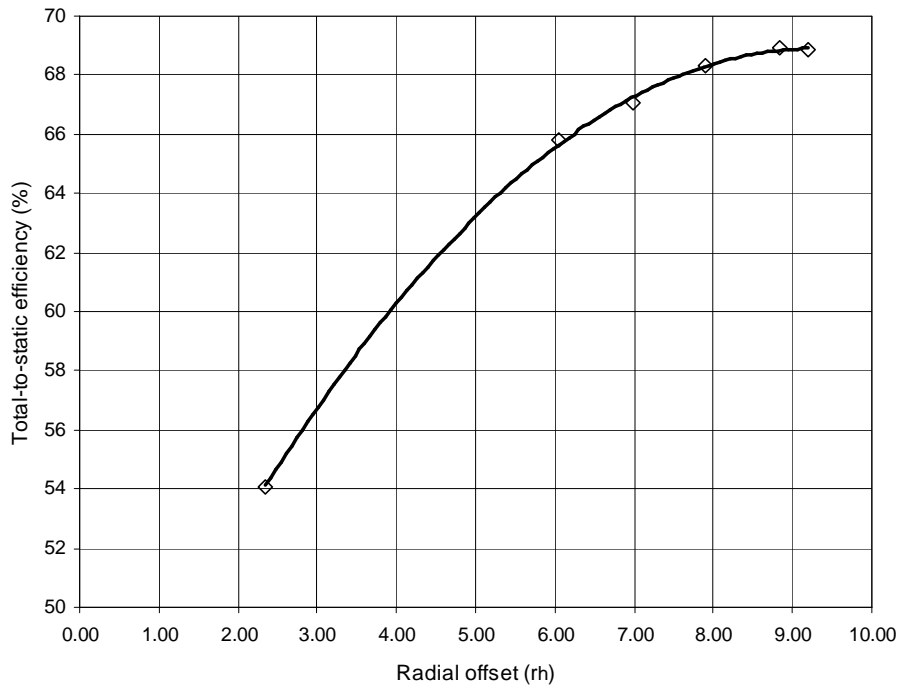


Figure 138 – Variation in efficiency with guide vanes at duct length of 5h

The benefits predicted by increasing the duct length to 5h suggested that further benefits could be obtained by further increases in length, and so a series of solutions were computed for ducts of axial length 6h. It was expected that with a duct length of 6h the maximum efficiency would be achieved at a greater radial offset than with the duct length equal to 5h. However, this was not the case, as it was found that the peak efficiency of 69.9% occurred at a radial offset of 7.91h.

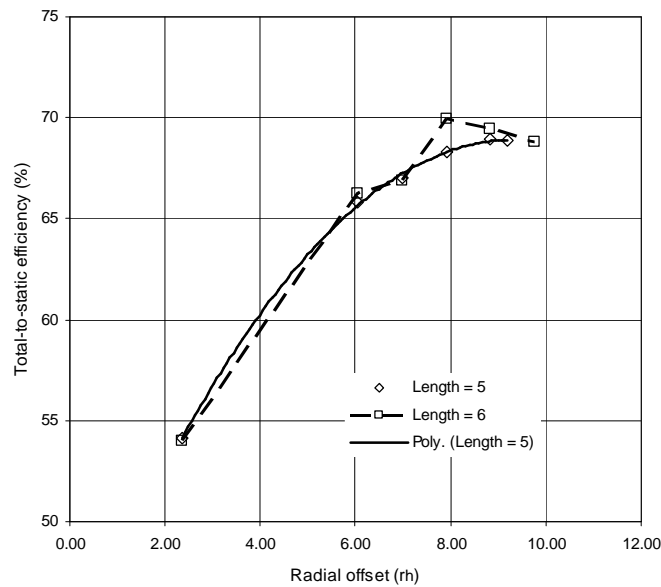


Figure 139 – Variation in efficiency for duct lengths  $h_1 = 5$  and 6

Closer examination of the CFD solution for the peak efficiency point obtained for the 6h duct, showed that the inflow to the rotor was not as well aligned as would be expected. The angular deviation observed suggested that the guide vane space/chord ratio was too high. A number of further solutions were thus calculated with increased numbers of guide vanes. The results of these confirmed that a small increase in performance of 0.4% to 70.3% could be obtained by increasing the number of guide vanes from the expected number of 72 to 74. The variation in peak efficiency with number of guide vanes was again parabolic as shown in Figure 140.

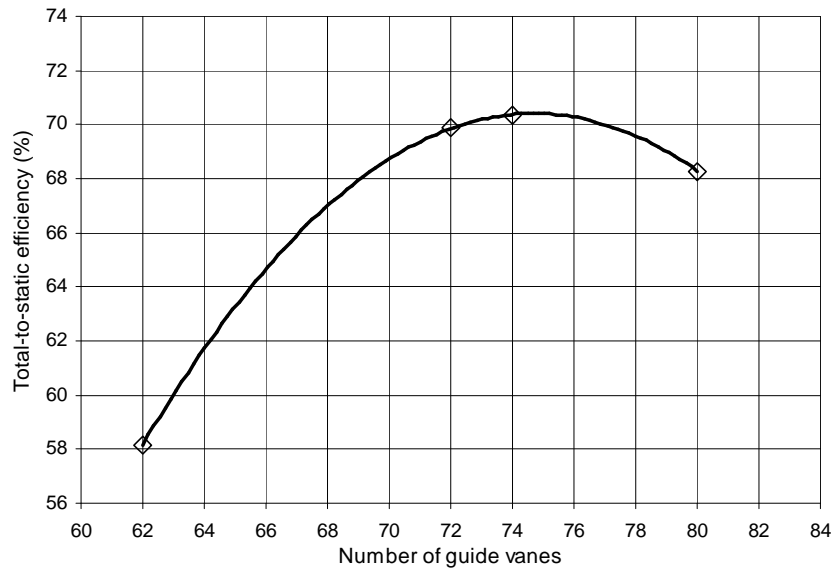


Figure 140 – Variation in efficiency with number of guide vanes,  $h_l = 6$ ,  $h_r = 7.91$

It was concluded from this that for axial duct lengths greater than 5h, and radial offsets greater than 6h, that more guide vanes would be required than would be predicted by the proportionate increase from the datum radius alone. Further computations were thus made to determine the optimum number of guide vanes for ducts of length 6h, and radial offsets greater than 6h. Similar parabolic variations were found for each radius. The variation in number of guide vanes with radius compared to the number required for duct length 5h is shown in Figure 141.

The completion of the analysis of the variation in the number of guide vanes required for the 6h duct length enabled a plot to be which defined the optimal performance in terms of efficiency that could be achieved by varying the radial offset of 5h and 6h length ducts. This plot is shown in Figure 142

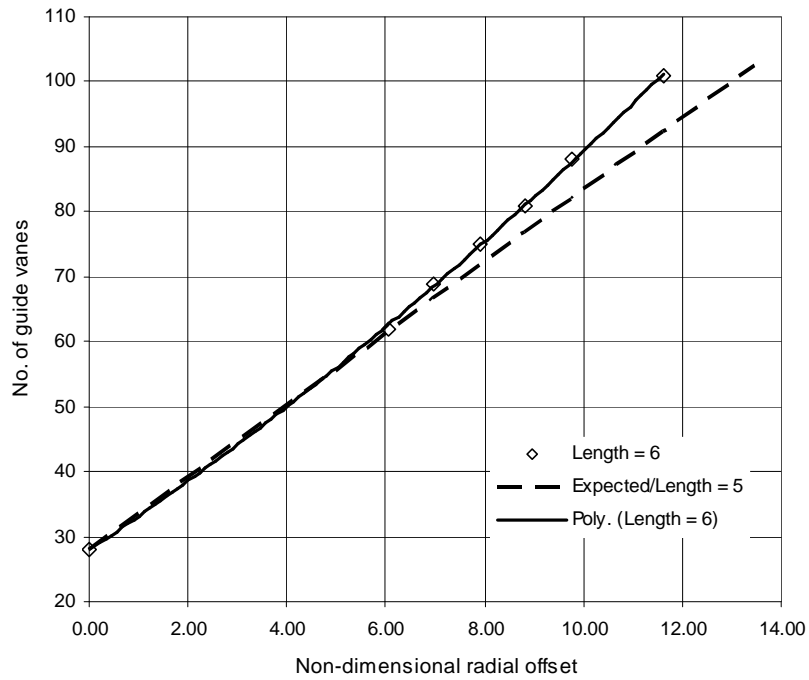


Figure 141 – Variation in number of guide vanes required for duct length  $h_1 = 6$

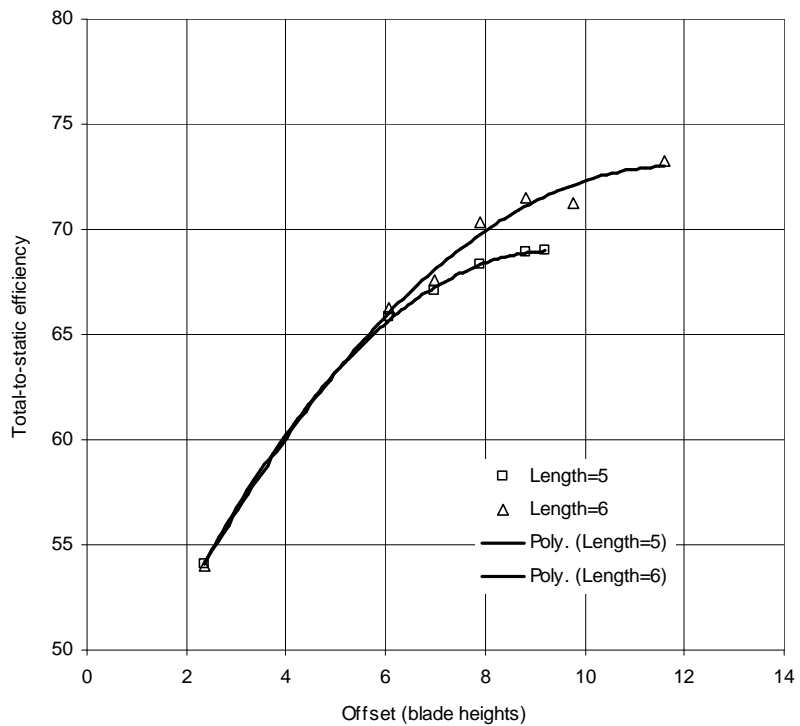


Figure 142 – Peak efficiency curves for ducts of length  $5h$  and  $6h$

The results obtained for axial duct lengths of the duct up 6 blade heights had not suggested that the maximum limit of improvement had been reached. Therefore simulations were made for a number of further cases with axial duct lengths of 7 and 8 blade heights, and various radial offsets. Following the process adopted for the shorter ducts a number of cases were calculated with different numbers of guide vanes. However, the trends in the results were noticeably less consistent than for the shorter ducts. In addition, whilst the results were good in that they were predicting efficiencies of over 70% there was a suspicion that they were too good to be true, in the same way that the results for the pseudo 2-D cases had been. This view was supported by the fact that the results were now at or above the level of the earliest cases run with no downstream guide vanes, even allowing for improved rotor design this began to seem unlikely. A summary of the best results for the longer ducts is given in Table 55.

Axial length (blade heights)	Radial offset (blade heights)	Total-to-static efficiency (%)	No. of guide vanes
7	9.76	72.6	90
	11.61	72.9	107
	13.46	75.3	110
8	11.61	72.1	101

*Table 55 – Best results for ducts of lengths 7 & 8 blade heights*

It was recognised that there were some minor simplifications in the CFD simulations carried out by Davin, as they had done on the basis of exploring the potential of the approach, and not as simulations within a design process. The most significant simplification was that the division between the guide vane rows and the rotor was halfway along the duct, which facilitated grid creation in Turbogrid. As independent checks had also been made on the grids it was believed that the solutions were essentially numerically correct. Unfortunately, it was not possible to pursue this work further as resources had to be concentrated upon the development of the test facility and test program, data acquisition, and post-processing software, and it was not until the second turbine build was defined that it was re-visited (section 9.2). At this point it was concluded that for the range of cases considered, the maximum improvement in efficiency that could be attained by using varying radius ducts with lengths and offsets of up to 8 and 13.5 blade heights had not been identified.

### **8.2.5 Further varying radius duct analyses**

The combinations of duct length and offset the levels of efficiency predicted by Davin’s simulations are summarised in Figure 143.

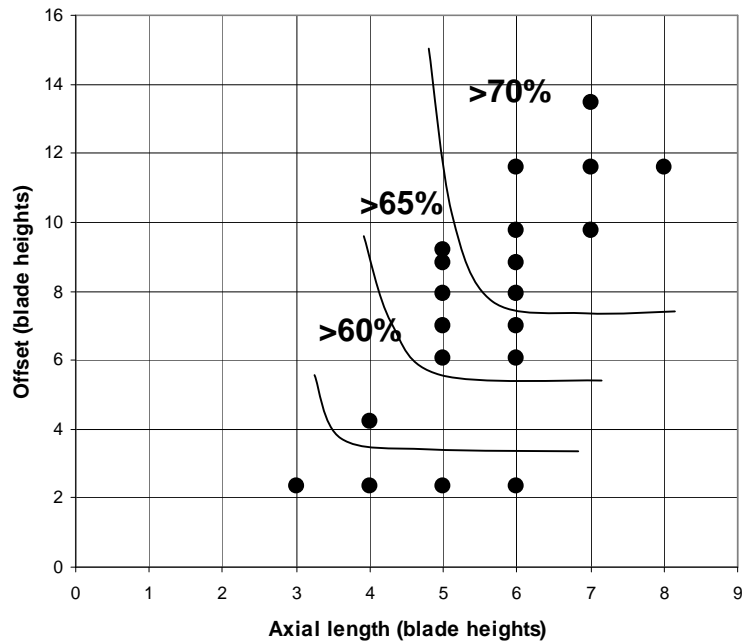


Figure 143 – Range of varying radius ducts analysed

When further simulations were carried out by Banks (Banks, 2007), the results suggested that the previous predictions were increasingly optimistic as duct offset was increased as shown in Table 56. The geometries analysed by Banks were more representative than those analysed by Davin, but it did not seem likely that these accounted for the reductions, which are discussed further in section 9.2.

Length (xh)	Offset (xh)	No. of guide vanes	Initial solution $\eta$ (%)	Later solution $\eta$ (%)	$\Delta\eta$ (%)
5	5.55	59	65.5	60.0	-5.5
6	12.54	108	72	65.4	-6.6
7	12.54	108	74	66.2	-7.8

Table 56 – Comparisons of initial and later CFD results

The variations of up to 8% in efficiency obtained from independent CFD solutions for the same geometries, clearly identified a need for experimental data to determine accuracy of the predictions, and to establish a ‘calibrated’ approach to setting up CFD simulations of varying radius duct turbine geometries.

Overall, if the trends indicated by the initial CFD analyses, and results in Table 56 are assessed together, they would indicate a maximum peak efficiency through simply coupling varying radius ducts to the datum geometry of ~68%.

### 8.2.6 Effect of twisting stator blades

The first step in adapting the design of turbomachinery blades to allow for the real three dimensional changes in the flow is to locally adjust the amount of turning produced by the blades along their span. At this stage in the development of the turbine the best assumption to make is that the spanwise turning should be varied to produce a free-vortex flow distribution, i.e. it is assumed that:

$$r v_w = \text{constant}$$

It was decided in the first instance to determine the effect of adjusting the spanwise turning only on the guide vanes. This was because it was thought that due to the relatively high hub/tip ratio of the datum turbine design, its effect on the guide vane performance would be very small, but that any real benefit would come from the reduced flow incidence onto the tips of the downstream guide vanes. The required spanwise turning distribution was therefore calculated by determining the constant in the above equation for the mean line flow, and then the turning at each radial station  $r_i$  from:

$$v_{wi} = \frac{\text{constant}}{r_i}$$

$$\alpha_2 = \tan^{-1} \left( \frac{v_{wi}}{v_a} \right)$$

The effect of incorporating a twist distribution into the datum guide vane design was evaluated by Davin (Davin, 2006) for a duct length  $6h$ , and non-dimensional offsets of 2.35, 6.06, 6.98, 7.91, 8.83, 9.76 and 11.61. Figure 144 shows that at low radial offsets the incorporation of spanwise twist did not make a significant difference to performance, but for non-dimensional radial offsets of 7.0 or more there was an increasing benefit, and a predicted benefit of more than 2% for the largest offsets.

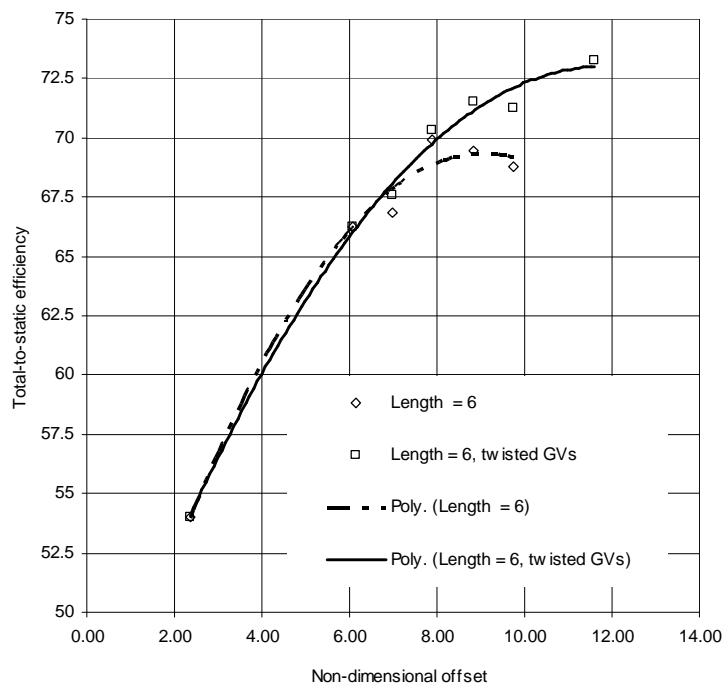


Figure 144 – Effect of incorporating spanwise twist distribution into guide vanes

### 8.2.7 Effect of incorporating guide vane sweep and lean

Examination of CFD solution in the blade-to-blade plane for the case with duct length  $6h$ , and radial offset  $6.06h$  showed that there was a significant spanwise variation in the flow around the downstream guide vane. In particular it was observed that the flow separation was more pronounced at the hub than at the tip. This might be expected due to the change in of rotational velocity with radius leading to a more axial outflow close to the hub, and a slightly more favourable incidence onto the guide vane at the tip. Using the principle that the extent of flow separation at a section on turbomachinery blades can be reduced by moving that section upstream, a series of cases were calculated by Davin (Davin, 2006) for which the tips of the guide vanes were swept away from the rotor using a linear movement. The results (Figure 145) showed a predicted benefit of just over 1% for a sweep angle of around 15 degrees.

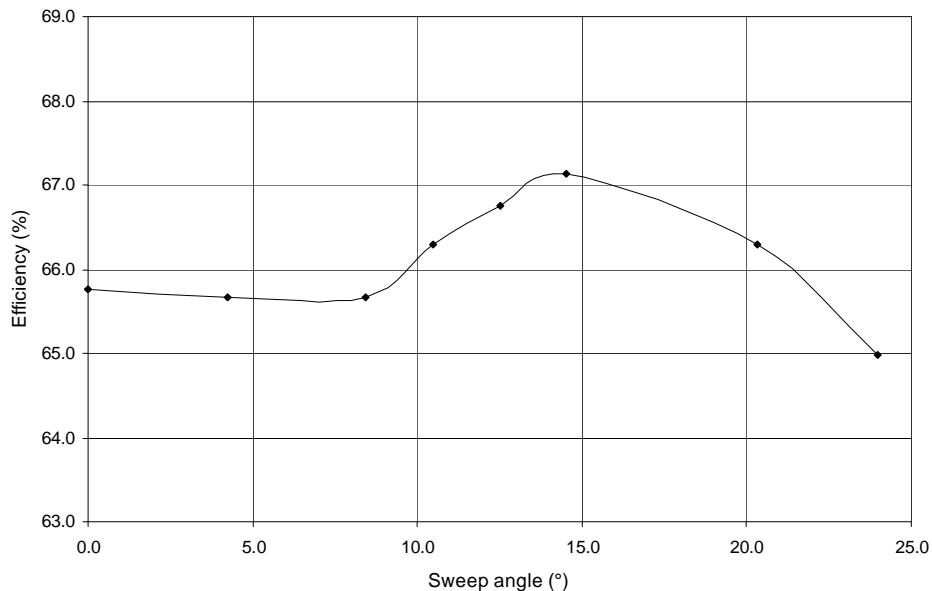
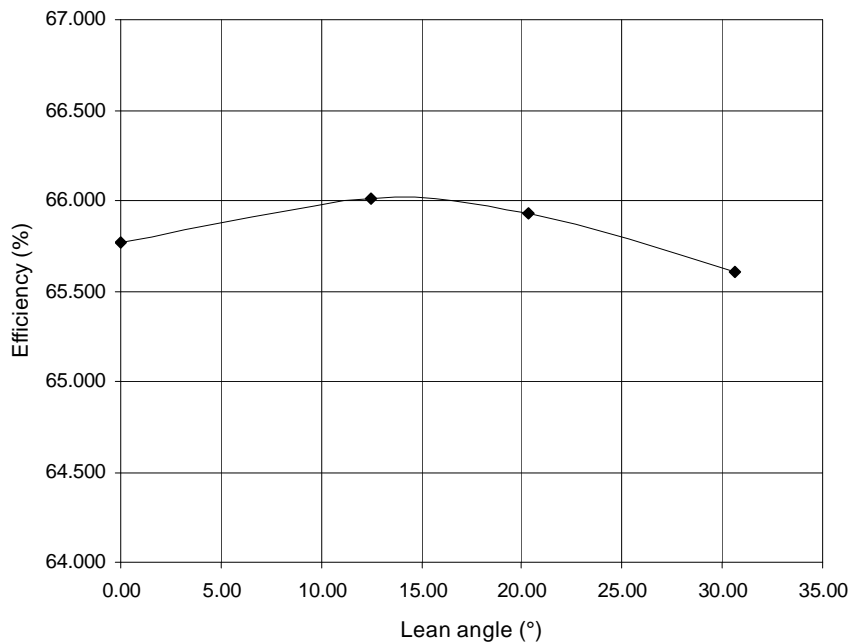


Figure 145 – Predicted effect of guide vane sweep on performance

In addition to the sweep, a number of cases were run to determine if any benefit was predicted due to the incorporation of linear guide vane lean. Positive lean was defined as moving the guide vane tip in the direction of rotation of the rotor. No, or even negative, benefit was predicted for negative lean, whilst a modest benefit of  $\sim 0.3\%$  was predicted for positive lean as shown in Figure 146. From this it was concluded that the incorporation of lean alone was of no significant benefit given the general level of uncertainty.



*Figure 146 – Predicted effect of guide vane lean on performance*

From the results above it was concluded that there was benefit of 1.5% in incorporating guide vane sweep of 15 degrees, but no significant benefit in lean alone. The analyses conducted have only looked at a tiny fraction of the possible geometries. It is therefore recommended that further work is carried out to determine the benefits that might be achieved by the using combinations of lean and sweep and non-linear stacking axes.

### **8.3 Advanced Turbine Concept**

Two approaches which offered the possibility of significantly reducing the losses associated with the downstream guide vanes of a fixed geometry impulse turbine arrangement were explored: the use of boundary layer blowing, and the use of varying radius ducts. The former suggested that performance could be raised to perhaps 60%, although this figure might be reduced when the need to create the required pressures was considered, without considering potential degradation in service. The latter approach offered the prospect of efficiencies >60% with a simple fixed geometry arrangement. The choice of the offset duct arrangement as the basis of the advanced turbine concept was therefore straightforward.

## 9. Definition of HydroAir Proof-of-concept turbine

### 9.1 Initial Considerations

In the first instance there was a significant concern that it would not be practical to test the varying radius duct configuration in the HydroAir test facility, without making considerable modifications to the facility. This was because the existing datum turbine rotor was sized to the smallest scale it was felt acceptable to go to, and so if this was kept and it was wished to test a varying radius duct geometry that gave the highest predicted performance, then the external diameter of the guide vane rows would be 2.05m. In addition to the difficulty of actually manufacturing and installing such large items, and the associated ducts to link them to the rotor, there was the problem of integrating them with the existing turbine module and outlet duct whose diameters were only 0.6m. The option of replacing the whole duct system attached to the PWG was considered, but in addition to the considerable expense involved the time required would have been prohibitive, and the facility would have to have been re-calibrated effectively. This approach was not therefore considered realistic.

The obvious alternative approach was to evaluate the concept at a smaller scale than the current turbine, with an intermediate step which enabled the performance impact of testing at the reduced scale to be evaluated. This was attractive with regard to minimising the design and manufacture activities. Given that the datum turbine had been tested the subsequent test process would then be to test the datum turbine design at a reduced scale, and then test the varying radius duct concept at reduced scale using the smaller scale rotor but with new guide vane rows at a larger radius. In this approach the need for new hardware would be minimised by using the varying radius ducts to reduce the diameter of the flow annulus to that required to test the reduced scale datum turbine configuration. Although this approach was initially attractive calculations showed that for the largest offset considered the rotor diameter would only be 175.2 mm, the height of the blades would be 15.8mm, there would be 110 guide vanes per guide vane row, and the output power of the reduced scale baseline configuration would be around 0.3kW.

Given the above figures, it seemed better to select an intermediate configuration which would, nevertheless, demonstrate a sufficiently large performance increment to validate the approach. On this basis, a duct configuration with an offset of 6.05 blade heights, and axial length of 6 blade heights was chosen which had a predicted peak efficiency of 65%. This would give a rotor diameter of 288.0mm, and blade height of 25.0mm, and a power output of 0.8kW. However, 0.8kW at 1775 rpm equated to a torque of only 4Nm, and as the torque required to just get the datum turbine moving was 1.6 Nm these values were considered unacceptably small, and would severely compromise the accuracy of the test facility data, in addition was the fact that it was considered extremely undesirable to test at Reynolds numbers of  $7 \times 10^4$ .

Given that it was impractical and costly to incorporate the greatest offset vaneless ducts, and that reducing the scale would seriously compromise the quality of the test data. The chosen approach to proving the validity of the offset varying radius duct

concept in the test facility was to examine the greatest offset that could sensibly be integrated with the existing components.

## 9.2 Determination of test geometry

Consideration of the results from Davin's CFD analyses of the varying radius ducts, showed that a considerable improvement in performance was predicted from radial offsets that might reasonably be integrated into the existing test facility. The issues associated with creating a build whose predicted efficiency was 65% were therefore considered. Whilst there was some concern with regard to ensuring that the rotor would be held sufficiently steady on the extended shaft that would be necessary, no other major difficulties were foreseen. It was decided that the guide vanes in the new build would be moved radially outward by 5.55 blade heights, taking the casing diameter to 0.6m, and the axial length of the duct would be 5 blade heights. This would inevitably lead to the Reynolds numbers achieved on the guide vanes being reduced by 50%, however, this was the best solution that could be achieved within the project constraints.

Whilst results had been produced that indicated how the performance might be improved by incorporating twist, lean and sweep into the guide vanes, it was considered best to keep the same blade designs as in the datum configuration, so that it was only the effect of incorporating the varying radius ducts that was measured. In addition to the new guide vane rings and ducts required for the new build, hardware was required to expand the existing flow annulus out to the radius required to match the inlet/outlets of the new guide vane rows. The most cost effective way of doing this was to simply make 4 instead of 2 varying radius ducts.

The geometry development program was modified to create the appropriate geometry, including allowing for small parallel annulus sections upstream and downstream of the guide vane rows which would be necessary to install pressure tappings and ease fitting of the components together. The resulting geometry is shown in Figure 147.

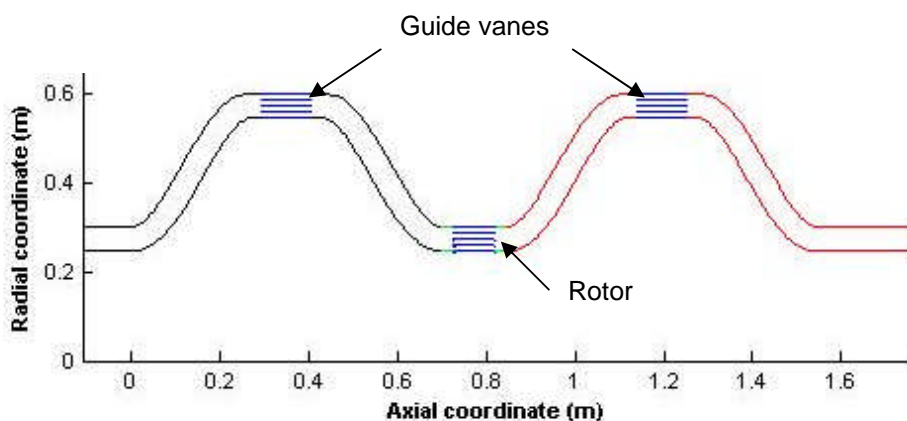


Figure 147 – Annulus geometry of varying radius duct proof-of-concept build

Examination of the CFD data for the variation in numbers of guide vanes with radius (Figure 141) gave the result that the appropriate number of guide vanes was 59.

It was evident that losses would occur in expanding the existing flow annulus to match the new larger guide vane annulus. This was not considered to be a problem in itself, as the performance would be measured, as for the datum build, by the pressure difference between the guide vane inlets and outlets. A significant concern, however, was that the flow might separate on the inlet side, and/or that significant flow non-uniformity might be introduced that would seriously compromise the evaluation of the benefit of the varying radius ducts. In order to mitigate this risk, and to verify the previously obtained results, Banks carried out simulations of the basic geometry with straight inlet and outlet ducts, and of the geometry with the additional s-ducts. In addition, due to the importance of the build and the resources that would be committed to design, manufacture and testing, it was thought prudent to conduct further simulations to determine the effect on the predicted performance of using boundary layer grid and SST turbulence model, rather than wall functions.

Neither of the simulations for the geometry with the additional s-ducts indicated the development of separated flow in the inlet duct. They did, however, show the development of some flow non-uniformity in the inlet that led to a 4-5% loss in efficiency due to an increased pressure drop, the rotor torque remaining constant. As there was no flow separation predicted, the performance of the configuration was still more than 15% higher than the datum turbine, and there was a need to begin the design and manufacture process to hold the project schedule, the geometry was considered acceptable.

A considerable amount of time was spent on the CFD simulations referred to above because the efficiency predicted for the configuration without the additional s-ducts was lower than expected. The results of a number of runs are shown in Table 57. It was found that when wall functions were used the predicted efficiency was about 0.2% higher. This difference was not considered significant within the context of the configuration to configuration differences being examined within the project, however, the additional computational time to determine it was very significant as the number of grid points was approximately doubled.

Inlet	Original prediction (%)	New prediction (%)
Straight	65.5	60.0
s-duct	-	56.5

*Table 57 – Predicted design point performance of offset duct geometries*

It was concluded from the CFD analyses carried out to verify the acceptability of the duct configuration for the proof-of-concept build, that for the range of duct geometries considered, wall functions should be used in preference to boundary layer grids, as the results were essentially the same at a much lower computational cost.

Investigation of the differences in the predicted efficiencies for similar cases highlighted above did not reveal any errors in the setting up of the cases, or in extracting results. It appeared that for the class of problem under investigation that although a case might appear satisfactorily converged at 400 iterations, if it was run to a greater number of iterations, 700 say, the predicted efficiency tended to fall, i.e. the predicted efficiency was more than usually sensitive to the level of convergence. The complication in this is that due to the extensive flow separation inherent in the problem convergence to very low residual levels is not expected. Another possible consideration is that the low pressures and velocities in the problem, coupled with the increasing aspect ratios of cells as the lengths of the ducts are increased may be beginning to compromise the numerical process. It is thus concluded that CFD analyses of varying radius duct geometries need to be run to a large number of iterations, and that experimental data is required to validate analyses of this class of problem. It is also recommended that further work is done to establish whether the geometry and flow conditions in this class of problem are likely to lead to numerical problems.

### 9.3 Specification of proof-of-concept turbine

The final specification for the proof-of-concept turbine was as detailed in Table 58.

Item	Value
Rotor	As per datum turbine
Length of offset duct	0.27 m
Casing diameter of offset duct	1.20 m
Guide vane shape	As per datum turbine
No. of guide vanes	59
$R_{mid}$	0.573 m
Predicted design point efficiency	56.5%

*Table 58 – Proof-of-concept turbine specification*

## 10. Discussion

### 10.1 General

An important commercial consideration within the project was that an independent IPR trail was established, and this has been achieved: the test facility uses a unique arrangement which permits a wide range of conditions to be produced; the turbine design process was developed from first principles; a novel turbine arrangement has been conceived; and finally the oscillatory flow simulation developed uses a different approach to that generally described in the literature.

The project has resulted in the development of a complete design and evaluation system for the development of turbines for use in OWC power plants, as shown in Figure 148. The programs impulse, OWCsimgui2, profile8/multiwave and PWGgui are all Matlab based codes created within the project.

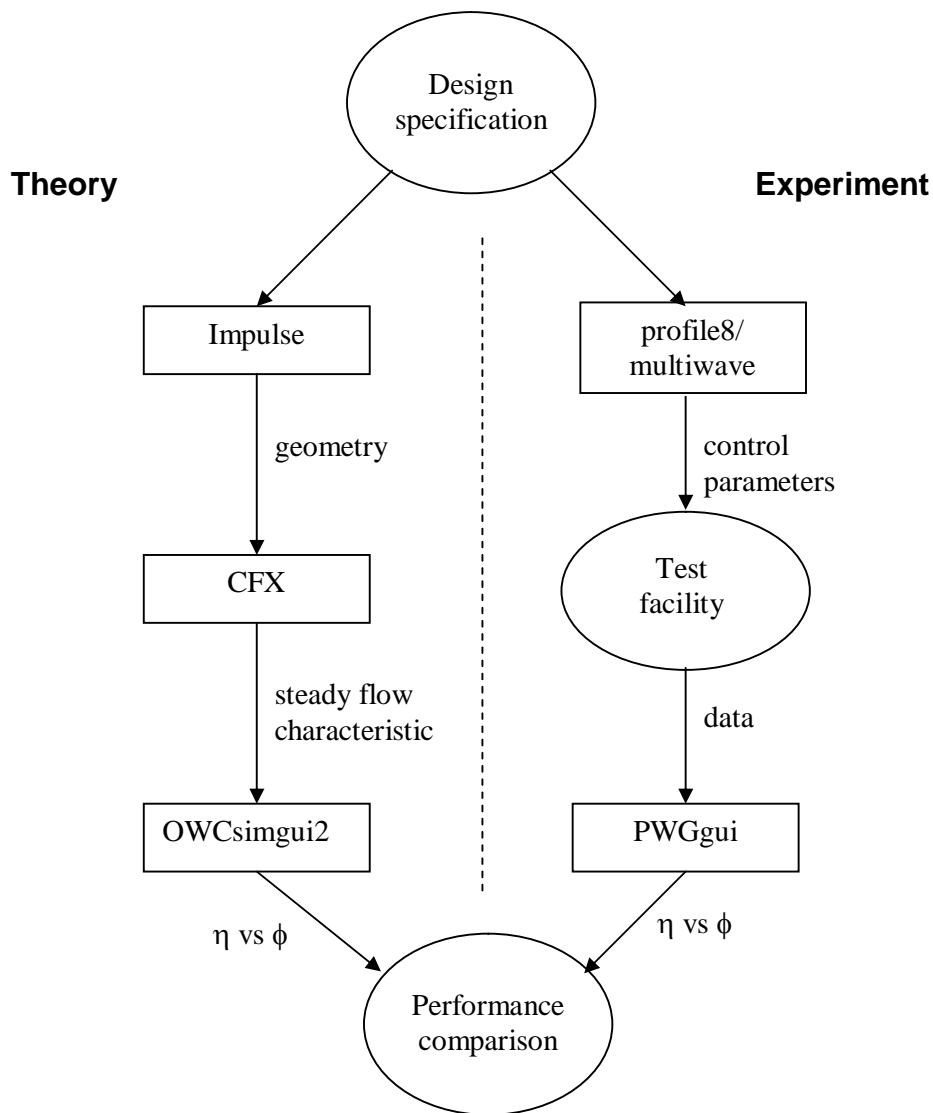


Figure 148 – Schematic of components within design and evaluation process

Given that the project only had a 2 year duration, but the objective was to achieve a 'dramatic' change in performance, which was to be demonstrated in a test facility developed within the project, and this will be achieved, it is evident that the synergy hoped for between PBL and CU has materialised.

## **10.2 Performance Data**

The oscillating flow performance data acquired from the facility for the datum turbine showed good agreement with the characteristic predicted by the oscillating flow simulation program. From this it was inferred that the steady flow performance characteristics of the datum turbine were close to the CFD prediction. It would be desirable though, to be able to obtain the steady flow performance characteristics of the datum turbine and compare them with those predicted by the CFD analysis directly.

It is not possible to calculate the instantaneous efficiency of the turbine from the test data directly because the continual acceleration means that the changes in axial flow velocity and rotational speed are out of phase with each other. It should be possible, however, to determine the steady flow characteristic by determining the rotational acceleration, and using a similar process to that used to evaluate the windage. Another alternative is to adopt a procedure similar to that used in the Saga University facility, in which the generator is used to motor the turbine up to the desired RPM, and then move the flap to create the desired constant flowrate for a short period of time during which the power input to the motor is stopped. In order to further prove the integrity of the data from the test facility it is recommended that further work is done to enable the steady flow performance of the test turbine to be determined.

In addition to deriving the steady flow performance of the turbine, it would also be desirable to examine the difference in efficiencies for the inhalation and exhalation parts of the cycle. This would assist with understanding how best to optimise the turbine design. This should also be linked to the taking of more detailed measurements of the flow in order to understand how much variability in the different parts of the cycle is linked to design of the test facility. Further work should also be carried out to understand what proportion of the airflow is being continually re-cycled in the facility, and hence how much work is being absorbed through this process.

## **10.3 Accuracy of test data**

The accuracy of the test data is a question of primary concern. The test procedures and reduction process developed have led to efficiency results which show a level of scatter significantly below the target accuracy of  $\pm 2\%$ . However, as noted elsewhere, the absolute value of efficiency obtained is very sensitive to the value of flowrate, and so there could be a significant - but unknown - bias in the results due to the process used to calculate the flowrate. As the other quantities should be reasonably accurate, the fact that peak efficiencies close to prediction were obtained suggests that the flow rate is under-estimated if anything. The possible presence of a bias error does not matter for the build-to-build comparisons which are currently the focus of the research. Due to the difficulty of establishing the true accuracy of the flow rate under

the varying flow conditions, the most effective way of verifying the accuracy of the results would be to test the datum turbine in a proven steady flow facility, which could be desirable when a more mature design is produced, in order to further calibrate the facility and results, before committing to production.

#### 10.4 Test Facility Performance

Examination of the data did not reveal any major pressure losses occurring at the inlet/outlet of the PWG. Furthermore, the circumferential differences in the instrumentation section static and total pressure measurements did not reveal any evidence of large flow non-uniformities. Given that the calculated discharge coefficients were also sensibly constant over the range of test flow conditions, it was concluded from the measurements taken so far, that a smoothly varying flow was obtained within the facility and through the test turbine.

The project schedule determined that the instrumentation rings were designed and manufactured before the turbine test module and datum turbine. This led to the need to introduce contraction/diffusion sections later into the casing to reduce the diameter, and also resulted in the instrumentation ring closest to the PWG being significantly further away from the turbine than intended, at 1.585m (as compared to 0.22m for the other instrumentation ring). In order to improve confidence and accuracy in the data, it is recommended that consideration is given to replacing the present instrumentation rings with ones that fit the reduced flow annulus, so that the velocities and hence pressure differences would be greatly increased.

The testing conducted on the datum turbine was restricted to a range of steady oscillating flow conditions. In principle there is no reason why a series of more irregular test waves cannot be defined and produced by the PWG as:

- The trapezoidal profile followed does not have to be the same on the positive and negative parts of the cycle
- Additional accelerations can be added to the basic trapezoidal profile.
- The program used to control the operation of the PLC can be developed further to permit a sequence of more than 8 profiles to be strung together

The potential thus exists to create a wide range of irregular wave inputs using the existing PWG control system. Perhaps the most difficult part of the problem is to determine which of the many possible irregular waves should be used, and it is recommended that further work should be done to identify a limited set of irregular wave patterns that could be input into the PWG to reveal the irregular flow performance of a test turbine.

The testing carried out on the facility with the datum turbine installed, but with no-load, showed that the flap movements required to achieve the maximum design peak flowrate of  $5.9 \text{ m}^3/\text{s}$  and rms profile of  $Q_{\text{rms}} = 3.6 \text{ m}^3/\text{s}$  could be achieved. However, the results of the actual testing showed that based on the linear relationship derived,

the maximum achievable flow rate is actually  $4.0 \text{ m}^3/\text{s}$ , or  $Q_{\text{rms}} = 2.8 \text{ m}^3/\text{s}$ . The data in Table 59 provides a summary of the range of operating conditions achieved during the testing of the datum turbine.

	Nominal rms flowrate ( $\text{m}^3/\text{s}$ )	
	1.77	2.3
Pressure range in PWG (kPa)	$\pm 3.2$	$\pm 7.2$
Actual rms flowrate ( $\text{m}^3/\text{s}$ )	1.64	2.44
Work put into PWG (kW rms)	4.0	15.0
Shaft power output (kW rms)	1.0	3.3
Maximum rotor tip Mach number	0.11	0.18
Range of Re (based on axial chord)	$1.7 \text{ to } 2.4 \times 10^5$	$2.7 \text{ to } 4.3 \times 10^5$
Range of St (based on $U_{\text{mid}}$ )	$0.2 \text{ to } 3.3 \times 10^{-3}$	$0.2 \text{ to } 1.9 \times 10^{-3}$

Table 59 – Summary of operating conditions and parameters achieved during testing

## 10.5 CFD

The differences in predicted *steady flow* efficiency obtained in different CFD simulations for the offset duct geometries have provided a compelling justification for the need for such a test facility as that developed in the project. Not only to help establish the true level of performance, but also to provide a means of obtaining detailed data to understand why the discrepancies in the CFD results arose. The discrepancies also reinforce the need to be able to derive the turbine steady flow performance from the test data.

## 10.6 Additional Turbine Performance Considerations

Two additional factors have to be considered in assessing the performance of turbines required for use in OWCs. The first is that the calculations of turbine efficiency carried out here have effectively removed inlet and outlet losses – which could be large in reality unless careful attention is paid to the design of the inlet and outlet for the oscillating flow conditions. The second factor is that the noise associated with the device may be dependent upon the interaction between the turbine and the ducting connecting it to the OWC and the outlet. These factors mean that if a turbine is to be taken forward to manufacture then it would probably be desirable that the turbine and ducting were designed as an integrated package which would be connected to an OWC which provided flow of specified characteristics. Otherwise there would be a significant risk that the turbine performance could be significantly compromised by poor quality flow. It is therefore recommended that should the results of the proof-of-concept turbine prove satisfactory, early consideration is given to examining a full-scale geometry and developing an integrated duct and turbine package.

## 10.7 Boundary Layer Blowing

Boundary layer blowing has not been extensively used in air vehicles due to the complexity of the systems required and their weight penalty. The importance of these issues is much reduced in the OWC power plant application, as the structure is likely

to be relatively massive, and to produce economic levels of power output the blades will have characteristic dimensions of the order of a metre or more which makes the production of the appropriate slot geometries and feed pipes a practical proposition. However, capital cost has a major impact on OWC economics, and so any practical solution must be simple and easily accommodated within the manufacturing process, and subsequent maintenance requirements must also be minimal, and so the degradation in system performance in the operating environment needs to be considered.

It was noted earlier that the guide vanes of the datum turbine were designed to allow for the incorporation of blowing, and at one point it was intended that when the datum turbine was tested it would be tested with and without blowing. Given that only relatively small amounts of air were required it was anticipated that the evaluation could be carried out relatively easily. However, further calculations showed that in fact a substantial air supply would be required, and that the analysis, design, and manufacture required to install such a system would be a substantial task, and it was determined that the most appropriate course would be to evaluate it in a cascade which had the advantage of accessibility for flow visualisation work.

### **10.8 Further Increasing Turbine Performance & Scaling up of Results**

A high hub/tip ratio was used on the datum and proof of concept turbines in order to achieve the desired values of  $Re$ . However, the work carried out by Maeda, Setoguchi and Thakker (section 2.2.7) showed a 20% increase in efficiency from 31% to 51% in changing the hub/tip ratio from 0.85 to 0.6. This seems rather a lot, but suggests that reducing the datum design to hub/tip ratio of 0.6 (as would be done in transforming it to full scale) should increase the peak efficiency by several percent by reducing end-wall effects. In addition, the CFD analyses predicted that introducing twist into the guide vanes led to improvements in performance of up to 2%, the beneficial effects of this might be even greater at lower hub/tip ratios. These figures alone coupled with the predictions for the offset duct geometries suggest that peak efficiencies of over 70% are achievable at full scale. In addition, the efficiency would be expected to be slightly higher at higher  $Re$ , and it should be possible to obtain greater performance by further reducing the diffusion rate in the outlet guide vane passage and using a 3-dimensional stacking axis for the guide vanes.

The literature search identified that turbine test results could be corrected for Reynolds number effects by using Soderberg's relationship. However, this would only be expected to apply to turbomachinery operating close to its design point, and not to the datum turbine arrangement where the outlet blade row is always operating highly off-design – although it could be applied to the inlet guide vane row and rotor. It is therefore recommended that further experimental and CFD work is carried out to determine where the losses occur in the turbine to enable some assessment of the Reynolds number effects to be made.

## 10.9 Flow Regime & Frequency Effects

The literature study revealed a need to determine the true nature of the boundary layer that exists under oscillatory flow conditions. Whilst no attempt was made to conduct a such a study of the nature of the boundary layers within the test facility during commissioning and datum turbine testing, the data acquired to determine the instrumentation plane discharge coefficients can provide some insight.

When the instrumentation plane traverses were performed the first point taken was with the probe fully retracted, so that the pitot probe was pulled up against the inner wall of the instrumentation ring. Given that static pressures were also recorded the resulting configuration was similar to that of a Preston tube used to evaluate the shear stress at the wall,  $\tau_w$ . Now, Ramaprian and Tu categorised the impact of the oscillatory flow on the boundary layer by the use of the ‘turbulent Stokes’ parameter:  $\omega D / \bar{U}_*$ , where:

$$\bar{U}_* = \left( \frac{\bar{\tau}_w}{\rho} \right)^{0.5}$$

Hence, in principle, a Preston tube could be used to determine  $\bar{U}_*$ , and the flow regime. The basic criteria for a Preston tube are that the external diameter of the pitot tube should be less than 1/10 of the boundary layer thickness, and the ratio of the internal to external diameters of the tube should ideally be 0.6 (Preston, 1954). Examination of the instrumentation plane 2 velocity profiles in Figure 84 showed a boundary layer thickness at the instrumentation ring surface of 20-30% of the annulus depth i.e. 30 – 45 mm, meaning the diameter of the pitot probe was sufficiently small for it to be used as a Preston tube at the maximum flow condition. However, the ratio of the inner to outer diameter of the tube was 0.7.

Even though the dimensions of the tube were not quite right it was felt worthwhile to evaluate the turbulent Stokes parameter for the maximum dynamic pressure point. The calculations detailed in Appendix N were thus made, and the values in Table 60 obtained. As  $U_*$  maximum, rather than  $\bar{U}_*$  was calculated, the values could well be high. The values also have to be treated with caution, not just because of the less than ideal arrangement, but also because the geometry and conditions were not the same as those of Ramaprian and Tu. In particular, Ramaprian and Tu had an oscillatory flow superimposed on a steady flow, rather than flow oscillating about a zero condition. Nevertheless, the values obtained showed trends in both flow rate and cycle period, and a comparison of the values with those in Table 17 suggested that the flows in the plane 2 instrumentation ring of the test facility covered the low and intermediate regimes, i.e. values of  $10^{-1} < \omega D / \bar{U}_* < 10$ . The boundary layer thickness and wall shear stress at the turbine inlet and outlet will differ from those in the instrumentation sections due to the distances between them, and the contraction/diffusion which takes place.

Zero point	Data point	Nominal $Q_{rms}$ ( $m^3/s$ )	Period (s)	Turbulent Stokes No.
399	400	1.77	7	0.91
452	453	2.3	7	0.68
478	479	2.65	7	0.53
610	611	2.3	5	1.14
638	639	2.3	9	0.63

*Table 60 – Variation of calculated turbulent Stokes number*

Overall the results obtained indicated that for the range of conditions produced in the test facility, the flow would be expected to depart from quasi-steady state behaviour, but the turbulent structure would not be affected and the use of quasi-steady turbulence models should be acceptable. This would mean that the use of steady flow CFD predictions should be adequate. Given the assumptions made though, and that the possible variations between the instrumentation section and turbine section flows, it is recommended that experimental measurements are made to determine the time varying nature of the boundary layers entering and leaving the test turbine.

If an experimental exercise was to be carried out to measure the nature of the time varying boundary layers, it would also be desirable to establish the turbulence intensity level entering the turbine. This is because the turbulence not only has an influence on the overall performance, but the broadband noise production is also influenced by the scale of the turbulence relative to the chord. Knowledge of the turbulence intensity is required firstly, to understand the quality of flow that is being produced in the test facility, and secondly to ensure that an appropriate value is input into CFD predictions. It is therefore recommended that further work is carried out to determine the quality of the flow entering the turbine.

At the outset of the project it was hoped that the test facility would be able to achieve similarity of Strouhal number for a quarter scale turbine suitable for installing in the LIMPET facility. Ultimately it did not prove possible to achieve this across the range of test conditions used so far. However, cycle periods down to 5 seconds have been achieved, which are not too far way from those required for similarity in Strouhal number. It is therefore recommended that if the detailed boundary layer measurements recommended above are taken, further work is done to determine whether the operating envelope can be expanded to acquire data at representative Strouhal number, even if only at low flow rates.

### **10.10 Development of simulation program**

Further development of the simulation program needs to be carried out. The obvious deficiency at present is that the calculations are initially made assuming that the rpm remains constant, and then the variation in rpm is derived. The method needs to be modified to enable the variation in rpm to be determined along with those in pressure etc, which will then enable the starting characteristic to be predicted.

### **10.11 Wave-to-wire model & Control**

The testing carried out on the datum turbine has enabled its performance under steady oscillating flows to be established. In order to maximise the economic viability of the OWC power plant, though, there is a need to link the turbine to a control system which is able to maximise the power take-off from it, whatever the input conditions. The incorporation of the MV3000 into the HydroAir test facility, coupled with the ability to produce a wide range of irregular inputs, provides an ideal test facility for developing the whole turbine and the power take-off control system. Due to the coupling and lags between various elements of the system: the OWC (or PWG in this case), turbine, generator and power electronics, the derivation of the control system will require the development of an accurate wave-to-wire model. This could be a further development of the simulation program.

If an accurate wave-to-wire simulation model can be developed, then this could form the basis of a real-time control system, which uses past and present data to establish the current operating point and determine the power to be taken-off in the next time period based on a forecast of the expected power input. There is thus a two stage process to be undertaken: the first is to develop an accurate 'wave-to-wire' model of the test facility which enables the behaviour and resulting power output to be accurately predicted from a limited number of inputs, such as: PWG pressure, demanded power take-off, and turbine rpm. The second would be to run the model with actual transducer inputs on a PC, and derive control commands which would be sent to the MV3000. In order to be able to achieve this there is a need to have a detailed knowledge of how power is transferred through the system. At present the instrumentation enables a break-down of the power transfer from the PWG to the turbine shaft to be obtained as shown in Figure 149. In order to be able to develop the wave-to-wire model it is also necessary that outputs are obtained from the MV3000 that reveal how much power is produced by the generator, and how much power is ultimately exported to the loadbank.

Even if a wave-to-wire model was not used for control purposes it is still required in order to carry out studies to determine the turbine design point and sizing under various input assumptions.

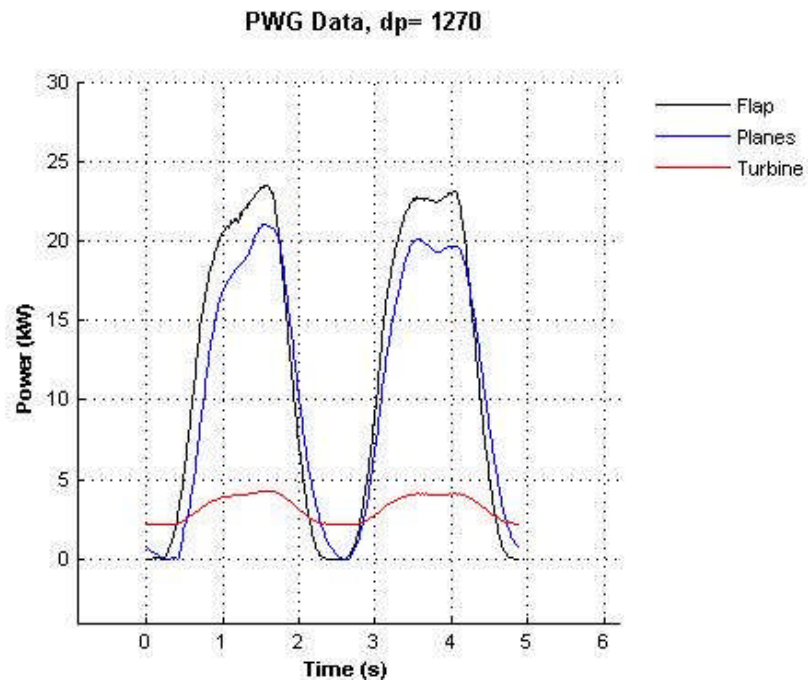


*Figure 149 – Power variations in PWG, instrumentation planes, and turbine shaft*

## **11. Conclusions**

### **11.1 General Conclusions**

The work conducted in the HydroAir project has led to the development of a unique test facility, which enables turbines intended for use in OWCs to be evaluated under oscillating flow conditions, at Reynolds large enough to give confidence in the data. In addition, the results from the commissioning tests and data from the datum turbine have shown good repeatability.

With respect to the design of turbines for OWCs, a design process has been established and validated by the manufacture and testing of the datum turbine, with data for the peak efficiency level and characteristic shape agreeing well with prediction.

Assessment of previous work identified target peak total-to-static efficiency requirements for the HydroAir turbine of 70% and 50%, under steady and irregular flow conditions respectively. Work within the project has determined that it is probable that these can be attained by the use of an impulse turbine configuration which uses variable radius ducts, and a patent application has been filed for this configuration.

All the work conducted can be shown to have an independent IPR trail.

The synergy hoped for between PBL and CU has materialised.

### **11.2 Detailed Conclusions**

#### **11.2.1 Test Facility Performance**

The following conclusions were made regarding the performance of the test facility:

- The HydroAir test facility and testing process have been developed to a level that enables turbine performance data to be acquired in an efficient manner to an acceptable degree of repeatability.
- Although the specified PWG volume was achieved, the maximum volume that could be swept by the flap of 15.1m<sup>3</sup> was 8% less than specified.
- The maximum acceleration that should be input, without further structural analysis, is 50 rev/s<sup>2</sup>.
- The period of the flap movement is typically repeatable to better than 0.01 seconds, and that the angular movement is typically short of that demanded by 0.5 degrees.

- The measurements taken so far indicate that a smoothly varying flow is obtained within the facility and through the test turbine.
- The discharge coefficients for the 2 instrumentation planes were constant for nominal rms flowrates of 1.5-2.65 m<sup>3</sup>/s, and cycle periods of 5 to 9 seconds, resulting in the calibration:

Plane	Discharge coefficient	Position of total probe (% from hub)
1	0.961	15%
2	0.968	15%

- The break-out torque of the rotor without the generator connected was 1.6 Nm.
- The consistency in the calculations of volumetric flow rate indicated that their accuracy was as good as could reasonably be expected, and there was a linear relationship between the actual and specified rms flowrates.
- The low scatter in the calculated flow rates made them acceptable for verifying the characteristics of the input profiles.
- The maximum achievable flow rate is 4.0 m<sup>3</sup>/s, or  $Q_{rms} = 2.8 \text{ m}^3/\text{s}$ .
- The joints between the fibreglass panels need to be sealed with tape in order to avoid significant leakage (5-10%).

### 11.2.2 CFD Analyses

A large number of CFD simulations were carried out in the course of designing the datum turbine, assessing concepts, and developing the varying radius turbine concept. These led to the following conclusions:

- Whilst pseudo 2-D CFD analyses can assist in identifying beneficial design features for the impulse turbine with inlet and outlet guide vanes problem, they provide a poor indication of the likely 3-D efficiency.
- CFD analyses of offset varying radius duct geometries should be run for a larger than usual number of iterations.
- The variations of up to 8% in efficiency obtained from independent CFD solutions for the same geometries, clearly identified a need for experimental data to determine accuracy of the predictions, and to establish a ‘calibrated’ approach to setting up CFD simulations of varying radius duct turbine geometries.

- The results obtained so far have indicated that for the range of conditions produced in the test facility, the use of quasi-steady turbulence models should be acceptable.
- From simulations of published Wells and impulse turbine designs it was concluded that CFD may be used to evaluate the relative merits of new turbine designs with reasonable confidence, but CFD characteristics for Wells turbines are too inaccurate for use in system performance calculations, and CFD characteristics for impulse turbines with fixed guide vanes should only be put into system performance calculations for the purpose of informing the design process.

### 11.2.3 Turbine Design

Subject to the observations made in 11.2.2, the CFD analyses conducted showed that:

- For the range of cases considered, the maximum improvement in efficiency that might be obtained by using varying radius ducts has not been identified.
- There was a beneficial effect in introducing spanwise twist into the guide vanes when they were radially offset by 7.0 blade heights or more, which was predicted to be more than 2% for the largest offsets examined.
- There was benefit of 1.5% in incorporating guide vane sweep of 15 degrees, but no significant benefit in lean alone.
- The high hub/tip ratio required for the datum turbine, coupled with the spanwise variation in local flow ratio led to highly 3-D flow around the outlet guide vanes.

### 11.2.4 Datum Turbine

The following conclusions were made:

- The measured peak efficiency of the turbine was in agreement with prediction.
- The shape of the efficiency characteristic was as predicted by the simulation program.
- The flowratio for peak efficiency was  $\phi=1.5$ , 0.2 higher than predicted.

### 11.2.5 Guide Vane Blowing

A number of conclusions which may be drawn from the work carried out so far:

- CFD analysis predicts that blowing may be used to effectively remove the separation that occurs on the downstream guide vanes of a fixed geometry OWC impulse turbine arrangement

- The effect of the injected mass flow is significantly influenced by guide vane geometry and jet location.
- For the 2 geometries analysed re-attachement and improvements in efficiency of 25% and 34.5% were obtained by the addition of 3.6% and 2% additional mass flow respectively.

### **11.2.6 Noise**

The observations and results showed that the measured sound pressure levels were as great as the highest predictions (105 dB(A)). This suggests that full scale noise levels could exceed 120 dB(A).

## 12. Recommendations

A significant number of recommendations can be made to further develop the work described in this thesis. These have been broken down into various areas and are presented in priority order in the sections below.

### 12.1 Further development of turbine design

From the work carried out so far it is recommended that further turbine development work should be carried out to:

- Determine how the guide vane and rotor turning can best be combined to reduce the turbine design point flow ratio.
- Examine the performance benefits that can be obtained by introducing lean and sweep and a non-linear stacking axis into the guide vanes.
- Determine whether there are modifications that could be introduced to improve the performance of the varying radius ducts.
- Determine the possible benefit from designing the turbine to operate at the most frequently occurring wave condition, rather than the most energetic.
- Determine the effect of producing a guide vane geometry with a constant area passage and diffusion only around the leading edge.
- An analysis is carried out to determine the performance of the turbine when scaled to full size with a hub/tip ratio of 0.6.
- Establish if the highly 3-D flow observed around the outlet guide vanes for the high hub/tip ratio case remains at more representative hub/tip ratios when spanwise changes in flow ratio are greater.
- Examine whether guide vane blowing may be used to further enhance performance.

It is also recommended that should the results of the proof-of-concept turbine prove satisfactory, early consideration is given to examining a full-scale geometry and developing an integrated duct and turbine package. In addition, further experimental and CFD work should be carried out determine where the losses occur in the turbine, to enable some assessment of the Reynolds number effects to be made.

### 12.2 CFD Validation

The development of the HydroAir turbine geometries has relied heavily upon the results of CFD analyses, and it is recommended that the following steps are taken with

respect to validating the present results before undertaking further developments, and progressing towards developing a large scale prototype or actual device:

- The results from the datum turbine and proof of concept turbine should be carefully compared to the CFD predictions to determine that the predicted trends are correct.
- Further testing should be carried out to determine whether the flow around the outlet guide vanes was steady or fundamentally oscillatory.
- Further testing should be carried out to determine the time varying characteristics of the boundary layers entering and leaving the turbine.
- Further testing is done to determine whether the operating envelope can be expanded to acquire data at representative Strouhal number, even if only at low flow rates.
- Further testing should be carried out to determine the quality of the flow entering the turbine.
- It is recommended that more comparisons between CFD predicted characteristics and experimental data from impulse turbines with fixed guide vanes are carried out.

It is also recommended that further work is done to establish whether the geometry and flow conditions in this class of problem are likely to lead to numerical problems.

### **12.3 Test Facility and Process Improvement**

It is recommended that the following modifications are made to further improve data accuracy and test efficiency:

- The low speed output of the frequency to voltage converter is measured to determine whether a filter is required to obtain accurate data below 300rpm.
- Further work is undertaken to determine the reason for the variation in calculated flowrate with flow ratio, and the reduction from the no-load point in particular.
- Further work should be done to define a standard range of representative irregular wave inputs that may be used in the evaluation of turbines.
- The pneumatic instrumentation system should be modified to enable all the pressure transducers to be calibrated simultaneously at least on a daily basis.
- The LabView data acquisition program should be modified and rationalised to:

- a. Enable instrumentation zero biases to be removed during data acquisition.
  - b. Produce a coherent presentation of the data and input fields required to run the test in a single window.
  - c. Provide a moving needle rpm display with a high update rate.
  - d. Provide a strip indicator, with high update rate, that displays a calculation of the instantaneous shaft power.
- Consideration is given to the fitting of an accelerometer/strain gauge to the turbine casing of the proof-of-concept build to enable vibration to be monitored.
  - The number of pressure transducer channels is increased to 60 to enable the mass/volumetric flowrate through the facility and the total-to-static pressure drop across the turbine to be measured to a greater level of confidence. However, such an expansion also requires that the recommendation above regarding pressure transducer calibration is carried out.
  - A thermocouple is installed to monitor the temperature of the torquemeter, and that the manufacturer be approached with regard to determining the temperature correction that should be applied, and that the PWG thermocouple is installed in a suitable probe.
  - Further work should be carried out to identify a limited set of irregular wave patterns that could be input into the PWG to reveal the irregular flow performance of a test turbine.
  - Further work is carried out to enable the steady flow performance of the test turbine to be determined.
  - Further work should be done to determine the impact on the data of the compromise made in the method used to determine windage. In particular, consideration should be given to making a bladeless rotor hub and using the MV3000 to run the generator as a motor to motor the hub up to speed so that the bearing and windage losses can be determined accurately.
  - In order to verify the performance measured in the facility, consideration should be given to testing the datum turbine in an alternative steady flow facility.
  - Outputs should be obtained from the MV3000 that reveal how much power is produced by the generator, and how much power is ultimately exported to the loadbank.
  - In order to improve confidence and accuracy in the data, it is recommended that consideration is given to replacing the present instrumentation rings with

ones that fitted the reduced flow annulus, so that the velocities and hence pressure differences would greatly increased.

#### **12.4 Data Analysis**

Much more information can be gained from further analysis of the data acquired from the datum turbine, specifically further analysis should be carried out:

- To determine how the turbine efficiency differs in the inhalation and exhalation parts of the cycle.
- To understand what proportion of the airflow is being continually re-cycled in the facility, and hence how much work is being absorbed through this process.
- To understand why the flow peak in the facility is not maintained at long periods in the way that it is at short periods.

#### **12.5 Testing and Development of Control Strategies**

In order to optimise that overall performance of power generation, there is a need to implement a system to control the speed of the turbine, and the following recommendations are made with regard to this:

- The HydroAir test facility should be used as a tool to define and assist in the development of an effective control system.
- Further testing should be carried out to determine the effects of changes in damping provided by the turbine and the effect of changing turbine inertia.
- The oscillating flow simulation program should be further developed to produce an accurate wave-to-wire model of the turbine and test facility.
- An accurate wave-to-wire model of the turbine and facility should be used as the basis of a real-time control system, using transducer inputs and providing control signals to the MV3000.

#### **12.6 Real Life Performance Effects**

There is a need to consider aspects of the real life environment that are likely to affect the performance of the turbine and power take-off system, it is therefore recommended that:

- An analysis/study is undertaken to ascertain the how salt and other matter in the air flow is likely to accrete on and/or corrode the turbomachinery blades and the extent that this is likely to reduce performance.

- An analysis/study is undertaken to estimate the quantity and size of water droplets that are likely to exist in the air flows, and how the presence of these is likely to reduce turbine performance.

### **12.7 Guide vane blowing**

The work carried out so far has indicated a need for the following further work to progress this technology:

- There is a need to verify that the predicted benefits of blowing are maintained across the operating range of the turbine.
- There is a need to consider how the predicted benefits are affected by a more detailed analysis of the additional work required to provide the jet velocities simulated, and whether it is practical to provide these in reality.
- There is a need to consider whether pulsed jets could be more efficient than steady ones.
- Experimental data is required to verify the accuracy of the present CFD analysis, and to assess the magnitude of scale effects associated with testing blowing configurations at sub-scale.
- There is a need for testing of the concept initially in a cascade type arrangement, and then in a facility that enables the fundamental unsteadiness of the flow to be assessed, and how the benefits of blowing would be affected by real irregular oscillating flow conditions.
- The possible degradation in system performance due to environmental effects needs to be considered.

### **12.8 Noise**

It is recommended that further work is carried out to obtain a better understanding of the cyclic noise profile, with a view to determining to what degree the measured levels are specific to the facility, and whether consideration needs to be given to developing a design with a reduced noise signature.

## References

- Arts, T., Boerrigter, H., Carbonaro, M., Charbonnier, J.-M., Degrez, G., Olivari, D., Riethmuller, M.L. and Van den Braembussche, R.A. (1994), *Measurement Techniques in Fluid Dynamics*, von Karmen Institute for Fluid Dynamics,
- Athanassoulis, G.A., Pontes, M.T., Tsoulos, L., Nakos, B., Stefanakos, Ch.N., Skopeliti, A., and Frutuoso, R. (1995), 'European Wave Energy Atlas: An Interactive PC-Based System', in Elliot, G. *The Second European Wave Power Conference*, Lisbon, Portugal,
- Banks, K. (2005a), *Impulse Turbine Simulations* ,
- Banks, K. (2005b), *Wave Power Turbine Simulations*,
- Banks, K. (2006), *Investigation into the Applicability of Blown Jet Flow Control to the Performance Improvement of Bi-Directional Impulse Turbines*,
- Banks, K. (2007), *Preliminary Report into the Use of Differential Radii Impulse Turbines for Wave Power Generation*, Unpublished report,
- Banks, K. and Herring, S. 'Performance Enhancement of Wave Power Turbomachinery by the Application of Boundary Layer Blowing', *Fluid Machinery - A Seminar for Developing Engineers*, Cranfield University, IMechE,
- Brito-Melo, A., Gato, L.M.C. and Sarmiento, A.J.N.A. (2002), 'Analysis of Wells Turbine Design Parameters by Numerical Simulation of the OWC Performance', *Ocean Engineering*, Vol. 29, pp. 1463-1477.
- Culley, D.E., Bright, M.M., Prahst, P.S. and Strazisar, A.J. (2004), 'Active Flow Separation Control of a Stator Vane Using Embedded Injection in a Multistage Compressor Experiment', *Transactions of ASME Journal of Turbomachinery*, Vol. 126, No. January 2004, pp. 24-34.
- Cumpsty, N.A. (1989), *Compressor Aerodynamics*, Longman Group UK Ltd.,
- Curran, R., Raghunathan, S., and Whittaker, T. J. T. The influence of flow profile on the Islay Wells turbine performance. Elliot, G. The second European wave power conference.
- Davin, M.-L. (2006), *Internship Report: Improvement of an Impulse Turbine*,
- Dhanasekaran, T.S. and Govardhan, M. (2005), 'Computational Analysis of Performance and Flow Investigation on Wells Turbine for Wave Energy Conversion', *Renewable Energy*, No. xx, pp. 1-19.
- DTi (1994), *New and Renewable Energy: Future Prospects for the UK*, Department

of Trade and Industry,

- DTi (1999), *New and Renewable Energy: Prospects for the 21st Century*, Department of Trade & Industry,
- ESDU (1977), *Geometrical Characteristics of Typical Bodies*, ESDU Data Item 77028,
- Gato, L. M. C., Justino, P. A. P., and Falcao, A. F. de O. Optimisation of power take-off equipment for an oscillating-water-column wave energy plant. 6<sup>th</sup> European Wave and Tidal Energy Conference. 2005.
- Gillanders, K. W. and Taylor, A. Development of wave hub. 6<sup>th</sup> European Wave and Tidal Energy Conference. 2005.
- Herring, S. (2005), *OWC Performance Matrix and Design Review*, Unpublished report,
- Herring, S. (2006), *HydroAir Test Facility: Description and Guide to Operation*, Cranfield University, Cranfield.
- Herring, S. and Banks, K. The Application of boundary layer blowing to a highly separated flow condition. ASME Turbo Expo:Power for Air Land and Sea. GT2007-27364. 2007a.
- Herring, S. and Banks, K. (2007b), *HydroAir Turbine Design Specification*, Unpublished Report,
- Herring, S., Freeman, C. and Banks, K. (2006), *Impulse Turbine, Patent Application No. 0614916.5*,
- Herring, S. and Laird, G.'A New Test Facility for Evaluating Turbines for Use in OWC Power Plants', *7th European Wave and Tidal Energy Conference*, Porto, Portugal,
- Hoffman, D. (1974), 'Analysis of Measured and Calculated Spectra', in Professor R.E.D. Bishop and Dr. W.G. Price *The Dynamics of Marine Vehicles and Structures in Waves*, Institution of Mechanical Engineers,
- Horlock, J.H. (1966), *Axial Flow Turbines*, Robert E. Krieger, New York.
- Houghton, E.L. and Carruthers, N.B. (1982), *Aerodynamics for Engineering Students, Third Edition*, Edward Arnold,
- Kaneko, K., Setoguchi, T., and Raghunathan, S. (1991), 'Self-Rectifying Turbines for Wave Energy Conversion', *First (1991) International Offshore and Polar Engineering Conference*, Edinburgh,
- Kim, T.H., Takao, M., Setoguchi, T., Kaneko, K. and Masahiro, I. (2001) Performance comparison of turbines for wave power conversion. *International Journal of*

- Thermal Sciences* **40** 681-689. Elsevier.
- Lewis, A., Fraenkel, P., and Elliot, G. Ocean Energy - the current state of development. The second European wave power conference. 95.
- Maeda, H., Santhakumar, S., Setoguchi, T. and Takao, M. (1999), 'Performance of an Impulse Turbine With Fixed Guide Vanes for Wave Power Conversion', *Renewable Energy*, Vol. 17, pp. 533-547.
- Martins, E., Siveira Ramos, F., Carrilho, L., Justino, P., Gato, L., Trigo, L., and Neumann, F. CEODOURO project: overall design of an OWC in the new Oporto breakwater. 6<sup>th</sup> European Wave and Tidal Energy Conference. 2005.
- Menter F.R. (1994), 'Two-Equation Eddy-Viscosity Turbulence Models for Engineering Applications', *AIAA Journal*, Vol. 32, No. 8,
- Miller, D.S. (1990), *Internal Flow Systems (Second Edition)*, BHRA (Information Services), Cranfield, Beds.
- Mustoe, J.E.H. (1984), *An Atlas of Renewable Energy Resources*, John Wiley & Sons Ltd.,
- Newman, B. G. The deflexion of plane jets by adjacent boundaries - Coanda effect. Lachman, G. V. Boundary layer and flow control its principles and application. 1. Pergamon Press. 61.
- Patel, M.H. (1989), *Dynamics of Offshore Structures*, Butterworths & Co. Ltd.,
- Perdigao, J. and Sarmento, A. (2005) Overall-efficiency optimisation in OWC devices. *Applied Ocean Research* **25** 157-166. Elsevier.
- Pervier, H. (2006), *Internship Report: Gas Turbine Department at Cranfield University*,
- Peter Brotherhood Ltd. and Cranfield University (2005), *Full Proposal, Air Turbine Development - Re-Submission TP/2/RT/6/S/10070*,
- Pontes, M. T., Candido, J., Henriques, J. C., and Justino, P. Optimizing OWC sitting in the nearshore. 6<sup>th</sup> European Wave and Tidal Energy Conference. 2005.
- Preston, J.H. (1954), 'The Determination of Turbulent Skin Friction by Means of Pitot Tubes', *Journal of the Royal Aeronautical Society*, Vol. 58,
- Previsic, M. and Sacramento, C. A. North American wave and tidal power collaboratives. 6<sup>th</sup> European Wave and Tidal Energy Conference. 2005.
- Professional Engineering (2006), *6 September 2006*, IMech E,

- Queen's University Belfast (2002), *Islay LIMPET Wave Power Plant*. Report no. Contract JOR3-CT98-0312, publishable report 30 Nov 98 to 20 April 02,
- Raghunathan, S. (1995), 'The Wells Air Turbine for Wave Energy Conversion', *Progress in Aerospace Sciences*, Vol. 31, pp. 335-386.
- Ramaprian, B.R. and Tu, S.W. (1983), 'Fully Developed Periodic Turbulent Pipe Flow. Part 2. The Detailed Structure of the Flow', *Journal of Fluid Mechanics*, Vol. 137, pp. 59-81.
- Saravanamuttoo, H.I.H., Rogers, G.F.C. and Cohen, H. (2001), *Gas Turbine Theory 5th Edition*, Pearson Education Ltd., Harlow, England.
- Seddon, J. and Goldsmith, E.L. (1985), *Intake Aerodynamics*, Collins, London.
- Setoguchi, T., Santhakumar, S., Maeda, H., Takao, M. and Kaneko, K. (2001) A review of impulse turbines for wave energy conversion. *Renewable Energy* **23** 261-292. Elsevier.
- Setoguchi, T., Santhakumar, S., Takao, M., Kim, T.H. and Kaneko, K. (2003) A modified Wells turbine for wave energy conversion. *Renewable Energy* **28** 79-91. Elsevier.
- Shaw, R. (1982), *Wave Energy a Design Challenge*, Ellis Horwood Ltd.,
- Tease, W.K. *Dynamic Response of a Variable Pitch Wells Turbine*, Report no. DTi Contract No.:V/06/00202/00/00, Wavegen,
- Thakker, A., Hourigan, F., Dhanasekaran, T.S., Hemry, M.El., Usmani, Z. and Ryan, J. (2005), 'Design and Performamnce Analysis of Impulse Turbine for a Wave Energy Plant', *International Journal of Energy Research*, Vol. 29, pp. 13-36.
- Thiruvenkatasamy, K. and Sato, M. On the hydrodynamics of oscillating water column (OWC) wave power device. 6<sup>th</sup> European Wave and Tidal Energy Conference.
- Thorpe, T.W. (1999), *A Brief Review of Wave Energy. ETSU Report ETSU-R120*,
- Tu, S.W. and Ramaprian, B.R. (1983), 'Fully Developed Periodic Turbulent Pipe Flow. Part 1. Main Experimental Results and Comparison With Predictions', *Journal of Fluid Mechanics*, Vol. 137, pp. 31-58.
- Wavegen (2002), *Research into the Further Development of the Limpet Shoreline Wave Energy Plant*, Report no. ETSU V/06/00183/REP URN 02/1487,
- WaveNet (2003), *Results From the Work of the European Thematic Network on Wave Energy* , Report no. ERK5-CT-1999-20001 2000-2003,
- Webb, I., Seaman, C., and Jackson, G. (2005), *Marine Energy Challenge. Oscillating Water Column Wave Energy Converter Evaluation Report*, The Carbon Trust,

White, P. The effect of non-axisymmetric flow on Wells turbine performance. The second European wave power conference. 95.

World Energy Council (1994), *New Renewable Energy Resources - A Guide to the Future*, Kogan page Ltd., London.

Wright, T. (1999), *Fluid Machinery Performance, Analysis, and Design*, CRC Press, Boca Raton, Florida.,

## Appendix A – Wave Spectra

### A.1 Spectral Parameters

Real seas contain waves which are random in height, period, and direction. Within a fixed period of time (corresponding to a sea state defined as lasting 2-6 hours), they can be satisfactorily modelled as a stationary stochastic field, i.e. the local sea state can be described by the means of a directional spectrum, that provides the distribution of energy density in the frequency and direction domains (Athanasoulis, Pontes, Tsoulos, Nakos, Stefanakos, Skopeliti, and Frutuoso, 1995). The spectrum can in turn be summarised by a few spectral parameters: the significant wave height ( $H_s$ ), the energy period ( $T_e$ ), the peak period  $T_p=1/f_p$ , where  $f_p$  is the frequency at which the frequency spectrum has its global maximum. However, comparison of work is complicated by the use of different nomenclature and because there have been at least four different definitions of significant wave height. The most commonly used definition of significant wave height has been the average height of the highest one third of waves defined as:

$$H_{1/3} = \frac{1}{n/3} \sum_{t=1}^{n/3} H_t$$

and  $T_e/T_{1/3}$  defined as the average time counted over at least 10 crossings between upward movements of the surface through the mean level. The problem with this is that it is sensitive to any change of bandwidth of the measurement system because higher bandwidths measure more zero crossings.

The use of  $H_{1/3}, T_{1/3}$  are no longer considered satisfactory, and the modern definition is based on 4 times the root mean square value of the water level relative to mean water level:

$$H_{rms} = \sqrt{\frac{\sum_{i=1}^n y_i^2}{n}}$$

and the significant wave height is then :

$$H_s = 4H_{rms}$$

$H_s$  is approximately equivalent to  $H_{1/3}$ . In deep water the 2 approaches are similar, but are different in shallow water (Wavegen, 2002). The ‘zero-crossing period’  $T_z$  is defined as:

$$T_z = \frac{D}{n_z}$$

Where  $D$  is the duration in seconds of the record, and  $n_z$  is the number of times the water surface moves through its mean level in an upward direction in that duration.

It has been suggested that  $T_z$ , should be replaced by the energy period,  $T_e$ , calculated from the wave spectrum and defined as the period of a regular wave which would have the same power density and the same root-mean-square amplitude.

If a wave record is assumed to be stationary and ergodic, i.e. the mean value and autocorrelation function of the random process can be computed at a time by taking the mean value of each sample function of the ensemble, and the ensemble average is also equal to the time averaged value for individual specific functions. Then the sea may be represented by a power spectral density function defined for a small frequency interval  $\Delta f$  at frequency  $f$  and obtained from a Fourier transform analysis:

$$S(f) = \lim_{\Delta f \rightarrow 0} \lim_{T \rightarrow 0} \frac{1}{(\Delta f)T} \int_0^T y^2(t, f, \Delta f) dt$$

If  $y(t)$  is measured relative to the mean value,  $S(f)$  will not exist at  $f=0$ , and the mean square value to relate the significant height to the energy of the wave

$$H_s = 4.0\sqrt{m_0} \quad T_e = \frac{m_{-1}}{m_0}$$

where  $m_0$  is the zeroth spectral moment, and the  $n^{\text{th}}$  spectral moment is defined as:

$$m_n = \int_0^{2\pi} \int_0^\infty f^n E(f, \theta) df d\theta$$

Unlike the ‘traditional’ zero-crossing period computed by

$$T_{m_{02}} = \left( \frac{m_0}{m_2} \right)^{1/2}$$

which is very sensitive to the high-frequency spectral tail,  $T_e$  depends mainly on the lower frequency band of the spectrum that contains most of the energy .

Knowledge of the directional spectrum permits the flux of power per unit crest length to be evaluated through the equation:

$$P_w = \rho g \int_0^{2\pi} \int_0^\infty S(f, \theta) c_g(f, h) df d\theta$$

where  $c_g$  = group velocity, which depends upon  $f$  and water depth  $h$ . In deep water  $c_g = g/4\pi f$  the equation may be simplified to:

$$P_w = \frac{\rho g^2}{4\pi} m_{-1}$$

which can be expressed in terms of  $H_S$  and  $T_e$  as:

$$P_w = \frac{\rho g^2}{64\pi} H_S^2 T_e$$

which is the equation for an ideal wave.

## A.2 Long-crested Irregular waves

If waves are assumed to be long crested, i.e. uni-directional, and it may be further assumed that:

1. process is a weakly stationary ergodic Gaussian random process with zero mean
2. wave spectral density functions are narrow banded
3. wave crest maxima are statistically independent
4. statistical properties of ocean waves are homogeneous

Then long-crested irregular waves for use in design processes may be described by a probabilistic power spectral density function in the frequency domain. A number of parameterised formulae for such functions have been derived from observations and theoretical work. When using such spectra, however, it is important to know whether they apply to partially or fully developed sea states (Patel, 1989). A fully developed sea exists when energy input from the wind is balanced by the dissipation of energy in breaking. The mathematical formulation commonly used to define wave spectra has the general form shown below:

$$S_\zeta(\omega) = A\omega^{-l} \exp[-B\omega^{-n}]$$

where  $S_\zeta(\omega)$  is the energy spectrum ordinate,  $\omega$  is the circular frequency, and  $A$ ,  $B$ ,  $l$ , and  $n$  are parameters of the spectrum. Various relationships have been proposed for  $A$  and  $B$ , for example when:

$$A = B \frac{H_S^2}{4} \quad \text{and} \quad B = \frac{5}{4} f_0^4$$

then the Pierson-Moskowitz spectrum is obtained.

The spectra have also been expressed in an alternative frequency formulation which recognizes that  $A$  and  $B$  are related to the significant wave height  $H_{\frac{1}{3}}$  and

characteristic period  $T_k$ , i.e.:

$$E(f) = A'H_{\frac{1}{3}}^2 T_k^{-l} f^{-m} \exp[-B'T_k^{-l} f^{-n}]$$

where  $A'$ ,  $B'$  are constants independent of  $H_{\frac{1}{3}}$  and  $T_k$  (Hoffman, 1974). When  $n = 4$  and  $l = 5$ , the above equation can also be expressed in terms of the peak frequency,  $f_0$ :

$$E(f) = H_{\frac{1}{3}}^2 P \left( \frac{f_0}{f} \right)^4 f^{-1} \exp \left[ -Q \left( \frac{f_0}{f} \right)^4 \right]$$

where  $P$  and  $Q$  are constants and are functions of  $f_0^4$ . The above equation is derived from the functional relationship between the peak frequency and a characteristic period  $T_k$ .

When  $n = 4$  and  $l = 5$  and  $T_2 = 2T(m_0 / m_2)^{\frac{1}{2}}$  the spectrum is generally referred to as the modified Pierson-Moskowitz spectrum:

$$S_{\zeta}(\omega) = \frac{H_{\frac{1}{3}}^2}{4\pi} \left( \frac{2\pi}{T_2} \right)^4 \omega^{-5} \exp \left[ - \left( \frac{2\pi}{T_2} \right)^4 \frac{\omega^{-4}}{\pi} \right]$$

or, in non-dimensional form:

$$\frac{S_{\zeta}(\omega)}{H_{\frac{1}{3}}^2 T_2} = \frac{1}{8\pi^2} \left( \frac{\omega T_2}{2\pi} \right)^{-5} \exp \left[ - \frac{1}{\pi} \left( \frac{\omega T_2}{2\pi} \right)^{-4} \right]$$

in terms of frequency the Pierson –Moskowitz spectrum can be written as (Patel, 1989):

$$S_{\zeta}(f) = \frac{Ag^2}{(2\pi)^4 f^5} \exp \left[ - \frac{5}{4} \left( \frac{f}{f_0} \right)^{-4} \right]$$

$$S_{\zeta}(f) = 5 \times 10^{-4} f^{-5} \exp \left[ - \frac{4.4}{f^4 U^4} \right] \quad \text{m}^2/\text{Hz}$$

where  $U = \frac{g}{2\pi f_0}$ , and  $U$  is the wind speed in m/s at 19.6m above the surface.

The Bretschneider spectrum is defined as:

$$S_{\zeta}(f) = \frac{5}{16} \frac{H_{m0}^2}{f_0} \left( \frac{f_0}{f} \right)^5 \exp \left[ -\frac{5}{4} \left( \frac{f}{f_0} \right)^4 \right]$$

where  $H_{m0} = 4\sqrt{m_0}$

The ISSC selected the same form as the equation above as the standard wave formulation, but used  $T_1$  instead of  $T_2$ . For  $n = 4$  and  $l = 5$ ,  $T_1 = 1.086T_2$ . Hence, the ISSC recommended spectral formulation in non-dimensional form using  $T_1$  is:

$$\frac{S_{\zeta}(\omega)}{H_{\frac{1}{3}}^2 T_1} = \frac{0.11}{2\pi} \left( \frac{\omega T_1}{2\pi} \right)^{-5} \exp \left[ -0.44 \left( \frac{\omega T_1}{2\pi} \right)^4 \right]$$

For the Neumann spectrum  $n = 2$  and  $l = 6$ , and the non-dimensional spectrum is:

$$\frac{S_{\zeta}(\omega)}{H_{\frac{1}{3}}^2 T_2} = \frac{3}{8\pi} \left( \frac{\omega T_2}{2\pi} \right)^{-6} \exp \left[ -\frac{3}{2} \left( \frac{\omega T_2}{2\pi} \right)^2 \right]$$

Attempts to fit any of the above spectral formulations to actual data have shown that none of them can be generalised to fit all measured spectra. While one formulation may be adequate in one specific case, others may be appropriate in other cases, and often none of the formulations can be used (Hoffman, 1974). Hoffman illustrates this by record examples from station 'India' which have virtually identical statistical characteristics of wave height and period, but whose spectra were actually quite different. If a spectrum is defined only in terms of wave height and period several different shapes having different peak frequencies and maximum spectral ordinates may result.

## Appendix B – Calculation of Efficiency

### B.1 Definitions

The efficiency of turbine stages is defined by comparing the actual work and the ideal work. However, in defining the ideal work which can be extracted, the ideal isentropic process can be defined as taking place from a given inlet pressure and velocity to the final pressure either with or without diffusion of the exhaust velocity. These 2 conditions determine the total to static, and total to total efficiencies respectively (Horlock, 1966):

$$\text{Total to static efficiency, } \eta_{TS} = \frac{h_{01} - h'_{03}}{h_{01} - h_3}$$

$$\text{Total to total efficiency, } \eta_{TT} = \frac{h_{01} - h'_{03}}{h_{01} - h_{03}}$$

The total-to-total efficiency is usually used in multi-stage turbines where the exhaust velocity from a stage is not lost, but transferred to the inlet of the next stage. However, when the stage outflow is exhausting to static pressure – as is the case for a single stage OWC turbine - then it is appropriate to use the total-to-static efficiency, as the remaining kinetic energy of the flow will be lost. This means that for a given set of conditions the total-to-total efficiency measurement is higher than the total-to-static, as  $(h_{01}-h_{03})$  is less than  $(h_{01}-h_3)$  as illustrated in Figure 150.

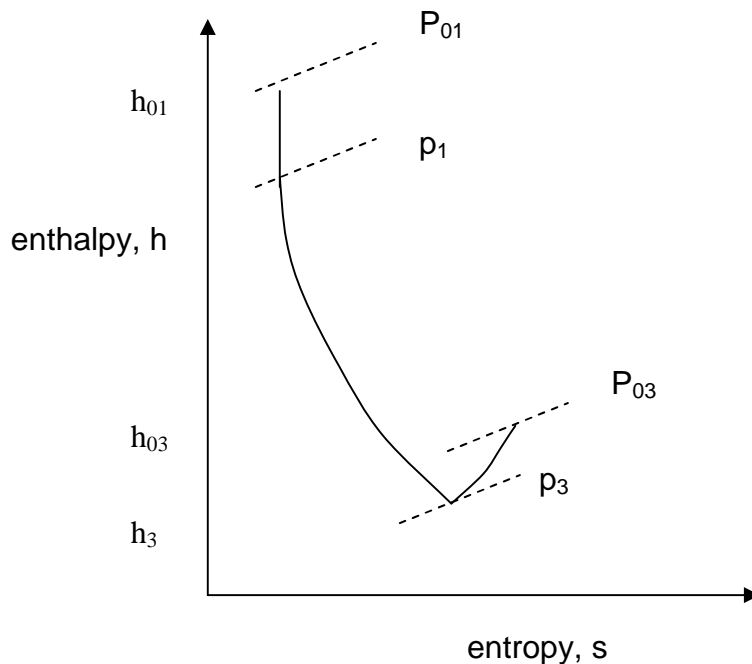


Figure 150 – Difference between total-to-total, and total-to-static efficiency

The total-to-total efficiency thus evaluates the useful output in relation to the ideal work obtained from the change in stagnation conditions across a stage, whilst the total-to-static efficiency evaluates the useful output in relation to the change in stagnation conditions across the stage, plus the residual kinetic energy.

## B.2 Determination of total-to-static efficiency

The total-to-static efficiency is defined in terms of enthalpy changes per unit mass flowrate, and if the specific heat is assumed to remain constant, then it can be expressed in terms of temperature changes. However, if the changes in pressure in the flow are relatively small – as is the case in OWC systems, then the changes in temperature through the turbine will only be small, in addition it is very difficult to measure static temperature directly, which means that significant errors could be made in measuring efficiencies by measuring temperature differences. This makes it desirable to re-cast the efficiency formula in terms of parameters that can be measured more easily.

The useful work output of the turbine corresponds to amount of kinetic energy in the flow which is transformed into shaft power (neglecting windage and bearing losses) i.e  $W = \omega \tau$ . In an ideal process there will be no swirl component at entry or exit, and assuming an adiabatic process, conservation of energy means:

$$C_p(T_{01} - T_3) = \frac{V^2}{2}$$

Now from Bernoulli's equation:

$$P_{01} - P_3 = \rho \frac{V^2}{2}$$

but  $P_{01} - P_3 = \Delta P$ , the total-to-static pressure drop, and so:

$$C_p(T_{01} - T_3) = \frac{\Delta P}{\rho}$$

Now considering the actual mass flowrate through the turbine  $\dot{m} = \rho VA$ , that leads to the measured shaft power, we obtain:

$$\dot{m} C_p(T_{01} - T_3) = Q \Delta P$$

where  $Q = VA$ , and so the total-to-static efficiency may be expressed in the form:

$$\eta_{TS} = \frac{\omega \tau}{Q \Delta P}$$

In this form the efficiency is evaluated in terms of parameters which can be measured more easily and accurately than the temperature changes.

## Appendix C – Scaling Spreadsheet calculations

### C.1 Scaling Spreadsheet

Inputs		Constants	
Full scale device		Scaled device	
Density	1.19		
Viscosity	1.73E-05	Scale factor	0.28
No. of blades	7	No. of blades	7
Chord	0.32	Chord	0.0896
Dtip	2.6	Dtip	0.7280
Dhub	1.612	Dhub	0.4514
Blade height	0.494	Blade height	0.1383
Annulus area	3.2684	Annulus area	0.2562
Rmid	1.053	Rmid	0.2948
Full area	1.8492		
Solidity	0.3386	Solidity	0.3386
Speed	1050	Speed	2250
Speed rad/s	109.96	Speed rad/s	235.62
Umid	115.78	Umid	69.47
Turbine efficiency	0.38	Turbine efficiency	0.38
Generator efficiency	0.9	Generator efficiency	0.9
Turbine delta P	6383	Turbine delta P	2297.88
Air flow rate	83.93	Air flow rate	3.95
Axial velocity	25.68	Axial velocity	15.41
Pressure coefficient	0.80		
Va/U	0.2218	Va/U	0.2218
Period	10.6	Period	4.9
Frequency	0.0943	Frequency	0.2022
Input power	535725.2	Input power	9072.2
O/p shaft power	203575.6	O/p shaft power	3447.4
Torque	1851.4	Torque	14.6
Power out	183218.0	Power out	3102.7
Re	2.54E+06	Re	4.27E+05
Strouhal	2.61E-04	Strouhal	2.61E-04
		Air volume displaced	9.8
		PWG volume	11.2

Figure 151 – Scaling spreadsheet for Wells turbine

The initial scaling spreadsheet constructed for a monoplane Wells turbine installed in the LIMPET OWC facility is shown in Figure 151. The numbers in red are specified values, whilst those in black are calculated. The relationships are straightforward but specific definitions used were:

$$\Delta p_{\text{model}} = \frac{1}{2} \rho U_{\text{mid model}}^2 C_{p_{\text{full scale}}}$$

$$\text{Re}_{\text{model}} = \frac{\rho U_{\text{mid model}} c_{\text{model}}}{\mu}$$

$$T_{\text{model}} = \frac{c_{\text{model}}}{\text{St}_{\text{full scale}} \cdot U_{\text{mid model}}}$$

$$\text{volume displaced} = v_a \times 0.5T$$

$$PWG \text{ volume} = \frac{8}{7} \times \text{volume displaced}$$

## C.2 Variation in test facility parameters

The sequence of calculations made to evaluate the variation required in test facility parameters to provide a simulation of a given range of full scale power inputs was as follows:

1. Given full scale power, rpm, and turbine geometry calculate the power coefficient:

$$\varepsilon = \frac{P_{FS}}{\rho U_{\text{mid FS}}^3 A_{FS}}$$

2. Use assumed scale factor to determine model geometry, and choose model design flow ratio ( $\phi_{\text{model}}$ ) and rotational speed.
3. Determine parameter values at model scale:

$$P_{\text{model}} = \varepsilon \rho U_{\text{model}}^3 A_{\text{model}}$$

$$V_{a \text{ model}} = \phi_{\text{model}} U_{\text{model}}$$

$$Q_{\text{model}} = V_{a \text{ model}} A_{\text{model}}$$

$$\Delta p_{\text{model}} = \frac{P_{\text{model}}}{Q_{\text{model}}}$$

4. Determine design work coefficient;

$$\psi = \frac{\varepsilon}{\phi}$$

It was further assumed that for powers other than the design point that the rotational speed of the full scale turbine varied with the cube root of the change in power, i.e.:

$$RPM = \sqrt[3]{\left(\frac{P}{P_{\text{Design}}}\right)} \cdot RPM_{\text{Design}}^3$$

## Appendix D – Instrumentation Response

The problem of determining the pressure response of a line-cavity system can be addressed in a number of ways. The method described here is the ‘rigid column approach’. This neglects compression of the fluid in the line and cavity, and assumes that all the fluid in the line starts moving at time  $t = 0$ . A diagram of the type of line-cavity system considered is given in Figure 152. The other principle assumption is that the wall friction is the same in unsteady flow conditions as in steady ones – this is the main weakness of this approach.

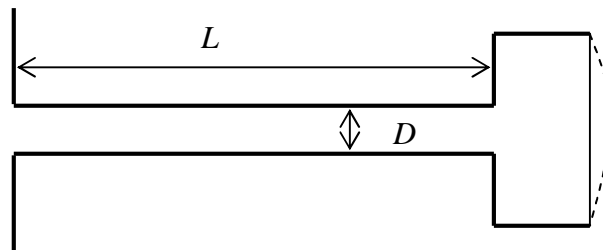


Figure 152 – Schematic of line-cavity system

The analysis leads eventually to the differential equation:

$$\frac{P_1}{\rho} - \frac{S}{\rho C} \int U dt = L \frac{dU}{dt} + k_1 U + k_2 \frac{U^2}{2}$$

where:

$P_1$	applied pressure
$\rho$	density of the air
$S$	cross-sectional area of the line
$U$	average velocity of the fluid in the line
$k_1$	constant for laminar flow = $\frac{32\nu L}{D^2}$
$k_2$	constant for laminar flow = $8/3$
$D$	diameter of line
$L$	length of line
$\nu$	kinematic viscosity
$C$	is the term: $C = \frac{dVol}{dP_3} + \frac{Vol}{nP_a}$
$P_a$	ambient pressure
$Vol$	volume of the cavity
$P_3$	relative pressure in the cavity
$n$	polytropic exponent (taken as 1.4)

The integral can be eliminated by differentiation, to obtain the non-linear, second order differential equation:

$$L \frac{d^2U}{dt^2} + (k_1 + k_2) \frac{dU}{dt} + \frac{S}{\rho C} U = 0$$

with the initial conditions:

$$U = 0 \quad \text{and} \quad \frac{dU}{dt} = \frac{P_1}{\rho l} \quad \text{at} \quad t = 0$$

The variation in U with time U(t) can be found by integration, and then U(t) can be used to find the pressure at the transducer from:

$$P_t(t) = \frac{S}{c} \int U dt$$

## Appendix E – Actual Test Facility Dimensions

This appendix presents the measurements made of the actual PWG and compares them with the design specification. The design and measured dimensions are listed in Table 61.

Dimension	Design (mm)	Measured (mm)
Internal floor to ceiling	2400	2403
Radius of plywood roof	1700	1700
Central pillar to inside surface of wall	157	157
Thickness of end of fibreglass panel	50	53
Distance between wall end and flap surface at Home position	-	176
Distance from Home stop	-	6
Thickness of flap		63
Distance between outer edges of wall ends		1840

*Table 61 – PWG Dimensions*

From the measurements, the total angular volume enclosed by the fibreglass walls is 294.7 degrees. The angular change in volume lost due to the position of the Home point and thickness of the flap is 4.85 degrees. Hence, the total angular volume enclosed is 289.8 degrees. This means:

$$\text{Actual volume of PWG cylinder} = \frac{289.8}{360} \times \pi \times 1.65^2 \times 2.403 = 16.54 \text{ m}^3$$

This is 0.66% greater than the swept volume originally specified of 16.43 m<sup>3</sup>.

The dimensional accuracy of the duct inlet and transition sections was taken to be sufficient by virtue of the fact that no significant fitting problems were found during assembly. The design internal volumes of the duct inlet and transition sections were 0.49 m<sup>3</sup>, and 0.94 m<sup>3</sup> respectively. If these are taken as correct, it means that the overall volume of the PWG when the flap is at the Home position is 17.97 m<sup>3</sup>.

Once the PWG facility was assembled the actual range of movement that could be achieved by the flap was measured using the output from the encoder on the top of the central shaft. The original design intent was that the flap would have a range of movement of 288 degrees, but this was found to have reduced in the course of engineering the rig to 270 degrees. Furthermore, in order to provide a small margin for error at the end of the flap movement before the limit switches were triggered to produce an emergency shutdown, and to ensure that when the Homing sequence was performed the flap would pick up the Home limit switch, and then move forward of it, the actual range of movement from the 'Home' position was fixed at 265 degrees. This meant that the maximum volume which would be swept by the flap was:

$$\text{swept volume} = \frac{265}{360} \times \pi (1.65^2 - 0.084^2) \times 2.4 = 15.1 \text{ m}^3$$

The design intent for the PWG was that the flap would have 288 degrees of movement, which would give a swept volume of  $16.43\text{m}^3$ . This meant that the actual maximum swept volume was 8% less than originally specified.

## Appendix F - Matlab Input Parameter Code

In order to enable a series of wave profiles to be produced and varied in a systematic way, the Matlab code 'profile' was written which defined a trapezoidal approximation to a desired sine wave profile, and then determined values for a1, a2, sp1,sp2, p1, and p2.

In order to be able to relate the conditions in the test facility back to full scale, it was assumed that the ideal speed profile followed by the flap would follow a Sine wave of specified RMS flowrate  $Q_{RMS}$ , and period  $T$ . The requirement for the code was then to determine the appropriate trapezoidal approximation to the Sine wave and to determine the appropriate values of a1,a2,sp1,sp2,p1,p2 that should be loaded into the PLC to produce it.

If the RMS flowrate is  $Q_{RMS}$ , and period  $T$ , then:

$$Q_{\max} = \sqrt{2} Q_{rms}$$

The relationship between angular speed and flowrate is:

$$Q = \frac{\omega}{2} (R_{Wall}^2 - R_{Pillar}^2) h_{pwg}$$
$$Q = \omega \cdot fvol$$

and so

$$\omega_{\max} = \frac{Q_{\max}}{fvol}$$

and the angular movement over half a cycle is:

$$\theta_{0.5} = \frac{\omega_{\max} T}{\pi} \times \frac{180}{\pi}$$

In the first instance the Sine wave was approximated by a true trapezoid as shown in Figure 153. This shows a reasonably close match between the two profiles over much of the cycle.

**Trapezoidal approximation to Sine wave**  
 Period = 7.0 s, Qrms = 2.3 Angular movement = 127.4 deg, max angular rate = 57.2 deg/s

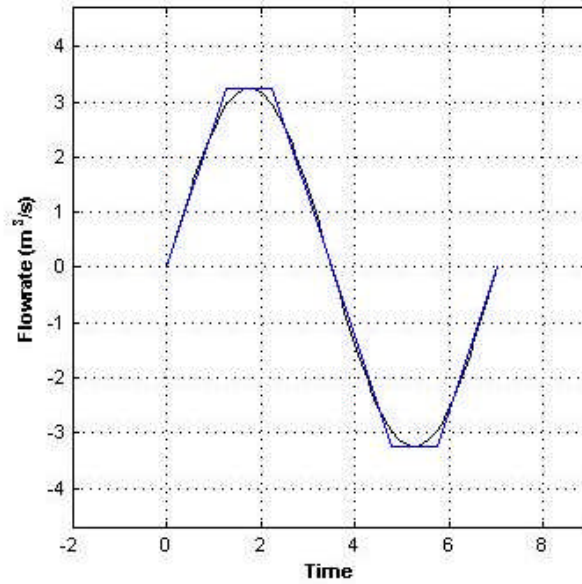


Figure 153 – Trapezoidal approximation to Sine wave

This approximation was derived by assuming that the maximum angular speed attained by the flap following the trapezoidal profile would be the same as that of the Sine wave profile, and that the flap would move the same distance. With these assumptions the time,  $t_1$ , taken for the flap to accelerate from rest up to its maximum speed could be determined as:

$$t_1 = T \left( \frac{1}{2} - \frac{1}{\pi} \right)$$

and the trapezoid is defined. The parameters for the PLC are then calculated as follows:

$$\text{speed} = \omega_{\max} \times \frac{30}{\pi} \times \text{gearing}$$

$$\text{acceleration} = \frac{\text{speed}}{t_1}$$

$$p_1 = \theta_{0.5} \times \text{gearing}$$

$$p_2 = 1$$

where  $\text{gearing} = 72$ , is the ratio between revolutions of the drive motor and flap. When the initial derived parameter values were input to the PLC it was found that the actual cycle periods were shorter than desired. The desired cycle period was then obtained by adjusting the values of the acceleration/deceleration parameters.

The results showed that in order to obtain a better calculation of the parameter values it was necessary to model the actual flap movement profile more accurately. This meant that the code had to allow for the 100ms dwell time that occurred in the ladder program, and for the fact that the actual acceleration/decelerations were not constant but rose and fell. This was implemented in the Matlab code by allowing for the dwell time by saying that the same total flow rate had to be passed in  $T - (2 \times T_{dwell})$  so:

$$t_1 = T \left( \frac{1}{2} - \frac{1}{\pi} \right) - t_{dwell}$$

and making the accelerations/decelerations follow Cosine profiles. It was initially assumed that the acceleration/deceleration required corresponded to the maximum gradient of the cosine speed curve (rounded down to the nearest integer):

$$\text{acceleration} = \frac{\omega_{\max}}{2t_1} \times \text{gearing rev/s}^2$$

but calibration against the actual movements showed that better correlation was given by:

$$\text{acceleration} = \left( \frac{\omega_{\max}}{2t_1} - 4 \right) \times \text{gearing rev/s}^2$$

A comparison between a Sine wave and an example calculated profile is shown in Figure 154.

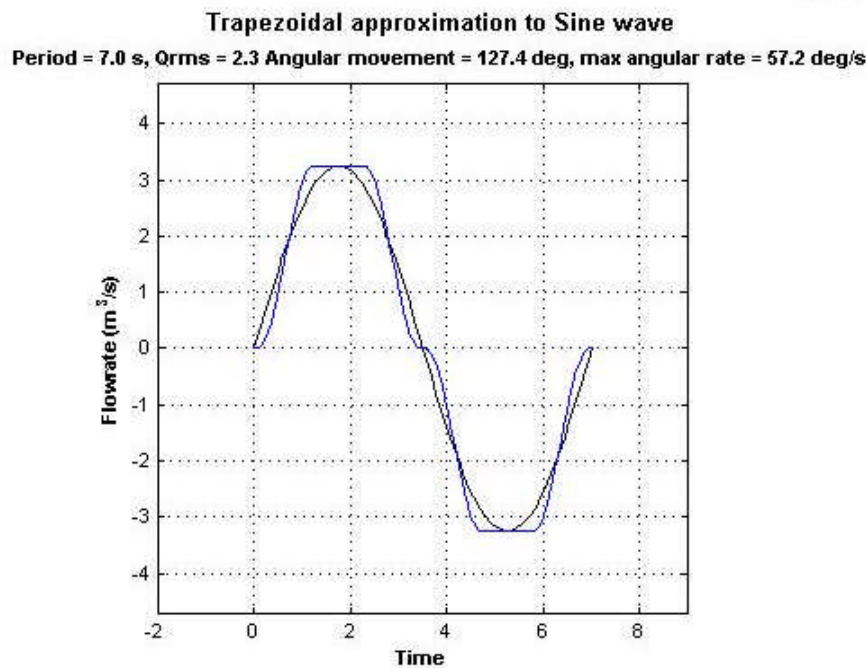


Figure 154 – modified trapezoidal approximation to Sine wave

## Appendix G – Test Rig Configurations

### G.1 Empty Duct

The initial duct configuration attached to the PWG was a simple assembly of straight duct sections together with the instrumentation rings and exit diffuser sections in the order shown in Table 62.

Item	Length (m)	Volume (m <sup>3</sup> )	Type
1	1.0	0.5026	Duct
2	0.485	0.2438	Duct
3	0.11	0.0553	Inst ring
4	1.5	0.7540	Duct
5	1.5	0.0754	Duct
6	0.485	0.2438	Duct
7	0.11	0.0553	Inst ring
8	1.0	0.5026	Duct
9	1.0	0.6102	Diffuser
10	1.0	0.8524	Diffuser
11	0.188	0.2068	Bellmouth
Total length	8.335	4.7808	

*Table 62 – Details of configuration 0*

### G.2 Porous Plate

The duct configuration with the porous plate installed is detailed in Table 63.

Item	Length (m)	Volume (m <sup>3</sup> )	Type
1	1.0	0.5026	Duct
2	0.485	0.2438	Duct
3	0.11	0.0553	Inst ring
4	1.5	0.7540	Duct
5	0.001	-	Porous plate
5	1.5	0.0754	Duct
6	0.485	0.2438	Duct
7	0.11	0.0553	Inst ring
8	1.0	0.5026	Duct
9	0.98	0.6102	Diffuser
10	0.98	0.8524	Diffuser
11	0.185	0.2068	Bellmouth
Total length	8.336	4.7808	

*Table 63– Details of configuration 1*

The volume of straight ducting upstream of the porous plate was 1.556 m<sup>3</sup>. This meant that the total enclosed volume upstream of the porous plate was 19.526 m<sup>3</sup>.

### G.3 Datum Turbine Duct Configuration

The final duct configuration attached to the PWG with turbine module installed is listed in Table 64.

Item	Length (m)	Volume within casing (m <sup>3</sup> )	Type
1	1.0	0.5026	Duct
2	0.485	0.2438	Duct
3	0.11	0.0553	Inst ring
4	0.4	0.1550	Diffuser
5	1.185	0.3350	Turbine module
6	0.4614	0.1305	Turbine stage
7	0.23	0.0650	Spacer
8	0.4	0.1550	Diffuser
9	0.11	0.0553	Inst ring
10	0.485	0.2438	Duct
11	1.0	0.5026	Duct
12	1.0	0.6102	Diffuser
13	1.0	0.8524	Diffuser
14	0.188	0.2068	Bellmouth
Total length	8.0544	4.1133	

*Table 64 – Details of datum turbine duct configuration*

The area of the flow annulus at the instrumentation planes was:

$$A_{annulus} = \pi(0.4^2 - 0.25^2) = 0.306305 \text{ m}^2$$

The volume of the components comprising the central hub (which had a diameter of 0.492 m) and the bullets is shown in Table 65. Combining the data from Tables 42 and 43, we find that the total volume within the turbine duct (including that occupied by the blades and the support vanes) was 3.3868 m<sup>3</sup>. The size of the volume between the centreline of the turbine rotor and the PWG outlet was thus 1.35695 – 0.45405 = 0.9029 m<sup>2</sup>.

Item	Length (m)	Volume (m <sup>3</sup> )	Type
1	1.0712	0.1089	Bullet
2	0.4	0.0760	Diffuser hub
3	1.185	0.2253	Turbine module
4	0.4614	0.0877	Turbine stage
5	0.23	0.0437	Spacer
6	0.4	0.0760	Diffuser hub
7	1.0712	0.1089	Bullet
Total length	4.8188	0.7265	

*Table 65 – Lengths and volumes of hub components*

## Appendix H – Evaluation of discharge coefficient

The discharge coefficient was evaluated by applying the same procedure to the data in each instrumentation plane. The procedure for one plane is described here.

The maximum value of dynamic pressure  $q_{max\ i}$  was first found for the each data point in the traverse. This was calculated by finding the maximum value of  $(\bar{P}_{0m} - \bar{p}_m)$ , where  $\bar{P}_{0m}$  was the average of the 3 total pressure readings, and  $\bar{p}_m$  was the average of the 6 static pressures at each of the  $m$  points within the averaged cycle data. Once, the sample at which  $q_{max\ i}$  occurred had been identified, the corresponding value of density was also calculated:

$$\rho_i = \frac{\bar{p}_m}{RT_m}$$

where  $\bar{T}_m$  was the average of the 2 instrumentation plane temperatures at the instant when  $q_{max\ i}$  was recorded. When this was known, the maximum velocity of the flow through the instrumentation plane was found:

$$v_{max\ i} = \sqrt{\frac{2q_{max\ i}}{\rho_i}}$$

Ideally there would be no boundary layers, and the velocity would be constant across the instrumentation plane, and the ideal maximum mass flowrate would be:

$$\dot{m}_{ideal} = \rho v_{max} A_{ip}$$

where  $A_{ip}$  is the area of the instrumentation plane duct. However, due to the development of the wall boundary layers, we have a velocity profile which means that, assuming the flow is circumferentially uniform, the actual mass flow rate is given by:

$$\dot{m}_{actual} = \int_0^h \rho v dA$$

Now, the discharge coefficient is defined as:  $C_D = \frac{\dot{m}_{actual}}{\dot{m}_{ideal}}$

which can be re-written as:

$$C_D = \frac{1}{A_{ip}} \int_0^h \frac{v}{v_{max}} dA$$

or in the discrete form:

$$C_D = \frac{\pi}{2A_{ip}} \sum_{i=2}^n \left( \frac{v_i + v_{i-1}}{v_{max}} \right) (r_i^2 - r_{i-1}^2)$$

# Appendix I - CFD Simulations of turbines

## I.1 Baseline Wells Turbine Simulation

### I.1.1 Baseline Wells turbine design

The turbine design selected as the Wells turbine baseline was that used by Setoguchi to assess the effect of blade setting angle (Setoguchi et al, 2003). This had the characteristics shown in Table 66. The characteristics of this turbine are not quite optimal, furthermore, as a baseline geometry it was modelled without guide vanes. The peak efficiency derived from the experiment data was about 38% - as compared to the 44% of a close to optimal design with guide vanes.

Parameter	Value
Profile	NACA0012
Chord length, l	0.075 m
Solidity	0.75
Number of blades, z	8
Tip gap	0.001 m
Hub/tip ratio	0.7
Tip diameter	0.298 m
Hub diameter	0.2086 m
Blade aspect ratio	0.6
Annular area	0.0356 m <sup>2</sup>

Table 66- Characteristic parameters of baseline Wells turbine design (Setoguchi, 2003)

### I.1.2 Derived Performance Data

In order to compare the results of the CFD simulation with the experimental data, the CFD results were processed to derive the non-dimensional parameters used by Setoguchi et al, which were defined as:

Flow coefficient: 
$$\phi = \frac{v}{U_R}$$

Torque coefficient: 
$$C_T = \frac{2T_o}{\rho(v^2 + U_R^2)blzr_R}$$

Input coefficient: 
$$C_A = \frac{2\Delta p Q}{\rho(v^2 + U_R^2)blzv}$$

Efficiency: 
$$\eta = \frac{T_o \omega}{\Delta p Q} = \frac{C_T}{C_A \phi}$$

Where:

$v$	= axial velocity
$U$	= blade speed at mean radius
$T_0$	= torque
$\rho_a$	= density of air
$b$	= blade height
$l$	= chord length
$z$	= number of blades
$r_R$	= mean radius
$\Delta p$	= total-to-static pressure drop
$Q$	= volumetric flow rate
$\omega$	= rotational speed

### 1.1.3 Details of CFD model

The computational grid used by Banks consisted of hexahedral elements, had approximately 770,000 nodes, and was constructed using ICEM Hexa. The grid was extended at the outlet side of the blade to a distance of about 4 chord lengths to avoid convergence instabilities due to vortices impinging on the boundary. The only information given Setoguchi's paper with regard to the test conditions was that the maximum flow conditions achievable were: axial velocity 9.0m/s and flowrate 0.32 m<sup>3</sup>/s at 471 rad/s (4500 rpm). Therefore Banks used this and varied the rotational speed to obtain results over a range of flow ratios from 0 to 1.5, although the axial velocity had to be varied at the lowest flow conditions as well to avoid unrealistically high rotational speeds.

A total of 16 simulations were carried out, using CFX-10 for solution, pre, and post processing. The cases were run as incompressible cases with no heat transfer ( $Ma \ll 0.3$ ). The Shear Stress Transport (SST) turbulence model was used. Good convergence was achieved in most cases but became more problematic for flow ratios  $\phi > 1$ , where the turbine was operating far from design, and large regions of separated flow existed. Since these simulations were steady state, it was no surprise that it was difficult to achieve convergence when such inherently unsteady flow features were present.

### 1.1.4 Results

The results of the simulations plotted and compared with the experimental data, as shown in Figure 155. In addition, the data was reduced to obtain a pressure drop versus mass flow rate characteristic which cannot be obtained from the data presented by Setoguchi, but was required for input into the wave-to-wire simulation program OWCsim.

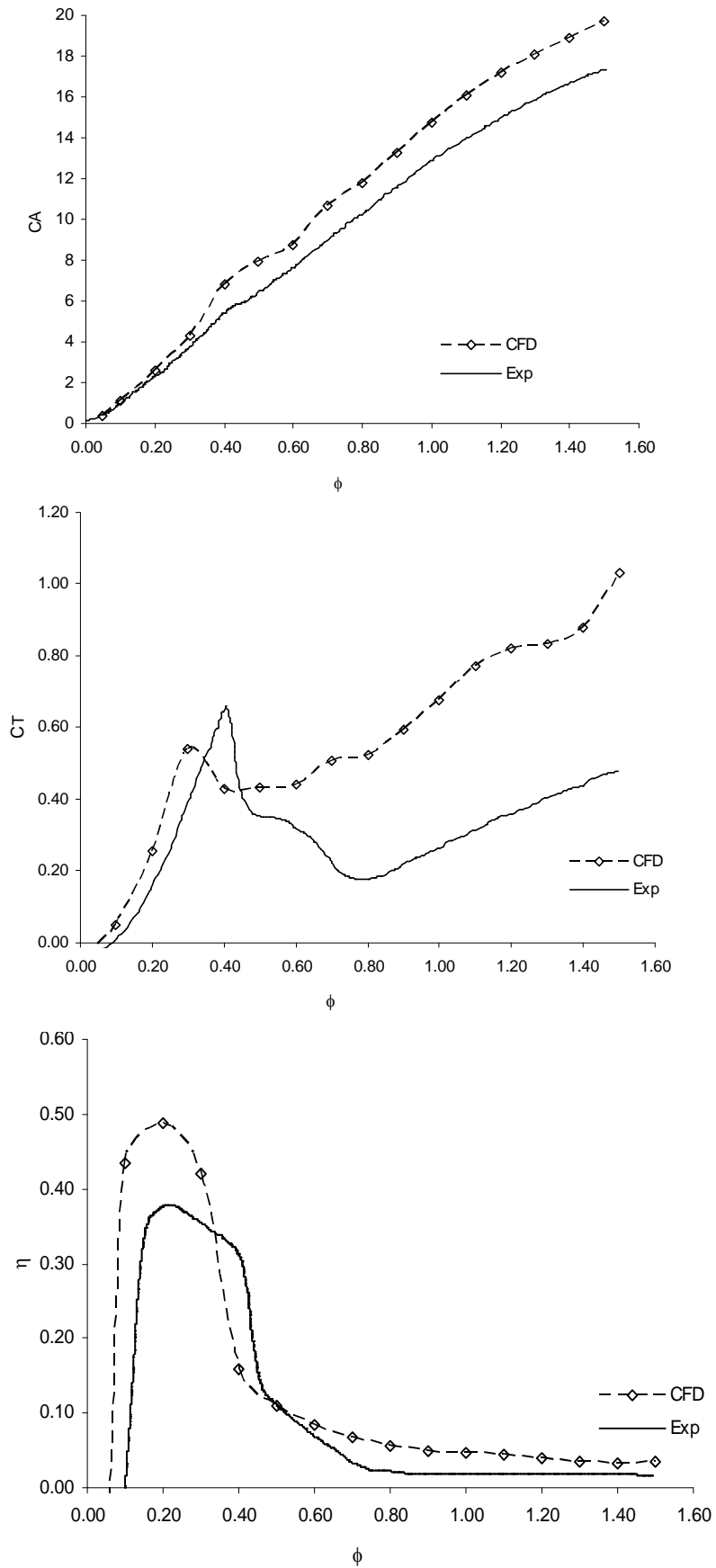


Figure 155 - Comparison of CFD and experiment baseline Wells turbine design

## I.2 Baseline Impulse Turbine Simulation

### I.2.1 Baseline Impulse turbine design

The design selected for the baseline impulse turbine design was the best fixed guide vane design evaluated by Maeda et al (Maeda et al, 1999). This differed from the optimum fixed guide vane impulse turbine design recommended by Setoguchi et al (see Table 10 and Table 11) in that the rotor blades were not swept to  $-7.5^\circ$ . The design parameters are given in Table 67.

Rotor:

Parameter	Value
Profile	Elliptical
Inlet angle ( $\gamma$ )	$60^\circ$
Radius of pressure surface	30.2
Semi minor axis of ellipse (e)	41.4
Semi major axis of ellipse (a)	125.8
Axial chord length ( $l_r$ )	0.054 m
Number of blades, z	30
Tip gap	0.001 m
Hub/tip ratio	0.7
Tip diameter	0.298 m
Hub diameter	0.2086 m
Annular area	$0.0356 \text{ m}^2$

Guide vanes:

Parameter	Value
Profile	plate
Guide vane thickness	0.005 m
Pitch angle ( $\theta$ )	$30^\circ$
Radius $R_a$	0.0372 m
Camber angle ( $\delta$ )	$60^\circ$

Table 67 – Design parameters for Baseline Impulse turbine design

### I.2.2 Details of CFD model

A similar approach was used as for the Wells turbine simulation. The outlet guide vane grid was again extended to a distance of about 4 chord lengths to avoid convergence instabilities caused by vortices impinging on the boundary.

As for the Wells turbine simulation, the only information given in the paper with regard to the test conditions was that the maximum flow conditions achievable. These were: axial velocity 17.7m/s and flowrate  $0.63 \text{ m}^3/\text{s}$  at 370 rad/s (3533 rpm). The same procedure was adopted as for the Wells turbine simulation. The maximum value of axial velocity that the Saga university test rig could produce was used to maximise the Reynolds number, and the same approach adopted in defining  $U$ ,  $\omega$  and  $v$  as for the Wells turbine simulation. These values corresponded to a range of  $\phi = 0 - 2.5$  in

common with the range of values measured by Setoguchi. A total of 14 CFD simulations were then made over the range of flow ratios. The simulation conditions similar to those for the Wells turbine, and whilst global convergence was reasonably good for all cases (RMS residuals  $< 10^{-4}$ ), it was hampered by extensive separated flow downstream of the outlet guide vane.

### **I.2.3 Results**

The results of the simulations were processed in a similar manner to those for the Wells turbine simulations to obtain coefficient values in the form used by Setoguchi. Plots were again created (Figure 156) which enabled the characteristics obtained from the simulations to be compared with the experimental data. In addition, the data was again reduced to obtain a pressure drop versus mass flow rate characteristic which could not be obtained from the data presented by Setoguchi, but was required for input into the simulation program OWCsim.

## **I.3 Analysis of CFD simulation results**

### **I.3.1 Input power coefficient**

The magnitude of the input power coefficient was over-predicted in both the Wells and Impulse turbine simulations. The magnitude of the difference increased with flowrate up to a maximum of about 10% for the Wells turbine and 5% for the impulse turbine.

### **I.3.2 Torque coefficient**

The prediction of torque coefficient was not very good for the Wells turbine, in terms of characteristic shape or magnitude, even in the pre-stalled flow region. This was probably because the geometry of the turbine was such that even in the pre-stalled region there was separated flow around the blade root. The flow close to the point of peak efficiency is shown for  $\phi=0.3$  in Figure 157, which also shows some of the tip leakage flow.

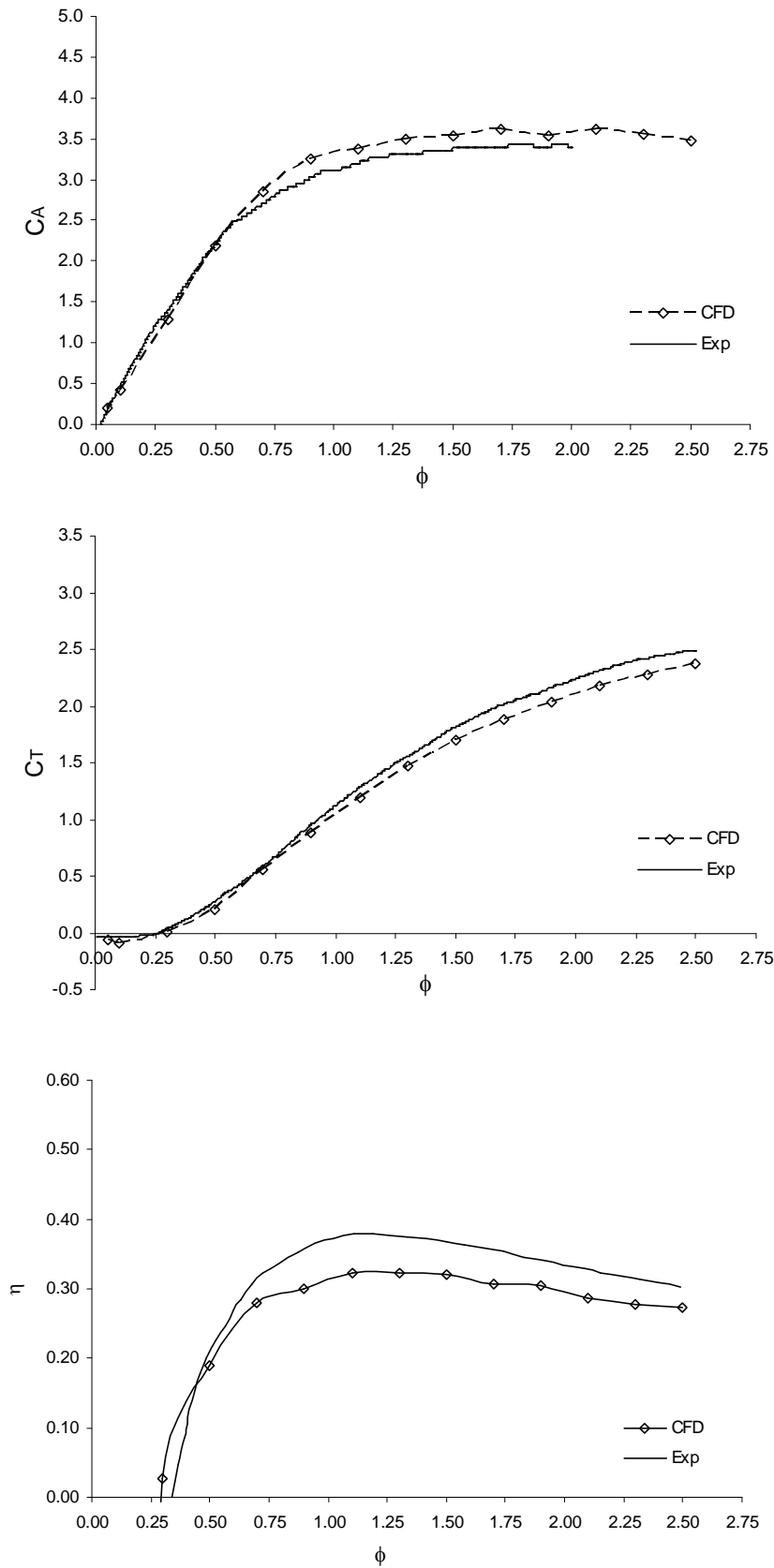


Figure 156 - Comparison of CFD and experiment for baseline impulse turbine design

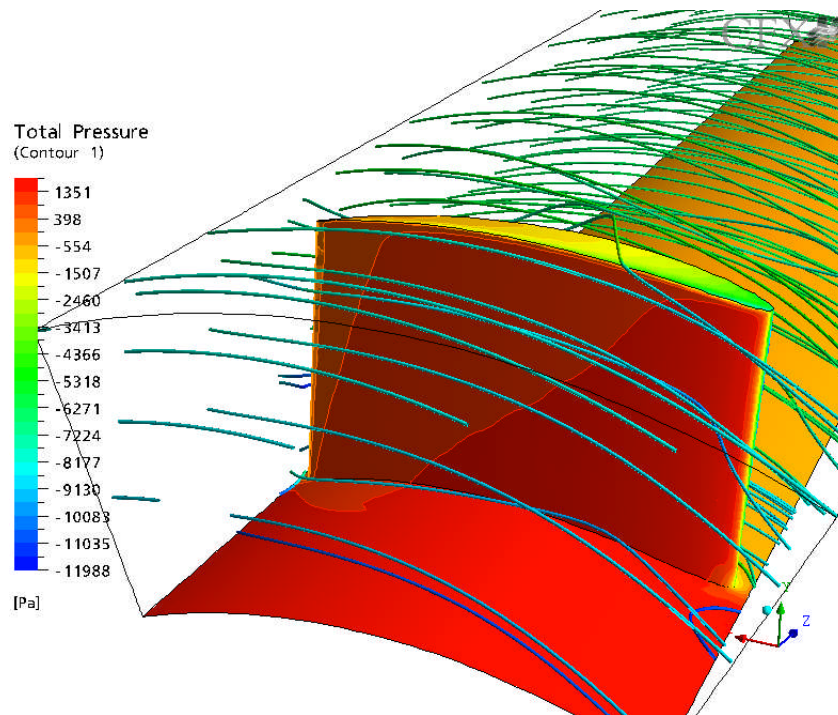


Figure 157 - Plot showing streamlines and total pressure contour for  $\phi = 0.3$  (Banks)

The peak torque coefficient for the Wells turbine was predicted to occur at a lower flow ratio and attained a lower peak value in the simulation than measured in the experiment. After the stall point was reached the torque coefficient was significantly over predicted. It thus appears that the SST model was leading to an earlier than actual prediction of separation, and an over-estimate of the work extracted post-stall. This is consistent with the known behaviour of the SST turbulence model to over predict separation (Menter F.R., 1994). In comparison, there was a consistent under-prediction of the torque coefficient for the impulse turbine, with the difference increasing with flow ratio up to about 10% at the maximum flow rate.

The prediction of torque coefficient was rather better for the impulse turbine. This was to be expected as the flow around the rotor was predicted to be relatively clean.

### 1.3.3 Efficiency

The differences between predicted and measured input power and torque coefficients for the Wells turbine led to a significant over-prediction of its efficiency (up to 12%) around the peak of its characteristic. In addition, the shape of the characteristic was changed and displaced towards lower flow ratios. The predicted efficiency of the Wells turbine was driven by the poor prediction of the variation in torque coefficient. Use of this (steady state) efficiency characteristic in system simulations would lead to an over-optimistic prediction of power output.

The results obtained in this work can be compared with those obtained by Dhanasekaran and Govardhan (Dhanasekaran and Govardhan, 2005), who carried out a simulation of a 4 bladed Wells turbine, which they compared with experimental data. In comparison to the Setoguchi design simulated here, the characteristics of the design used by Dhanasekaran and Govardhan were much closer to the optimum design values recommended by Raghunathan, as shown in Table 68.

Parameter	Raghunathan design values	Setoguchi	Dhanasekaran & Govardhan
Hub/tip ratio	0.6	0.7	0.619
Solidity	0.5	0.75	0.6
Aerofoil section thickness/chord	20%	12%	20%
Blade aspect ratio	0.5	0.6	0.5
Blade off-set	0.15	0.0	0.1
Tip clearance	<0.02	2.2%	2%

*Table 68 – Comparison of design parameters of Wells turbines*

It can be seen that the Setoguchi design had a significantly higher solidity, hub/tip ratio, blade aspect ratio, and thinner blade sections in relation to both the recommended design values and the Dhanasekaran and Govardhan design. All of these differences would be expected to reduce the efficiency of the Setoguchi design relative to the other turbines.

The simulation carried out by Dhanasekaran and Govardhan was a steady incompressible flow analysis conducted using FLUENT 6. The computational grid included modelling of the hub and nose bullet and all 4 blades, so that the measured inlet velocity profile could be applied. The downstream extent of the grid was not stated, but appears to have been 2-3 chord lengths (in comparison to 4 in the current work). The grid was composed of unstructured tetrahedral elements and comprised 620,000 nodes (in comparison to the 770,000 nodes for a single passage in the current work), and the  $k-\varepsilon$  turbulence model was used (in comparison to the SST model). The characteristics of the 2 turbines are compared in Table 69. It would thus be expected that the present solution should be a better calculation

Turbine	No. of blades	Solidity	Hub/tip ratio	Tip diameter (mm)	Section	Chord (mm)
Setoguchi	8	0.75	0.7	0.298	NACA0012	75
Dhanasekaran & Govardhan	4	0.6	0.619	0.263	NACA0021	100

*Table 69 – Comparison of Wells turbine characteristics*

The comparison between CFD and experiment efficiencies obtained by Dhanasekaran and Govardhan is shown in Figure 158. This figure shows a rather flat characteristic with no obvious peak up to stall for the experiment and some significant scatter in the experimental data. In comparison to the experimental data the CFD has over-predicted the efficiency by around 7%, and predicted stall to occur at a flow ratio of 0.17, rather than the experimentally measured flow ratio of 0.2. Thus there is consistency between

the present results and the work of Dhanasekaran and Govardhan in the trends of the CFD predictions relative to the experimental data.

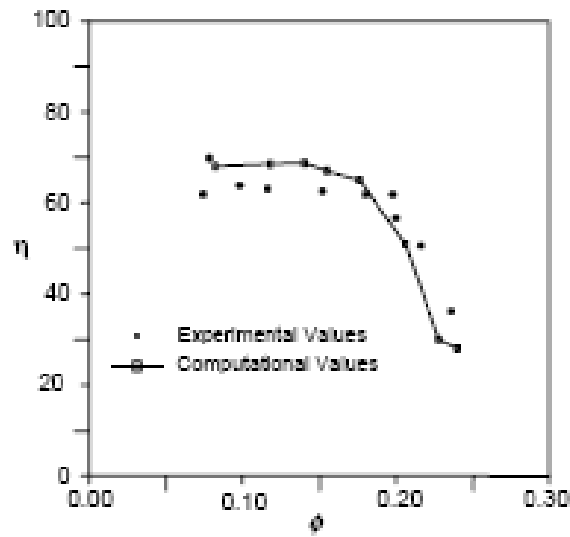


Figure 158 – Comparison of predicted and measured efficiencies with flow coefficient (Dhanasekaran and Govardhan)

In contrast to the Wells turbine simulation, the efficiency of the impulse turbine was generally under-predicted at all but the lowest flow rates. Again the maximum discrepancy occurred close to the peak efficiency flow ratio, and was some 7%. The predicted efficiency of the impulse turbine was again driven by the combination of over-estimating the input power coefficient and under-estimating the torque coefficient. The accuracy of the derived characteristic was influenced by the large region of separated flow predicted around the downstream guide vane. The extent of the separated flow at a flow ratio of  $\phi = 0.7$  is shown in Figure 159, which demonstrates the problem of using a fixed geometry as both an inlet and outlet guide vane.

Another possible contributory factor is that the static pressure used by Setoguchi in his calculation of efficiency was probably not taken in the same plane as that used in the CFD calculations. Unfortunately, he did not define where his pressure was taken, or at how many points. Furthermore, the measurement of static pressure is always subject to inaccuracies.

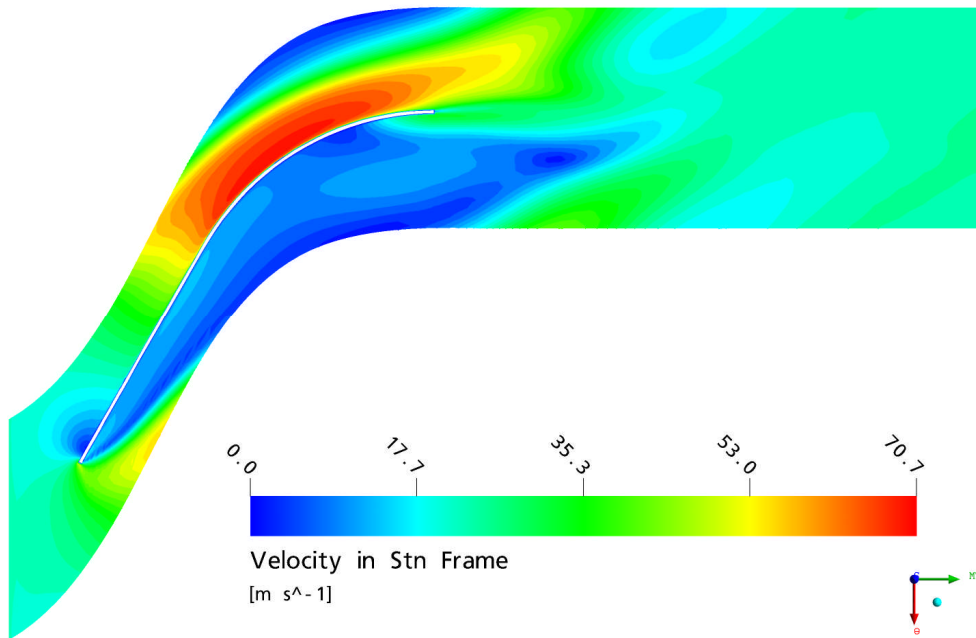


Figure 159 - Plot showing velocity contour around outlet guide vane for  $\phi = 0.7$ (Banks)

## Appendix J – Turbine Design Procedure

### J.1 Method and definitions

The approach used was based on that of Saravanamuttoo et al (Saravanamuttoo et al, 2001). The definitions of the various velocity components in the vector triangles are shown in Figure 160 and Figure 161. Velocities and angles in the absolute frame are denoted by  $C$  and  $\alpha$  respectively, whilst those in the relative frame are denoted by  $V$  and  $\beta$ . The velocity vectors shown also have axial and whirl components i.e. the absolute velocity vector  $C_1$  has axial and whirl components  $C_{a1}$  and  $C_{w1}$ .

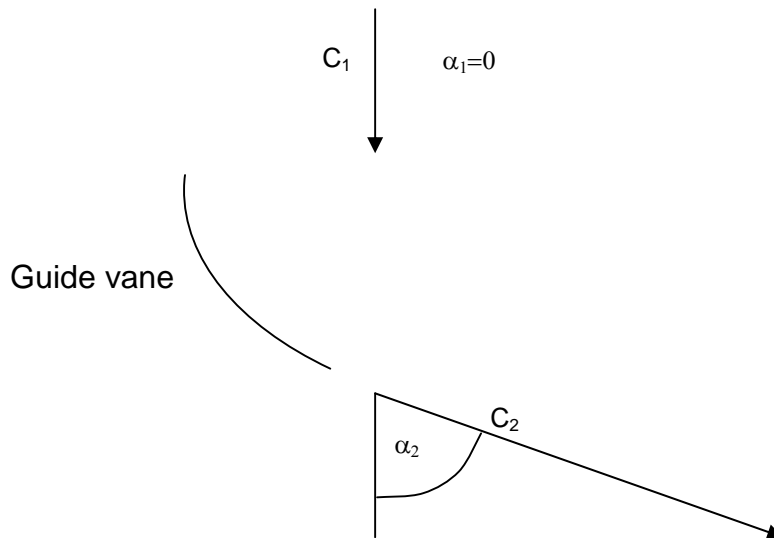


Figure 160 – Guide vane velocity vectors and angles

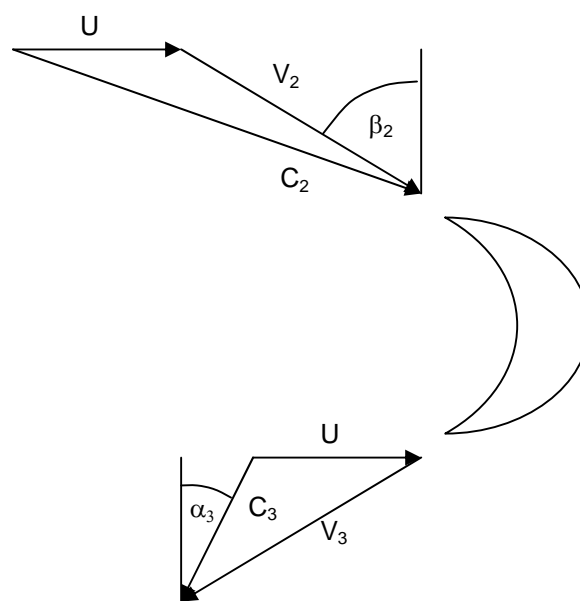


Figure 161 – Rotor velocity vectors and angles

## J.2 Inputs

The required inputs are:

Input	Parameter	Value
Power	W	4600
Design point rotational speed	RPM	850
Design $V_a/U_{mid}$	$\phi_{des}$	1.0
Tip radius	$R_{tip}$	0.3
Hub/tip ratio	h	0.82
Isentropic stage efficiency	$\eta_s$	0.85
Nozzle loss coefficient	$\lambda_n$	0.05
Inlet total pressure	$P_{0in}$	107414
Inlet total temperature	$T_{0in}$	288.15
Inlet density	$\rho_0$	1.225

Where:  $\eta_s = \frac{T_{01} - T_{03}}{T_{01} - T_{03i}}$  and  $\lambda_n = \frac{T_2 - T_{2i}}{\left(\frac{c_2^2}{2Cp}\right)}$

## J.3 Preliminary Calculations

$$A_{annulus} = \pi R_{tip}^2 (1 - h^2)$$

$$R_{mid} = \frac{1}{2} (1 + h) R_{tip}$$

$$\omega = RPM \cdot \frac{\pi}{30}$$

$$U_{mid} = \omega \cdot R_{mid}$$

$$V_a = \phi_{des} \cdot U_{mid}$$

Volumetric flowrate,  $Q = V_a \cdot A_{annulus}$

Mass flow rate,  $\dot{m} = Q \cdot \rho_0$

Stage temperature drop,  $\Delta T_0 = \frac{W}{\dot{m} Cp}$

Temperature drop coefficient,  $\psi = \frac{Cp \Delta T_0}{U_{mid}^2}$

$$\text{Stage pressure ratio, } \frac{P_{01}}{P_{03}} = \frac{1}{\left(1 - \frac{\Delta T_0}{\eta_s T_{01}}\right)^{\frac{\gamma}{\gamma-1}}}$$

#### J.4 Nozzle Calculations

Assume:

- 1) temperature drop through the nozzles is equal to the stage temperature drop.
- 2) Constant axial velocity

Inflow conditions:  $\alpha_1 = 0, \quad c_{a1} = c_1 = V_a$

From the assumptions:  $c_{a2} = V_a, \quad T_{02} = T_{01}$

$$T_1 = T_{01} - \frac{c_1^2}{2Cp}$$

$$P_1 = \left(\frac{T_1}{T_{01}}\right)^{\frac{\gamma}{\gamma-1}} \cdot P_{01}$$

$$\rho_1 = \frac{P_1}{RT_1}$$

$$A_1 = \frac{\dot{m}}{\rho_1 c_{a1}}$$

$$c_2 = \sqrt{2Cp\Delta T_0 + c_1^2}$$

$$\alpha_2 = \text{Cos}^{-1}\left(\frac{c_{a2}}{c_2}\right)$$

$$c_{w2} = c_2 \text{Sin}(\alpha_2)$$

Temperature equivalent of outlet velocity,  $T_2 = T_{02} - \frac{c_2^2}{2Cp}$

Isentropic static temperature,  $T_{2i} = T_2 - \frac{\lambda_n c_2^2}{2Cp}$

Nozzle outlet static pressure,  $P_2 = \frac{P_{01}}{\left(\frac{T_{01}}{T_{2i}}\right)^{\frac{\gamma}{\gamma-1}}}$

$$P_{02} = P_2 \cdot \left(\frac{T_{02}}{T_2}\right)^{\frac{\gamma}{\gamma-1}}$$

$$\rho_2 = \frac{P_2}{RT_2}$$

$$A_2 = \frac{\dot{m}}{\rho_2 c_{a2}}$$

Area of nozzle throat required,  $A_{2n} = \frac{\dot{m}}{\rho_2 c_2}$

## J.5 Rotor Calculations

$$v_{w2} = c_2 \sin(\alpha_2) - U_{mid}$$

$$v_{a2} = c_2 \cos(\alpha_2)$$

$$\beta_2 = \tan^{-1}\left(\frac{v_{w2}}{v_{a2}}\right)$$

$$v_2 = \frac{c_{a2}}{\cos(\beta_2)}$$

Limit feasible solutions to those with  $v_{w2} < 0.5U_{mid}$  or  $c_{w2} \geq 2U_{mid}$

Assume  $\beta_3 = \beta_2$ ,  $v_3 = v_2$

$$c_{a3} = v_3 \cos(\beta_3)$$

$$c_{w3} = v_3 \sin(\beta_3) - U_{mid}$$

$$c_3 = \sqrt{c_{a3}^2 + c_{w3}^2}$$

$$\alpha_3 = \tan^{-1} \left( \frac{c_{w3}}{c_{a3}} \right)$$

Temperature equivalent of inlet (and outlet) kinetic energy

$$T_{03} = T_{01} - \Delta T_0$$

$$T_3 = T_{03} - \frac{c_3^2}{2 C_p}$$

$$P_{03} = \frac{P_{01}}{PR}$$

$$P_3 = P_{03} \cdot \left( \frac{T_3}{T_{03}} \right)^{\frac{\gamma}{\gamma-1}}$$

$$\rho_3 = \frac{P_3}{R T_3}$$

$$A_3 = \frac{\dot{m}}{\rho_3 c_{a3}}$$

## J.6 Blade dimensions

$$\text{Blade height, } b = A \times \left( \frac{RPM}{60 U_{mid}} \right)$$

$$R_{hub} = R_{mid} - 0.5b$$

$$R_{tip} = R_{mid} + 0.5b$$

$$\text{Hub/tip ratio, } h = \frac{R_{hub}}{R_{tip}}$$

## J.7 Stage Performance Calculations

$$\text{Blade speed ratio, } Z = \frac{U_{mid}}{c_2}$$

Optimum blade speed ratio,  $Z_{opt} = \frac{\sin(\alpha_2)}{2}$

Implied value of rotor loss coefficient:

$$T_{3i} = \frac{T_2}{\left(\frac{P_2}{P_3}\right)^{\frac{\gamma-1}{\gamma}}}$$

$$\lambda_r = \frac{T_3 - T_{3i}}{\left(\frac{v_3^2}{2C_p}\right)}$$

Diagram efficiency  $\eta_d = 4\left(\frac{U_{mid}}{c_2}\right)\left[\sin(\alpha_2) - \left(\frac{U_{mid}}{c_2}\right)\right]$

Power output  $W = 2\dot{m}U_{mid}(c_2\sin(\alpha_2) - U_{mid})$

Loading coefficient  $\psi = \frac{c_{w2} + c_{w3}}{U_{mid}}$

Implied loading coefficient if rotor turning is fixed by defining  $\beta_2$   $\psi' = \frac{2v_a \tan(\beta_2')}{U_{mid}}$

## Appendix K- Development of Rotor Blade Geometry

### K.1 Profile 1

The first rotor blade profiles were created by first specifying a circular arc pressure surface  $R_1$  to give the required amount of turning. The thickness of the blade was then determined from a calculation of the number of blades required, which gave  $S_c$ , and then the passage width  $S_p$  required to maintain the relative velocity  $V_2$  through the rotor.  $R_2$  was then determined and the suction surface defined by simply joining the 2 circular arcs by straight lines as shown in Figure 162.

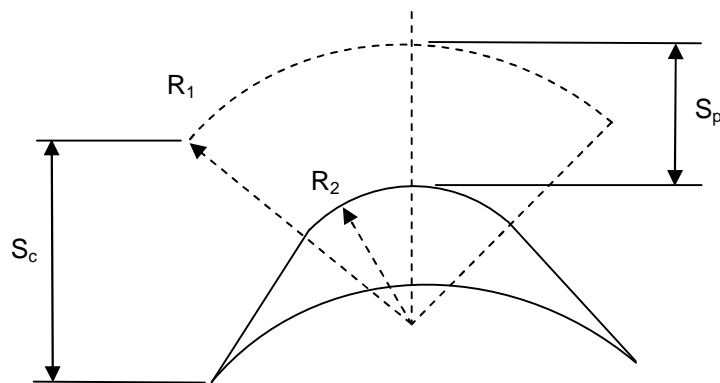


Figure 162 – Definition of first rotor blade profiles

An obvious problem with this approach was that there were dis-continuities in surface curvature where the straight lines joined arc  $R_2$ , particularly as the downstream one occurred where the flow begins to diffuse rapidly.

### K.2 Profile 2

The first profile was improved by replacing the circular arc plus straight line suction surface with a parabola through the point of maximum thickness, leading and trailing edges, as shown in Figure 163. The use of his profile led to a reduction in the amount of separation that occurred on the downstream side of the rotor, but an area of separation was evident just behind the pressure surface leading edge.

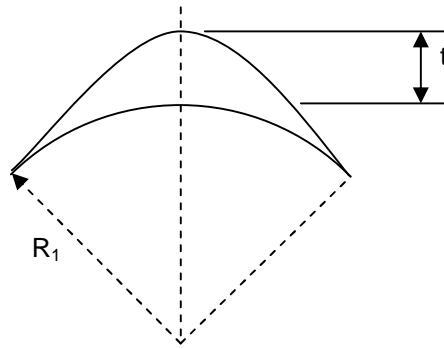


Figure 163 – Definition of second rotor blade profiles

### K.3 Profile 3

Although it was not believed that the leading edge separation observed in analyses using the second profile had a great effect on the overall performance, a third profile was developed which sought to address this, and also the amount of separation that was still observed towards the suction surface trailing edge.

The new profile was developed by using the circular arc  $R_1$  as a camber line, determining mid-points on both suction and pressure surfaces at half the maximum thickness, and then forming both surfaces by parabolic fits through the leading and trailing edge points and the mid points, as shown in Figure 164. This geometry had the effect of reducing the incidence at the leading edge and the rate of diffusion towards the suction surface trailing edge and benefits were seen with regard to both aspects.

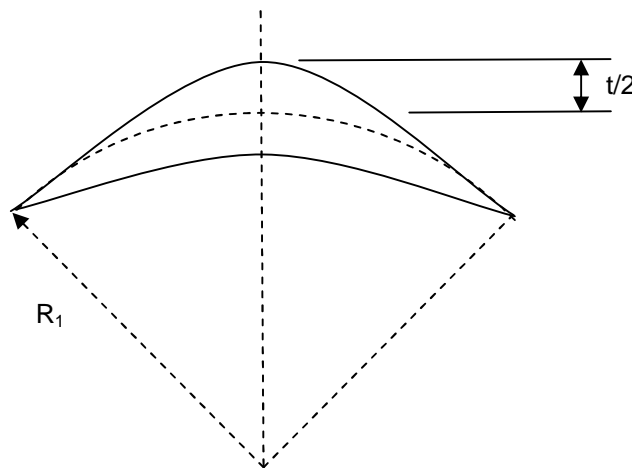


Figure 164 – Definition of third rotor profile

## Appendix L - Derivations of system simulation equations

### L.1 Basic Equation

The equation of state for a volume of gas is:

$$PV = mRT$$

Differentiating this with respect to time:

$$P \frac{\partial V}{\partial t} + V \frac{\partial P}{\partial t} = RT \frac{\partial m}{\partial t} + mR \frac{\partial T}{\partial t}$$

Dividing by  $V$ :

$$\frac{P}{V} \frac{\partial V}{\partial t} + \frac{\partial P}{\partial t} = \frac{RT}{V} \frac{\partial m}{\partial t} + \frac{mR}{V} \frac{\partial T}{\partial t}$$

$$\frac{P}{V} \frac{\partial V}{\partial t} + \frac{\partial P}{\partial t} = \frac{RT}{V} \frac{\partial m}{\partial t} + \frac{P}{T} \frac{\partial T}{\partial t}$$

Now,

$$\frac{\partial T}{\partial t} = \frac{\partial T/T}{\partial P/P} \cdot \frac{\partial P/P}{\partial t} \cdot T$$

and so,

$$\frac{P}{T} \frac{\partial T}{\partial t} = \frac{\partial T/T}{\partial P/P} \cdot \frac{\partial P}{\partial t}$$

Now in an isentropic process,

$$\left( \frac{T_2}{T_1} \right) = \left( \frac{P_2}{P_1} \right)^{\frac{\gamma-1}{\gamma}}$$

Differentiating:

$$\frac{\partial(T_2/T_1)}{\partial(P_2/P_1)} = \frac{\gamma-1}{\gamma} \left( \frac{P_2}{P_1} \right)^{-\frac{1}{\gamma}}$$

Now for small changes  $\left(\frac{P_2}{P_1}\right)^{-\frac{1}{\lambda}} \approx 1$ , and we may thus write:

$$\frac{P}{T} \cdot \frac{\partial T}{\partial t} = \frac{\gamma - 1}{\gamma} \frac{\partial P}{\partial t}$$

and so:

$$\frac{P}{V} \frac{\partial V}{\partial t} + \frac{\partial P}{\partial t} = \frac{RT}{V} \frac{\partial m}{\partial t} + \frac{\gamma - 1}{\gamma} \frac{\partial P}{\partial t}$$

Re-arranging:

$$\frac{P}{V} \frac{\partial V}{\partial t} + \frac{1}{\gamma} \frac{\partial P}{\partial t} = \frac{RT}{V} \frac{\partial m}{\partial t}$$

$$\gamma \frac{\partial V}{\partial t} + V \frac{\partial P}{\partial t} = \gamma RT \frac{\partial m}{\partial t}$$

$$\gamma P \frac{\partial V}{\partial t} = \gamma RT \frac{\partial m}{\partial t} - V \frac{\partial P}{\partial t}$$

Now,  $\gamma RT = a^2$ , and the change in the mass of gas in the volume is equal to the mass flowrate through the turbine  $\dot{m}_T$

$$\gamma P \frac{\partial V}{\partial t} = -a^2 \dot{m}_T - V \frac{\partial P}{\partial t}$$

$$\frac{\partial P}{\partial t} = \frac{1}{V} \left[ -a^2 \dot{m}_T - \gamma P \frac{\partial V}{\partial t} \right]$$

This provides an equation for the pressure of a gas within a volume as the size of the volume is varied, and gas is allowed to enter or leave the volume. Now, if we are considering an OWC then the size of the gas volume depends on the cross sectional area  $A_c$  and the height of the water in the column, i.e:

$$V = V_0 - A_{owc} \cdot h_{water}$$

$$\frac{\partial V}{\partial t} = -A_c \cdot \frac{\partial h}{\partial t}$$

$$\frac{\partial P}{\partial t} = \frac{1}{V} \left[ \gamma P A_c \frac{\partial h}{\partial t} - a^2 \dot{m}_T \right]$$

If it is assumed that the initial pressure in the OWC is due to the adiabatic compression of the gas by the water rising to the initial height, then as  $PV^\gamma = \text{constant}$

$$\Delta P = P_1 \left[ \left( \frac{v_1}{v_2} \right)^\gamma - 1 \right]$$

The density of the gas can be found at any time can then be found from:

$$\rho = \rho_1 \left[ 1 + \frac{\Delta P}{P_1} \right]^\frac{1}{\gamma}$$

or assuming that the changes in pressure are small:

$$\frac{\partial P}{P} = \gamma \frac{\partial \rho}{\rho}$$

$$\rho = \rho_1 \left[ 1 + \frac{\Delta P}{\gamma P_1} \right]$$

## L.2 Determination of power output from turbine

The pressure differential across the turbine is converted to an equivalent across the reference turbine using the relationship:

$$\Delta P_{ref} = \Delta P \cdot \frac{\rho_0 U_{ref}^2}{\rho U^2}$$

The mass flow rate through the reference turbine and the corresponding value of efficiency ( $\eta$ ) are then found from its characteristic by interpolation, and the mass flowrate through the actual turbine determined from:

$$\dot{m} = \dot{m}_{ref} \cdot \frac{\rho U A_{Turbine}}{\rho_0 U_{ref} A_{ref}}$$

The volumetric flowrate  $Q$  is then determined from the variation of density with time, and the power output from:

$$P_{out} = Q \Delta P \eta$$

### L.3 Variation in Generator RPM

It is important to understand how the speed of the turbine, and hence generator vary in the OWC application. This is carried out in the simulation program after the variation in pressure in the volume and power output have been determined, as follows. The torque ( $\tau$ ) due to a change in angular acceleration is:

$$\tau = I \frac{d\omega}{dt}$$

where  $I$  is the moment of inertia of the turbine, drive train and generator.

Now, neglecting windage and bearing losses, the net output power of the turbine is  $P_{turbine} = \omega\tau$ , and revolutions per second,  $RPS = \omega/2\pi$ , and we may substitute for  $\tau$  and  $\omega$  to obtain::

$$\frac{d RPS}{dt} = \frac{P_{turbine}}{(2\pi)^2 RPS \cdot I}$$

If we now define a reference RPM for the generator and say that the generator will run at this speed when the turbine produces a power output equal to its mean power output over the whole time period, then if we assume that the torque on the generator changes with the square of rotational speed then the angular acceleration of the generator due to changes in turbine power relative to a reference RPM can be defined as:

$$\frac{d RPS}{dt} = \frac{P_{turbine} - \bar{P}_{turbine} \left( \frac{60 \cdot RPS}{RPM_{ref}} \right)^2}{(2\pi)^2 RPS \cdot I}$$

This is a differential equation which can then be solved to find the variation in turbine and generator RPM.

## Appendix M – Test Conditions for Datum Turbine

The test conditions which were input to the PWG in testing the datum turbine are detailed in Table 70.

Desired Profile		PWG control parameters		
Nominal rms flowrate (m <sup>3</sup> /s)	Nominal period (s)	Acc	Speed	P1
1.5	14	3	448	11968
	10	4	448	8549
	9	4	448	7694
	7	6	448	5984
	5	11	448	4274
1.77	14	4	528	14122
	10	6	528	10087
	9	5	528	9079
	7	8	528	7061
	5	13	528	5044
2.3	14	4	686	18351
	10	8	686	13108
	9	8	686	11797
	7	11	686	9175
	5	18	686	6554
2.65	12	7	791	18123
	10	8	791	15103
	9	9	791	13592
	7	14	791	10572
	5	22	791	7551
3.0	10	10	895	17097
	9	11	895	15387
	7	16	895	11968
	5	25	895	8549

Table 70 – PWG control parameters for Datum Turbine test conditions

## Appendix N - Calculation of turbulent Stokes parameter

The friction velocity was evaluated by assuming a Preston tube arrangement (Preston, 1954) by making the following calculations, based upon the average instrumentation plane values when the difference between the total and static pressures was a maximum.

- p average instrumentation plane static pressure  
 $P_0$  average instrumentation plane total pressure  
 T average instrumentation plane temperature (assuming the difference between the total and static temperature is small)

$$\rho = \frac{P}{RT}$$

$$\mu_{wall} = 1.458 \times 10^{-6} \left( \frac{T^{\frac{3}{2}}}{T + 110.4} \right)$$

$$v = \frac{\mu_{wall}}{\rho}$$

$$x = -1.396 + 0.875 \log_{10} \left[ \frac{(P_0 - p)d^2}{4\rho v^2} \right]$$

Then:

$$\tau_w = \frac{4\rho v^2}{d^2} \times 10^x$$

and the maximum friction velocity is:

$$U_* = \sqrt{\frac{\tau_w}{\rho}}$$

The turbulent Stokes parameter  $\omega D/U_*$  can then be calculated knowing that the hydraulic diameter at the instrumentation plane is  $0.308 \text{ m}^2$ , and the relevant period of the oscillatory flow.